

Development and Testing of a Detector to Study Neutrino Oscillations at Palo Verde

Thesis by
Brian M. Cook

In Partial Fulfillment of the Requirements
for the Degree of
Doctor of Philosophy



California Institute of Technology
Pasadena, California

1996
(Submitted May 13, 1996)

© 1996

Brian M. Cook

All Rights Reserved

Acknowledgements

I wish to express my gratitude for the guidance and support given me by my advisor, Professor Felix Boehm. His wealth of experience and clear thinking have been an inspiration to me throughout my graduate studies.

I also wish to thank Petr Vogel who always had time to answer my questions and whose sense of humor made our many discussions so enjoyable.

I feel privileged to have worked closely with so many wonderful colleagues. Thanks to Austyn Griffiths and fellow graduate student Mark Chen for their friendship, and to Albert Young who taught me the value of persistence. Thanks to Ralf Hertenberger, Nick Mascarenhas, and Kegang Lou for all their help, and to Vladimir Novikov, who always had a new way of looking at things. Yongzhong Qian provided an invaluable theorist's perspective, and I'm indebted to him for many helpful discussions. I also wish to thank Andreas Piepke with whom I've worked very closely over the past couple of years. He has taught me much about experimental physics, including the proper techniques for moving several tons of lead bricks.

Herb Henrikson has been enormously helpful; I truly believe he can fix anything. Most of all, he taught me not to take myself too seriously. Without him, I'm not sure I could have maintained my sanity.

Special thanks go to Sylvie Bradley and Elsa Villate. Their help and friendship has made working with this group a true delight.

I gratefully acknowledge the financial support of the California Institute of Technology and the National Science Foundation.

I would also like to thank my parents and parents-in-law who always believed in me and supported my every endeavor. And to my grandfather, in whose footsteps I am following, I wish to express my heartfelt thanks. His example has been an inspiration, and I dedicate this thesis to him.

And finally, to my wife, Nipa, and daughter, Tori, I express my deepest gratitude

for their love and understanding.

Abstract

A detector for the study of neutrino oscillations with a projected sensitivity to Δm^2 of 10^{-3} eV² and to $\sin^2 2\theta$ of 0.1 is described. It is to be installed 800 m from three pressurized water reactors at the Palo Verde Nuclear Generating Station near Phoenix, Arizona. The detector is segmented and filled with 12 tons of gadolinium-loaded liquid scintillator. It will be placed in an underground vault with an overburden of 46 *mwe* and surrounded by a 1-m-thick water buffer and a hermetic active muon veto. Reactor antineutrinos are detected through proton inverse β decay in the hydrogen-rich scintillator, and the resulting positrons are discriminated from fast neutron background by requiring a prompt coincidence across several cells between the positron and its annihilation radiation.

Test results from prototype detector elements are presented showing excellent stability of the scintillator and acrylic target cells. A method of calibrating the positron detection efficiency is described in detail, and results of a prototype experiment using a small-scale detector are presented. The results of a full-detector Monte Carlo simulation, based on the CERN and Oak Ridge packages GEANT and GCALOR, are discussed: anticipated backgrounds due to natural radioactivity and to fast neutrons are described in detail.

Contents

Acknowledgements	iii
Abstract	v
1 Searching for Neutrino Oscillations	1
1.1 The Physics of Neutrino Oscillations	1
1.2 Experimental Searches	4
1.2.1 The Solar Neutrino Puzzle	4
1.2.2 Reactor Experiments	6
1.2.3 Accelerator Experiments	8
1.2.4 The Atmospheric Neutrino Anomaly	10
1.3 The Next Generation	11
1.3.1 The Palo Verde Experiment	13
2 The Experiment	14
2.1 The Detector	15
2.1.1 The Detection Concept	15
2.1.2 The Target Cells	16
2.1.3 The Water Buffer	17
2.1.4 The Muon Veto	18
2.2 The Neutrino Source	19
2.2.1 An Estimate of the Reactor-Induced Positron Spectrum at Palo Verde	21
2.3 The Experimental Sensitivity	23
3 Tests of a Prototype Detector	29
3.1 Mechanical Stability	29

3.2	The Detector γ Response	30
3.3	The Energy Resolution	32
3.4	The Cell Timing Response	34
3.5	The Detector Time Stability	36
3.6	Gadolinium in the Scintillator	39
3.7	Conclusion	42
4	Calibration of the Positron Detection Efficiency	44
4.1	The Concept	44
4.2	Efficiency Calibration Requirements	47
4.3	Source Calibration	48
4.3.1	The Electronics Readout	49
4.3.2	Data Analysis	50
4.3.3	Precision and Reproducibility	52
4.4	Summary of Source Tests and Results	57
4.5	Prototype Calibration Experiment	58
4.5.1	Cell Array Energy Calibration	59
4.5.2	Data Acquisition	61
4.5.3	The Experiment	64
4.5.4	The Monte Carlo Simulation	65
4.5.5	Efficiency Results	75
4.6	Conclusion	77
5	Full Detector Simulation Using GEANT-GCALOR	81
5.1	Introduction	81
5.2	General Parameters of the Simulation	81
5.2.1	The Detector Geometry	81
5.2.2	The Tracking	82
5.2.3	The Data Structure	84
5.3	The Neutrino Detection Efficiency	86
5.3.1	The Positron Detection Efficiency	86

5.3.2	The Neutron Detection Efficiency	93
5.4	The Correlated Background	101
5.4.1	Fast Neutron Correlated Background	101
5.4.2	The Simulation	101
5.4.3	Neutron Background Analysis	104
5.4.4	Correlated Background From μ -Induced Radioactivities	105
5.4.5	Summary of Correlated Backgrounds	107
5.5	The Uncorrelated Background	108
5.5.1	Natural Radioactivities	108
5.5.2	Muon-Induced Radioactivities	116
5.5.3	Neutron Soup	117
5.5.4	Summary of Uncorrelated Backgrounds	121
5.6	Conclusion	122
6	Systems Under Development	125
6.1	The Neutron Detection Efficiency	125
6.1.1	The SbBe Source	125
6.1.2	The AmBe Source	126
6.2	The Energy Calibration System	127
6.3	The LED Gain Monitor	128
A	Details on the Positron Detection Efficiency Calibration	131
A.1	Chemical Preparation of the Source	131
A.1.1	Isotope Exchange Procedure	131
A.1.2	Tetra-n-butylgermane Synthesis	132
A.2	Effect of Ge Loading on Scintillator Properties	134
A.2.1	Attenuation Length	134
A.2.2	Light Yield	135
B	Details of the Detector Simulation	140
B.1	The Tracking of Neutrons From the Walls	140

B.2	Analysis of the Neutron Spectra From Muon Capture and Spallation	147
B.2.1	Neutrons From Muon Capture	147
B.2.2	Neutrons From Muon Spallation	149
B.2.3	Leakage Through the Veto	153
B.3	Modeling Radioactive γ Cascades	157
C	Tests of Neutron Tracking with GEANT-GCALOR	162
C.1	Summary	162
C.2	Introduction	162
C.3	Neutron Transport Through Concrete and Iron	163
C.3.1	Effect on the Palo Verde Detector Simulation	166
C.4	Neutron Detection Efficiency of Liquid Scintillator	166
C.4.1	Neutron Light Production in Scintillator	166
C.4.2	Neutron Detection Efficiency	168
C.5	Conclusion	170
D	AmBe Neutron Background Measurement	176
D.1	Introduction	178
D.2	The Experiment	179
D.2.1	The Neutron Source	179
D.2.2	The Detector	179
D.2.3	Data Taking	183
D.3	Experimental Results	184
D.3.1	Evidence That the Measured Signal is Due to Neutrons	187
D.3.2	Experimental Triple Coincidence Probabilities	189
D.3.3	Influence of the Trigger Topology	190
D.3.4	Threshold Dependence	193
D.3.5	Systematic Errors	196
D.4	Neutron Capture and Thermalization	197
D.5	The Monte Carlo Simulation	197
D.5.1	Inputs	197

D.5.2	The Energy Distribution of the Neutron Source	199
D.5.3	The Simulation	200
D.5.4	Results and Comparison with the Experiment	202
D.6	Conclusion	209
	Bibliography	211

List of Figures

1.1	Oscillation parameters allowed by solar neutrino experiments	6
1.2	A three-flavor mixing hypothesis	7
1.3	Excluded oscillation parameters coupling to ν_e	8
1.4	Excluded oscillation parameters coupling to ν_μ	10
1.5	$\nu_\mu - \nu_e$ oscillation parameter space allowed by KAMIOKANDE.	12
2.1	Schematic depiction of reactor site.	14
2.2	Detection of reactor $\bar{\nu}_e$ by inverse β decay.	16
2.3	The neutrino detector	17
2.4	Expected positron spectrum at Palo Verde for no oscillations.	24
2.5	The positron spectrum in the presence of oscillations.	25
2.6	$\nu_e \rightarrow \nu_x$ oscillation parameter space excluded at 90% C.L.	28
3.1	Details of a 9-m prototype cell.	30
3.2	Spectrum of ^{232}Th in a 9-m prototype cell.	31
3.3	The position dependence of the energy calibration	33
3.4	LED spectra measured by a 9-m prototype cell.	35
3.5	Calculation of the 9-m cell resolution	36
3.6	Time difference spectra of the 9-m detector at 1 MeV	37
3.7	The timing resolution of the 9-m detector at 1 MeV	38
3.8	Relative attenuation as a function of distance in a 9-m cell	40
3.9	Relative attenuation as a function of time	41
3.10	Gamma spectrum of activated scintillator	42
4.1	Topologically-distinct positron cell positions for efficiency calculation: top, side, corner, and center.	46
4.2	Simplified level scheme of ^{68}Ge decay.	47

4.3	^{68}Ge calibration apparatus	50
4.4	Calibration system electronics readout	51
4.5	Relative shift of ^{68}Ge singles and coincidence spectra.	53
4.6	Decay scheme of ^{22}Na	54
4.7	Reproducibility of the ^{68}Ge activity measurements	56
4.8	Gösgen cell array used in prototype efficiency calibration.	60
4.9	Compton edge energy calibration	62
4.10	Typical calibration curves	63
4.11	The measured ^{68}Ge spectrum in the Gösgen cell array	66
4.12	Experimental and simulated gamma spectra in the Gösgen cells . . .	68
4.13	Calculated ^{68}Ge - ^{68}Ga β^+ spectrum	69
4.14	LED energy resolution determination	70
4.15	Position dependence of the Gösgen cell energy calibration	71
4.16	Experimental and simulated spectrum of ^{68}Ge stuck to the cell walls .	73
4.17	Comparison of the experimental and simulated ^{68}Ge spectra in the Gösgen cell array	74
4.18	Positron detection efficiency: horizontal topology	76
4.19	Positron detection efficiency: 9-block topologies	78
4.20	Positron detection efficiency: 9-block comparison of experiment and simulation	79
4.21	Positron detection efficiency: Logical OR of 9-block	80
5.1	Detector end view	82
5.2	Detector cut away side view	83
5.3	Detector exploded view	84
5.4	Energy correction vs. position along target cell.	86
5.5	Input positron spectrum.	87
5.6	Detected positron spectrum.	88
5.7	Topological analysis cuts.	90
5.8	Positron triple coincidence analysis.	91

5.9	Map of cell numbers.	92
5.10	Neutron containment in scintillator.	95
5.11	Detected gamma spectra from neutron capture on gadolinium.	98
5.12	Detected gamma spectra from neutron capture on gadolinium.	99
5.13	Neutron 9–block triple coincidence efficiency	104
5.14	Signal and background reduction factors due to topological cuts.	105
5.15	Gamma production volume saturation	109
5.16	Propagation of ^{232}Th gammas from the wall to the fiducial volume.	110
6.1	Placement of energy calibration tubes	129
A.1	Tetra-n-butylgermane synthesis apparatus	133
A.2	Tetra-n-butylgermane synthesis reaction.	133
A.3	Attenuation length measuring apparatus	135
A.4	Attenuation length of unloaded and Ge–loaded scintillator	136
A.5	Light yield measurement of unloaded and Ge–loaded scintillator	138
B.1	Neutron production volume saturation	141
B.2	Neutron propagation from walls.	142
B.3	Secondary gammas from neutron propagation.	144
B.4	Shielding factors for veto and water/oil buffer.	145
B.5	Extracted neutron removal lengths for water, oil, and concrete	146
B.6	Triples rate due to neutrons from muon capture	149
B.7	Muon paths for spallation integration	150
B.8	Candidate neutron production spectra from muon spallation	152
B.9	Triples rate due to neutrons from muon spallation	154
B.10	Contour plot of the background triple rate.	155
C.1	Peak fluence of neutrons traversing iron and concrete	164
C.2	Total Neutron Cross Section on Iron. Points extracted from a GEANT– GCALOR simulation are compared with experimental data.	165
C.3	Simulated and experimental energy to light conversion	169

C.4	Neutron detection efficiency: experiment of Howe et al. vs. GEANT-GCALOR	171
C.5	Neutron detection efficiency: experiment of Paticchio et al. vs. GEANT-GCALOR	172
C.6	Neutron detection efficiency: experiment of Ito et al. vs. GEANT-GCALOR	173
C.7	Neutron detection efficiency: experiment of Cierjacks et al. vs. GEANT-GCALOR	174
D.1	The experimental apparatus	181
D.2	^{137}Cs Compton calibration spectrum	182
D.3	^{232}Th Compton calibration spectrum	182
D.4	Energy spectrum of the <i>AmBe</i> neutron source	185
D.5	Distance vs. counting rate in detector cells	188
D.6	Energy spectra of side cells using measured calibration	191
D.7	Energy spectra of side cells using shifted calibration	191
D.8	Horizontal triple coincidences	194
D.9	Vertical triple coincidence probabilities	195
D.10	Neutron thermalization and capture time	198
D.11	Monte Carlo inputs for <i>AmBe</i> neutron source spectrum generation .	200
D.12	Monte Carlo input neutron spectrum	201
D.13	Measured and simulated energy spectrum of cell 3	203
D.14	Measured and simulated energy spectrum of cell 8	204
D.15	Simulated spectral contribution of 4.4 MeV gamma rays	205
D.16	Measured and simulated triple coincidence probabilities	207
D.17	Overview of neutron background rejection	208

List of Tables

4.1	^{22}Na point source test calibration	55
4.2	^{68}Ge source calibration: dependence on energy interval	55
4.3	Investigation of ^{68}Ge source chemical stability	58
5.1	Simulated positron detection efficiency	91
5.2	Gamma detection efficiency from neutron capture.	100
5.3	Summary of correlated backgrounds in the neutrino detector	107
5.4	Uncorrelated triple-coincidence background from natural radioactivities.	123
5.5	Uncorrelated background rate.	124
5.6	Signal and background rates in the neutrino detector	124
A.1	Light yield measurement of unloaded and Ge-loaded scintillator	139
B.1	Background from spallation neutrons	153
B.2	Background from neutrons produced inside the detector	156
B.3	Cascade probability table for the ^{238}U decay chain.	158
B.4	Cascade probability table for the ^{232}Th decay chain.	159
B.5	Cascade probability table for the ^{222}Rn decay chain.	160
B.6	Cascade probability table for ^{40}K decay.	160
B.7	Cascade probability table for ^{60}Co decay.	161
D.1	Comparison of the mean free path lengths of neutrons and γ -radiation, measured and estimated for lead, copper and liquid scintillator	187
D.2	Experimental triple coincidence probabilities for different cells and trig- ger topologies.	192
D.3	Integrated singles event rates for various trigger conditions	202
D.4	Simulated triple coincidence probabilities.	206
D.5	Neutron and gamma contributions to triple rate	209

Chapter 1

Searching for Neutrino Oscillations

In a 1955 paper [1], Gell-Mann and Pais introduced the exciting possibility of particle-antiparticle oscillations in the neutral kaon system. They argued that the eigenstates K^0 and \bar{K}^0 , produced in strong interactions, were actually superpositions of the states, later known as K_L^0 and K_S^0 , responsible for the weak decay of the kaon. This idea led Pontecorvo [2], in 1958, to suggest that the neutrino, too, was a mixed state, leading to lepton-number-violating $\nu-\bar{\nu}$ oscillations. Later, after the muon neutrino was proved to be a distinct particle, Maki et al. [3] extended this idea to oscillations between the neutrino flavors. Pontecorvo continued to pursue neutrino oscillations and worked to tie them in with the new Weinberg-Salam [4] unified electroweak theory, postulating a mixing of the leptons analogous to the Cabibbo mixing of the quarks. The production of neutrinos by the weak interaction, he argued, was analogous to the production of K's by the strong interaction. Then, just as $K^0 - \bar{K}^0$ oscillations were induced by the strangeness-violating weak interaction, $\nu_e - \nu_\mu$ oscillations were induced by a new, even weaker, lepton-number-violating force. In 1978, Pontecorvo and Bilenky [5] wrote a review article summarizing the experimental situation and laying out the now standard treatment of neutrino flavor oscillations.

1.1 The Physics of Neutrino Oscillations

In analogy with the quark sector in which the mass eigenstates of the d, s , and b quarks are observed to mix in weak interactions according to the Kobayashi–Maskawa mixing matrix [6], we can write the familiar neutrino flavor eigenstates as a linear

combination of mass eigenstates:

$$\nu_l = \sum_{i=1}^N U_{li} \nu_i, \quad (1.1)$$

where $\nu_l (l = e, \mu, \tau, \dots, N)$ are the N flavor eigenstates which participate in weak interactions, $\nu_i (i = 1, 2, 3, \dots, N)$ are the mass eigenstates, and U_{li} are components of a unitary mixing matrix. The mass eigenstates propagate through time according to

$$|\nu_i(t)\rangle = e^{-iE_i t} |\nu_i(0)\rangle. \quad (1.2)$$

Thus a neutrino of flavor l created in a weak interaction at $t = 0$ can be described at time t by the state

$$|\nu_l(t)\rangle = \sum_i U_{li} |\nu_i(t)\rangle \quad (1.3)$$

$$= \sum_i U_{li} e^{-iE_i t} |\nu_i(0)\rangle. \quad (1.4)$$

Then the probability of detecting some other flavor, $l' \neq l$, at time t is given by

$$P_{ll'} = |\langle \nu_{l'} | \nu_l(t) \rangle|^2 \quad (1.5)$$

$$= \left| \sum_{i,j} \langle \nu_j | U_{j l'}^\dagger U_{li} e^{-iE_i t} | \nu_i \rangle \right|^2 \quad (1.6)$$

$$= \left| \sum_i U_{i l'}^\dagger U_{li} e^{-iE_i t} \right|^2 \quad (1.7)$$

$$= \sum_{i,k} U_{l' i}^* U_{li} U_{l' k} U_{lk}^* e^{i(E_k - E_i)t} \quad (1.8)$$

$$= \sum_i |U_{li}|^2 |U_{l' i}|^2 + \text{Re} \sum_{i,k \neq i} U_{li} U_{l' i}^* U_{lk}^* U_{l' k} e^{i(E_k - E_i)t}. \quad (1.9)$$

In the ultrarelativistic limit,

$$E_i = \sqrt{p_{\nu_i}^2 + m_i^2} \approx p_\nu + \frac{m_i^2}{2p_\nu},$$

where m_i is the mass of the eigenstate and p_ν is the common neutrino momentum. Then 1.9 can be written

$$P_{ll'} = \sum_i |U_{li}|^2 |U_{l'i}|^2 + \text{Re} \sum_{i,k \neq i} U_{li} U_{l'i}^* U_{lk}^* U_{l'k} e^{i \frac{m_k^2 - m_i^2}{2p_\nu} L}. \quad (1.10)$$

Here time, t , has been replaced by length, L , which are equivalent in these units.

From 1.10 it is clear that the ‘‘oscillation probability’’ of detecting a system in state l' , starting from a system in state l , is periodic in distance with a characteristic oscillation length that is a function of the squared-mass differences of the various eigenstates and the neutrino momenta.

From equation 1.10 we see that in the case of three neutrino flavors, the oscillation will depend in general on two independent mass differences and, just as in the Kobayashi–Maskawa [6] mixing of the quarks, three mixing angles and a phase. Six independent parameters make analysis of experimental results (and display of exclusion plots) very complicated. However, since no confirmed evidence of neutrino oscillations has ever been found, we can simplify the analysis by considering oscillations between only two neutrino flavors. This reduces the number of parameters to two: one mass difference and one mixing angle, and allows for a simpler description of the parameter space explored by an experiment. (See Refs. [7] and [8] for examples of a limited three-flavor analysis using four parameters). In this simple case the unitary mixing matrix, U , can be written as

$$U = \begin{pmatrix} \cos \theta & \sin \theta \\ -\sin \theta & \cos \theta \end{pmatrix}. \quad (1.11)$$

Equation 1.10 then simplifies to

$$P_{ll'} = \sin^2 2\theta \sin^2 \left(\frac{\Delta m^2 L}{4p_\nu} \right) \quad (1.12)$$

$$= \sin^2 2\theta \sin^2 \frac{1.27 \times \Delta m^2 [eV^2] \times L [m]}{E_\nu [MeV]}, \quad (1.13)$$

where $\Delta m^2 = |m_2^2 - m_1^2|$ is in units of eV^2 , the distance, L , is in meters, and the approximation $E_\nu \approx p_\nu$ has been made. From 1.13 we see right away that a reactor experiment with $E_\nu \sim \text{few MeV}$ and $L \sim 1000$ meters will be sensitive to Δm^2 of $\sim 10^{-3} \text{ eV}^2$. Indeed, because of the low energy (up to about 8 MeV) of reactor neutrinos, stringent limits on Δm^2 can be set with quite reasonable source-detector distances using relatively small and inexpensive detectors. For this reason, reactor-based neutrino experiments played an important role in early oscillation searches and continue to provide the best sensitivity to small mass differences.

1.2 Experimental Searches

In the early 1970's, results began to come in from a C_2Cl_4 radiochemical detector installed deep in the Homestake Mine in South Dakota. Using the detection reaction

$$\nu_e + {}^{37}\text{Cl} \rightarrow e^- + {}^{37}\text{Ar},$$

the experiment was designed to look for neutrinos produced through nuclear fusion in the sun. Periodically, the ${}^{37}\text{Ar}$, which decays by K-shell electron capture, would be extracted and counted in shielded, low-background proportional counters to determine the production rate. The reported results [10] for the 1970-1975 data indicated that only about 22% of the expected flux was observed. These early results prompted a flurry of activity in the mid 70's. Oscillation experiments were planned at a number of reactors and accelerators, and soon other underground experiments began to confirm the Homestake results. Today, over twenty years later, the Homestake flux deficit persists; the 1970-1992 data set [11] can account for only 35% of the expected solar neutrino flux, calculated according to the "Standard Solar Model" (SSM).

1.2.1 The Solar Neutrino Puzzle

In 1986, the KAMIOKANDE [12] detector, a large underground water Cherenkov detector, turned its attention to the solar neutrino flux anomaly. Neutrinos are detected

in KAMIOKANDE through Cherenkov light produced by ν_e -electron scattering. By the directionality of the Cherenkov cone, the trajectory of the incoming neutrino can be determined, verifying that it does indeed point back to the sun. Results from KAMIOKANDE indicate that only 50% of the expected solar neutrino flux is accounted for.

Similarly, two radiochemical experiments, SAGE [13] and GALLEX [14], exploit the low energy threshold for neutrino capture on gallium to explore a fraction of the solar neutrino spectrum much less sensitive to the solar core temperature uncertainty allowed by the SSM. These experiments also report a large deficit in the expected neutrino flux, measuring 55% and 58% of the expected rate, respectively.

These experiments impose severe constraints on solar model explanations of this so-called “solar neutrino puzzle.” There is no resolution of this puzzle at present, but many have suggested that electron neutrinos produced in the sun could oscillate into other types not detected by the underground experiments. In fact, the density profile of the sun could amplify this oscillation through the MSW [15, 16] effect: because ordinary matter is made of electrons and nucleons (as opposed to muons or taus), the ν_e components of a neutrino state propagating through matter can interact via charged-current in addition to neutral-current weak interactions whereas the μ and τ -type neutrino components can interact only via the neutral current. This extra interaction of electron-type neutrinos produces a different refractive index for the neutrino components and can produce a resonant conversion of electron neutrinos into another type, effectively depleting the solar ν_e flux.

Solutions of the solar neutrino problem involving matter oscillations require mass differences, Δm^2 , to be in the range of $10^{-4} \sim 10^{-7} \text{ eV}^2$, much smaller than the 10^{-3} eV^2 range probed by the Palo Verde reactor experiment (see Figure 1.1). However, a recent consideration of maximal three-fold lepton mixing [17] suggests that the solar neutrino deficit and the atmospheric anomaly, discussed below, could be explained by a hierarchical neutrino mass structure with a dominant $\Delta m^2 = 7.2 \times 10^{-3} \text{ eV}^2$ and full mixing, an area of parameter space easily accessible to the Palo Verde experiment. Figure 1.2, taken from [17], displays the survival probability measured

in a number of disappearance experiments as a function $L[m]/E[\text{MeV}]$. Also shown is the L/E range to be explored by the Palo Verde experiment. If this mixing hypothesis is correct, Palo Verde should measure a large effect.

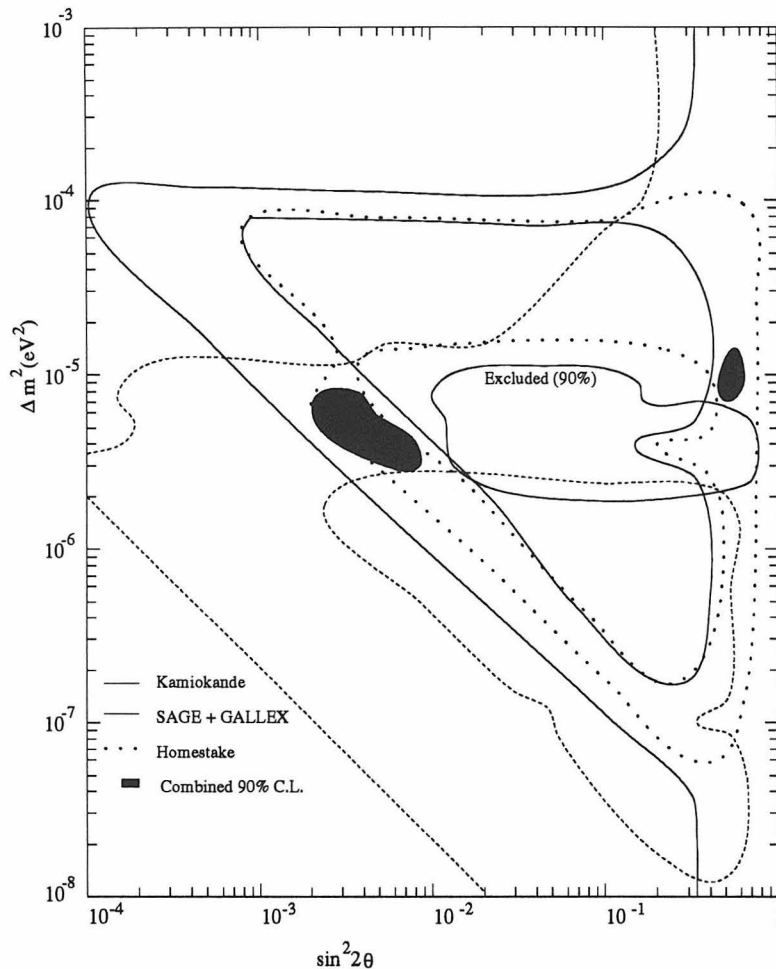


Figure 1.1: Oscillation parameters allowed by a matter neutrino oscillation explanation of solar neutrino flux deficits observed in the Homestake, KAMIOKANDE, GALLEX, and SAGE experiments.

1.2.2 Reactor Experiments

In 1976, an experiment was initiated at the ILL pressurized water reactor in Grenoble [18]. A detector, based on the reaction $\bar{\nu}_e + p \rightarrow e^+ + n$ was installed 8.7 m from the core of the reactor to investigate $\bar{\nu}_e$ disappearance. By a comparison of the number and spectral shape of the detected electron antineutrinos, oscillations at large mixing angle were ruled out down to Δm^2 of 0.1 eV². The ILL group relocated to

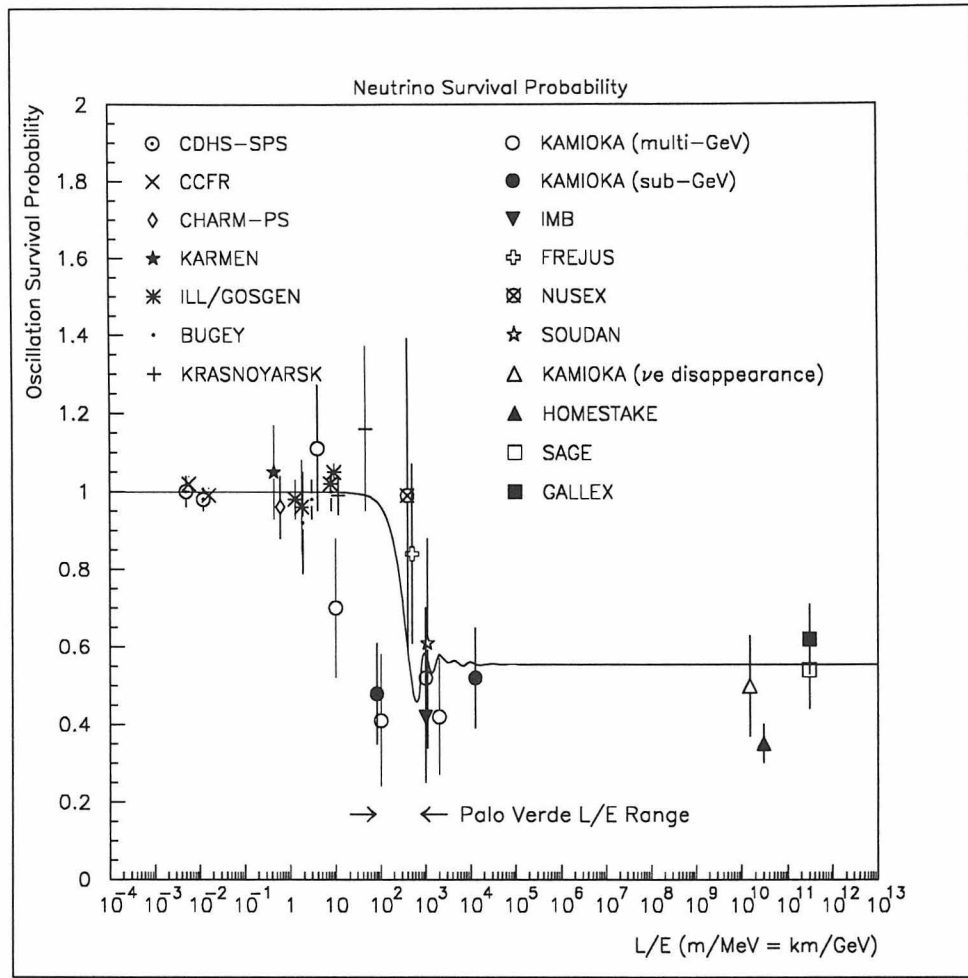


Figure 1.2: A three-flavor mixing hypothesis fit to experimental results from neutrino experiments [17]. The L/E region to be explored by the Palo Verde experiment is shown.

the more powerful reactor at Gösigen in 1981, and more measurements were made at distances of up to 67 m from the reactor core. $\nu_e \rightarrow X$ oscillations were ruled out for mixing angles, $\sin^2 2\theta$, larger than 0.1 and Δm^2 larger than $2 \cdot 10^{-2} \text{ eV}^2$ [19]. Excellent agreement of the measured and calculated reactor-induced positron spectra demonstrated a clear understanding of the neutrino source, critical for such a disappearance experiment. More recently, a high statistics measurement [20] 15 m from the core of the Bugey nuclear reactor allowed a measurement of the integral inverse β decay cross section to 1.4% and demonstrated monitoring of the reactor fuel burn-up at the level of 2%. A subsequent oscillation search [21], made at 15, 40, and 95 m from the Bugey reactor has extended the excluded region of parameter space down to Δm^2 of

$1 \cdot 10^{-2} \text{ eV}^2$ and $\sin^2 2\theta$ of 0.02. Figure 1.3 summarizes the excluded parameter space relevant for oscillations coupling to ν_e .

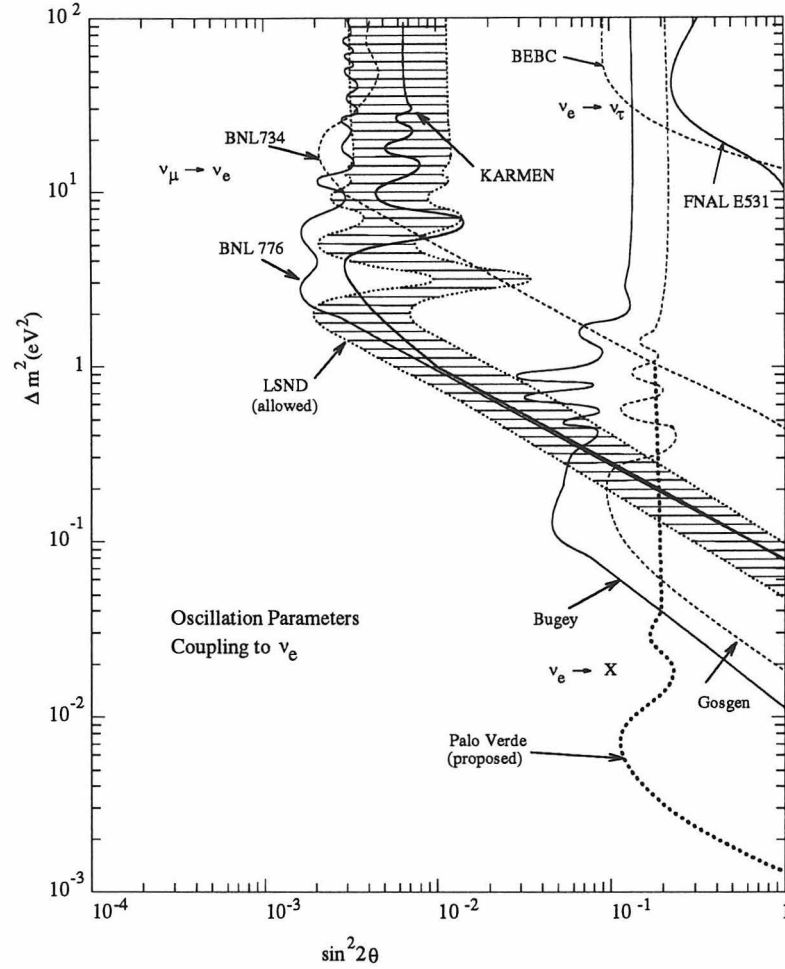


Figure 1.3: Excluded oscillation parameters coupling to ν_e . The region to the right of the curves is excluded at 90% C.L.

1.2.3 Accelerator Experiments

At about the time of the Gösigen reactor experiment, results began to appear from a number of accelerator-based oscillation searches. These experiments generally used high-energy ν_μ beams to investigate the ν_e or ν_τ appearance channels as well as $\nu_\mu \rightarrow X$ disappearance. The appearance experiments, in which one looks, for example, for evidence of ν_e 's appearing in a ν_μ beam, are capable of exploring very small mixing angles because the sensitivity is limited only by the purity of the ν_μ beam; the precise

normalization and spectral shape of the neutrinos at production is not critical as it is for disappearance experiments. The disadvantage of the accelerator experiments is that the neutrino energy, ~ 1 GeV, is a factor of 1000 larger than for reactor experiments, and similar sensitivity to Δm^2 thus requires baselines 1000 times longer and detectors proportionally larger and more expensive.

Early experiments searching for ν_e appearance were undertaken at LAMPF [22] (the Los Alamos Meson Physics Facility), at Brookhaven (BNL 734,776) [23, 24], and at CERN (CHARM [25] and BEBC [26]), among others. Most recently, results from LSND [27] at LAMPF seem to show some evidence for oscillations in the $\bar{\nu}_\mu \rightarrow \bar{\nu}_e$ appearance channel. Most of the parameter space allowed by the LSND results is excluded at 90% C.L. by the recent Bugey [21] reactor data, and by results from BNL 776 and KARMEN [28], both accelerator ν_e appearance experiments. However, a small region near $\Delta m^2 = 1$ eV² and $\sin^2 2\theta = 0.01 \sim 0.001$ is not ruled out, and this is a result demanding further attention.

A number of accelerator experiments have also explored oscillations through ν_τ appearance. Early experiments at Fermilab (FNL E338, E564) [29, 30] used an Ne-H₂ bubble chamber to look for evidence of τ^+ 's produced by $\bar{\nu}_\tau$'s appearing in a $\bar{\nu}_\mu$ beam. The current best limits are from a ν_τ appearance emulsion experiment carried out at Fermilab (FNL E531) [31] and a ν_μ disappearance experiment carried out by the CDHS [32] group at CERN. From these experiments, $\nu_\mu \rightarrow \nu_\tau$ oscillations are excluded down to mixing angles of 10^{-2} and to Δm^2 of about 0.2 eV². The current CHORUS and NOMAD [33] ν_τ appearance experiments at CERN should be able to extend the excluded parameter space by another order of magnitude in mixing angle. Another ν_τ appearance experiment proposed at Fermilab (FNL E803) [34] is scheduled to begin data taking shortly after the main injector turns on in 1999. This experiment should be sensitive to $\sin^2 2\theta$ down to $2 \cdot 10^{-5}$ and Δm^2 as small as 0.2 eV². Figure 1.4 summarizes the excluded parameter space relevant for oscillations coupling to ν_μ .

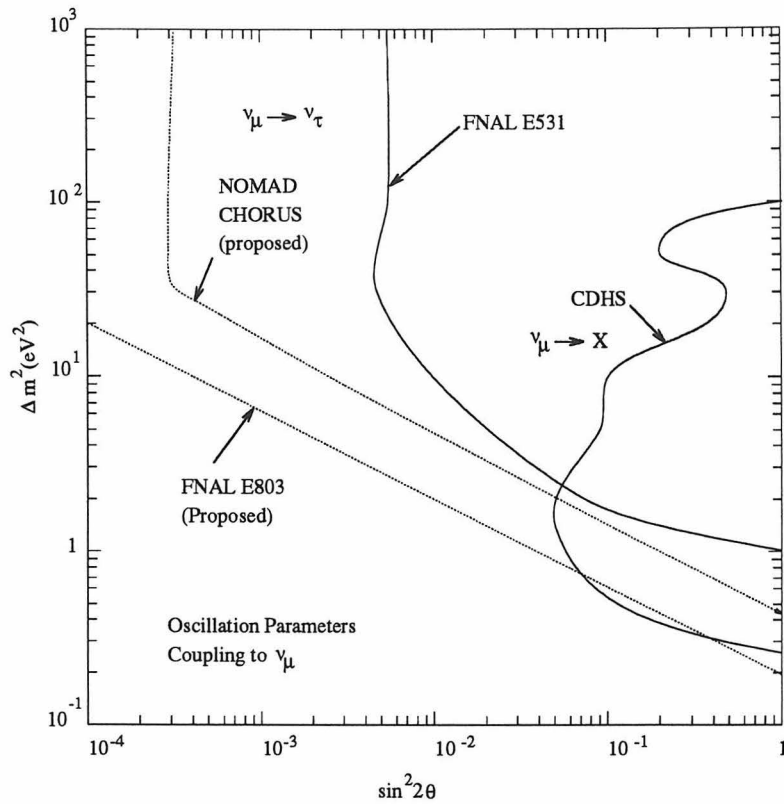
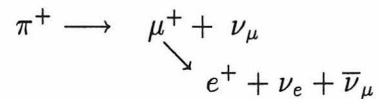


Figure 1.4: Excluded oscillation parameters coupling to ν_μ . The region to the right of the curves is excluded at 90% C.L.

1.2.4 The Atmospheric Neutrino Anomaly

A curious result confirmed by several underground detectors is the so-called “atmospheric neutrino anomaly.” High energy hadrons from cosmic rays interact with nuclei in the upper atmosphere producing pions and kaons which in turn give rise to “atmospheric” neutrinos. Through the π^+ decay shown below (and similarly for π^- ’s and K ’s), we expect the ratio of muon-type to electron-type neutrinos to be approximately equal to two.



Detectors sensitive to muon and electron-like events generally report the ratio $R \equiv (\mu/e)_{DATA}/(\mu/e)_{MC}$, such that the measured ratio of muon to electron-like events

is compared with the calculated ratio. The KAMIOKANDE [36] water Cherenkov detector has presented analyses of independent data samples characterized by sub-GeV and multi-GeV energy deposits and presents ratios, R , of 0.57 ± 0.10 and 0.60 ± 0.07 for the multi- and sub-GeV samples, respectively. Neutrino oscillations can be invoked to explain this anomalously small ratio caused by either a deficit in the muon neutrino flux, an excess in the electron neutrino flux, or both. Thus both $\nu_\mu - \nu_\tau$ and $\nu_\mu - \nu_e$ oscillations are considered as possible explanations for this effect, and the Multi-GeV data is fit to the mixing parameters $(\Delta m^2, \sin^2 2\theta) = (1.8 \cdot 10^{-2} eV^2, 1.0)$ for $\nu_\mu - \nu_e$ and $(1.6 \cdot 10^{-2} eV^2, 1.0)$ for $\nu_\mu - \nu_\tau$.

This anomalous ratio is confirmed by the IMB [37] water Cherenkov detector, which measures a ratio of 0.71 ± 0.09 , and the SOUDAN [38] tracking calorimeter, which reports $R = 0.64 \pm 0.19$. However, the tracking calorimeters Frejus [39] and NUSEX [40] see no significant deviation from $R = 1$, reporting $R = 1.0 \pm 0.17$ and $R = 0.99 \pm 0.29$, respectively. The parameter space allowed by the KAMIOKANDE results for $\nu_\mu \rightarrow \nu_e$ oscillations is shown in Figure 1.5. The Palo Verde experiment is fully sensitive to this region.

1.3 The Next Generation

Spurred on by anomalous atmospheric data from KAMIOKANDE, SOUDAN, and IMB, the current push of neutrino oscillations experiments is toward small Δm^2 . The Palo Verde reactor experiment, capable of exploring Δm^2 down to $10^{-3} eV^2$, is part of this effort. In addition, a number of proposals for long-baseline accelerator experiments have been presented. For example, the MINOS [41] collaboration proposes to aim a ν_μ beam from Fermilab, near Chicago, toward the SOUDAN detector in Northern Minnesota, about 750 km away. Similar proposals call for aiming a CERN beam at the ICARUS [42] detector in the Gran Sasso tunnel in Italy or at the HELLAS [43] detector in Greece. These accelerator experiments, because of the high neutrino energy (10 GeV at FNL and 100 GeV at CERN), will be sensitive to ν_τ appearance and will thus be able to shed light on both the $\nu_\mu - \nu_e$ and $\nu_\mu - \nu_\tau$ oscillation channels.

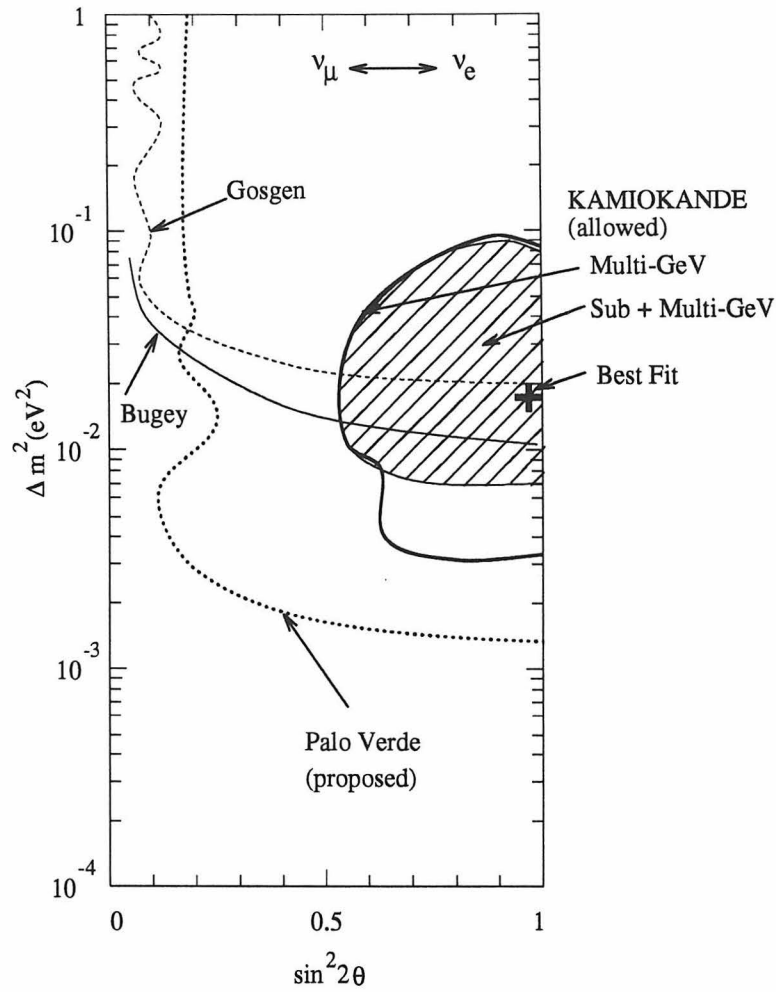


Figure 1.5: $\nu_\mu - \nu_e$ oscillation parameter space allowed by KAMIOKANDE for reconciliation of the anomalous atmospheric flux. The cross indicates the best fit oscillation solution to the full data sample. $(\Delta m^2, \sin^2 2\theta) = (1.6 \cdot 10^{-2}, 0.98)$

However, as the proposed experiments require quite large (several kT) detectors and extensive modifications of the accelerator beam lines, they are quite costly and require rather long lead times. Indeed results are not anticipated until after the turn of the century. On the other hand, reactor experiments can explore the same region of $\nu_\mu - \nu_e$ parameter space at a distance of only 1 km and at a fraction of the cost, owing to the thousand-fold smaller energy of reactor neutrinos.

1.3.1 The Palo Verde Experiment

The Palo Verde neutrino oscillation experiment, formerly designated the San Onofre experiment, was initiated by our Caltech group [44]. Subsequently a similar experiment was proposed by a French-Italian group at the Chooz [45] reactor in Northern France. The Palo Verde detector should begin taking data in early 1997. It will be able to confirm or refute atmospheric neutrino oscillations through the $\nu_\mu - \nu_e$ channel before 1999. It is the goal of this thesis to describe the developments leading to the final design and construction of the Palo Verde detector.

Chapter 2

The Experiment

The neutrino detector for the proposed oscillation experiment consists of a segmented liquid scintillation detector to be installed near three fission reactors at the Palo Verde Nuclear Generating Station in Arizona. The detector will be installed outside the controlled area fence at a distance of 740 m from the closest reactor and about 15% farther from the other two. See Figure 2.1. At this distance the experiment will be sensitive to $\nu_e \rightarrow X$ oscillations characterized by mass-squared differences as small as 10^{-3} eV^2 and $\sin^2 2\theta$ down to 0.1. The detector will be installed in an underground vault with an overburden of 46 meters water equivalent (mwe) of concrete and earth in order to reduce backgrounds from cosmic muons and hadronic showers. The three reactors at Palo Verde have a combined thermal power of 10.9 GW, resulting in a neutrino flux of about $10^{10} \bar{\nu}_e \text{ cm}^{-2} \text{ sec}^{-1}$ at the detector.

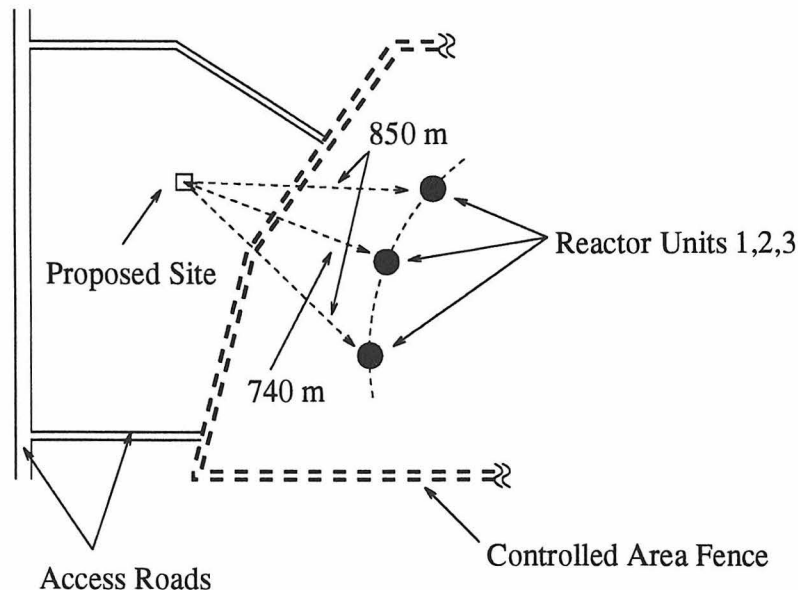
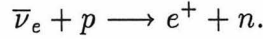


Figure 2.1: Schematic depiction of the reactor site showing the placement of the detector 740 m from the closest reactor and 850 m from the other two.

2.1 The Detector

2.1.1 The Detection Concept

Reactor antineutrinos are detected through inverse β decay,



This reaction has a relatively low threshold of 1.8 MeV and, because of the small $\log ft$ value for neutron decay, the highest yield of any neutrino detection reaction. It is also highly suitable for the proton-rich hydrocarbon scintillator to be used in the Palo Verde detector. The liquid scintillator acts as a detector for both the positron and the neutron, the former as it ionizes and annihilates, and the latter through de-excitation γ radiation from neutron capture on gadolinium, with which the scintillator has been loaded at the level of 0.1% by weight.

At the relatively shallow depth of 46 mwe , backgrounds caused by muon-induced fast neutrons are significant. To discriminate between positrons and recoiling fast neutrons, the detector is segmented into 66 individual cells, thin enough that the two 511-keV γ rays from the annihilating positron may penetrate to surrounding cells, producing a characteristic fast “triple coincidence” as the signature of a positron. Clearly, fast-neutron-induced proton recoils do not in general give rise to such a signature. Neutrino interactions in the detector are thus identified as follows. (See Figure 2.2). The positron quickly loses its kinetic energy through ionization, producing scintillation light which is nearly always fully contained within one cell. At the end of its track, the positron annihilates. The resulting annihilation radiation is relatively penetrating and tends to deposit energy, through Compton scattering, in several surrounding cells. A “positron-like” cell, defined as containing between 1 and 10 MeV, along with at least two “annihilation-like” cells, defined as containing between 50 and 600 keV, is the “triple coincidence” signature of a positron. The low 50 keV threshold is found to greatly enhance the signal efficiency. Meanwhile, the neutron thermalizes and eventually captures on gadolinium, which de-excites by

gamma emission from an 8 MeV excited state. The neutron capture time in scintillator containing 0.1% gadolinium is $28\mu\text{sec}$. Thus the signature of a reactor antineutrino is a fast–slow coincidence consisting of a prompt triple coincidence followed, within a $100\ \mu\text{s}$ window, by an 8 MeV gamma burst. The details of this detection process are described in Chapter 5.

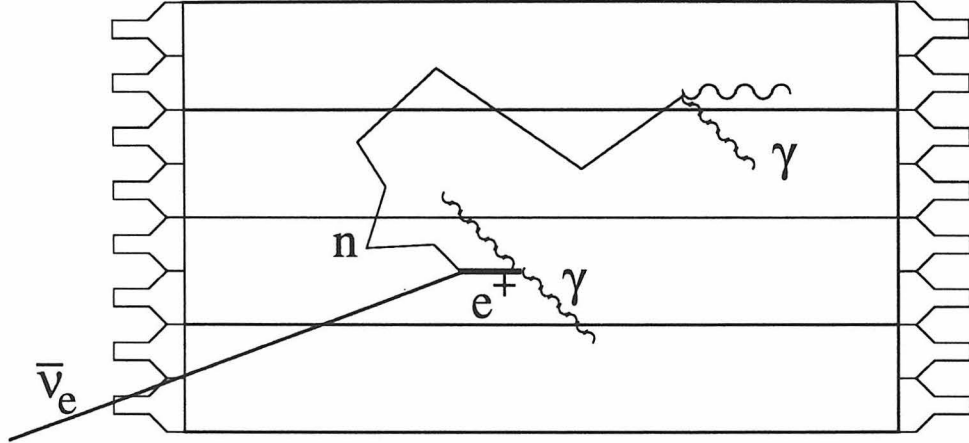


Figure 2.2: Detection of reactor $\bar{\nu}_e$ by inverse β decay.

2.1.2 The Target Cells

The detector, pictured in Figure 2.3, consists of 66 individual clear acrylic target cells filled with Gd-loaded liquid scintillator. Each cell is 9 m in length, 0.25 m high, and 0.13 m wide. They are stacked in an array 11 cells wide and 6 cells high. A region 0.8 m in length is partitioned off at both ends of each cell and filled with pure mineral oil to act as a buffer to external sources of background. Thus only the central 7.4 m of each cell is active detector with a total mass of about 12 tons. Two 5-inch photomultiplier tubes are coupled to each end of every cell to collect the scintillation light. The propagation of light through the cell is aided by total internal reflection from the outer acrylic–air interface: mineral oil and acrylic have nearly identical indices of refraction of $1.46 \sim 1.48$ and $1.48 \sim 1.49$, respectively. Thus light passes from the scintillator to the acrylic essentially without refraction but is totally reflected from the acrylic–air interface if the angle of incidence is greater than 43 degrees ($= \sin^{-1} \frac{1}{1.48}$) from normal. The cells are optically isolated from each other

and kept light tight using a black plastic cover which touches the acrylic cells but does not destroy the optical properties of the acrylic-air interface.

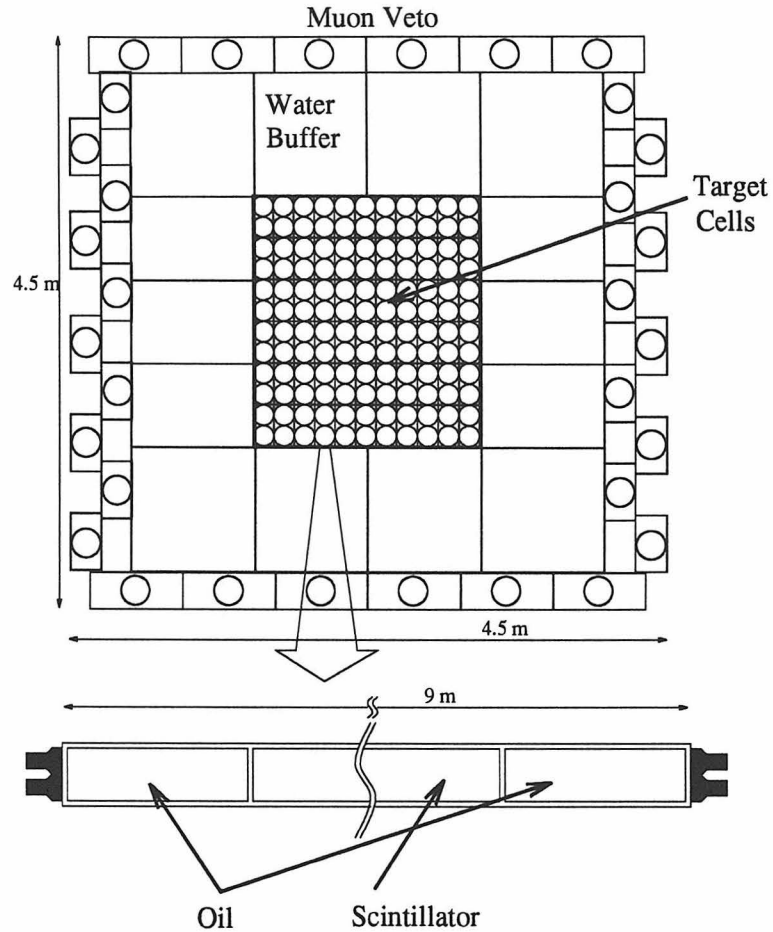


Figure 2.3: The neutrino detector.

2.1.3 The Water Buffer

The 66 target cells are surrounded by a one-meter-thick water buffer to shield the detector from external radioactivities and muon-induced neutrons. The buffer cells are made of low activity steel and will be filled with ultra-pure water produced in a distillation plant operated by the Nuclear Generating Station. The buffer surrounds the target cells on four sides; the end caps are not covered as one requires access to the phototubes. The 80-cm mineral oil partition serves as buffer here.

2.1.4 The Muon Veto

Surrounding the water buffer is a hermetic active muon veto system. This veto allows the detector to be killed when cosmic muons enter the buffer or active cells, possibly to produce dangerous fast neutrons that could recoil in the target cells and subsequently capture on gadolinium, completing a fast–slow neutrino–like coincidence. The veto is constructed from 12–meter–long opaque PVC cells left over from the MACRO [46] experiment. Six “horizontal–type” cells, measuring $0.75 \times 0.26 \times 11.9$ m, cover the top and bottom of the detector, and ten “vertical–type” cells, measuring $0.23 \times 0.49 \times 11.7$ m, cover each side. The cells are filled with a relatively low–light–yield liquid scintillator. The ends of the detector will be covered by 10–cm–thick liquid scintillator panels.

The veto cells are read out by two 5” phototubes per end. From descriptions of the cell performance by the MACRO collaboration [46], it is calculated that muons going through the center of the MACRO cell will deposit at least 30 MeV, and will generate 300 photoelectrons at the phototubes. Accidental firing of the veto due to gammas from natural radioactivity would cause unnecessary dead time. Thus, the firing threshold should be set above the gamma energies of the uranium and thorium decay chains, or at about three MeV for energy deposits near the phototube. This corresponds to an effective threshold of about 12 MeV, or 120 photoelectrons, at the center of the cell considering light attenuation. Thus the possibility of not detecting a muon which does not clip corners is negligible. In the case of muons that do clip corners, any that enter the detector will have to go through other veto cells as well and will be identified through multiple veto hits. Thus the inefficiency of the muon veto is dominated by the physical gaps in the coverage where the cells are butted together and in the end caps where the staggered profile of the side veto cells creates rectangular holes in the coverage (see Figure 2.3). A very conservative estimate of the leakage through these gaps assumes that any muon incident on inactive material will leak through. (This assumption would be valid only if all muons were incident normal to the surface). The leakage rate calculated in this manner is about 2%. However, in

order that a muon actually be undetected, it must slip through the veto both as it enters and exits the detector, bringing the missed-muon rate to $4 \cdot 10^{-4}$. Of course, for muons stopping in the detector, the miss rate is the full 2%. These leakage fractions are used in the estimate of the detector background (see Chapter 5).

The muon veto is the dominant source of detector dead time. Muon hits initiate veto times as follows:

Muon Event Type	Veto Time
Muons pass through buffer	10 μsec
Muons pass through target cells	100 μsec
Muons stop in buffer or target cells	300 μsec

At 46 *mwe* the flux of muons through a horizontal surface is 14 per m^2 and sec, and through a vertical surface, from one side, 3.5 per m^2 and sec (calculated assuming a muon flux of 8.9 per m^2 , sec, and sterad and an angular distribution of $\cos^2 \theta$). Then the total flux into a box measuring $11 \times 4.5 \times 4.5$ m is 1200 Hz. The fraction of these hitting the target cells is roughly 30%. The muon stopping rate at 46 *mwe* is about 12 per kg and day (see section B.2.1), leading to a stopping rate in the approximately 120 tons of buffer and target of 17 Hz. Thus the total dead time is estimated as

$$17 \cdot 300 \cdot 10^{-6} + 360 \cdot 100 \cdot 10^{-6} + 840 \cdot 10 \cdot 10^{-6} = 4.9\%.$$

However, the leakage of the veto adds to this as some through-going muons are tagged as they enter but not as they leave the detector. They then appear to be stopped muons and initiate the long 300 μsec veto time. The $< 2\%$ leakage estimate then adds another $2\% \times 1200 = 24$ Hz of “false stops.” This increases the total dead time to 5.6%.

2.2 The Neutrino Source

The Palo Verde Nuclear Generating Station consists of three reactors with a combined thermal power of 10.9 GW. They operate continuously on a staggered shut-down

schedule so that only one reactor at a time is down for refueling. There are generally two refueling periods of 60 days each per year. Typically, about 60% of the reactor thermal power comes from fissions of ^{235}U , about 30% from ^{239}Pu , and the rest from ^{238}U and ^{241}Pu . The fuel composition changes slowly with time as ^{239}Pu and ^{241}Pu are bred from ^{238}U . From a knowledge of the fuel composition and thermal power at all times (measured by the power station), the neutrino spectrum can be determined. A precise knowledge of the neutrino spectrum is critical for a “disappearance” oscillation experiment such as the present one in which a deficit in expected flux or deformation of the spectral shape will be taken as evidence for neutrino oscillations. There are two complementary approaches to the calculation of the neutrino spectrum: first, measurements of the electron spectra associated with the β decays of the fission products of the important fissile isotopes (^{235}U , ^{239}Pu , ^{241}Pu) have been made [47, 48, 49]. The electron and neutrino energies are simply related, and the neutrino spectra can thus be calculated essentially without loss of precision. The measured spectra are known to about 3% accuracy.

Secondly, one can take the results of a number of high-statistics reactor neutrino oscillation searches as a direct measurement of the antineutrino spectrum for a given fuel composition and detector efficiency. For example Ref. [55] finds excellent agreement of the neutrino spectra measured and calculated at the Gösigen reactor. In addition, recent experiments at the Bugey reactor [20, 21] find agreement between the measured and calculated positron spectra at the level of 2% at low energy, worsening to about 5% near the endpoint, around 6 MeV. The integral yield of the detection reaction is also verified at the level of 1.4%.

So from a knowledge of the reactor thermal power and fuel composition, both of which are readily available from the power station, one can calculate and cross check the expected neutrino spectrum and expect to achieve an accuracy of a few percent.

2.2.1 An Estimate of the Reactor-Induced Positron Spectrum at Palo Verde

A detailed calculation of the reactor neutrino spectrum will be performed from the reactor data once the experiment is underway. But for the present purpose of estimating the expected event rate in the Palo Verde detector, a simplified three parameter fit to the antineutrino spectrum described by Vogel and Engel [50] will be used. Here measured neutrino spectra are fit as a function of energy and fissile isotope:

$$\frac{dN_\nu}{dE_\nu} = \exp[a_0 + a_1 E_\nu + a_2 E_\nu^2],$$

where dN_ν/dE_ν is in units of $\bar{\nu}_e$ per MeV and fission, and the constants a_i are fit independently for each fuel element.

a_i	^{235}U	^{239}Pu	^{238}U	^{241}Pu
a_0	0.870	0.896	0.976	0.793
a_1	-0.160	-0.239	-0.162	-0.080
a_2	-0.0910	-0.0981	-0.0790	-0.1085

Taking, for the moment, the fuel composition to be that of the Gösgen power reactor [55], the rate of fissions of each isotope can be calculated for 10.9 GW of thermal power:

Isotope	Contribution to Thermal Power	Energy release [MeV / fission]	Fissions per second
^{235}U	61.9%	201.7	$2.03 \cdot 10^{20}$
^{239}Pu	27.2%	210.0	$8.58 \cdot 10^{19}$
^{238}U	6.7%	205.0	$2.16 \cdot 10^{19}$
^{241}Pu	4.2%	212.4	$1.31 \cdot 10^{19}$

Column three, effective energy release per fission, is taken from [55] and includes contributions from the fission itself, subsequent β decays, and neutron capture in the surrounding material. The neutrino spectrum is then generated, normalized to the fission rate of each isotope.

From the antineutrino spectrum, the spectrum of positrons produced in the detector by inverse β decay can be calculated. The positron spectrum is given by

$$\frac{dN_{e^+}(E_{e^+})}{dE_{e^+}} = \frac{dN_\nu(E_\nu)}{dE_\nu} \cdot \frac{P}{4\pi L^2} \cdot \sigma(E_\nu) \cdot \delta_{rec}(E_\nu), \quad (2.1)$$

$$(2.2)$$

where P is the number of target protons, L is the detector distance from the reactor, σ is the weak cross section for infinitely heavy nucleons, and δ_{rec} is a spectral correction factor to take into account the neutron recoil. The positron energy is simply related to the neutrino energy by

$$E_{e^+} = E_\nu - (M_n - M_p) - m_e = E_\nu - 1.804 \text{ MeV},$$

where M_n , M_p , and m_e are the neutron, proton, and electron masses, respectively. The cross section, σ , can be written [51] in analogy to that of neutron β decay as

$$\sigma(E_\nu) = \frac{2\pi^2 \hbar^3}{m_e^5 c^7 f \tau_n} p_e E_e \cdot [1 + \delta_{WM} + \delta_{rad}],$$

where τ_n is the neutron mean lifetime, taken as 888.6 ± 3.5 sec [52], and f is the Fermi phase space factor, taken to be 1.71465 ± 0.00015 [55]. The terms δ_{WM} and δ_{rad} are corrections for weak magnetism and radiative effects and are calculated following [51]. Numerically, this becomes

$$\begin{aligned} \sigma(E_\nu) = & (9.548 \pm 0.022)[E_\nu - 1.2933] \cdot [(E_\nu - 1.2933)^2 - (0.511)^2]^{1/2} \times \\ & [1 + \delta_{WM} + \delta_{rad}] \cdot 10^{-44} \text{ cm}^2, \end{aligned}$$

with the correction functions parameterized [51, 55] as

$$\delta_{WM} = -1.727 \cdot 10^{-3} \left[E_\nu + \frac{(E_\nu - 1.804)^2 - (0.511)^2}{E_\nu - 1.804} \right]$$

and

$$\delta_{rad} = 11.7 \cdot 10^{-3} (E_\nu - 1.804)^{-0.3}.$$

And δ_{rec} , from equation 2.1, can be expressed [55] as

$$\delta_{rec} = 1 - 0.155e^{(E_\nu-8)/1.4}.$$

Finally, the number per day and energy spectrum of positrons created in the detector are calculated based on three reactors 740, 850, and 850 m away, and a total target size of $9.4 \cdot 10^{29}$ protons. Figure 2.4 displays the expected positron spectrum calculated in this manner. The total positron production rate is calculated to be 197 per day.

It is illustrative to look at the deformation of the spectrum caused by neutrino oscillations for some hypothetical oscillation parameters. The deformed spectra are calculated by folding the oscillation survival probability, $1 - P_{\mu l}$ (see equation 1.13), with equation 2.1. Figure 2.5 displays the expected positron spectrum for two sets of parameters. The upper spectrum is calculated using the oscillation parameters obtained by a best fit to the KAMIOKANDE [36] atmospheric data: $\Delta m^2 = 1.6 \cdot 10^{-2}$ eV², $\sin^2 2\theta = 0.98$ for $\nu_\mu - \nu_e$ mixing. The lower spectrum is calculated using the parameters obtained by [17] for a three-flavor maximal mixing scenario incorporating all experimental neutrino data (see Figure 1.2) $\Delta m^2 = 0.72 \cdot 10^{-2}$ eV² and $\sin^2 2\theta = 1.0$. The interference caused by two different source-detector distances is taken into account.

2.3 The Experimental Sensitivity

The experimental sensitivity is calculated based on estimates of the detector efficiency and background rates. These estimates are discussed in detail in Chapter 5 and are summarized here. The expected four-fold (positron + neutron) detection efficiency is 26%. Per day, 197 positrons are produced in the detector, giving rise to a neutrino signal rate of 51 per day.

The background is divided into two categories: correlated and uncorrelated. *Cor-*

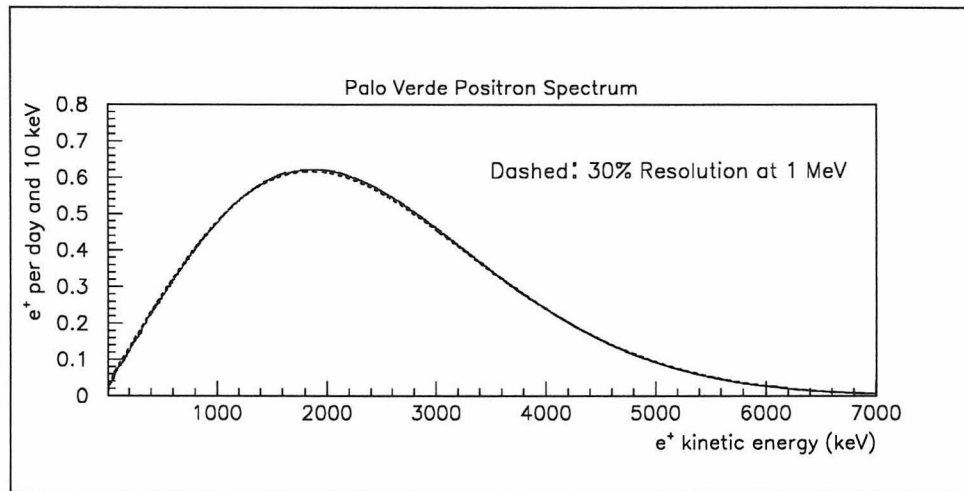


Figure 2.4: Expected neutrino-induced positron spectrum (solid curve) at Palo Verde assuming no oscillations. The dashed curve shows the positron spectrum folded with the detector energy resolution (30% FWHM at 1 MeV).

related backgrounds are those in which the full neutrino signal (a fast triple coincidence followed by a delayed neutron capture) is mimicked. As these events are indistinguishable from the neutrino signal, they must be measured during the reactor-off refueling cycle and subtracted statistically. This subtraction dominates the statistical error of the experiment. *Uncorrelated backgrounds* are those which mimic only part of the neutrino signal: a fast triple coincidence or a capture-like signal, but not both. If a fast-triple-type background and a capture-like background happen to occur near each other in time, it could look like a neutrino signal, giving rise to an uncorrelated background event. However, the rate of accidental triple coincidences and of capture-like events can be measured continuously and the uncorrelated rate thus cal-

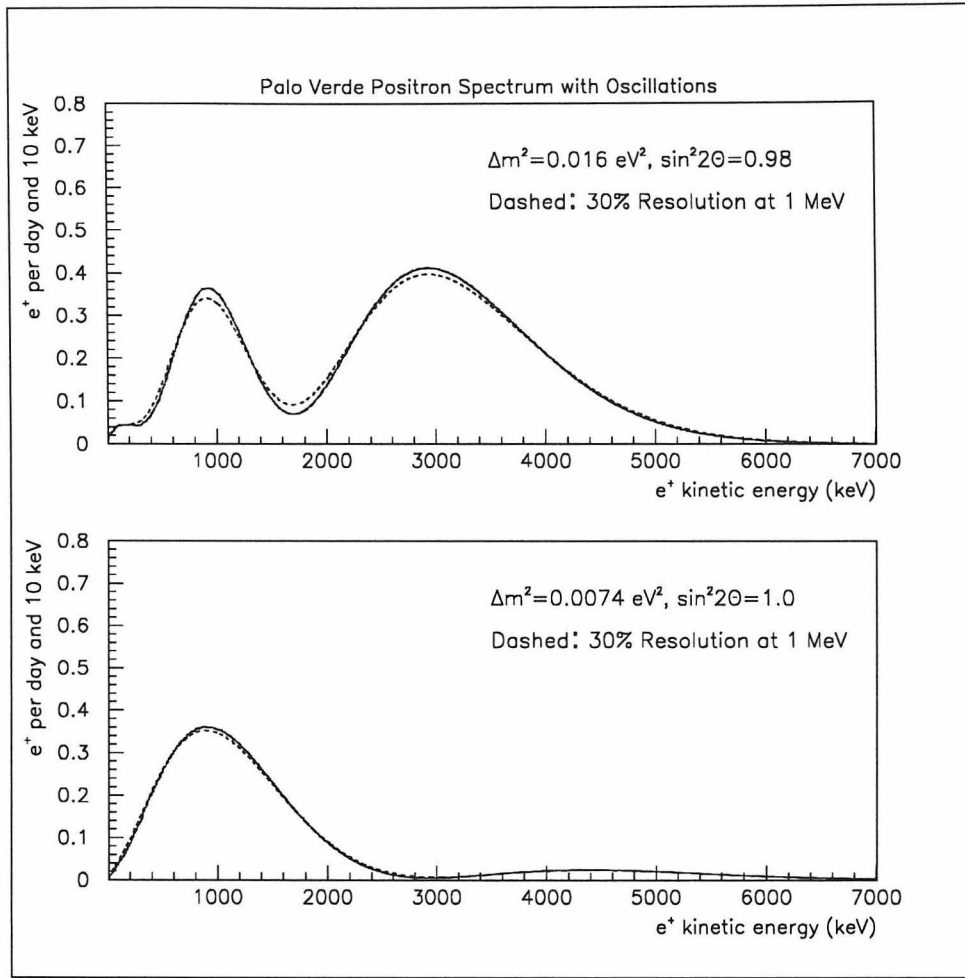


Figure 2.5: The positron spectrum in the presence of oscillations. The upper figure shows oscillations with $\Delta m^2 = 1.6 \cdot 10^{-2} \text{ eV}^2$, $\sin^2 2\theta = 0.98$, the best fit to the KAMIOKANDE atmospheric data. The lower shows oscillations with full mixing and $\Delta m^2 = 0.72 \cdot 10^{-2} \text{ eV}^2$, suggested by [17]. In both cases the dashed line indicates folding with the energy resolution of the detector.

culated with high precision. Nevertheless, this background, too, must be statistically subtracted from the reactor-on data. The following table summarizes the expected signal and background rates:

Signal	Correlated Background	Uncorrelated background
51 / day	9 ~ 79 / day	5 ~ 24 / day

There is a relatively large range in the background estimate on account of an imprecise knowledge of the spectrum of neutrons produced by muon spallation; a recently obtained neutron spectrum from the KARMEN experiment [71] would result in a

correlated background of 34 per day and an uncorrelated rate of 15 per day.

To estimate the experimental sensitivity, a hypothetical 1.5 year data run is considered. A run of this length would incorporate three refueling cycles of 60 days each. This would result in a total of $t_{ON} = 360$ days of full power reactor-on data and $t_{OFF} = 180$ days of 2/3 power “reactor off” data with one reactor shut down for refueling. Thus the event rates, N_{ON} and N_{OFF} , measured during the two periods are given by

$$N_{ON} = S + B,$$

and

$$N_{OFF} = \frac{2}{3}S + B,$$

where S is the signal rate (per day) and B is the total background rate. Thus the signal rate is given by the expression

$$S = 3 \cdot [N_{ON} - N_{OFF}],$$

and the statistical error, δS , by

$$\delta S = 3 \cdot \sqrt{\delta N_{ON}^2 + \delta N_{OFF}^2}.$$

If we assume Poisson statistics, the statistical errors in the measurements of N_{ON} and N_{OFF} are given by the expressions

$$\delta N_{ON} = \sqrt{t_{ON} \cdot (S + B)} / t_{ON},$$

and

$$\delta N_{OFF} = \sqrt{t_{OFF} \cdot (\frac{2}{3}S + B)} / t_{OFF}.$$

So

$$\delta S = 3 \cdot \sqrt{\frac{S + B}{t_{ON}} + \frac{\frac{2}{3}S + B}{t_{OFF}}}.$$

To calculate the total experimental error, the statistical error must be added in

quadrature to the following systematic uncertainties:

Positron efficiency calibration	3%
Neutron efficiency calibration	3%
Neutrino Cross section and reactor flux	3%

Listed in the following table are the total experimental errors (1σ) for the extremes of the background range as well as for an intermediate value using the neutron spallation spectrum measured by the KARMEN [71] collaboration.

Signal Rate [d^{-1}]	Total Background [d^{-1}]	Statistical Error [%]	Total Error [%]
51	14	3.9%	6.5%
51	49	5.1%	7.3%
51	103	6.4%	8.2%

The region of parameter space excluded by a null oscillation result from Palo Verde can then be calculated: the actual data set will include spectral information on both the signal and background, and a bin-by-bin analysis may yield the best exclusion. At this point, however, little is known about the shape of the background. For the moment it will be assumed to be flat, and the exclusion plot will be calculated based on the integral detected positron rate. The 90% Confidence Level (C.L.) exclusion plot is the set of all points in the $\sin^2 2\theta - \Delta m^2$ plane which produce an integral signal rate in the detector 1.28σ below the expected rate. Figure 2.6 displays such a plot for the three background cases considered above.

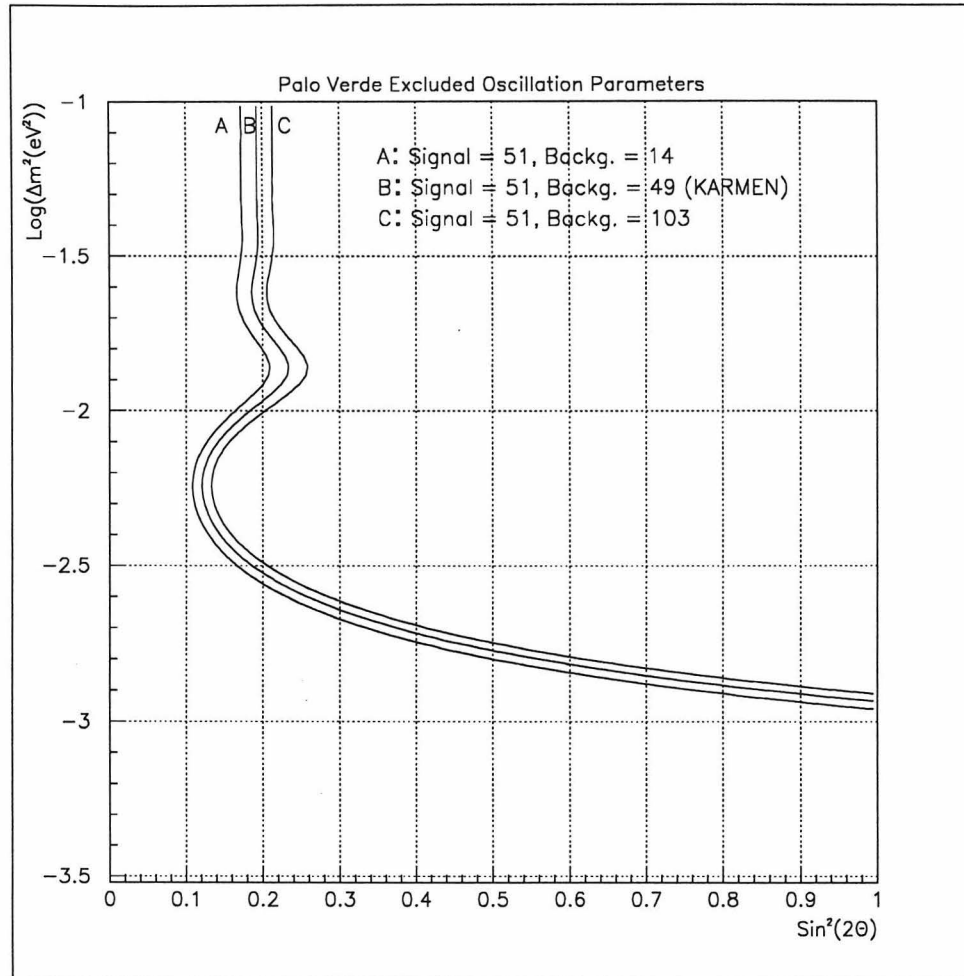


Figure 2.6: $\nu_e \rightarrow \nu_x$ oscillation parameter space excluded at 90% C.L. for a null result at Palo Verde. The detector is assumed to be 740 m from one reactor core and 850 m from the other two. The excluded region is to the right of the curve, shown for three different background scenarios.

Chapter 3

Tests of a Prototype Detector

Four full-size prototype detector cells have been constructed for performance and stability tests performed at Caltech. One cell was constructed at Caltech and the three others by Signcraft Plastics, a Los Angeles plastics company. Two cells, the Caltech cell and one of the commercial cells, were filled with Gd-loaded scintillator for performance tests described below. The scintillator itself was the object of a lengthy development process undertaken by colleagues in this Caltech group and NE Technology, Ltd. The scintillator concentrate, assigned the commercial code NE345, is diluted at Caltech with pseudocumene, purchased from Bicon, and mineral oil, purchased from Witco, Inc. The final scintillator contains, by volume, 20% concentrate, 20% pseudocumene, and 60% mineral oil. Tests of the scintillator properties were performed in conjunction with tests of the stability of the acrylic cells. The scintillator was found to have a long (~ 7 meter) and stable attenuation length. The gadolinium complex, dissolved in the scintillator at the level of 0.1% by weight, was found to be stable.

3.1 Mechanical Stability

The target cells are constructed of clear acrylic sheets which are cut and cemented together into sealed tanks. Acrylic filling caps, sealed with O-rings, allow the central scintillator volume and the buffer end partitions to be filled individually. Figure 3.1 illustrates the mechanical detail. The large glue joints present mechanical concerns as the scintillator, which contains about 30% by volume pseudocumene (1, 2, 4, trimethyl benzene), aggressively attacks many plastics. Indeed tests have shown that the scintillator will quickly craze acrylic that has not been properly machined and

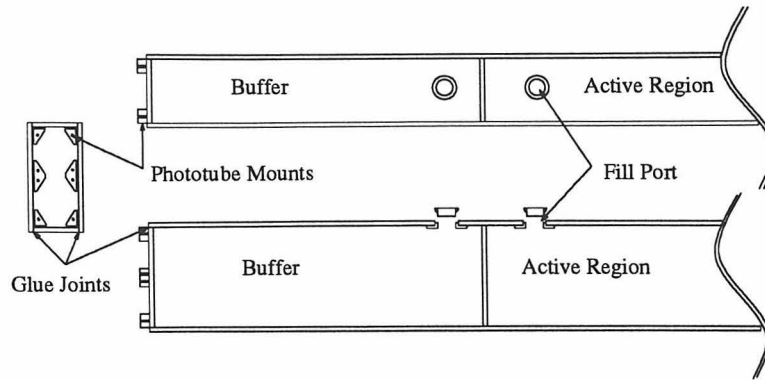


Figure 3.1: Detailed view of a 9-m prototype cell. The fill ports and phototube mounting brackets, all made from clear acrylic, are illustrated.

annealed to relieve residual stresses. This crazing can eventually lead to failure of the joints causing the cell to develop leaks. While the small mechanical pieces, such as the fill-hole plugs and phototube mounting brackets, can easily be annealed after machining, the 9-meter-long sections of the tank present a problem as the cost of such a large annealing oven is prohibitively expensive. Thus great care must be taken during the cutting process to minimize induced stresses in the material. Happily, a year-long test of one of the commercial cells filled with 200 liters of scintillator shows no signs of crazing where the scintillator contacts the joints; the mechanical stability is excellent, and no indication of a leak has been discovered. In fact, the filled cell was manipulated and even lifted with no adverse effects. It was discovered, however, that a region of the cell exterior which was exposed to scintillator for several days, did develop cracks. This was traced to stresses induced during an exterior flame polishing process performed after the cell was glued up. The plastics company agreed to abandon this (purely esthetic) procedure, and a subsequent test cell prepared without this polishing procedure was found to be resistant to crazing.

3.2 The Detector γ Response

The 9-meter target cell, filled with 200 liters of Gd-loaded scintillator, was instrumented with one 5" Philips XP4512 phototube per end (though the ends are designed to accept two phototubes). A black PVC casing was installed around the cell to make

the assembly light tight, and the performance of the cell was investigated.

The energy scale of the response spectrum was calibrated using a number of gamma emitters: owing to the low density and low Z of the hydrocarbon scintillator, the Compton effect dominates the interaction of gammas with the scintillator. An example of the detector response to a ^{232}Th source, which has a strong gamma line at 2614 keV, is shown in Figure 3.2. The standard assignment of the 1/2 maximum point of the Compton structure to the backscatter energy is not, in fact, correct. Monte Carlo calculations [53] show that because of multiple scattering, gammas frequently deposit energy beyond the Compton edge. This results in the identification of the 90% maximum point of the Compton structure with the backscatter energy. The process of calibrating a liquid scintillation detector is described in some detail in section 4.5.1.

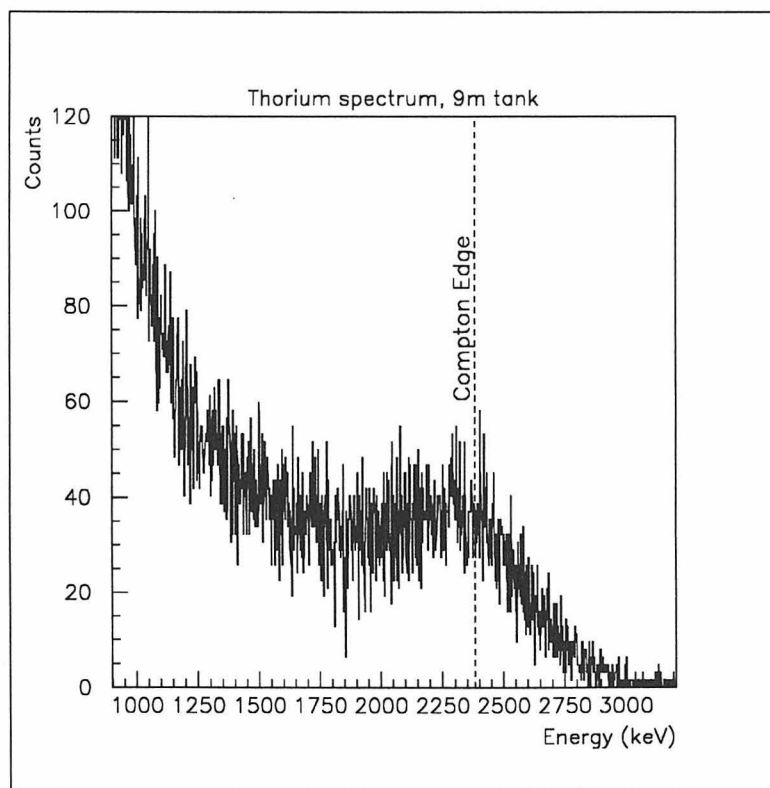


Figure 3.2: Spectrum of ^{232}Th in a 9-m prototype cell. The Compton edge energy, 2382 keV, is associated with the 90% maximum point of the spectral structure.

The calibration process is essentially an assignment of deposited energy to collected light at the phototube. Thus it depends on the transparency of the liquid

scintillator and the acrylic, on the distance of the energy deposit from the phototube, and on the quantum efficiency of the phototube (about 25%) for converting incident γ radiation to photoelectrons. Thus the energy calibration is defined at one distance from the phototubes and is mapped to the rest of the cell. By measuring timing differences between tubes at each end of the cell, the longitudinal position of the energy deposit can be reconstructed and the correct energy calibration for that point applied. The prototype 9-m cell was used to map out this calibration profile. The position of the Compton edge of ^{60}Co (in ADC channels) was measured as a function of the source position along the cell. Figure 3.3 displays the variation in the calibration as a function of distance. From the figure, there is approximately a factor of two variation in the energy scale between the center and ends of the cell.

3.3 The Energy Resolution

The energy resolution of the detector is also a function of collected light and thus of position in the cell. The energy resolution is dominated by photon counting statistics at the phototube where photons are absorbed and photoelectrons emitted in a Poisson process. Thus for a given position in the cell, any source of light is equivalent, and an LED tuned to deposit, say, the equivalent of 1 MeV of light can be used to measure the energy resolution. This measurement was performed as follows: a blue LED was mounted on the side of the instrumented 9-m cell at a distance of 2 m from one end. The LED was fired using a stabilized pulser which also gated an ADC used to read out the charge of one phototube. As the pulser intensity was varied, the position and width (in ADC channels) of the LED peak measured by the phototube allowed a mapping of the number of photoelectrons created to the ADC channel number. Figure 3.4 illustrates several of these measurements. From the shape of the LED peak, the number of photoelectrons is calculated as follows: taking the Gaussian limit of the Poisson distribution (valid for mean values greater than about 10), one can relate the position of the peak to its width. The ADC measures charge produced

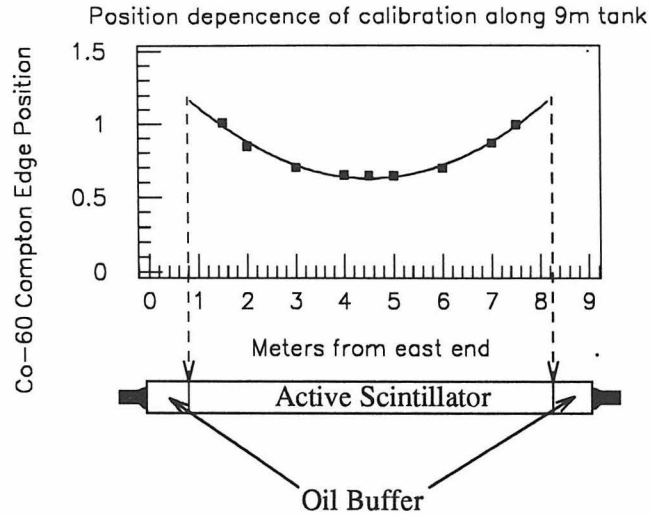


Figure 3.3: The position dependence of the energy calibration in the 9-m cell. The position (in ADC channels) of the Compton edge of a ^{60}Co source is plotted as a function of its position along the cell. The data is normalized to 1 at the 1.5-m point.

by the phototube:

$$Q = G \cdot N$$

where N is the number of photoelectrons produced, G is the gain of the system (including whatever factor converts charge in Coulombs to ADC channel number), and Q is the measured “charge” in units of ADC channels. Poisson statistics then provides that a distribution of mean value N will have a σ of \sqrt{N} . A Gaussian approximation to the shape relates the full width at half maximum ($FWHM$) to σ

by

$$FWHM = 2 \cdot \sqrt{2 \cdot \ln 2} \sigma \approx 2.35\sigma.$$

So

$$FWHM = 2.35 \cdot G \cdot \sqrt{N}.$$

Then in terms of the measured peak position, Q , and the $FWHM$,

$$N = \left(2.35 \frac{Q}{FWHM} \right)^2.$$

Figure 3.5 illustrates measured calibrations relating ADC channel, energy, and photoelectrons for one tube at a distance of 2 meters. The calculated relation of energy and photoelectrons then gives 34.6 photoelectrons produced per MeV of deposited energy at 2 meters from one phototube. To calculate the full resolution, measured at the center of the cell and for four phototubes (2 per end), we first scale the photoelectron yield to the center of the tank using the one-tube scaling relation of Figure 3.8. Going from 2 meters to 4.5 meters introduces an attenuation of a factor of 2.18, dropping the photoelectron yield to 15.9 photoelectrons per MeV and tube from the center of the cell. Four tubes then collect 63.6 photoelectrons, producing a resolution of 29.5% $FWHM/E$ at 1 MeV for energy deposited at the center of the cell. This translates to 3.2 photoelectrons for a 50 keV deposit at the center of the cell and implies that it is reasonable to extend the “annihilation-like” cell threshold down to this low value to gain detection efficiency.

3.4 The Cell Timing Response

The timing resolution of the detector was investigated using two Philips XP4512 5” phototubes, one coupled to each end of the prototype cell. The gains of the tubes were matched by placing a ^{60}Co source at the center of the cell and adjusting the high voltage to match the positions of the Compton edge. The output of each tube was then fed to a constant fraction discriminator, and the discriminator outputs were used

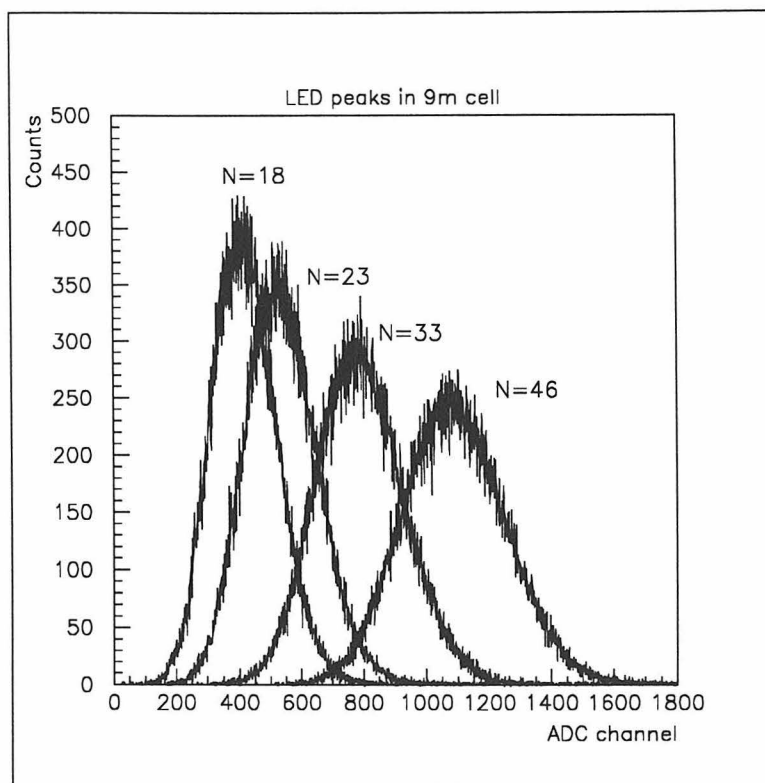


Figure 3.4: LED spectra measured by a 9-m prototype cell. The calculated number of photoelectrons corresponding to each peak is indicated.

to start and stop a 12-bit TDC with a resolution of 0.25 nanoseconds per channel. The ^{60}Co source, which emits 1 MeV γ rays, was then moved along the tank at intervals of about 1 meter and time-difference histograms were acquired. Figure 3.6 displays the time difference of the phototubes for the nine distances investigated along with a Gaussian fit to the distribution at each point. The distance is measured from the face of one of the tubes. Figure 3.7 displays the mean value of the timing distribution as a function of the position along the cell. A fit to this data gives a slope of 9.87 nsec/meter. The lower section of the figure displays the timing resolution (σ) as a function of distance along the cell. As expected, the resolution is best (2.5 nsec) at the center of the tank and falls off near the ends (to 3 nsec) as the far phototube sees only a few photons. Using the time-to-distance calibration slope of 9.87 nsec/meter gives a (1σ) position reconstruction resolution of 25 to 30 cm. In other words, the position of a 1 MeV energy deposit can be localized with 90% confidence to a region of about 80 cm. One should keep in mind, however, that the timing resolution will deteriorate

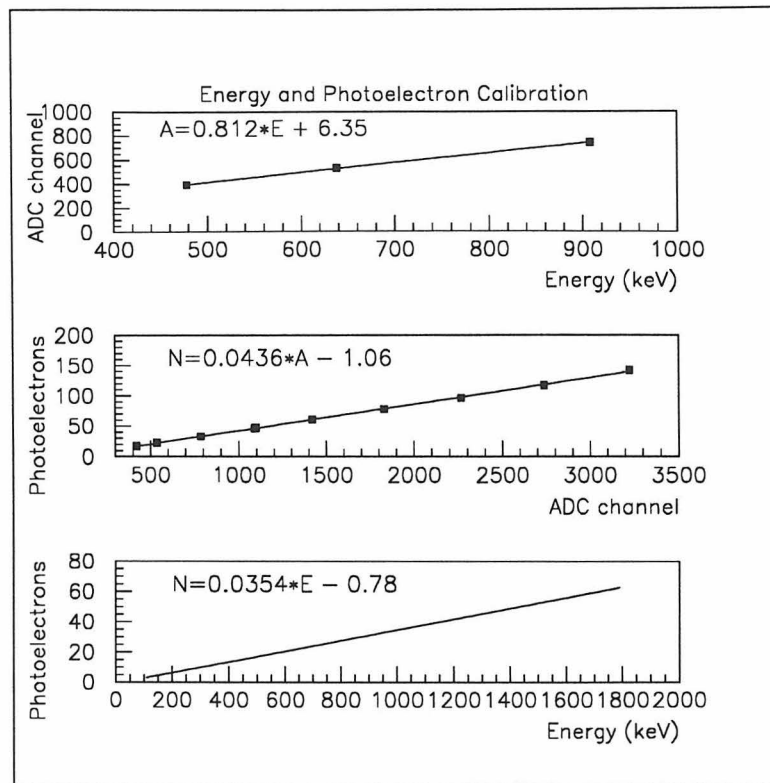


Figure 3.5: Three calibration fits are shown for the 9-m cell at 2 meters distance from one phototube. The top curve maps energy to ADC channel number using the Compton edges of ^{137}Cs , ^{54}Mn , and ^{65}Zn . The middle curve is a map of ADC channel to photoelectrons, and the bottom curve is the calculated number of photoelectrons per energy deposit in the cell.

for lower energy deposits. In addition, penetrating radiation often multiply scatters in the cell over large distances and could also contribute to a smearing out of the timing resolution. The imperfect reconstruction of position was taken into account in the Monte Carlo calculations presented in Chapter 5 by folding in the measured position dependence of the energy calibration.

3.5 The Detector Time Stability

The stability of the scintillator and acrylic cell system was investigated over a period of about one and a half years. It was a concern that the highly aggressive scintillator could etch the walls of the acrylic cell or dissolve the glue, changing the optical properties of the cell or the scintillator. Any poisoning of the scintillator could con-

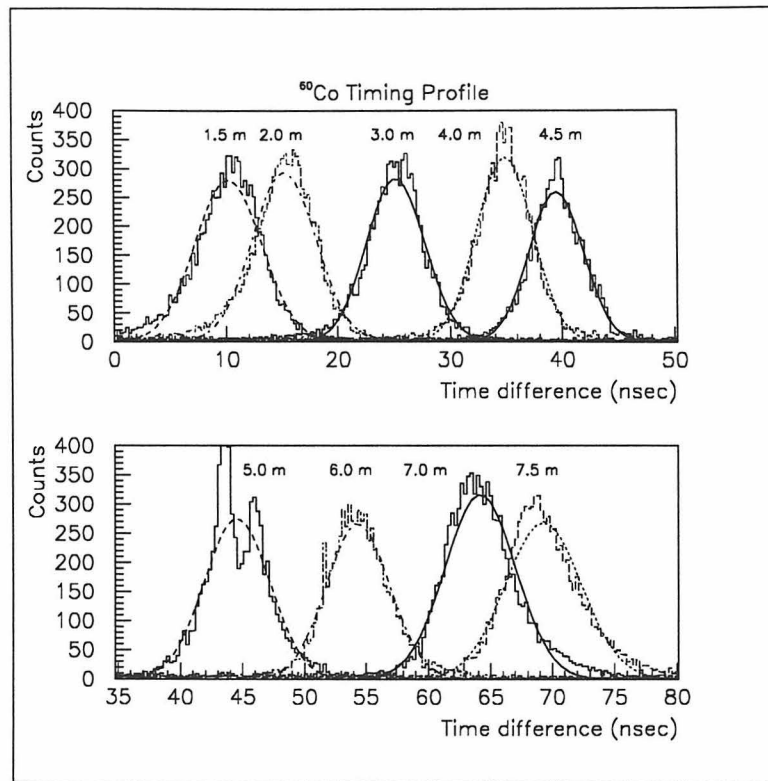


Figure 3.6: The timing resolution of the 9-m detector is measured using a ^{60}Co source and a Philips XP4512 tube at each end. The time difference spectra of the two tubes is shown for 9 positions of the source along the cell.

ceivably cause a degradation in the effective attenuation length of the scintillator and acrylic and thus reduce the light detected by the phototubes. One way to keep track of this effective attenuation length is to measure the position dependence of the cell calibration over time. If the attenuation length were degraded, the difference between far and near points would presumably become more pronounced.

This type of measurement scheme was employed between October 1994 and March 1996. A ^{232}Th source was placed at several distances along the tank, and the position of the Compton edge was measured as a function of the distance from one phototube. To factor out tube gain (since the tubes were often turned off, adjusted, etc., for other reasons during this time), the measurements were normalized to 1 at the 1.5 m distance point. Measurements were begun in October 1994 using the Caltech cell. In March 1995, a commercial cell was installed and the scintillator was siphoned into the new cell. Measurements then continued with the new cell. Figure 3.8 displays this

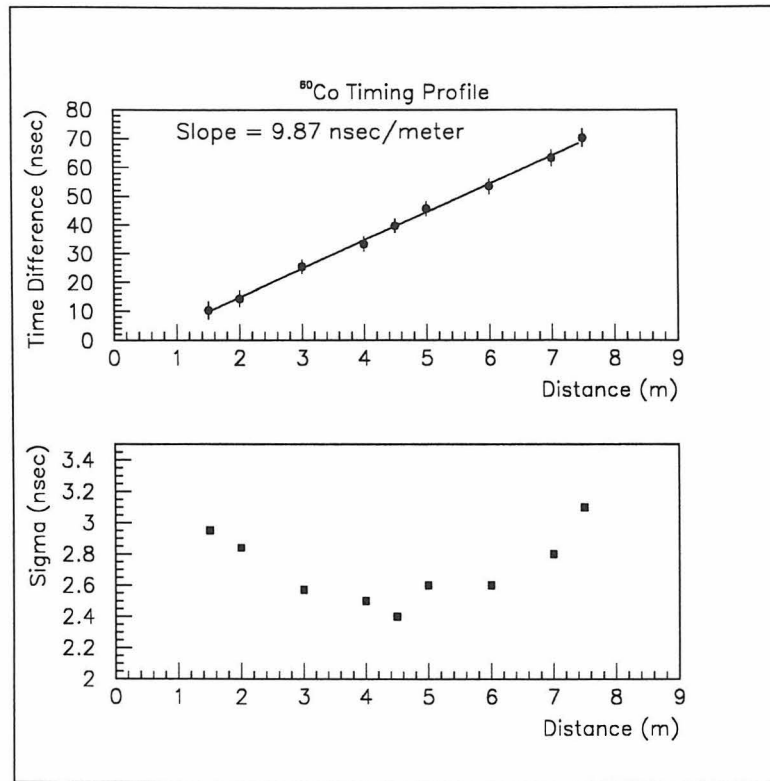


Figure 3.7: The upper curve is a fit to the ^{60}Co timing data yielding an effective signal propagation speed of about 10 cm/nsec. The lower figure illustrates the (1σ) timing resolution of the detector at 1 MeV.

normalized position dependence using data from October 1994 and March 1996. The 1.5-year average is also displayed. Figure 3.9 displays the full data set another way: the position of the Compton edge, normalized to the 1.5 m point, is displayed as a function of time for each of the positions investigated. A linear fit at each distance gives a measure of the fractional change of the relative attenuation per day. The result of these fits is summarized in the following table which presents the total change in relative attenuation over a 1.5 year period. Note that data is presented for a distance of 4.68 rather than 4.5 m. This is because the original Caltech cell was actually 9.36 m long and this represents the center of that cell.

Change in Relative Attenuation Ratio Over 1.5 Years	
Distance	Change
1.5	—
2.0	$-0.4 \pm 2.0\%$
3.0	$-4.7 \pm 2.5\%$
4.0	$-9.1 \pm 3.1\%$
4.68	$-9.6 \pm 4.0\%$
5.0	$-12 \pm 4.3\%$

To interpret this change, we can calculate that the number of photoelectrons produced per MeV at the center of the tank will decrease from 63.6 to 57.5 over 1.5 years of exposure. This represents a change in the cell resolution from 30% to 31% at 1 MeV at the center of the cell.

3.6 Gadolinium in the Scintillator

The scintillator is shipped to Caltech by Nuclear Enterprises in the form of a concentrate containing 0.5% Gd by weight. It is then diluted to 0.1% by the addition of pseudocumene and mineral oil. It is important to verify that the gadolinium complex remains in solution during the mixing and subsequently as the scintillator sits in the detector cell. A 100 ml sample of the scintillator was taken from the 9-meter prototype cell and its gadolinium content was measured by neutron activation and subsequent gamma spectroscopy.

Natural gadolinium consists of the following isotopes:

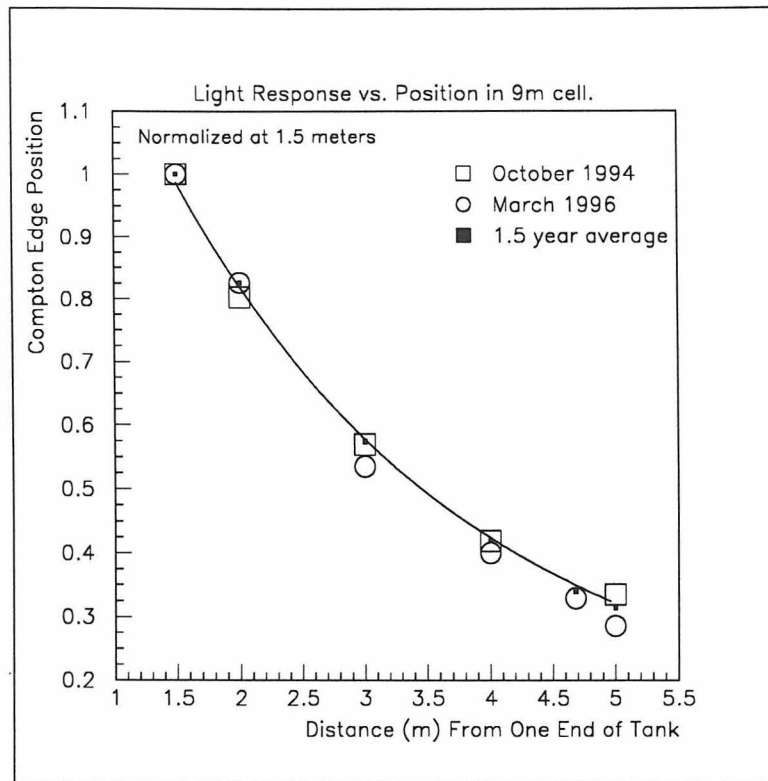


Figure 3.8: Relative attenuation as a function of distance from one phototube. Data from October 1994 and March 1996 are plotted. In addition, the average of all data during the intervening 1.5 years is plotted.

Isotope	Abundance
154	2%
155	15%
156	21%
157	16%
158	25%
160	22%

Thus neutron capture will lead to the production of the β -unstable isotopes ^{159}Gd and ^{161}Gd with half-lives of 18.6 hours and 3.7 minutes, respectively. The β^- decay of ^{159}Gd produces ^{159}Tb which de-excites via a 363 keV gamma with a branching ratio of 11%, making this a reasonable candidate for gamma spectroscopy.

The scintillator sample was placed in a glass bottle and lowered into a water tank containing a Californium fission source. The sample was neutron activated for

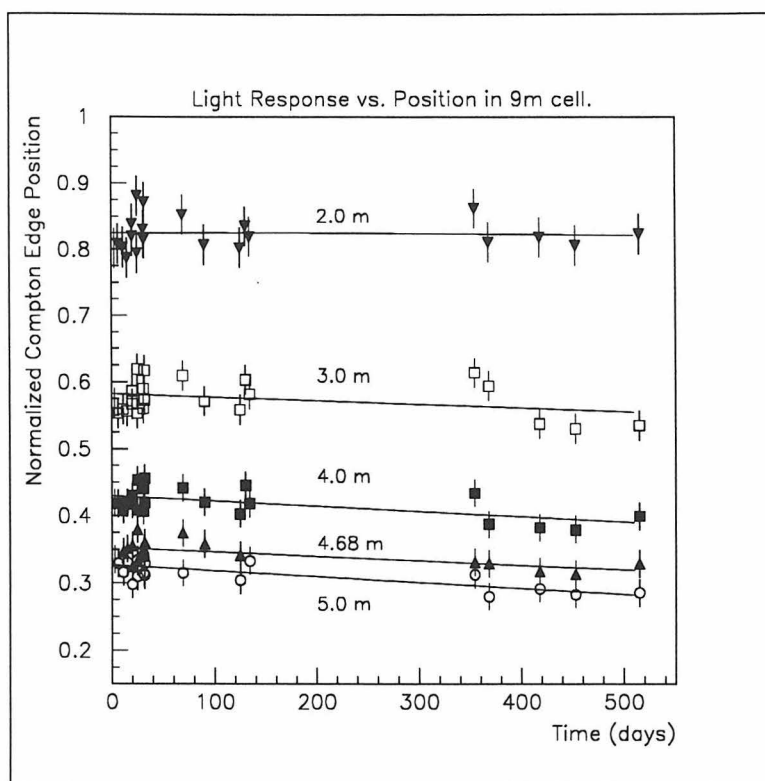


Figure 3.9: Relative attenuation as a function of time. Measurements made between October 1994 and March 1996 are displayed. The position of a ^{232}Th Compton edge is measured for several tube-source distances. The 1.5-meter point is normalized to an edge position of one.

approximately two days and then transferred to a new glass bottle (since the old one was now active) and placed near a hyper-pure germanium detector which had been shielded from external radioactivities by two inches of copper and six inches of lead. The germanium detector was read out into a multichannel analyzer and a spectrum was saved every two hours for 36 hours while the induced activity died away. Meanwhile, a calibrated standard was prepared by dissolving $\text{Gd}(\text{NO}_3)_3$ in ethanol at the level of 0.1% gadolinium by weight. Ethanol was chosen because it is a good solvent for gadolinium nitrate and because it has a density very nearly equal to that of the scintillator. An identical mass of this calibration solution was activated for the same length of time and at the same distance from the source as the scintillator sample. A direct comparison of the gamma spectra led to the conclusion that the 9-m cell scintillator contains gadolinium at the level of $0.11 \pm 0.02\%$. Figure 3.10

displays the ^{159}Gd gamma spectrum relative to the background counting rate.

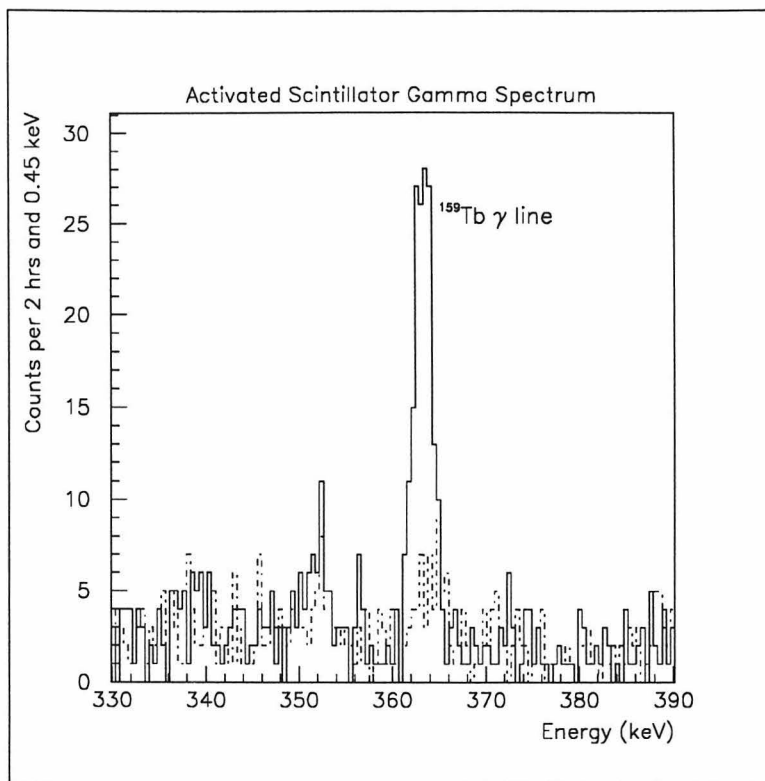


Figure 3.10: Gamma spectrum of activated Gd-loaded scintillator. The solid histogram is the activated scintillator and the dashed spectrum is the background. The 363 keV de-excitation gamma from ^{159}Tb is clearly visible.

3.7 Conclusion

Tests of a prototype 9-meter detector show that the glued acrylic cell is mechanically and optically quite stable. Over the course of a year and a half, the acrylic and glue joints were able to stand up to the high pseudocumene content of the liquid scintillator with no visible degradation. The detector was calibrated and its resolution measured to be quite reasonable: 3.2 photoelectrons are expected from a 50 keV energy deposit at the center of the cell. The phototubes were found to perform well and will allow reconstruction, through timing, of the position of large energy events to less than a meter. The Gd-loaded scintillator was found to degrade slightly in attenuation length over a 500 day period, but to an extent that the resolution is degraded by only a few

percent. The gadolinium complex in the scintillator showed no signs of instability and remained dissolved in the liquid over the 1.5 year test period.

Chapter 4

Calibration of the Positron Detection Efficiency

A precise knowledge of the neutrino detection efficiency is critical for a “disappearance-type” neutrino oscillation experiment such as Palo Verde. In particular, the positron detection efficiency, because of its reliance on a very low (50 keV) annihilation cell threshold, must be measured experimentally. This can be done using a positron emitter that will be dissolved uniformly into the scintillator of one of the detector cells *in situ* using the method detailed here. The other half of the neutrino detection efficiency, the neutron capture, must also be measured. This is part of an ongoing development project and is discussed briefly in Chapter 6.

4.1 The Concept

The neutrino-induced inverse β decay in the Palo Verde detector may be simulated by uniformly dissolving a pure positron emitter in the scintillator of one cell. This cell then acts as the “positron-like” cell and the surrounding cells are used to detect the annihilation radiation. Since the cross section for positron annihilation goes as one over the velocity, nearly every positron annihilates at rest producing two back-to-back annihilation gammas of 511 keV each, as required by energy-momentum conservation. Thus the annihilation radiation produced by any positron emitter is identical to that produced by the neutrino inverse β decay detection reaction. In addition, positrons of a few MeV (such as those produced by a neutrinos from a nuclear reactor) have essentially no chance of penetrating the acrylic cell walls and thus deposit all of their energy in one cell. So the annihilation signature in the cells

surrounding the positron cell is completely independent of the energy of the parent positron. This allows a β^+ emitter to mimic a neutrino signal.

For the efficiency calibration one cell will be removed from the 6 by 11 array and replaced by a cell filled with liquid scintillator which has been loaded with approximately 1000 Bq of a suitable positron emitter. The rate of valid “triple coincidences,” in which the positron cell fires along with at least two surrounding cells in an accepted back-to-back topology, will be compared with the firing rate of the positron cell alone. This measured ratio is simply the positron detection efficiency, though with a few complications. The first complication is the positron cell energy threshold setting. Obviously, the number of positrons detected above some (software implemented) energy threshold depends on the spectral shape of the positrons emitted by the source, which is different from the spectrum of positrons produced by the reactor. However, both spectra are well known and the spectral fraction above a given threshold may be calculated easily, assuming the energy value of that threshold is well known. (Section 4.5.1 describes a method for calibrating the threshold). However, this calculation is complicated by the fact that the annihilation gammas sometimes scatter in the positron cell before escaping to the surrounding cells, altering the measured spectral shape. But since the production of annihilation radiation is independent of the positron energy, the measured spectrum is just the calculated positron spectrum added to the Compton spectrum of 511 keV gammas in the cell. The modification of the spectrum is identical for the source and reactor-induced positrons. A detailed Monte Carlo simulation is required to really understand this modification and to translate it to the spectrum of positrons produced by the reactor neutrinos. However, the simulation can be fine tuned if the activity of the positron source is accurately known. In this case the expected count rate above any threshold can be measured and compared to the results of the simulation which has now been independently normalized to the known source activity. The tuned Monte Carlo can then be used to modify the reactor positron spectrum in exactly the same way.

The second complication is the distribution of the efficiency calibration over the entire array. It would be impractical to repeat the procedure for each of the 66

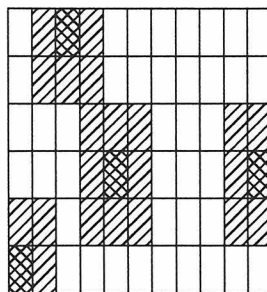


Figure 4.1: Topologically-distinct positron cell positions for efficiency calculation: top, side, corner, and center.

cells. Instead, one can use symmetry arguments to obtain a fully integrated detector efficiency. Using a block of nine cells as the fundamental unit, there are only four topologically-distinct positions as illustrated in Figure 4.1. The top, side, and corner cells all show lower efficiency than the center cells because of “missing” surrounding cells. It is thus necessary to repeat this calibration procedure in four places to cover each topology. Of course the edge or corner topologies could be simulated by turning off (in software) several cells surrounding a center cell, but in this way, one does not eliminate gamma events that might scatter from a dead cell to a live one.

The efficiency of the entire array can then be calculated by summing the efficiencies of each cell by its topological type. However, before this can be done, every cell in the array must have its energy calibrated and its software threshold set to exactly the same value. Since all the cells are dimensionally identical, are made of the same acrylic, and are filled with the same scintillator, they have identical optical properties. Then even though all the phototubes do not perform identically and may not be precisely matched in gain, the cells will perform identically, in terms of a hit/no-hit determination, if each cell’s software threshold is set at the same absolute energy point (nominally 50 keV). Once the thresholds are matched, an LED monitor can be used to assure stability by monitoring the ADC channel at which a feature such as the single photoelectron peak appears. This allows the four-point efficiency calibration to be extended to the full integral detector efficiency.

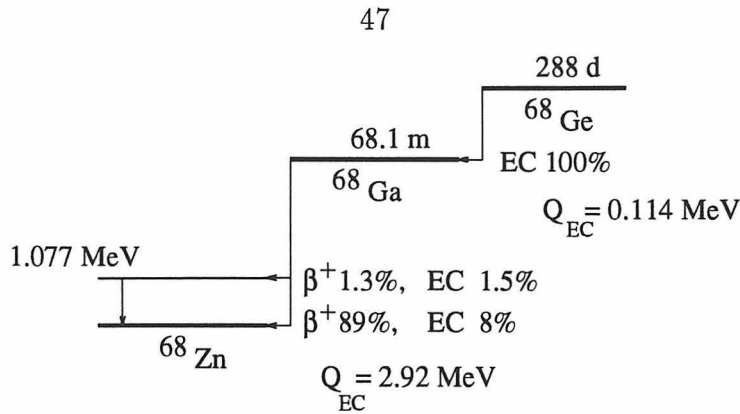


Figure 4.2: Simplified level scheme of ^{68}Ge decay.

4.2 Efficiency Calibration Requirements

The calibration procedure outlined above requires the selection of a suitable positron emitter. It should have a reasonably long half life, should have a high endpoint energy to be comparable to the reactor positron spectrum, which extends to about 6 MeV, and should be free from gamma emission which could contaminate the 511 keV annihilation radiation. Once identified, the isotope should be commercially available or simple to produce with good purity, and must be placed in a chemical compound that can be dissolved in organic liquid scintillator. The one isotope found that satisfies all of the above is ^{68}Ge . It is widely used in the medical field for positron emission tomography (PET) and is thus available commercially. ^{68}Ge decays by electron capture to the ground state of ^{68}Ga with a half life of 288 days. ^{68}Ga then decays by β^+ emission and electron capture to ^{68}Zn with a 68-minute half life. A simplified level scheme is shown in Figure 4.2.

This source has a high (89%) positron yield and only a 3% branch to the 1 MeV excited state. In addition, its relatively high β^+ endpoint of 1.9 MeV makes it a good candidate for this calibration. In order to be useful, however, the source must be dissolved in liquid scintillator. After two failed attempts by a local radiochemical company to produce a stable compound, it was decided to synthesize a source based on tetra-*n*-butylgermane here at Caltech. The detailed chemical procedure is described in Appendix A.1.

4.3 Source Calibration

As the chemical efficiency of the procedure described in Appendix A.1 is unknown, the source must be calibrated experimentally. A source calibration method, based on a hyper-pure germanium (HPGe) detector, was developed for measuring the activity of the dissolved ^{68}Ge . An extended source presents calibration problems as the effects of geometry and self absorption are difficult to estimate with the required precision. However, by exploiting the coincidence of the positron and annihilation radiation, one can make use of counting ratios in which the various efficiencies cancel out. The apparatus used for the calibration is depicted in Figure 4.3. Liquid scintillator, loaded with radioactive ^{68}Ge , is filled into a small cylindrical acrylic tank measuring 10 cm in diameter and about 7 cm in length. A 3-inch photomultiplier tube is coupled to one side of the tank and the apparatus placed up against an HPGe detector which is enclosed in a lead house to attenuate natural radioactivities from the walls. A large plastic scintillator above the entire apparatus rejects cosmic muons. In the scintillator, the positron loses energy and then annihilates, producing 511-keV gammas which are detected in the HPGe detector. The source activity is then evaluated as follows: let $N_{\gamma 511}$ be the counting rate observed in the 511 keV peak in the germanium detector spectrum. Let N_s be the counting rate of the scintillator, read out by the phototube, in some energy interval, and let N_c be the rate at which both the germanium detector and the scintillator fire together in the correct energy intervals. Let the efficiency of the germanium detector for 511 keV gammas, including geometric factors and self absorption in the scintillator, be given by ϵ_{Ge} . Let b_0 and b_1 be the positron branching ratios to the ground state and 1.077 MeV excited state of ^{68}Zn , respectively. Then define ϵ_{s0} and ϵ_{s1} as the positron detection efficiencies in the scintillator of positrons from the ground state branch and the excited state branch, respectively (see Figure 4.2). These efficiencies are not equal because they include threshold (spectral fraction) cuts, i.e., ϵ_{s1} goes to zero if the threshold is raised beyond the endpoint of the excited state positron branch. The annihilation quanta produced by the two positron states is, of course, exactly the same, so the germanium detection

efficiency is the same for either branch. We can write the following expressions:

$$N_{\gamma 511} = 2 \cdot A \cdot (b0 + b1) \cdot \epsilon_{Ge},$$

$$N_s = A \cdot b0 \cdot \epsilon_{s0} + A \cdot b1 \cdot \epsilon_{s1},$$

$$N_c = A \cdot b0 \cdot \epsilon_{s0} \cdot 2 \cdot \epsilon_{Ge} + A \cdot b1 \cdot \epsilon_{s1} \cdot 2 \cdot \epsilon_{Ge}.$$

So

$$\frac{N_s \cdot N_{\gamma 511}}{N_c} = \frac{A \cdot (b0 \cdot \epsilon_{s0} + b1 \cdot \epsilon_{s1}) \cdot 2 \cdot A \cdot \epsilon_{Ge} \cdot (b0 + b1)}{2 \cdot A \cdot \epsilon_{Ge} \cdot (b0 \cdot \epsilon_{s0} + b1 \cdot \epsilon_{s1})} = A \cdot (b0 + b1),$$

or

$$A = \frac{N_s \cdot N_{\gamma 511}}{(b0 + b1) \cdot N_c}.$$

The activity, A , is thus determined independently of the individual detector efficiencies. They cancel because the experimental conditions are the same for the singles and coincidence measurements (apart from a small correction because of annihilation radiation scattering inside the scintillator, see section 4.3.2). Indeed, to ensure precisely the same experimental conditions, the singles and coincidence data are taken together, and coincidences are identified off line so that any gain drift or other environmental change affects both data sets identically.

4.3.1 The Electronics Readout

A schematic of the electronics readout is shown in Figure 4.4. The main event trigger comes from an OR of the germanium detector and the phototube signal. This OR gates a LeCroy 2249 charge ADC which acts as a register, latching the logic state of four input lines which indicate whether or not the scintillator, the HPGe detector, the muon veto, and a mercury pulser (described below) were active during the event, i.e., within 100 ns of each other. This module generates a CAMAC look-at-me (LAM) which then causes a readout of the register ADC, a peak-sensing LeCroy 3511 ADC used to measure the HPGe energy, a LeCroy 2249W charge ADC used to measure

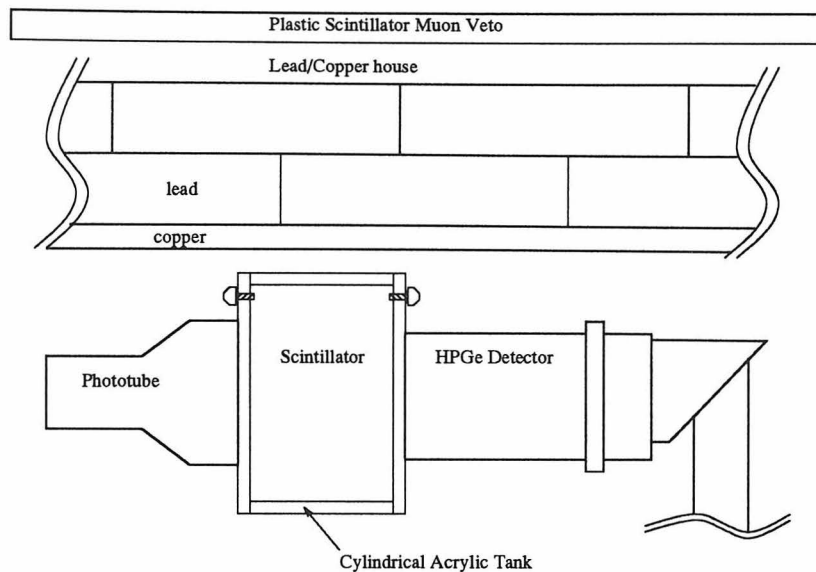


Figure 4.3: Apparatus used to calibrate the ^{68}Ge source. The apparatus is completely enclosed inside a 2-inch copper and 6-inch lead house. A large, 24-by-36-inch plastic veto sits above the house to reject cosmic muons.

the scintillator energy, and a LeCroy 2228A TDC which measures the time difference between the HPGe detector and the phototube. A mercury pulser firing at about 1 Hz is fed into the test input of the germanium detector preamp and used to monitor the stability of the preamp and shaping amplifier gain. This was found to be stable to better than 1% during all data runs.

4.3.2 Data Analysis

The germanium singles rate, or $N_{\gamma 511}$ above, is determined by fitting a Gaussian plus a linear background to the 511 keV spectral peak and integrating the Gaussian. The no-source background, obtained by filling the cell with fresh scintillator, is also subtracted off, but this contribution is typically about 1% for the activities used. In this analysis, muons and pulser events are rejected by placing the appropriate cuts on the hit register, but any light deposit in the scintillator is disregarded. The phototube singles count rate, or N_s above, is determined by integrating the measured β spectrum over some energy range regardless of the germanium detector hit condition. Again, muon events and pulser events are removed in this analysis and no-source backgrounds are

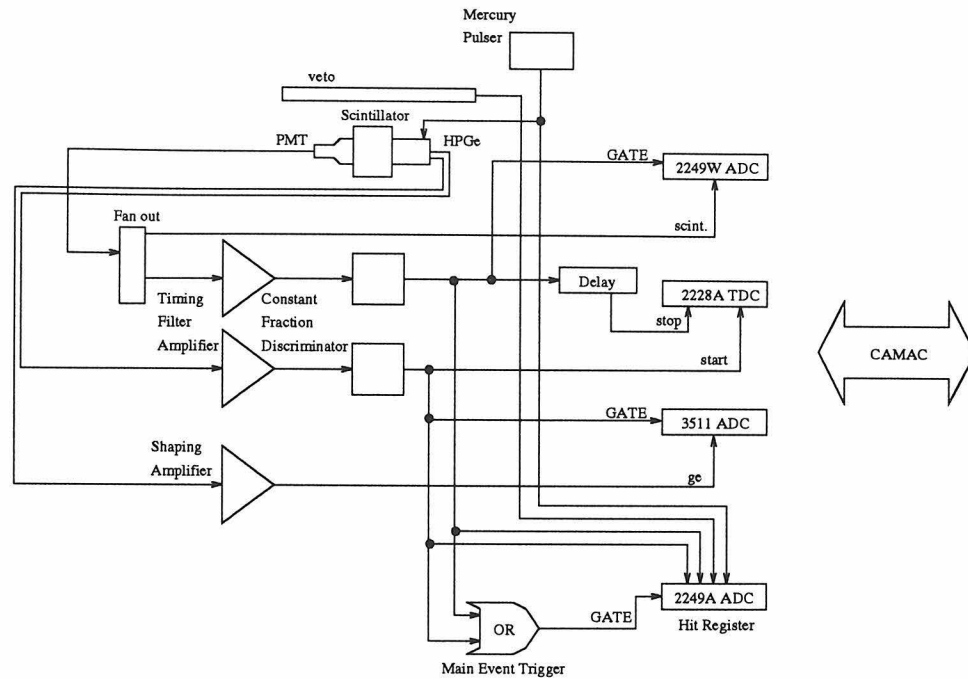


Figure 4.4: Block diagram of electronics readout. A 2249A ADC acts as a hit register and overall event trigger. When it generates a LAM, four modules are read out via CAMAC.

measured with an unloaded scintillator sample. Finally, the coincidence counting rate, or N_c , is determined by integrating the β spectrum over the same energy interval using the data subset generated by requiring that 511 keV be deposited in the germanium detector within 30 ns of the scintillator's firing as measured by the TDC. These three rates are then used to calculate the source activity as described above. The activity calculation was found to be independent, as expected, of the scintillator energy interval used in the analysis (see section 4.3.3).

In fact, there is a slight complication in the analysis since the annihilation radiation absorption is different in the singles and coincidence cases. In the singles case, two annihilation gammas are free to scatter and deposit energy in the scintillator. However, in the coincidence case, the scintillator spectrum is taken from the subset of data in which one 511-keV gamma has been completely absorbed in the germanium detector. This requires an adjustment of the spectrum before analysis. It turns out in this case that a simple shift of the energy scale is all that is needed to correct for the removal of one annihilation quanta. This can be understood as follows: the energy

and angular distribution of the annihilation radiation is completely independent of the positron energy so all positron energies are affected identically by the absorption of gamma energy. In the case of an infinitely large detector, then, all the annihilation radiation would always be absorbed, resulting in a positron spectrum shifted up in energy by 1022 keV but undistorted in shape. Similarly, for the opposite extreme of no gamma absorption, we would obviously see an undistorted and unshifted positron spectrum. In the intermediate case, we would see some distortion of the shape as well as a shift as the positron spectrum was added to the Compton spectrum of absorbed annihilation radiation. However, for the present case, with a scintillation detector rather small compared to the interaction length of a 511 keV gamma, the average gamma energy loss is small and we approach the “no-absorption” limit. In fact, on average less than 10% of the gamma energy is lost in the tank and a shift of about 50 keV reproduces the singles spectrum with only a small distortion visible at the endpoint. The shift required is calculated by normalizing the singles and coincidence spectra to the same total area and then minimizing the squared bin-by-bin subtraction while varying the bin offset. Figure 4.5 illustrates this spectral adjustment.

4.3.3 Precision and Reproducibility

The accuracy of this technique was evaluated by measuring the activity of a calibrated ^{22}Na source. The source used was an encapsulated point source so the positron spectrum could not actually be used, but the coincidence technique could still be demonstrated by making use of the 1.275 MeV gamma line in coincidence with the positron (and annihilation radiation). A level diagram of ^{22}Na β^+ decay is shown in Figure 4.6.

The small point source was placed between the acrylic tank filled with pure scintillator and the germanium detector. To form the coincidence, the germanium detector was used to detect the 511 keV annihilation gammas, and the scintillator was used to measure the Compton spectrum of the 1275 keV gamma. Of course, the other annihilation gamma was also able to enter the scintillator and contribute to the scin-

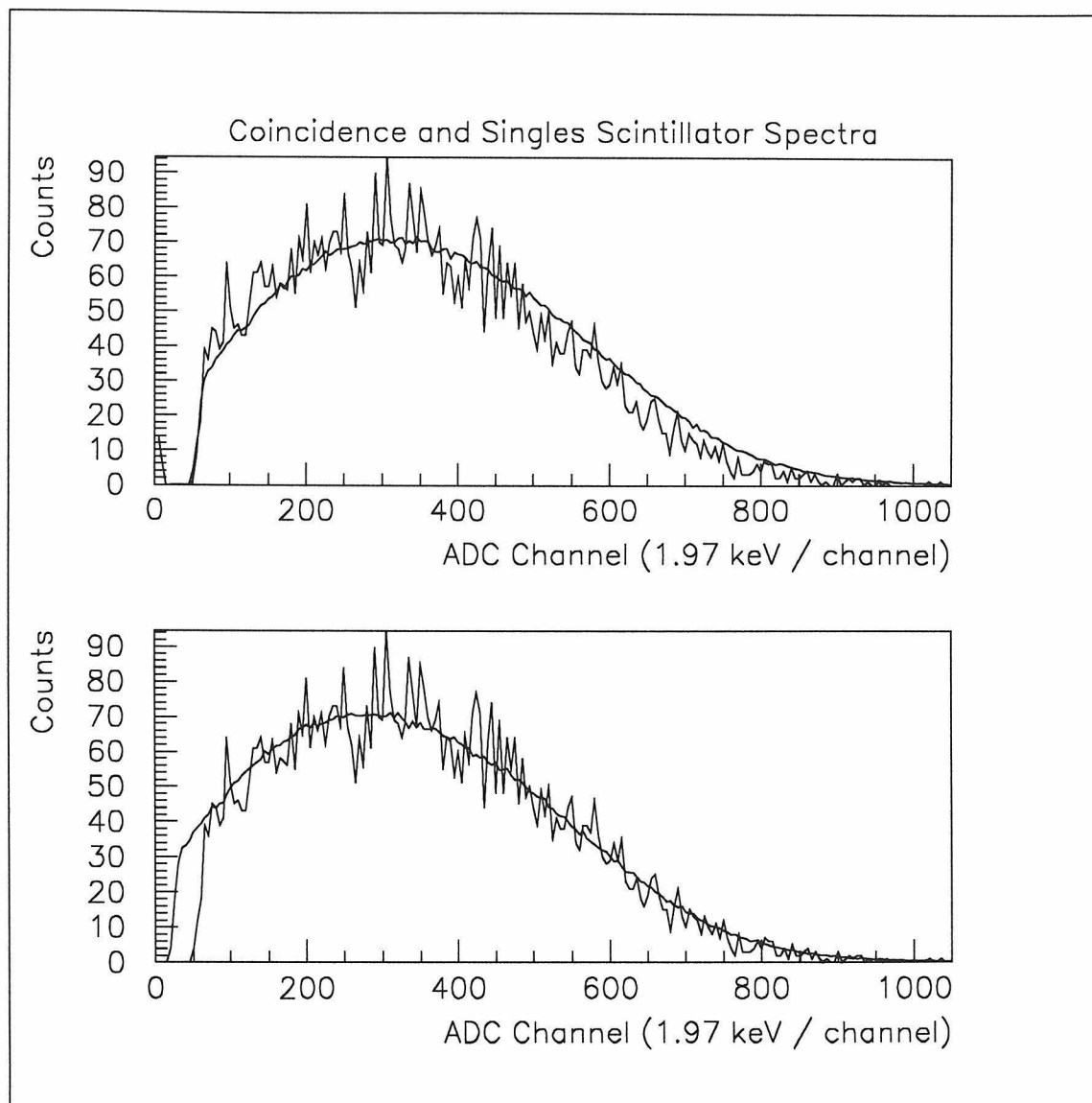


Figure 4.5: The top figure illustrates the relative shift between the singles (smooth curve) and the coincidence spectra of ^{68}Ge . The singles spectrum has been normalized to the same area as the coincidence spectrum by multiplying by a factor of $\frac{1}{137}$. Both spectra are rebinned by a factor of five for clarity. The lower figure illustrates the match of the two spectra after shifting the singles spectrum by 33 channels (65 keV).

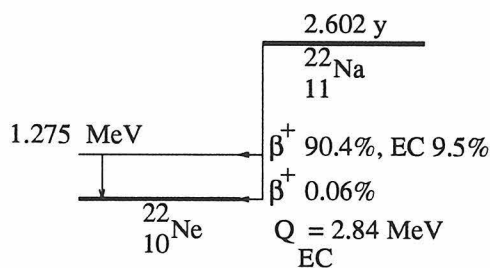


Figure 4.6: Decay scheme of ^{22}Na .

tillator spectrum. This produced a systematic error in this test measurement insofar as the 511 keV gamma tail leaked into the 1275 keV gamma Compton spectrum. This effect was minimized by setting a lower threshold in the scintillator at about 750 keV, above the tail of the 511 keV distribution. This did not completely eliminate this background, however, because the 511 keV and 1275 keV can also add if both scatter in the detector during a single event.

The source used was calibrated on June 1, 1979 by Isotope Products, Inc., at an activity of $11.5 \pm 3\% \mu\text{Ci}$, giving a strength of $0.192 \mu\text{Ci}$, or 7110 ± 210 decays per second on October 11, 1994, when the test calibration was undertaken. The 511 keV radiation was detected in the germanium detector, and the 1275 keV gamma in the scintillator. The expression for the activity is then given by $A = \frac{N_{\gamma 511} \cdot N_s}{0.9994 \cdot N_c}$, where the symbols are defined as previously. Table 4.1 summarizes the results of the calibration for two different data samples and three different energy intervals used to analyze the scintillator spectrum. The measurements all show good agreement with the reported value of 7110 decays per second.

Tests of the precision were made using ^{68}Ge . A cell was filled with scintillator to which a small quantity of ^{68}Ge had been added and measurements of its activity were made. The source remained in the tank for four days during which several measurements were made to investigate the reproducibility of the activity measurement and the dependence of the measurement on the analysis interval selected. For these measurements, the source-correlated background was subtracted. This background comes from Compton scattering of 1.077 MeV γ radiation which happens to leave enough energy in the germanium detector to appear to lie in the 511 keV photopeak.

Table 4.1: Results of a ^{22}Na point source test calibration. The activity of the source is known to be $0.192 \mu\text{Ci}$, or 7110 ± 210 decays per second. Two different data sets are shown: the first three measurements are from one data set in which the scintillator analysis interval was varied. The last entry is from a second, higher statistics data set.

Analysis Interval (channels)	Analysis Interval Energy (keV)	$N_{\gamma 511}$	N_s	N_c	Activity (dps)
400 – 700	788 – 1367	498 ± 6	182 ± 4	12.7 ± 0.9	7125 ± 541
400 – 600	788 – 1175	498 ± 6	173 ± 4	12.0 ± 0.9	7180 ± 552
300 – 700	596 – 1367	498 ± 6	295 ± 5	20.3 ± 1.2	7241 ± 558
400 – 700	788 – 1367	513.4 ± 1.7	180.5 ± 1.0	12.92 ± 0.28	7171 ± 150

To estimate this contribution, a window was set in the germanium analysis of a width equal to the width of the 511 keV peak, but displaced one peak width in energy with the assumption that the Compton background is roughly flat and will thus be equal in any interval near the peak. A coincidence data set was then generated using the displaced germanium energy cut and this background was statistically subtracted off. The background subtracted was generally less than 2%.

Table 4.2 illustrates the insensitivity of the activity measurement to the analysis interval selected, and the β spectra from this run are displayed in Figure 4.5. Figure 4.7 illustrates the reproducibility of the activity measurements over several days.

Table 4.2: Results of a ^{68}Ge source calibration. The dependence of the calculated activity on the energy interval selected for analysis is investigated.

Analysis Interval (channels)	Analysis Interval Energy (keV)	$N_{\gamma 511}$	N_s	$N_c - bkg$	Activity (dps)
120 – 700	307 – 1450	3.54 ± 0.04	352.6 ± 0.4	2.52 ± 0.03	548.5 ± 9
200 – 600	465 – 1253	3.54 ± 0.04	270.2 ± 0.3	1.95 ± 0.03	543.2 ± 9
120 – 500	307 – 1056	3.54 ± 0.04	282.1 ± 0.3	2.04 ± 0.03	542.1 ± 9
120 – 767	307 – 1582	3.54 ± 0.04	360.9 ± 0.4	2.57 ± 0.03	550.5 ± 9
100 – 800	268 – 1647	3.54 ± 0.04	375.5 ± 0.4	2.66 ± 0.03	553.4 ± 9

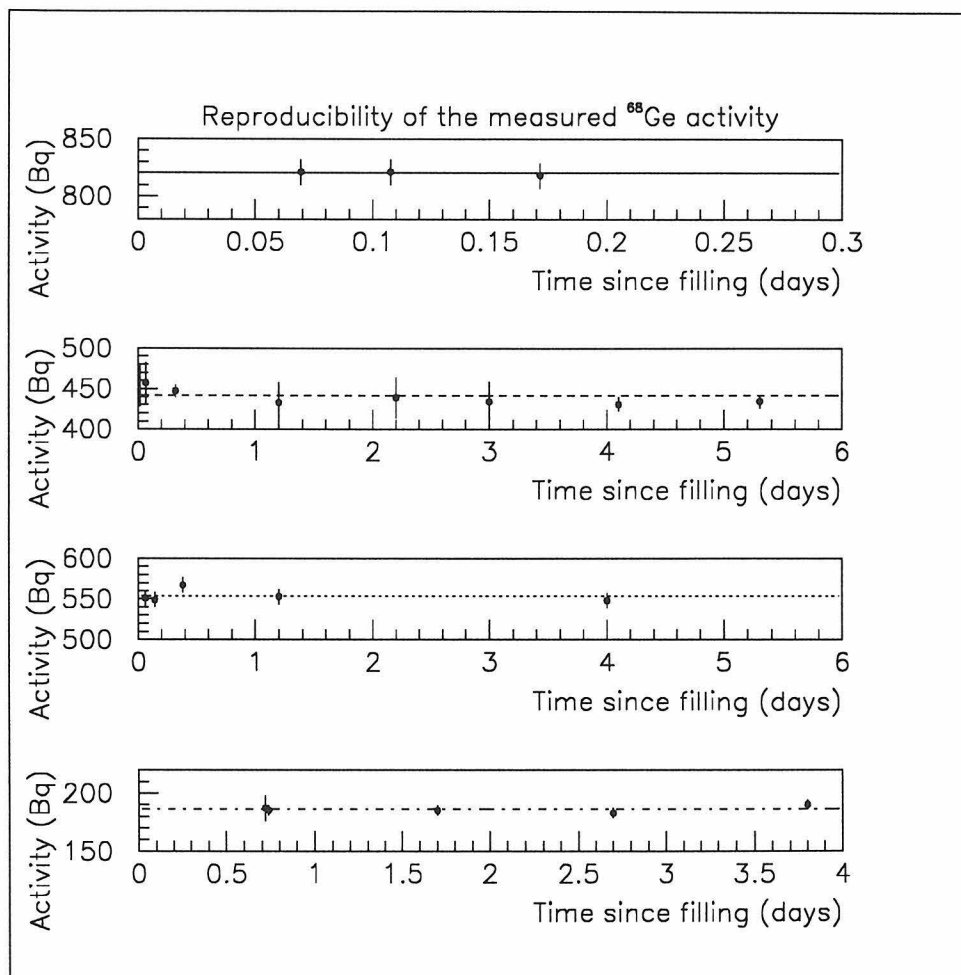


Figure 4.7: Reproducibility of the ^{68}Ge activity measurements. Measurements made over several days during four separate runs are displayed. The average value is plotted as a horizontal line.

4.4 Summary of Source Tests and Results

With a working calibration system, tests were performed to investigate the chemical stability of the ^{68}Ge in the source and the influence of the source loading process on the physical properties of the liquid scintillator.

Early attempts by a local radiochemical company to produce a ^{68}Ge source suitable for dissolving in liquid scintillator were plagued by problems with chemical instability. Determinations of how much of the source was sticking to the walls were made using the calibration system described above. The source, in liquid scintillator, was placed into an acrylic test tank where it remained for a length of time ranging from an hour to over a month in various runs. The activity of the source was calibrated by the above method, and the scintillator was then dumped out, the acrylic tank washed with clean scintillator, and then refilled with fresh, unloaded scintillator. The activity remaining in the tank was then calibrated to determine the fraction of the source bound to the cell walls. Measurements of this type were performed both for the early commercial sources and for sources prepared by the method described in Appendix A.1. Two tetra-*n*-butylgermane sources were prepared at Caltech: one containing about 370 Bq/ml of ^{68}Ge activity and 213 ppm of germanium carrier, the other containing about 18 kBq/ml of ^{68}Ge and 112 ppm of germanium carrier. The carrier concentration measurements were performed by Elemental Research, Inc. The source sticking was investigated as a function of the time spent in the cell and of the germanium carrier concentration in the scintillator sample. The results of these measurements are summarized in Table 4.3. It is clear from the table that the tetra-*n*-butylgermane source shows markedly better stability in the tank and a very low rate of sticking to the walls. For reference, the 9m cell calibration would involve inserting about 1 kBq of ^{68}Ge activity into 200 liters of scintillator, where it would remain for about one day. Using the first source (370 Bq/ml and 213 ppm Ge) would result in a germanium concentration in the cell of about 3 ppb. Of course, this concentration to activity ratio can be adjusted arbitrarily.

Because this source is to be used to calibrate the efficiency of the large Palo Verde

Table 4.3: Investigation of ^{68}Ge source chemical stability. Source type **A** is the commercial source based on GeCl_4 . Type **B** is the tetra-n-butylgermane source synthesized at Caltech.

Source Type	Ge Concentration	Exposure Time (days)	Fraction Sticking (%)
A	635 ppb	0.2 days	2.4 ± 0.6
A	1540 ppb	1.9 days	3.7 ± 0.4
A	276 ppb	4.0 days	21.6 ± 0.6
A	89 ppb	28 days	40 ± 1
B	938 ppb	4.0 days	0.11 ± 0.03
B	137 ppb	4.0 days	0.37 ± 0.5
B	3.3 ppb	4.2 days	1.9 ± 0.2
B	4480 ppb	5.3 days	0.15 ± 0.04

detector, it is important that its loading into the scintillator does not significantly affect the physical properties, most critically, the light yield and attenuation length. To this end, a sample of scintillator was loaded with tetra-n-butylgermane at the level of 2 ppm of germanium, a factor of 1000 higher concentration than will typically be used for the calibration. The light yield and attenuation length of this loaded scintillator was measured and compared to that of the unloaded scintillator. No significant difference was measured. These measurements are described in Appendix A.2. In addition, samples of the germanium-loaded scintillator were sent out for commercial mass-spectroscopic analysis and were measured to contain 0.1% by weight of gadolinium. This indicates that the germanium loading process does not affect the gadolinium dissolved in the scintillator for the purpose of increasing the thermal neutron cross section.

4.5 Prototype Calibration Experiment

As a proof-of-principle test, a positron efficiency calibration was performed on an array of 15 short acrylic test cells. The cells used were taken from the Gösgen reactor neutrino oscillation experiment [55] and measure $88 \times 20 \times 9$ cm. Each cell is read out by four 3-inch XP2312 photomultiplier tubes, two on each end. The two PM's on

each end were analog summed at the tube, and the summed signals from each end of the cell were sent to a fan-in where the full energy of the cell was summed and then digitized in a charge ADC. The small cells, of course, allow no direct conclusions to be drawn about the efficiency of the 9 m cell setup, but it does allow a precise comparison of experiment and Monte Carlo simulation, proving the utility of the method for efficiency calibration. The test was undertaken before the more stable tetra-*n*-butylgermane source was available, so the commercial source was used instead. Some sticking of the source to the cell walls did occur, but this was kept at low levels by minimizing the time the source was in the cell. The Monte Carlo simulation was also able to model the sticking quite well, so the source instability was not a problem for this test.

Fifteen Gösgen cells were stacked in an array five cells wide by three cells deep (see Figure 4.8). The entire array was enclosed in a house of lead bricks to shield the setup from natural radioactivities in the walls and floor of the lab. The center cell, cell 8, was filled with the ^{68}Ge -doped scintillator and thus acted as the “positron” cell while the surrounding 14 cells were analyzed as “annihilation” cells. The positron detection efficiency was investigated as a function of the energy thresholds of the annihilation cells, of the positron cell, and of the topological patterns of fired cells.

4.5.1 Cell Array Energy Calibration

The first step of the efficiency experiment was to gain match and calibrate the energy scale of all the cells in the matrix to precisely determine the energy thresholds. The dynamic range of the side cells was adjusted to extend to about 800 keV to encompass the nominal energy cut of 50–600 keV for the annihilation radiation. The range of the positron cell was extended to about 3 MeV to include the full positron spectrum (endpoint 1.9 MeV). The gain of the two ends of each cell were first matched by adjusting the high voltages independently using the Compton edge of a ^{54}Mn source (646 keV) placed at the middle of the cell as a reference. The matching was done in such a way as to bring the summed energy scale of each cell to roughly the same

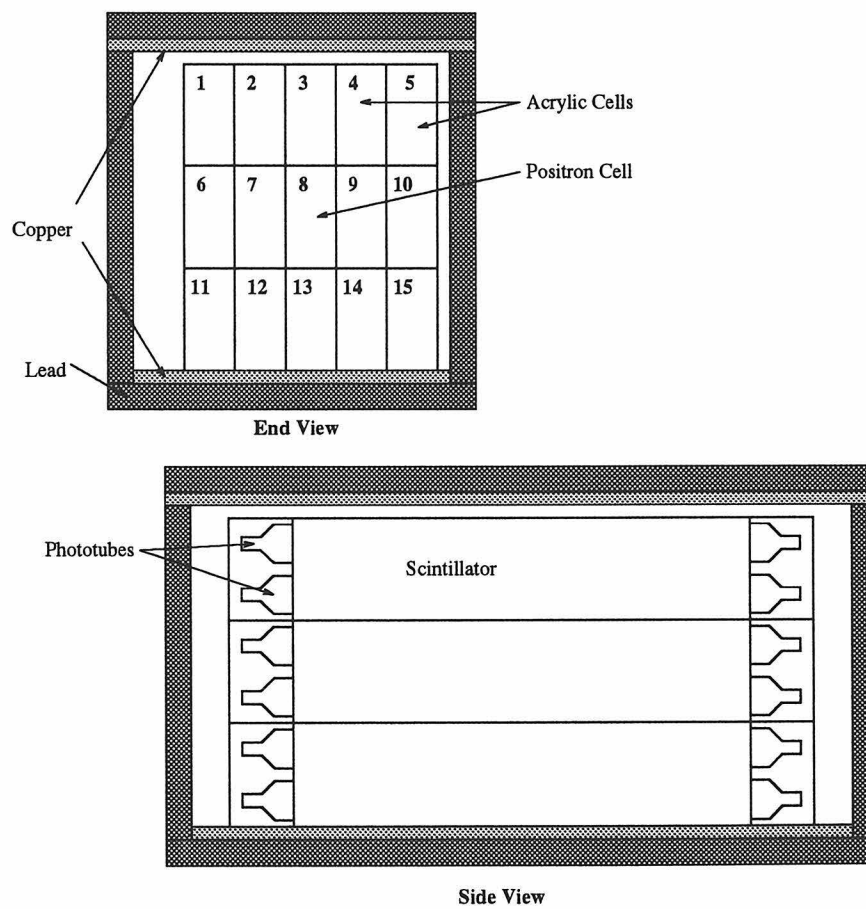


Figure 4.8: Gösgen cell array used in prototype efficiency calibration.

point. A precise energy calibration of each cell was then performed, using a number of radioactive calibration sources, and the energy thresholds were then matched in software during the data analysis. The calibration sources were attached to a meter stick and inserted in turn into the array, and calibration data was acquired with the source at the middle of each cell. The following sources were used for the calibration:

Annihilation Cell Calibration		
Source	γ Energy (keV)	Compton Edge (keV)
^{54}Mn	842 keV	646 keV
^{137}Cs	662 keV	478 keV
^{203}Hg	279 keV	146 keV
^{57}Co	123 keV	40 keV
Positron Cell Calibration		
Source	γ Energy (keV)	Compton Edge (keV)
^{232}Th	2614 keV	2381 keV
^{65}Zn	1119 keV	911 keV
^{54}Mn	842 keV	646 keV
^{137}Cs	662 keV	478 keV
^{22}Na	511 keV (annih.)	341 keV

The Compton spectrum of the sources in each cell were analyzed and the energy deposit of the backscattered gamma (the Compton edge) was assigned to the 90% maximum point of the edge structure, see Figure 4.9. The calibrations show good linearity. Figure 4.10 shows the calibration data for two cells, cell 8, the positron cell, and cell 3, a side cell just above cell 8. Generally, with this calibration scheme, the 50 keV threshold could be set with a precision of about 10%.

4.5.2 Data Acquisition

The data acquisition system for the efficiency calibration test was quite simple. Any energy deposit in the center cell, cell 8, above a low hardware threshold of about 300 keV initiated a readout of all 15 cells into a 16-channel LeCroy FERA 4300B

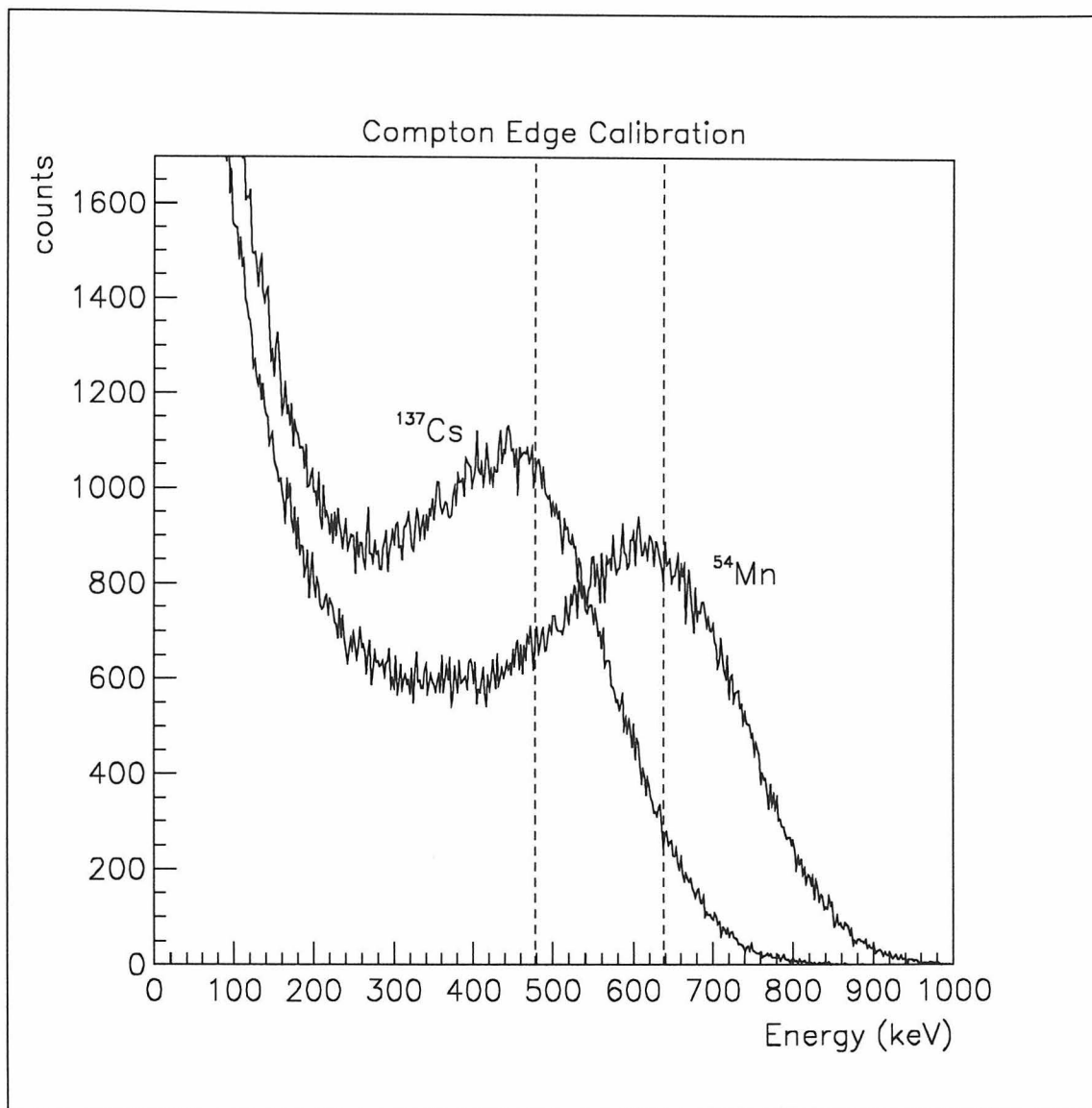


Figure 4.9: Simulated Compton spectra of ^{137}Cs ($E_\gamma=662$ keV) and ^{54}Mn ($E_\gamma=842$ keV) in a Gösgen cell are displayed. The energy deposited by a backscattered photon is indicated by a dashed line: 478 keV in the case of ^{137}Cs and 646 keV for ^{54}Mn . The energy resolution of the cell and multiple Compton scatters of the incident gamma produce the continuous spectra shown, indicating that the backscatter energy should be identified with the 90% maximum point of the spectral peak structure.

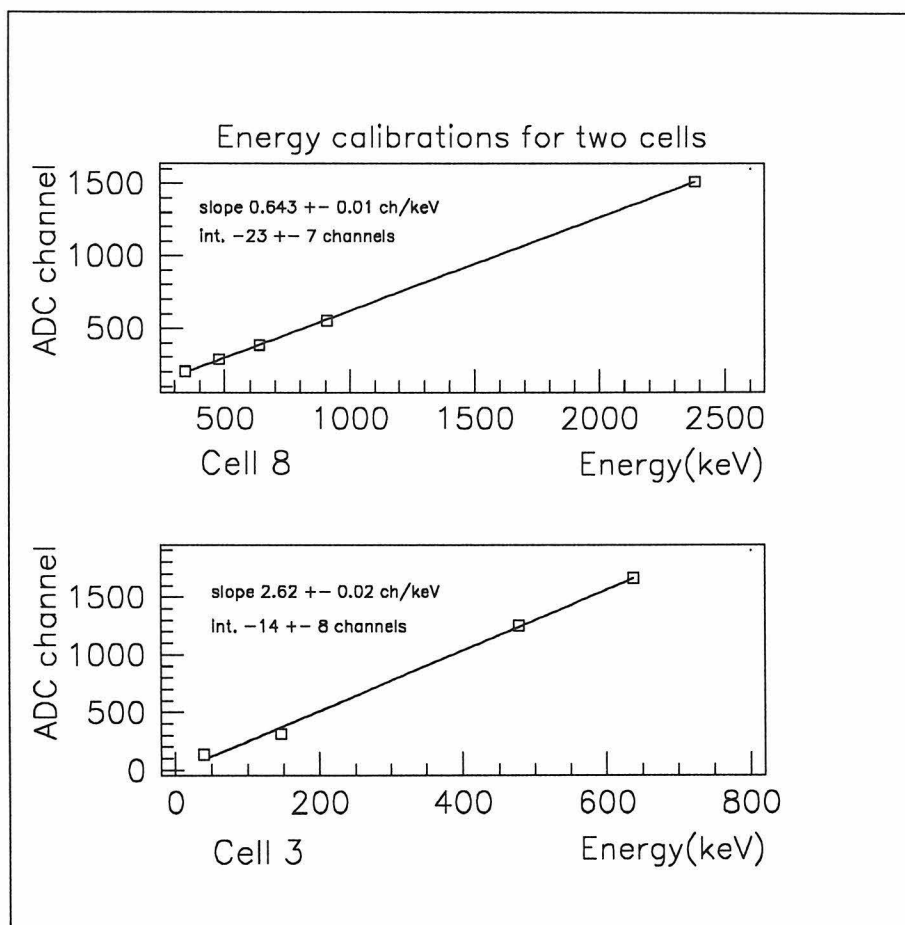


Figure 4.10: Typical calibration curves for two cells: central cell 8, top, and side cell 3, bottom.

charge ADC. The cells were all timed relative to the center cell such that a 150 ns gate created by the center cell would fully contain simultaneous energy deposits in all other cells. All coincidences were then analyzed off line allowing complete flexibility in deciding which topologies and energy conditions would constitute a “detected” event.

4.5.3 The Experiment

With the fully energy-calibrated array, one million triggers of background data were acquired with no ^{68}Ge loaded into the center cell. About 330 ml of scintillator loaded with about 1 kBq of ^{68}Ge was then placed into a small calibration vessel and its absolute activity measured as described above. The center cell of the Gösgen cell array was then removed and a fraction of the scintillator was taken out. The active scintillator from the small calibration tank was then emptied into the Gösgen cell and the cell was agitated vigorously to distribute the ^{68}Ge . After mixing, a sample of the liquid was drawn from the Gösgen cell and placed into a second acrylic calibration vessel in order to provide an independent measurement of the source activity in the cell. Finally, the scintillator originally removed was added back to the Gösgen cell to refill it completely, and the cell was reinserted into the array. Meanwhile, fresh scintillator was added back to the first small calibration vessel to determine, through a difference measurement, how much activity was added to the Gösgen cell.

Back in place, the Gösgen cell was recalibrated, as was cell 3, which had to be turned off and moved in order to remove the center cell. Four million triggers were then acquired in approximately two hours with the source present in the center cell. The center cell was then removed again, and another sample of scintillator was drawn from it into a third small calibration cell in order to measure any change in the source concentration over the two hours indicative of activity sticking to the walls of the Gösgen cell. Unfortunately, this cell developed a leak before the measurement could be performed and had to be discarded. Finally, the Gösgen cell was drained, rinsed, and refilled with fresh scintillator, and the background measurement was repeated to

look for direct evidence of ^{68}Ge sticking to the walls of the Gösgen cell.

The following table summarizes the results of the source activity measurements and the final conclusion as to how much activity was inserted into the Gösgen cell:

Test Cell 1:	<i>Initial source preparation</i>
Sample Mass:	291.1 g
Activity:	830.4 ± 11 Bq
Test Cell 1:	<i>Residual activity after dumping</i>
Sample Mass:	288.9 g
Activity:	20.0 ± 5 Bq
Test Cell 2:	<i>Sample taken from Gösgen cell after mixing</i>
Sample Mass:	290.2 g
Activity:	20.5 ± 0.5 Bq
Gösgen Cell:	<i>Calculated activity in cell</i>
Scintillator Mass:	10903 g
Activity:	789.9 ± 12 Bq

The measured positron spectrum of the center cell, cell 8, is shown in Figure 4.11. The background spectrum, measured before introducing the ^{68}Ge , is also plotted as is the subtracted spectrum used for analysis. The data was analyzed and compared with a detailed Monte Carlo simulation.

4.5.4 The Monte Carlo Simulation

The calibration experiment was simulated using the CERN GEANT Monte Carlo package. The full geometry of the Gösgen cell array and the chemical makeup of the scintillator was modeled. The response of the Monte Carlo was tuned using a number of calibrated gamma emitters: experimental data was taken by placing a calibrated gamma source on the surface of a cell. This monoenergetic gamma source was then modeled in GEANT and the absolute rate and energy calibration were

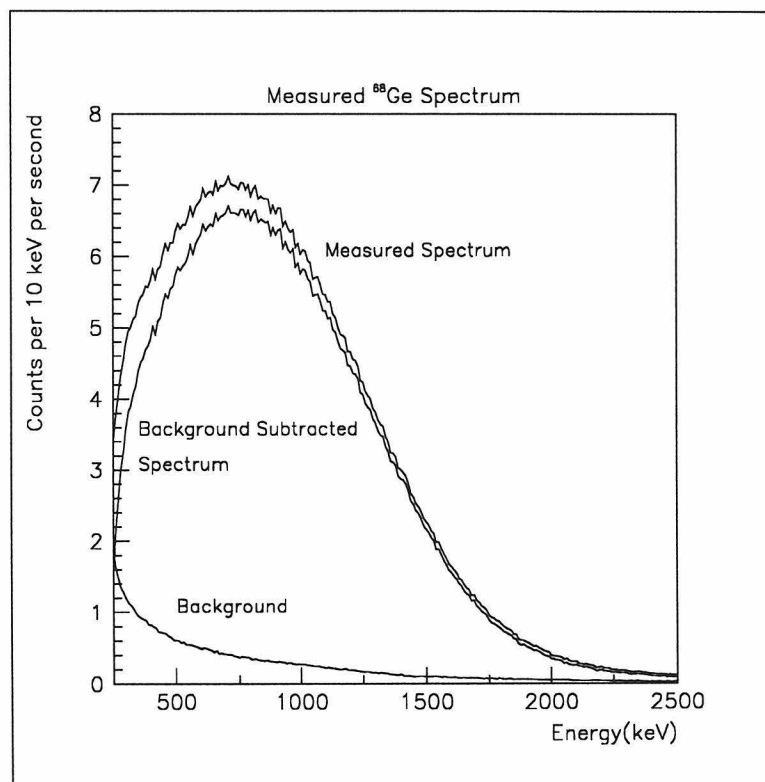


Figure 4.11: The measured positron spectrum of the center cell, cell 8, is shown. The background spectrum, measured before introducing the ^{68}Ge , is subtracted from the measured spectrum to give the true experimental positron spectrum used in the analysis.

compared. It was found that the simulation consistently overestimated the gamma efficiency by about 20%. The physical properties of the scintillator input into the simulation, such as the H to C ratio and the density, were adjusted, and it was found that good agreement of the experimental and simulated gamma spectra could be achieved by lowering the simulated scintillator density from 0.84 g/cc to 0.7 g/cc; it was not necessary to alter the H to C ratio. Figure 4.12 illustrates a comparison of simulation and experiment for three sources, ^{137}Cs , ^{54}Mn , and ^{65}Zn . The Monte Carlo spectra were independently normalized to the known activity of the calibrated source to arrive at an absolute number of counts per second. It is not understood why the gamma cross sections should overestimate the efficiency, but this empirical adjustment produces excellent agreement for all three calibration sources.

It has been shown [56] that the β^+ decay of ^{68}Ga is well described by the standard Kurie plot. A Monte Carlo input spectrum was generated numerically by adding two β spectra: one with the full (ground state) endpoint energy of 1.90 MeV and the other with the smaller (excited state) endpoint energy of 0.822 MeV (see Figure 4.2). The calculated spectrum used as an input for the GEANT simulation is shown in Figure 4.13.

Positrons generated according to the calculated ^{68}Ga spectrum were distributed uniformly through the volume of the center cell, cell 8. For each decay simulated, the energy of the center cell and each surrounding cell was stored on disk as an event. Each energy deposit was adjusted before being written out to include the effects of the detector resolution and the position dependence of the gain. These inputs were determined experimentally using gamma sources and LEDs as follows:

The Detector Energy Resolution

The energy resolution of the detector cells was determined using an LED to do photon counting statistics and gamma sources to fix the energy scale. An LED was coupled to the center of each Gösgen cell and driven by a pulser. The width of the LED peak, which obeys Poisson photon counting statistics, was plotted as a function of the peak position; see Figure 4.14. The width grows as the square root of the peak

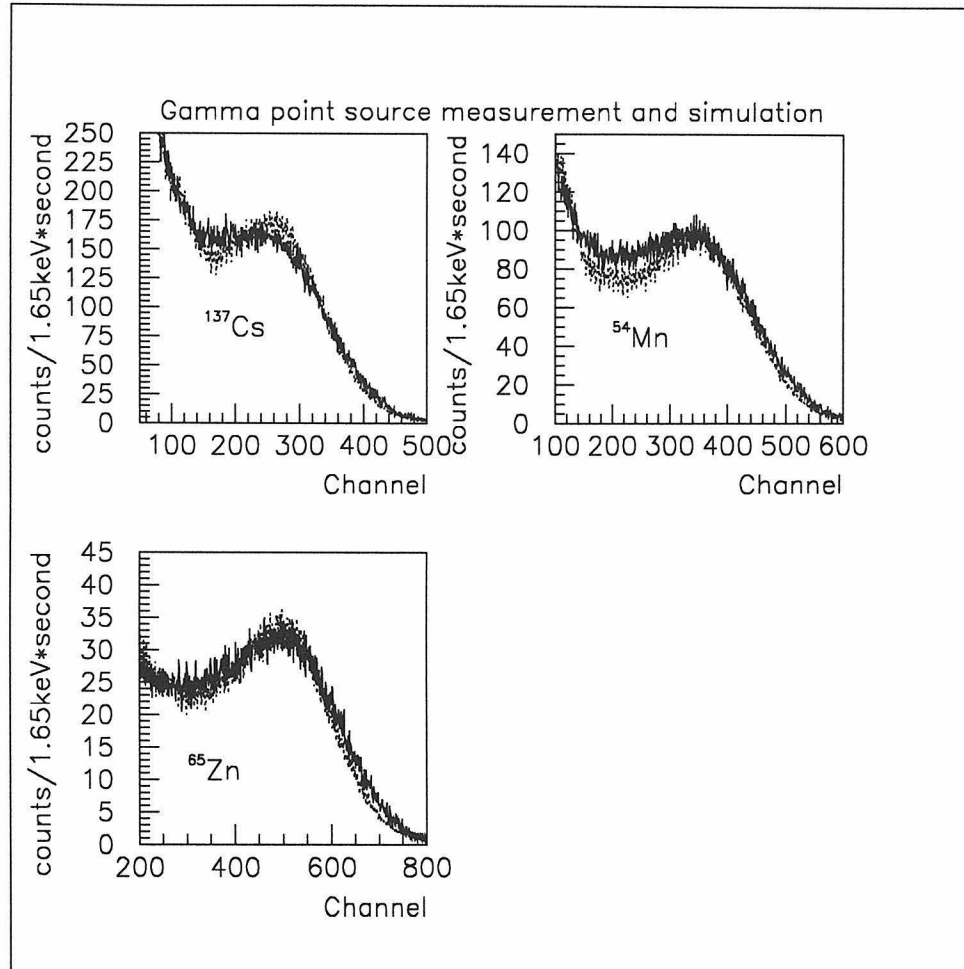


Figure 4.12: The measured gamma spectra (dotted curves) of ^{137}Cs , ^{54}Mn , and ^{65}Zn are compared with the simulated spectra (solid curves) for a simulated scintillator density of 0.7 g/cc (actual: 0.84 g/cc). The simulated spectra are independently normalized to the calibrated activity of the point sources. With this adjustment, the simulated gamma efficiency and spectral shape agree well with the measured values.

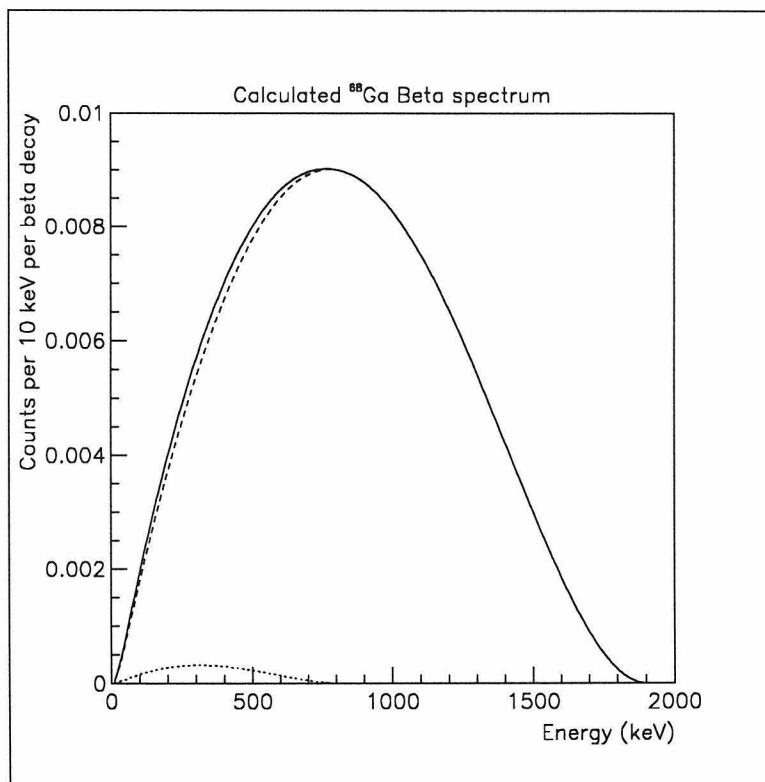


Figure 4.13: Calculated ^{68}Ge – ^{68}Ga β^+ spectrum. The dashed lines show the contributions of the ground state and first excited state positron decay branches. The solid curve is the sum and was used as an input to the GEANT simulation.

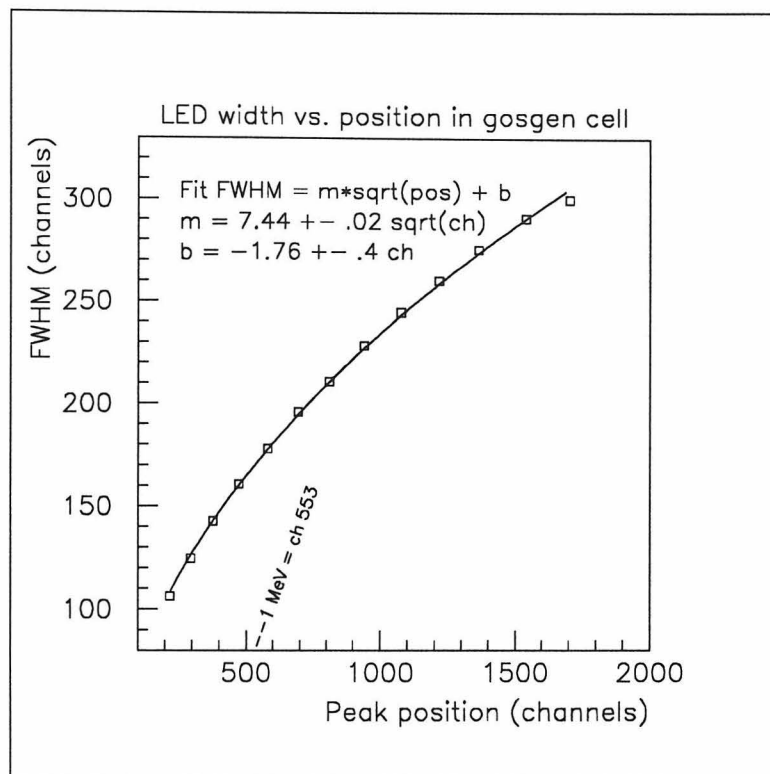


Figure 4.14: The energy resolution of the Gösigen cell array was determined by analyzing the width of an LED peak. The width of the peak, in ADC channels, is plotted as a function of the peak ADC position. The constant of proportionality between the width and the square root of the peak position gives a measure of the resolution. The connection to energy is made using gamma sources to map ADC channel number to energy.

position, as expected. Gamma sources were then used to calibrate the energy scale, and the resolution was determined to be 29% at 1 MeV. This result was used in the simulation: to each energy deposit was added a random value generated according to a Gaussian distribution with a width given by the resolution appropriate to that energy.

The Position Dependence of the Energy Calibration

Because of differences in the length of scintillator traversed and the solid angle to the phototubes, the amount of light collected in a Gösigen cell for a given energy deposit depends on the position of the interaction in the cell. This position dependence results in an additional energy smearing when deposits from everywhere in the cell

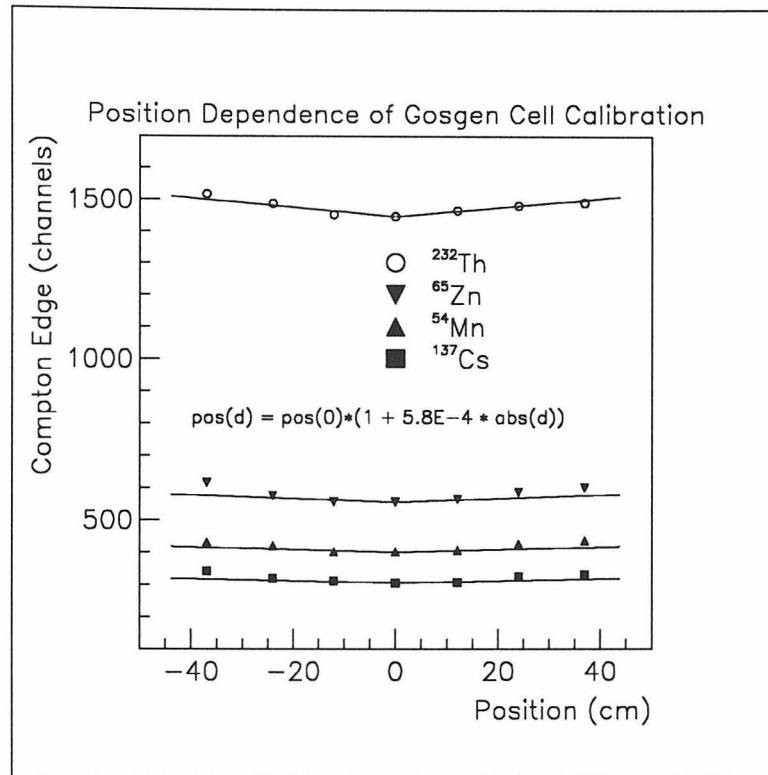


Figure 4.15: Position dependence of the Gösgen cell energy calibration. The position of the Compton edge for a number of gamma emitters is shown as a function of the distance from the center of the cell. A linear fit to the energy binwidth does a reasonable job of describing the dependence at all energies investigated.

are integrated at the phototubes. This effect had to be included in the Monte Carlo to produce the correct detector response. Again this input came from measurements made with the Gösgen cells using gamma emitters. Calibration point sources were placed at various distances along the wall of a Gösgen cell and the position of the Compton edge, in ADC channels, was investigated as a function of distance from the center of the cell. Figure 4.15 shows the position of the Compton edge in channels as a function of the distance from the center of the cell for four gamma emitters: ^{137}Cs (662 keV), ^{54}Mn (842 keV), ^{65}Zn (1119 keV), and ^{232}Th (2614 keV). A linear fit was found to reproduce the position dependence for all the sources reasonably well. This linear function was used in the simulation to correct the energy based on the interaction position.

Generation of the ^{68}Ge Data Set

A Monte Carlo spectrum was generated for ^{68}Ge uniformly distributed in the center cell. However, before this could be compared with the experimental spectrum, allowance had to be made for the ^{68}Ge sticking to the walls of the cell. Monte Carlo events were generated for ^{68}Ge uniformly distributed on the inner surface of the cell walls. This spectrum was then compared with the experimental data taken after the radioactive scintillator had been removed from the center cell, and it had been refilled with fresh scintillator. The absolute normalization of the Monte Carlo was then allowed to float as a free parameter. Matching the areas of the experimental and simulated spectra then allowed a determination of the activity bound to the surface of the walls. Figure 4.16 depicts the experimental spectrum, which has been background subtracted, and the simulated spectrum which has been normalized in area to the experimental one. In this way, it was determined that 105 ± 20 Bq, or about 13% of the initial activity remained stuck to the walls.

The final simulated positron spectrum was then produced by adding 87% of the spectrum from ^{68}Ge uniformly suspended in the scintillator to 13% of the spectrum from ^{68}Ge uniformly coating the inner surface of the cell. This spectrum was folded with the measured cell resolution and position dependence and was independently normalized to the known activity of ^{68}Ge introduced into the cell. The simulated spectrum of the center cell shows good agreement with the measured spectrum. See Figure 4.17. The excess of experimental counts near the endpoint is probably due to the approximate longitudinal position dependence curve, (Figure 4.15), used in the Monte Carlo. In addition, the lateral, (x-y), position dependence of the energy calibration becomes important for energy deposits very near the tubes; this effect was not included in the simulation. (Note that this is not true for the 9-m cells in which the phototubes are separated from the active region by an 80-cm oil buffer). Both of these effects scale up energy deposits near the tubes and could be responsible for the excess counts seen. Presumably, better agreement will be achieved with more tuning.

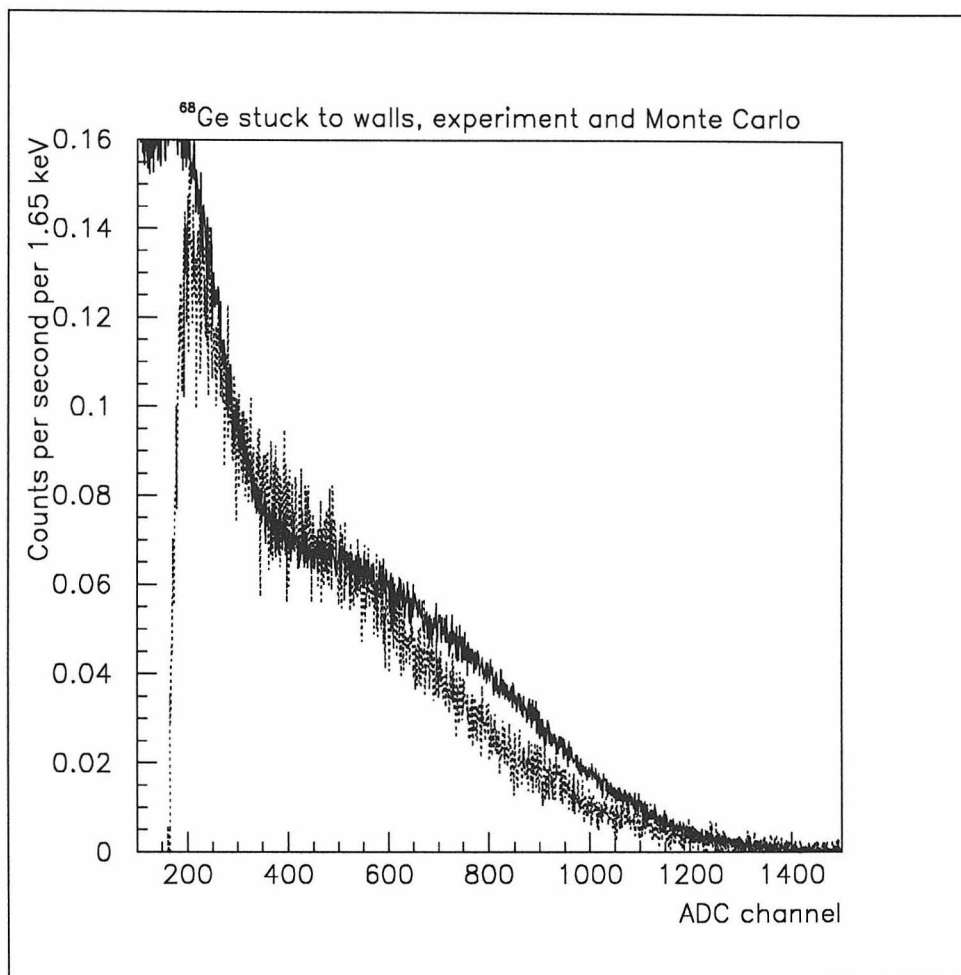


Figure 4.16: The measured spectrum (dotted curve) of the center cell containing ^{68}Ge stuck to the inner surface. Background, measured before the ^{68}Ge was introduced, has been subtracted. The simulated spectrum (solid curve) has been normalized to the area of the experimental one to determine the activity of the source remaining in the cell. The activity was evaluated to be 105 ± 20 Bq, or about 13% of the total activity introduced.

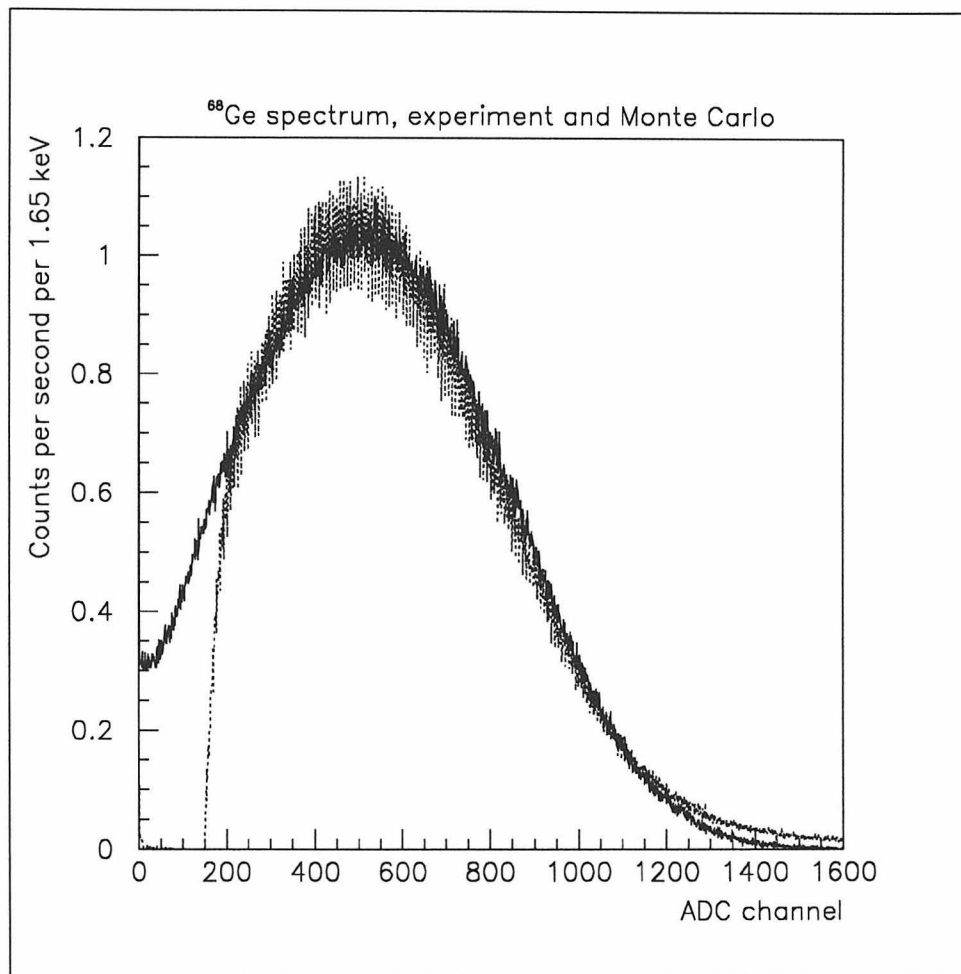


Figure 4.17: Comparison of the experimental (dotted curve) and simulated (solid curve) spectra produced by ^{68}Ge in the center cell of the array. The experimental spectrum is background subtracted. The simulated spectrum includes 13% of the activity stuck to the walls of the cell and has been folded with the measured cell energy resolution and position dependence. The small disagreement of the spectra near the endpoint is probably due to approximations made in the position dependence of the calibration.

4.5.5 Efficiency Results

The positron detection efficiency was evaluated as a function of the energy threshold in the center and side cells and as a function of the geometrical hit pattern accepted as a valid event. Experimental and simulated data were compared and found to show very good agreement. In the following a “single” event is defined as an energy deposit in the center cell, cell 8, falling inside the accepted energy window. A “triple” event is defined as a “single” accompanied by hits in at least two other cells in the appropriate side cell energy interval. The “triple probability” is then the true detection efficiency defined as the number of “triples” divided by the total number of β^+ decays. In addition, the ratio of “triples” to “singles” is used as a calibration-independent way of comparing the experiment with the simulation.

The topological pattern with the largest solid angle acceptance is the so-called “horizontal triple” consisting of the center cell firing along with the cells to the immediate left and right (cells 7 and 9). The efficiency of this topology is discussed in detail below as a function of the annihilation cell and positron cell energy thresholds. Figure 4.18 illustrates the absolute detection efficiency, in triples per β^+ decay as a function of the lower energy threshold in the annihilation cells and in the positron cell; in the upper plot the energy cut of the center cell is fixed at 800–3000 keV, and the upper threshold of the annihilation cells is fixed at 600 keV while the lower threshold of the annihilation cells is varied. In the lower plot, the side cell cut is fixed at 50–600 keV and the lower threshold of the center cell is varied. Background is subtracted from the experimental efficiencies, and they show excellent agreement with the simulated values.

The detection efficiency was investigated for a number of hit topologies. In a block of eight cells centered around the positron cell, there are 20 distinct topologies with side cells that are roughly back to back. Figure 4.19 illustrates these topologies along with the absolute detection efficiency measured and simulated. In all figures, the center cell is the positron cell. The energy cuts are fixed at 500–3000 keV for the center cell and 50–600 keV for the side cells. Figure 4.20 summarizes the previous

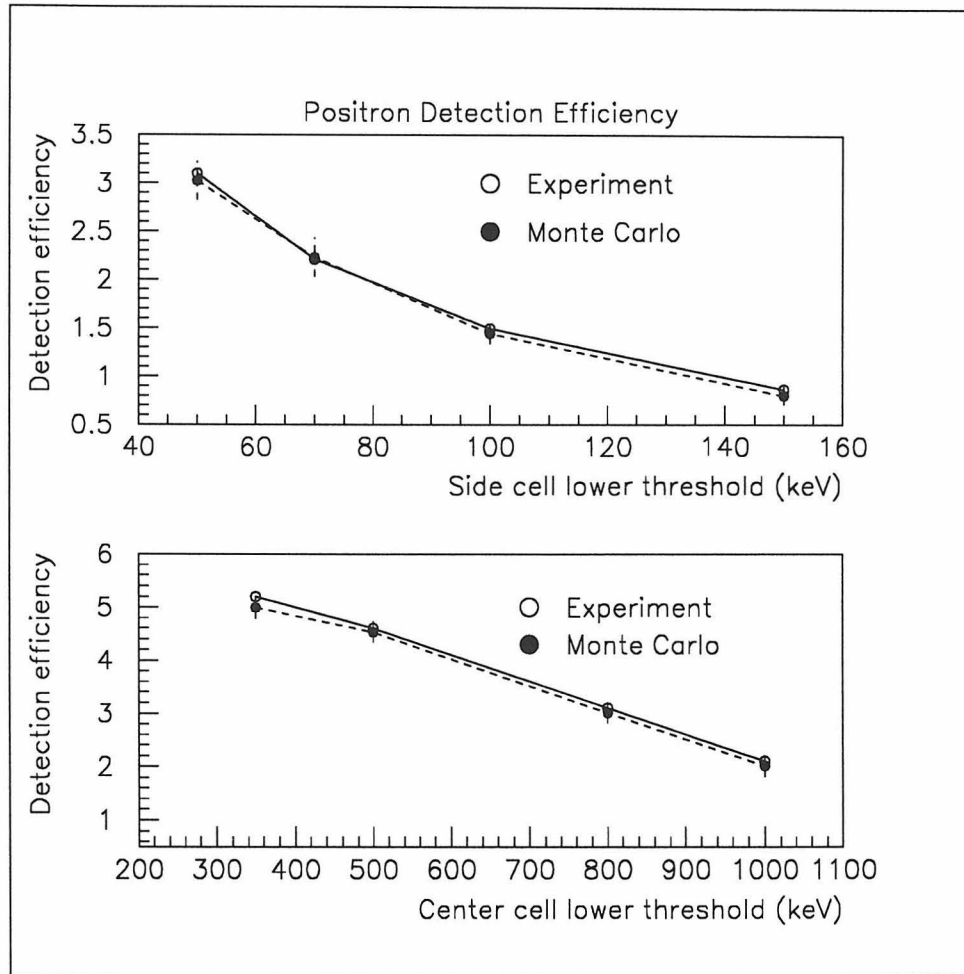


Figure 4.18: The positron detection efficiency for the horizontal topology (cells 7,8, and 9) is investigated as a function of the lower energy threshold in the center and side cells. In the upper plot, the center cell energy cut is set at 800–3000 keV, and the side cell upper threshold is set at 600 keV. The side cell lower energy threshold is plotted along the abscissa. In the lower plot, the side cell cut is set at 50–600 keV and the center cell lower threshold is varied.

results graphically to show the residual deviation between experiment and Monte Carlo. As a more realistic event trigger, the efficiency of the logical OR of these 20 patterns was investigated as a function of the annihilation cell energy threshold. Figure 4.21 illustrates this comparison of experiment and Monte Carlo.

4.6 Conclusion

A technique has been developed to accurately calibrate the positron detection efficiency of the Palo Verde neutrino oscillation detector. A method of dissolving the positron emitter ^{68}Ge in liquid scintillator has been developed and tested and shows good stability. It has also been shown that introducing this source into the scintillator to be used for the Palo Verde experiment causes no detectable degradation in scintillator performance in terms of light yield or attenuation length. In addition the germanium loading of the scintillator does not affect the chemical stability of the gadolinium which has been loaded at the level of 0.1% to facilitate neutron detection.

A system has been constructed to absolutely calibrate the ^{68}Ge source based on coincidence detection of the positron and its annihilation radiation. Activity measurements made with this apparatus are reproducible to better than 2%.

A prototype calibration experiment has been undertaken by injecting ^{68}Ge into an array of 15 small Gösgen cells. Data from this experiment were compared with a detailed simulation using GEANT and show excellent agreement. The GEANT simulation is easily extended to the geometry of the full 9-m-long cells used in the Palo Verde experiment and will be used to analyze and calibrate the full detector efficiency.

Positron Detection Efficiency [%]							
	Measured	Monte Carlo		Measured	Monte Carlo		
1		0.273 ± 0.005	0.28 ± 0.05	11		1.535 ± 0.031	1.36 ± 0.12
2		0.704 ± 0.014	0.77 ± 0.1	12		0.611 ± 0.012	0.57 ± 0.08
3		0.681 ± 0.014	0.62 ± 0.08	13		0.678 ± 0.014	0.77 ± 0.09
4		1.546 ± 0.031	1.48 ± 0.12	14		0.333 ± 0.007	0.28 ± 0.05
5		0.449 ± 0.009	0.51 ± 0.07	15		4.596 ± 0.092	4.78 ± 0.02
6		1.776 ± 0.036	1.87 ± 0.14	16		1.581 ± 0.032	1.55 ± 0.12
7		1.775 ± 0.035	1.80 ± 0.13	17		1.906 ± 0.038	1.87 ± 0.14
8		0.606 ± 0.012	0.67 ± 0.08	18		1.306 ± 0.026	1.45 ± 0.12
9		1.091 ± 0.022	1.287 ± 0.01	19		1.875 ± 0.038	2.00 ± 0.05
10		0.693 ± 0.014	0.59 ± 0.08	20		0.404 ± 0.008	0.46 ± 0.07

Figure 4.19: The positron detection efficiency is investigated as a function of the triple topology. For a block of nine cells, the positron cell at the center, there are 20 distinct triple topologies having a roughly back-to-back geometry. For every topology the following energy cuts were used: center cell: 500–3000 keV, side cells: 50–600 keV.

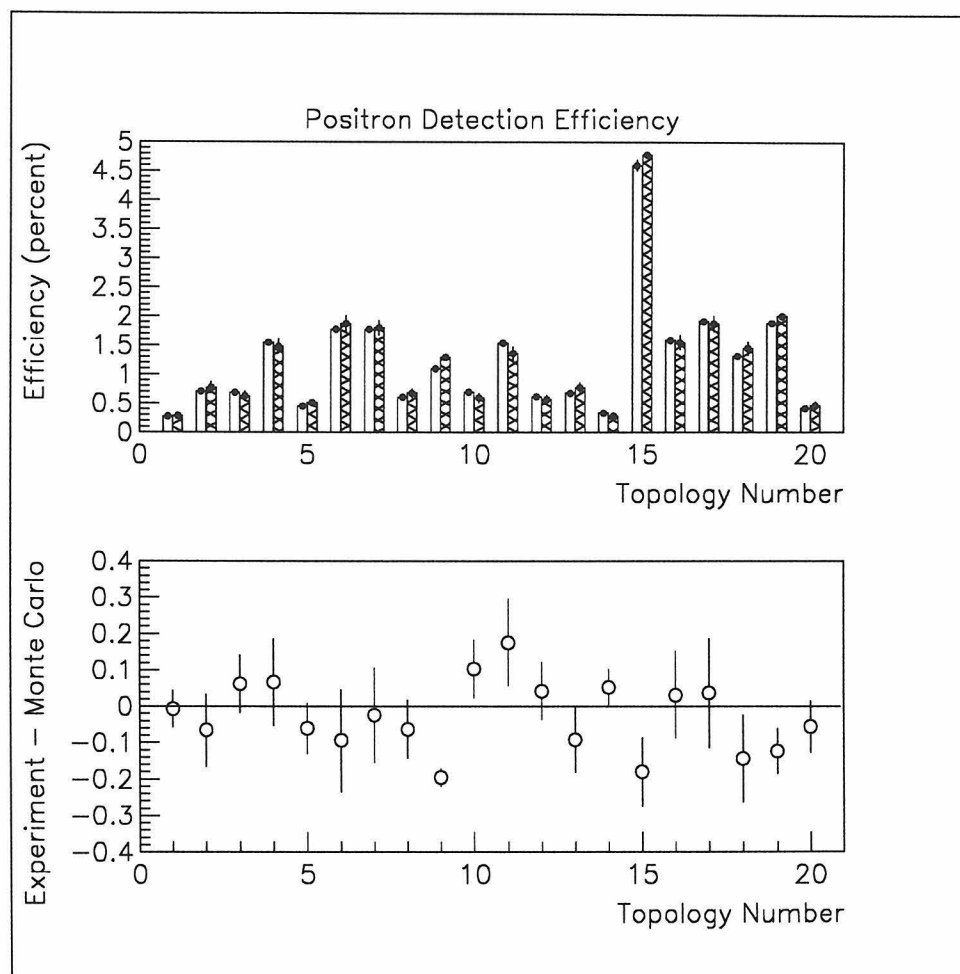


Figure 4.20: The detection efficiencies of the 20 topologies from the previous figure are summarized. The shaded bars represent the simulated efficiency and the unshaded bars represent the experimental measurements. The simulated data are subtracted from the experimental, and a residual plot is displayed in the lower figure. Experiment and simulation show excellent agreement.

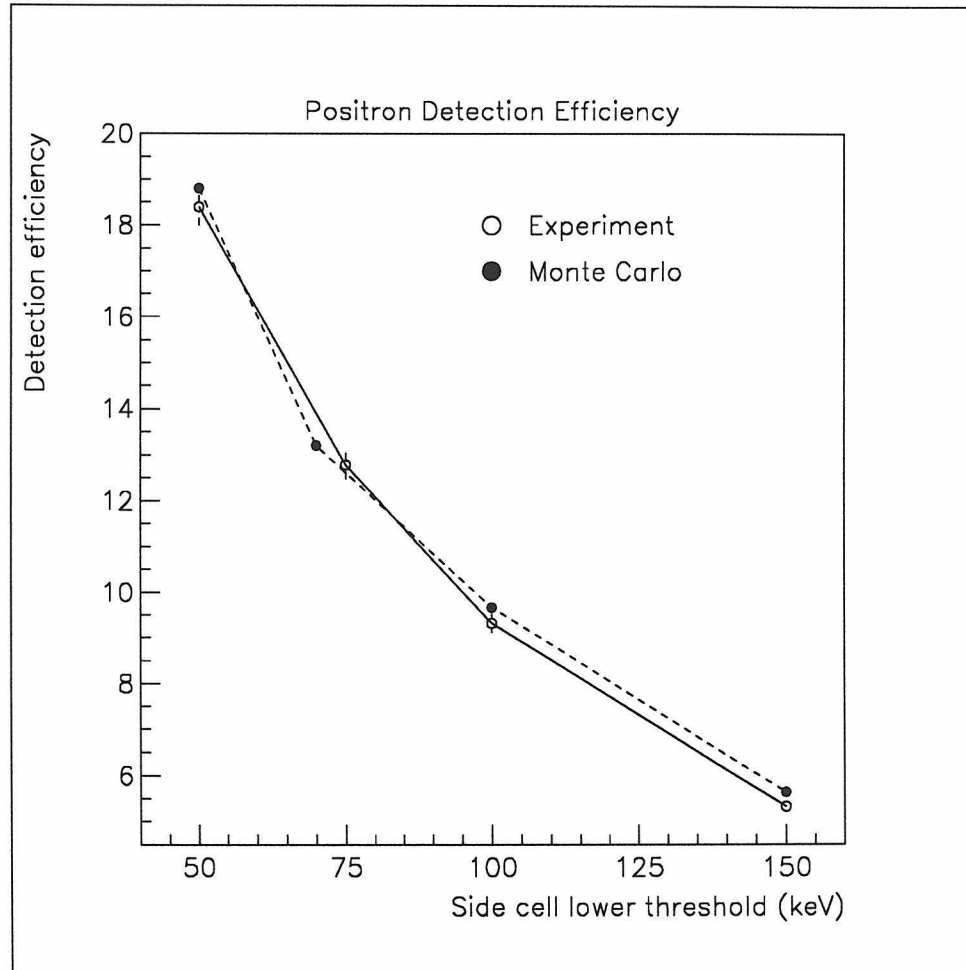


Figure 4.21: The positron efficiency of the more realistic logical OR of all 20 9-block topologies is investigated. The center cell cuts are fixed at 500–3000 keV, and the lower threshold of the side cells is varied. The upper threshold of the side cells is fixed at 600 keV. The experimental and simulated data show excellent agreement.

Chapter 5

Full Detector Simulation Using GEANT–GCALOR

5.1 Introduction

The GEANT–GCALOR [57] simulation package was adapted to carry out a full simulation of the neutrino detection efficiency and to model the detector response to background neutrons and gamma radiation. Positrons and neutrons were generated in the target cell scintillator to model the response of the detector to neutrinos. Radioactivities in the laboratory walls and in the construction materials were simulated by modeling the gamma decay cascades of uranium, thorium, potassium, cobalt, and radon. Neutrons produced by the interactions of cosmic muons were tracked from their origins in the laboratory walls and in the detector itself.

5.2 General Parameters of the Simulation

5.2.1 The Detector Geometry

The geometry of the neutrino detector is modeled in detail. The 66 acrylic target cells are individually placed and filled with 0.1 % Gd-loaded liquid scintillator. The total simulated mass of the target scintillator is 11.5 tons. The outer 80 cm on either end of each target cell is partitioned off from the active volume and filled with pure mineral oil to act as a buffer to external backgrounds. Glass phototubes are simulated and placed at the ends of each cell. Around the target cells, 144 steel strips, with a total mass of 0.5 tons, are placed to simulate the support lattice. To form the main water buffer, 42 steel tanks filled with water are packed around the target cells. The

total mass of this buffer is about 105 tons. The active veto is made from 32 PVC tanks filled with liquid scintillator and placed around the water buffer. The total mass of the veto is about 50 tons. Another ton of support steel is simulated around the buffer and vetoes, and the entire detector is enclosed inside a concrete box with inner dimensions of approximately $14(l) \times 8(w) \times 6.5(h)$ m. Figures 5.1, 5.2 and 5.3 illustrate the simulated volumes.

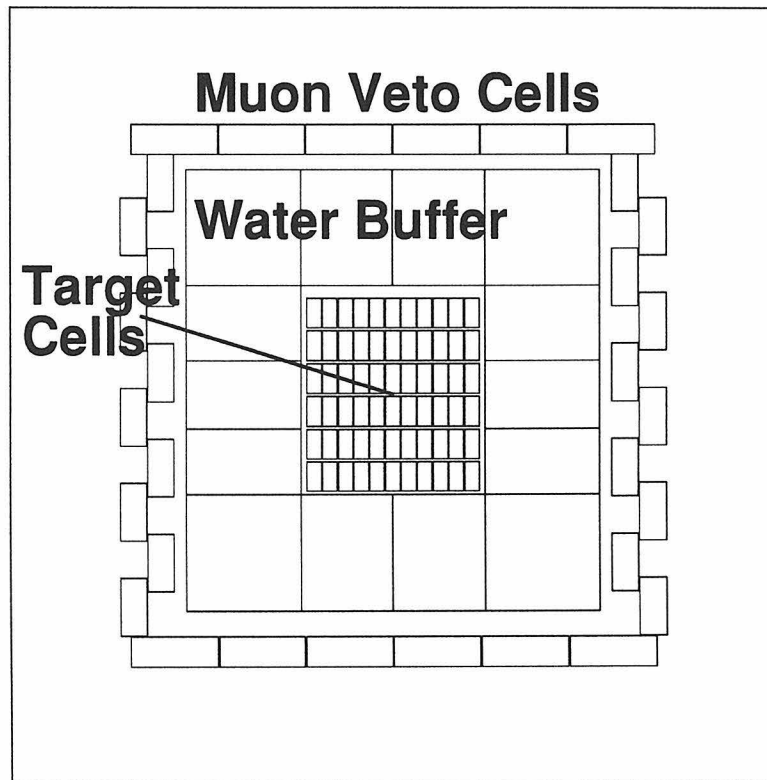


Figure 5.1: End view of the simulated detector geometry. The steel support structures and end vetoes have been removed for clarity.

5.2.2 The Tracking

Electromagnetic interactions and the tracking of charged particles are handled by GEANT. Hadronic interactions and the tracking of neutrons are handled by GCALOR through a user-invisible interface. Particles are tracked down to a threshold of 10 keV, the minimum allowable by GEANT, at which point their kinetic energy is assumed to be deposited in the current tracking medium. One exception is the tracking of

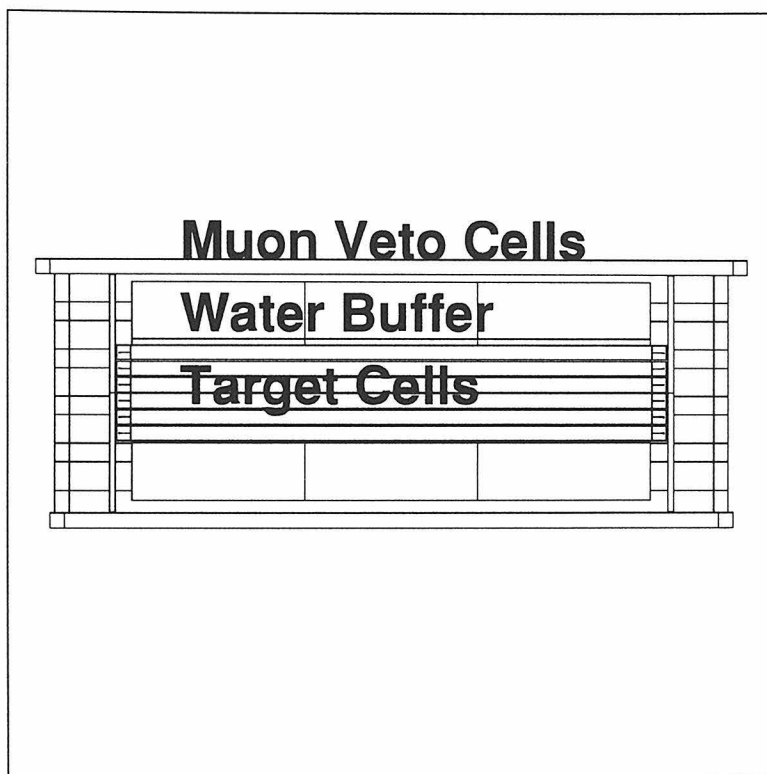


Figure 5.2: Cut away side view of the simulated detector geometry. The steel support structures have been removed for clarity.

neutrons which were followed down to 0.1 eV during some runs in which neutron thermalization and capture were investigated.

Interaction cross sections are tabulated and calculated by GEANT and GCALOR for the materials defined by the user. In addition to several standard GEANT materials, the following materials were defined for use in the simulation by specifying their chemical makeup:

- Mineral oil
- Gd-loaded scintillator
- Acrylic
- Muon-veto scintillator
- PVC

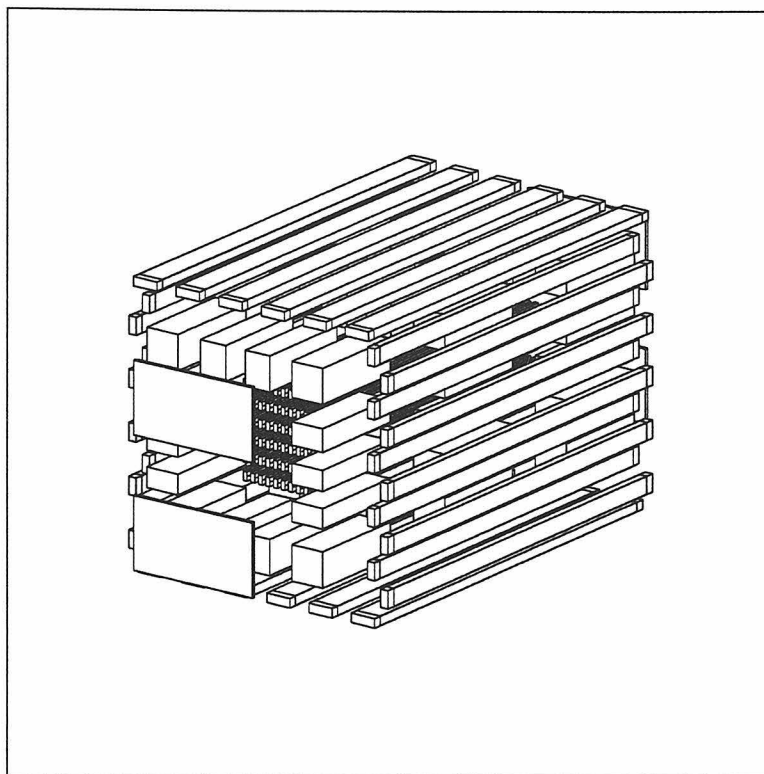


Figure 5.3: Exploded view of the simulated detector geometry. The steel support structures have been removed for clarity.

- Stainless steel
- Water
- Concrete
- Glass

5.2.3 The Data Structure

Data is stored during the simulation in the form of HBOOK histograms which tabulate input particle energy, position, and direction and histogram particle fluxes through various volumes. In addition, for particles entering the active target volume of the detector, event-by-event data is written to record the energy deposit in each of the 66 cells along with any energy deposit in the muon veto during that event.

Energy deposits in the scintillator (dE/dx) are summed step by step as the particle

is tracked. At this stepping level, two corrections are made to the deposited energy: first, the energy loss is corrected for its position in the tank: an event near the phototube will produce more light for a given energy deposit than one near the center of the tank. The energy calibration is defined at the center of the tank thereby introducing a correction which scales up energy deposits occurring near the phototubes. This correction factor reaches a maximum value of two for energy deposits at the extreme ends of the cell and follows a curve measured experimentally using a prototype target cell. Figure 5.4 illustrates the measured position dependence used to perform this correction. It is true that timing information from the tubes at both ends of each cell could be used to unfold this dependence, but for small energy deposits where light is lacking or for long track lengths and multiple scattering, this may be more difficult. In any case, both signal and background are scaled identically, and the scaled picture is the correct one to use for an estimation of the hardware trigger rate of the detector since all position reconstruction must be done off line.

Second, a correction is made for the light yield response of the scintillator to various types of particles. A heavily ionizing particle such as a proton, especially at the end of its track, produces less light per unit energy loss than does an electron because of strong quenching effects. The correction of heavy particle light production to electron-equivalent energy is described in section C.4.1.

No adjustment of the deposited energy due to the finite energy resolution of the detector is implemented at the tracking step. Instead, since event-by-event data is saved to disk, this randomization of energy is done at the analysis level. Each energy deposit is randomized by adding a (positive or negative) random value taken from a Gaussian distribution of mean zero and sigma equal to the measured resolution width at that energy.

The event-by-event data is analyzed by placing energy and geometrical cuts on the energy deposits in the cells. The detailed procedures are described below.

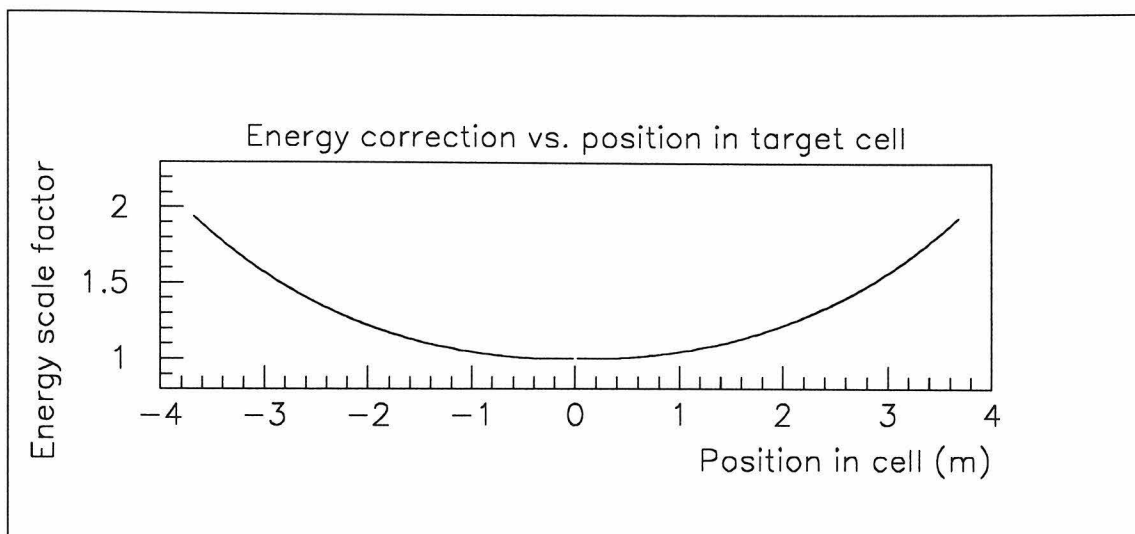


Figure 5.4: Energy correction factor as a function of the distance along a target cell. The energy calibration is assumed to be fixed at the center of the tank (position 0). The active volume of each detector cell extends from -3.7 to +3.7 m.

5.3 The Neutrino Detection Efficiency

Electron antineutrinos interact in the detector by the inverse β decay of a proton in the liquid scintillator ($\bar{\nu}_e + p \rightarrow n + e^+$). The positron quickly slows and annihilates in the detector giving a prompt flash of light. The neutron then thermalizes and finally captures on gadolinium in the scintillator to produce a delayed flash of light. This full detection efficiency is modelled in two separate pieces: first, positrons are created in the target cells according to the calculated reactor $\bar{\nu}_e$ spectrum and their detection efficiency is modeled. Second, neutrons of a few 10's of keV are distributed through the fiducial volume and their detection efficiency is separately modeled. The full detection efficiency is then the product of these two partial efficiencies.

5.3.1 The Positron Detection Efficiency

The energy spectrum of reactor-induced positrons is calculated as described in section 2.2.1.

Positrons are generated according to this spectrum and placed uniformly into the Gd-loaded scintillator of the target cells. Their directions are generated randomly

in 4π . The positrons are tracked through the scintillator as they ionize and finally annihilate producing two 511-keV gammas which are tracked down to 10 keV kinetic energy. Data is written to disk event by event such that the energy deposit in each of the 66 cells is recorded for each incident positron. A total of 10,000 positrons was generated in the target cells. Figure 5.5 displays the input positron spectrum, and Figure 5.6 illustrates the total energy loss in the detector and the sum spectrum of the 66 individual cells.

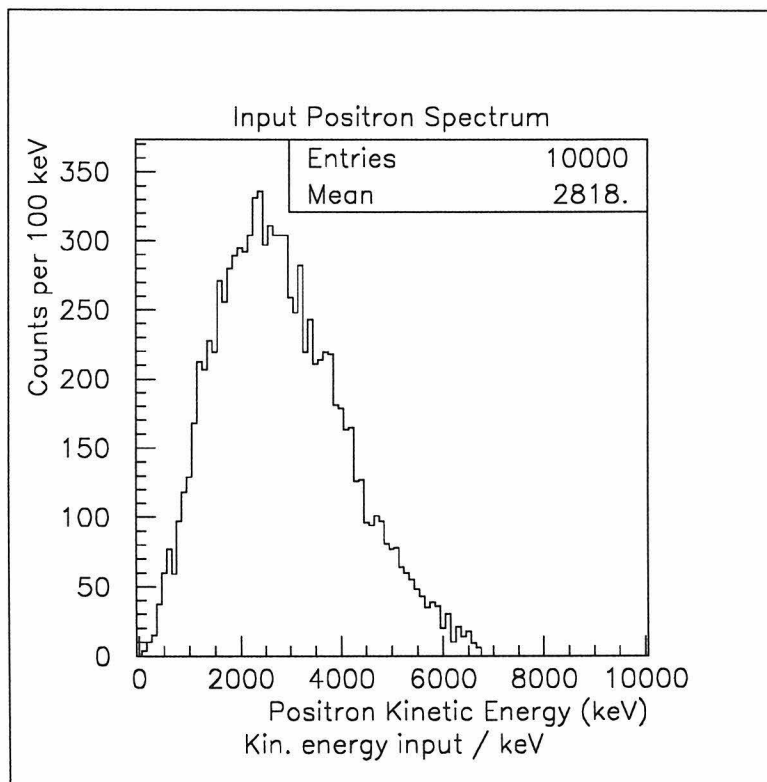


Figure 5.5: Spectrum of input positrons. Positrons are generated uniformly through the scintillator volume with a uniform 4π angular distribution.

The data is analyzed by making energy and spatial cuts on the energy loss in the target cells. The positron is generally fully contained within one cell. When it annihilates, two 511-keV gammas are emitted back to back and, in general, deposit energy in the surrounding cells. So essentially, one expects that a positron will fire one cell at a few MeV and a few surrounding cells at a few hundred keV. Strictly, the positron-like cell should be at the center, and the annihilation-like cells should fire on opposite sides of the center cell. However, because of multiple scattering and

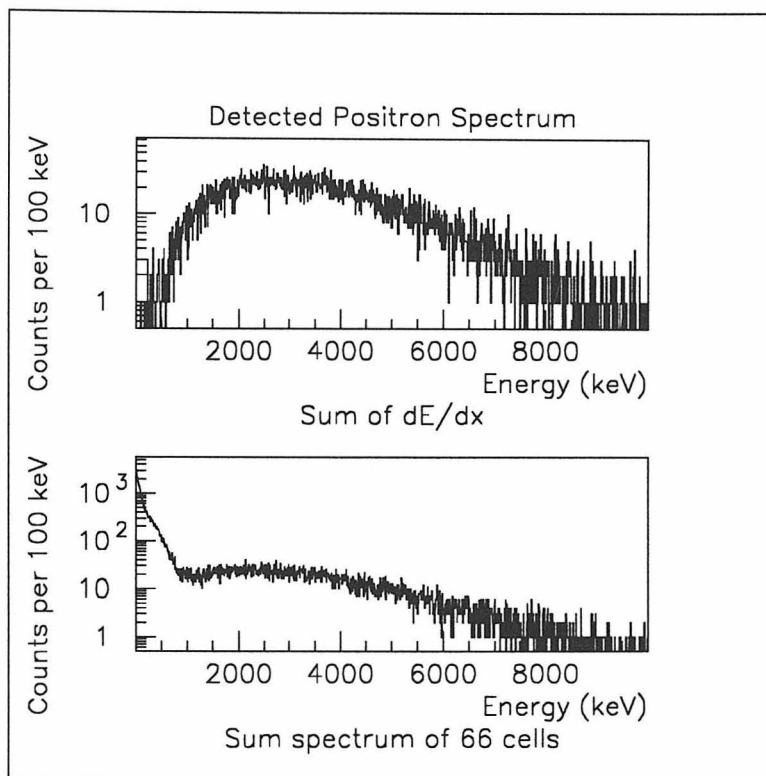


Figure 5.6: Spectrum of positrons detected in the target cells. The total energy loss in all 66 cells is plotted in the upper figure. The digital sum of the 66 individual energy loss spectra is plotted in the lower figure.

penetration of the annihilation radiation, it is likely that several cells on one side of the positron-like cell may fire. Efficiency can be gained by loosening the back-to-back requirement without significantly affecting the signal-to-background ratio but improving statistics. Three levels of topological cuts were investigated as described below. Common to all levels is the requirement that one and only one cell may look like a positron cell, having an energy deposit between one and ten MeV. In addition there must exist at least two annihilation-type cells, defined as having an energy deposit between 50 and 600 keV. This defines a “triple coincidence.” Finally, since the annihilation radiation carries 1.02 MeV of energy, a sum cut is placed on the entire detector: the total energy deposited in the detector minus the energy of the positron cell must not exceed 2.5 MeV. 2.5 MeV is selected because a 1-MeV energy deposit near the phototubes would be scaled up by the position correction factor to nearly 2 MeV.

The 9–Block Topology

The least restrictive topology analyzed is the so-called “9–block topology.” Here we require that one positron cell and two side cells all touch such that a block of nine cells can be selected that includes all three. However, no requirement is placed on the position of the positron cell relative to the annihilation cells. Figure 5.7 helps to clarify the differences between the different triple–coincidence topologies. For a given positron cell, 84 distinct annihilation cell arrangements satisfy this condition.

The Restricted 9–Block Topology

A more restrictive topology is the so-called “restricted 9–block topology.” Here we require that the 9–block requirements are met with the additional restriction that the positron–like cell must touch both annihilation cells. In other words one is able to select a block of nine cells including all three cells such that the positron–like cell is placed at the center of the block. For a given positron cell, 28 distinct annihilation cell arrangements satisfy this condition.

The Back–to–Back Topology

The most restrictive topology is the so-called “back–to–back topology”. Here the restricted 9–block requirements must be met with the additional requirement that the annihilation cells must be roughly back to back. Effectively, this is defined as a positron cell at the center of a block of nine cells, surrounded by two annihilation cells which do not touch each other (except at corners). For a given positron cell, 20 distinct annihilation cell arrangements satisfy this condition.

In general a single event may contain more than two annihilation cells. In this case, every combination of positron cell and two annihilation cells is considered in turn. If one or more sets meet the requirements for a given triple level, the event is considered to have passed that analysis level.

The positron data was analyzed introducing an energy resolution in the detector cells of 30% FWHM at 1 MeV, which is the value measured using a prototype

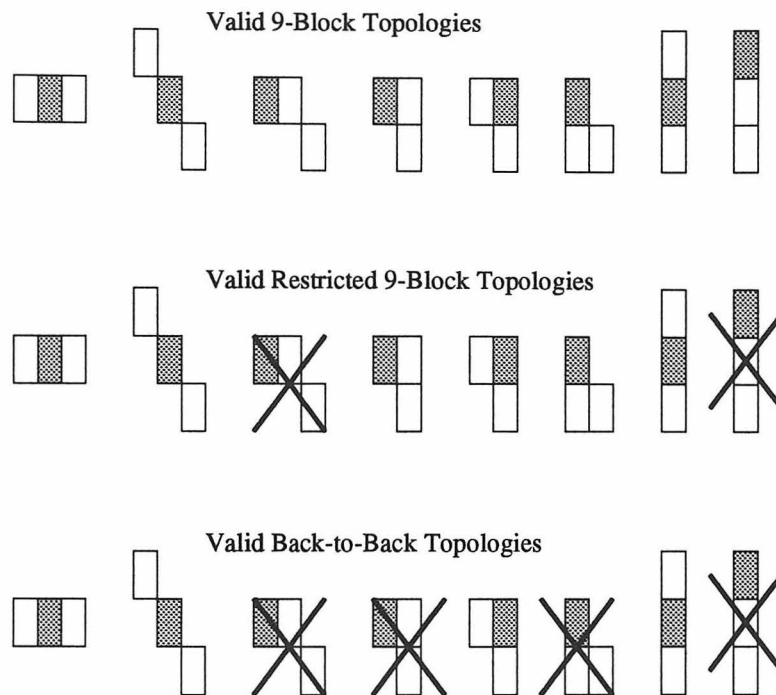


Figure 5.7: Topological analysis cuts. Examples of event topologies are shown. The shaded cell is the positron-like cell, and the unshaded cells are the annihilation-like cells. The figure illustrates the events removed by application of successively stricter topological requirements.

target cell. The energy resolution has little effect on the detection efficiency. Figure 5.8 shows the energy spectrum of the positron cell for events passing the various topological cuts. Also depicted there is the number of the fired positron cell; a cell number map of the detector is shown in Figure 5.9. From the figure it is clear that edge and corner cells exhibit a smaller efficiency because of missing annihilation cell possibilities. Table 5.1 summarizes the detection efficiency calculations.

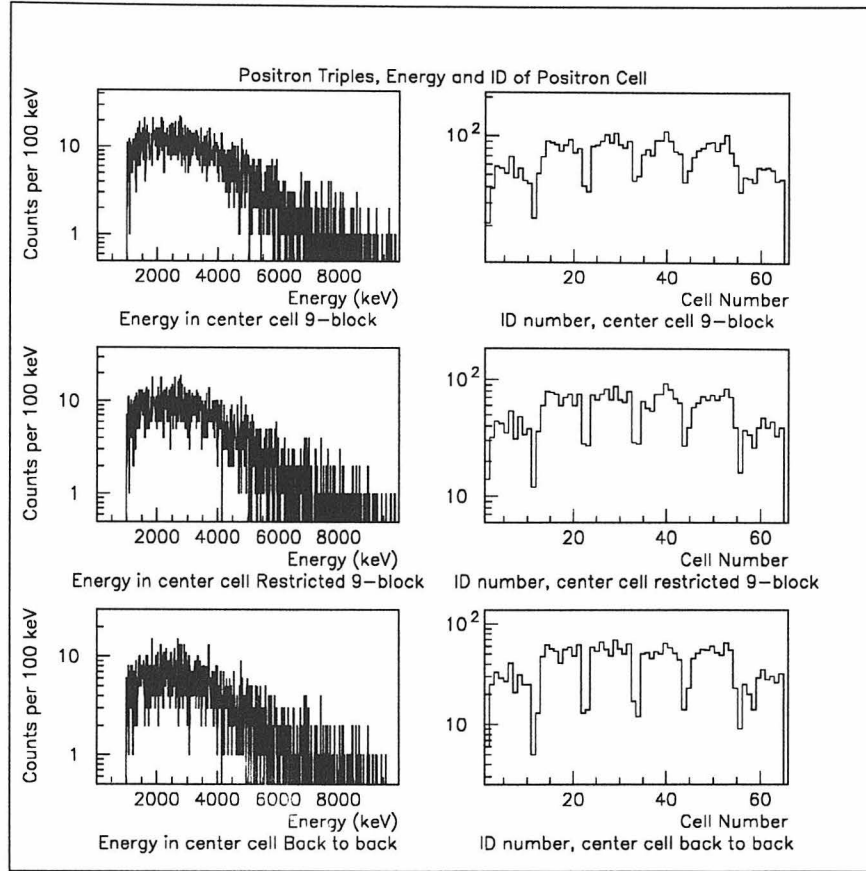


Figure 5.8: Positron triple coincidence analysis. The first column displays the energy spectrum of the positron-like cell for the three analysis topologies. The second column is a frequency table of the ID number of the fired positron cell (see Figure 5.9). Corner and edge cells show a smaller efficiency because of missing annihilation cells.

Table 5.1: Simulated positron detection efficiency of the neutrino detector. The efficiency for various topological cuts and with and without energy resolution are shown. Here the positron cell is required to contain between 1 and 10 MeV, and the side cells between 50 and 600 keV.

Topology	Detection Efficiency	
	$E_{res} = 30\% @ 1 \text{ MeV}$	No Energy Resolution
9 Block	$44.7 \pm 0.7\%$	$46.7 \pm 0.7\%$
Restricted 9 Block	$35.6 \pm 0.6\%$	$37.2 \pm 0.6\%$
Back to Back	$26.2 \pm 0.5\%$	$27.7 \pm 0.5\%$

1	2	3	4	5	6	7	8	9	10	11
12	13	14	15	16	17	18	19	20	21	22
23	24	25	26	27	28	29	30	31	32	33
34	35	36	37	38	39	40	41	42	43	44
45	46	47	48	49	50	51	52	53	54	55
56	57	58	59	60	61	62	63	64	65	66

Figure 5.9: Map of cell numbers in the detector.

5.3.2 The Neutron Detection Efficiency

The second half of the neutrino detection efficiency comes from detection of the neutron produced in the inverse β decay of the proton. This neutron shares available energy with the positron and is generally left with a few 10's of keV of kinetic energy. The neutron thermalizes in the scintillator and either escapes the fiducial volume or is captured on gadolinium or on a proton in the scintillator. In the case of capture on gadolinium, the resulting nucleus decays via complex 8-MeV gamma cascades. The detection of this gamma cascade following a positron signal is the signature of a neutrino event. For a real neutrino, the probability of detecting the neutron after the positron falls exponentially with time. The length of the window during which to accept captures will be set to maximize signal significance and will be assumed here to be 100 μ s. So the probability of neutron detection, ϵ_N , is actually a product of several factors:

$$\epsilon_N = \epsilon_c \cdot \epsilon_{Gd} \cdot \epsilon_\gamma \cdot \epsilon_\tau.$$

Here ϵ_c is the containment efficiency, or probability that a neutron will not leak out of the fiducial volume. ϵ_{Gd} is the probability that the neutron will capture on gadolinium rather than on a proton. ϵ_γ is the detection probability of the 8-MeV Gd gamma burst, and ϵ_τ is the probability of capture during the 100 μ s time window.

The Neutron Capture Time: Determination of ϵ_{Gd} and ϵ_τ

The neutron capture probability can be calculated through a knowledge of the capture cross sections and the gadolinium and proton number densities in the liquid scintillator. The following table summarizes the composition of the Gd-loaded scintillator.

Composition of Gd-loaded Scintillator			
$\rho = 0.856 \text{ g/cm}^3$			
Element	Atomic Weight	Mass Fraction	Number Density (cm^{-3})
C	12.001	86.74%	$3.72 \cdot 10^{22}$
H	1.0079	13.16%	$6.73 \cdot 10^{22}$
Gd	157.25	0.1%	$3.28 \cdot 10^{18}$

The thermal neutron capture cross section on natural gadolinium is dominated by the isotopes ^{155}Gd and ^{157}Gd which have capture cross sections of 61,400 and 255,000 barns and isotopic abundances of 14.8% and 15.7%, respectively [58]. This results in a natural gadolinium capture cross section of 49,100 barns, 82% of which is due to ^{157}Gd . The capture cross section on hydrogen is 0.328 barns [59], and on carbon, a negligible $3 \cdot 10^{-3}$ barns. Multiplying the cross section with the number density yields the macroscopic capture cross sections for this Gd-loaded scintillator: for capture on Gd, $\Sigma_{Gd} = 0.161 \text{ cm}^{-1}$, and on protons, $\Sigma_H = 0.021 \text{ cm}^{-1}$. This immediately gives $\epsilon_{Gd} = 87.9\%$, the capture probability on Gd versus on protons. Then taking the average velocity of thermal neutrons to be 2200 m/sec [59], the capture time on gadolinium is calculated as 28 μs and on protons, 206 μs . (The total capture time is then 25 μs). From this we calculate that the probability of capture on gadolinium during the 100 μs time window, ϵ_τ , is 97%.

The Neutron Containment Efficiency, ϵ_c

The neutron containment efficiency was calculated by simulating 10 and 100 keV neutrons in the fiducial volume of the detector and tracking them until they either left the scintillator or fell below a very low energy threshold in the scintillator, presumably to be captured. This threshold was varied from 1 keV to $1 \cdot 10^{-4}$ keV to investigate any bias the threshold might produce. Neutrons were assumed to be lost if they fell below threshold in the acrylic cell walls or in some volume outside the target cells. It is evident from tests of GCALOR that the thermal neutron cross section on gadolinium is not implemented; while neutron capture on protons is observed when tracking is allowed to proceed down to 10^{-5} eV, neutrons being tracked in Gd-loaded scintillator often simply disappear at very low energies with no indication from the program that a capture has taken place. For this reason, the containment efficiency was estimated “by hand:” it was assumed that if a neutron falls below some very low threshold in the scintillator, it will surely capture eventually. By setting this threshold progressively lower, the fraction of neutrons contained in the fiducial volume was investigated as a function of this threshold. It was found that this function levels off at thresholds

below 1 keV at a containment probability of about 87% for both 10 and 100 keV neutrons. Thus the containment efficiency, ϵ_τ , is calculated to be 87%. Figure 5.10 illustrates the fraction of low-energy neutrons contained in the fiducial volume as a function of the tracking energy threshold.

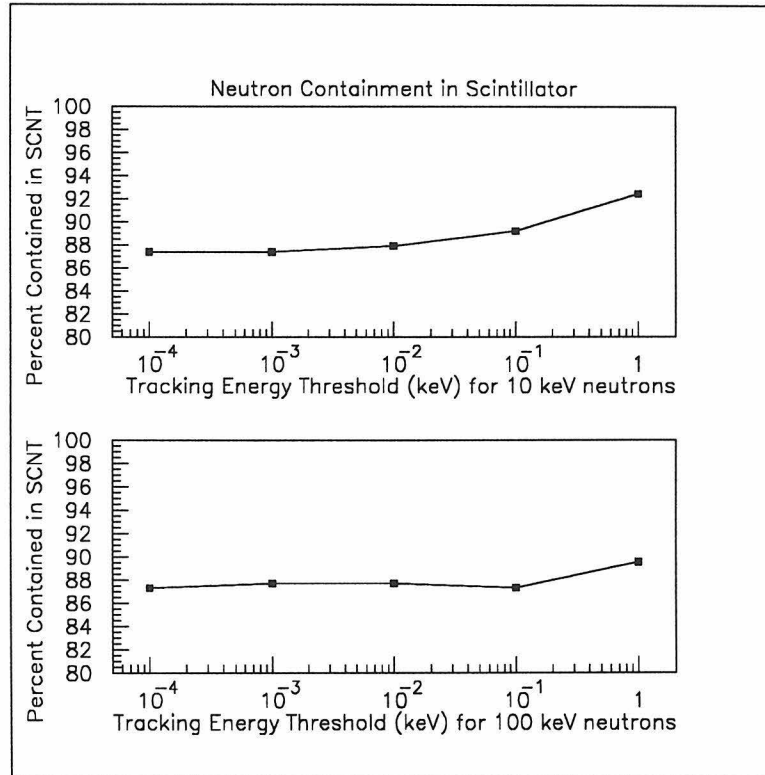


Figure 5.10: Low energy neutron containment in scintillator. 10 keV (upper) and 100 keV (lower) neutrons are introduced uniformly into the scintillator fiducial volume. The fraction of neutrons which fall below a low cutoff threshold inside the scintillator is plotted as a function of that cutoff threshold. The curves for both energies flatten out at 87% containment efficiency.

The Gd Gamma Cascade Detection Probability, ϵ_γ

Finally, once a neutron has captured on gadolinium, the resulting nucleus decays from an excited state at 7.94 MeV via gamma emission. The cascade is experimentally detected by requiring an energy deposit of more than about 3.5 MeV in the sum of all target cells. The level scheme of ^{158}Gd , the isotope resulting from more than 80% of the neutron captures, is not completely cataloged, and many of the emitted gamma

rays are unresolved. [60] This makes an accurate description of the de-excitation difficult so various approximations were made. As a first approximation, relatively strong high energy lines were identified in the experimentally measured spectrum of ^{158}Gd following neutron capture on ^{157}Gd . Gamma lines at 6.8 MeV and 5.9 MeV, with absolute branchings of 2.7% and 1.4%, respectively, were prominent, and a number of lower intensity lines with energy near 4 MeV were observed [61, 62]. To investigate the sensitivity of the detection efficiency to the nature of the de-excitation cascade, several cascades of gamma multiplicity 2, 3, and 4 were simulated. Figures 5.11 and 5.12 display the detected energy spectra for the various cascade assumptions including a simple statistical model described below. Table 5.2 summarizes the detection efficiency for different capture energy thresholds. The gamma detection efficiency ranges from around 60% to 85% depending on the assumptions made about the de-excitation cascade. A statistical model which generates gamma energies and multiplicities based on the energy and spin of the excited state was employed to gain some insight into the nature of the de-excitation [63]. 2500 decays were simulated resulting in the gamma spectrum tabulated below:

^{158}Gd decay from 7.94 MeV excited state	
Gamma Energy (MeV)	Population
0 - 1	39%
1 - 2	28%
2 - 3	20%
3 - 4	8.1%
4 - 5	3.8%
5 - 6	1.1%
6 - 7	0.1%
Average cascade multiplicity: 5.1	

The relatively large value for the cascade multiplicity calculated by this model tends to favor the larger efficiency values determined by simulating the 3 and 4-gamma cascades. The statistical model was used to generate another candidate

de-excitation cascade: gammas were picked randomly from the above population distribution until the sum energy reached or exceeded the excitation energy. At this point the last gamma energy was truncated such that the total energy in the cascade was 7.94 MeV. This process resulted in de-excitation cascades with an average gamma multiplicity of 4.2. The detector spectrum resulting from this cascade model is shown at the bottom of Figure 5.12.

Based on the results of modeled cascades, the gadolinium gamma cascade detection efficiency is taken to be 80% above 3.5 MeV. The uncertainties in this efficiency, however, clearly demonstrate the need for an experimental calibration of the neutron detection efficiency. See Chapter 6.

The full neutron detection efficiency is then the product of the partial efficiencies:

$$\epsilon_N = \epsilon_c \cdot \epsilon_{Gd} \cdot \epsilon_\gamma \cdot \epsilon_\tau = 0.87 \cdot 0.88 \cdot 0.80 \cdot 0.97 = 0.59,$$

or 59% total efficiency for neutron detection.

Finally the total neutrino detection efficiency can be expressed as the fraction of detected events per neutrino-induced inverse β decay in the scintillator. At Palo Verde, the number of neutrino interactions in the detector is expected to be 197 per day which gives the expected signal rate tabulated below:

Topology	Full Detection Efficiency	Detected Events per Day
9 Block	26%	51
Restricted 9 Block	21%	41
Back to Back	15%	30

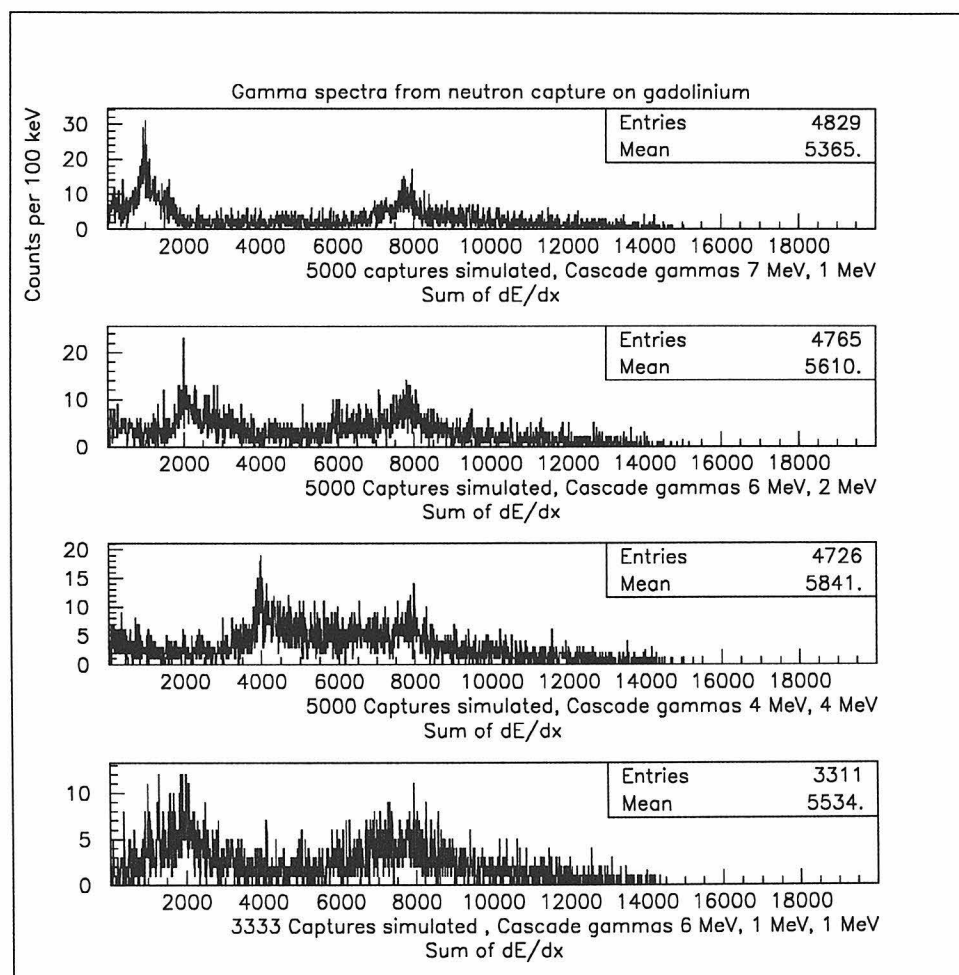


Figure 5.11: Detected gamma spectra from neutron capture on gadolinium. The detection efficiency for simple cascades is estimated. Here cascades of gamma energy 7,1; 6,2; 4,4; and 6,1,1 are simulated.

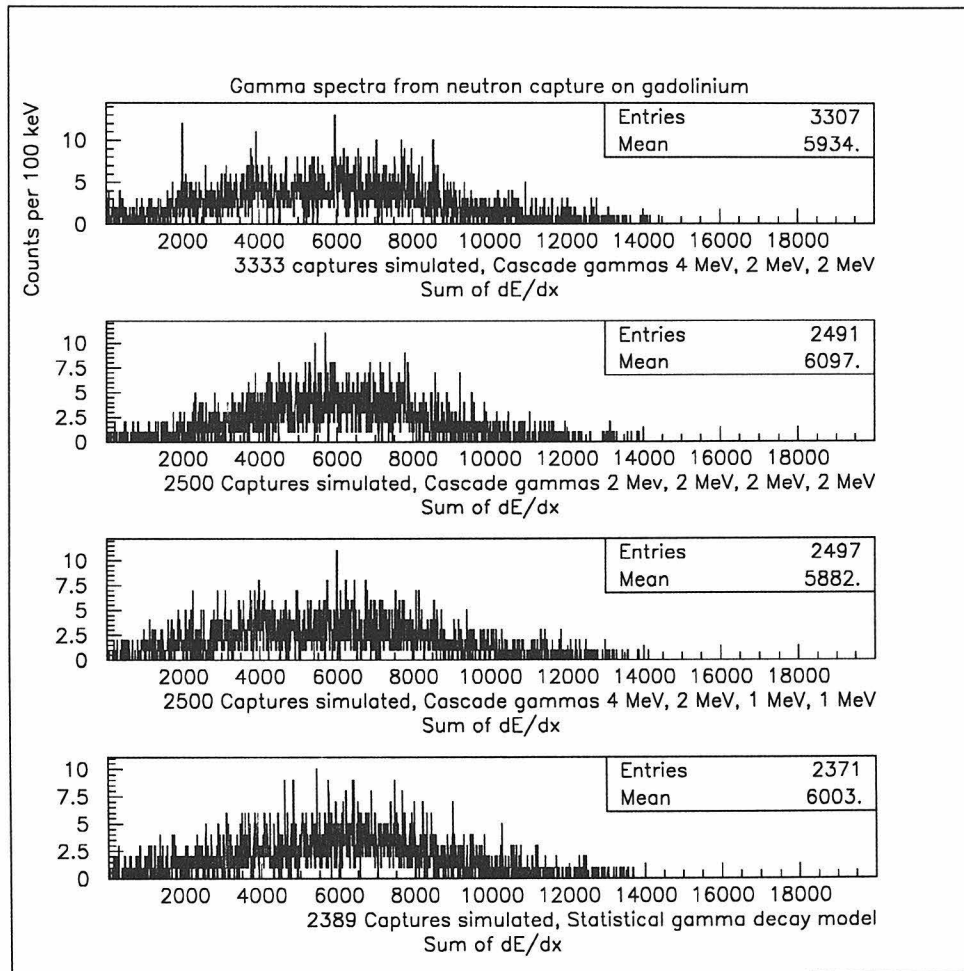


Figure 5.12: Detected gamma spectra from neutron capture on gadolinium. The detection efficiency for simple cascades is estimated. Here cascades of gamma energy 4,2,2; 2,2,2,2; and 4,2,1,1 are simulated as well as gammas calculated using a simple statistical model.

Table 5.2: Gamma detection efficiency from neutron capture on gadolinium. The probability of detection, for three energy thresholds, is tabulated for a number of assumed de-excitation cascades. The 3.5 MeV threshold will be taken for the experiment to minimize the contribution of natural radioactivities.

Energies of Gammas in Cascade (MeV)	Detection Efficiency and Threshold		
	2 MeV	3 MeV	3.5 MeV
7, 1	63%	59%	58%
6, 2	78%	65%	61%
4, 4	83%	79%	75%
6, 1, 1	78%	66%	62%
4, 2, 2	91%	83%	78%
2, 2, 2, 2	96%	90%	86%
4, 2, 1, 1	92%	84%	79%
Statistical Model	92%	86%	81%

5.4 The Correlated Background

The term “correlated background” refers to background events in the detector capable of producing both a fast positron-like triple coincidence as well as a time-delayed neutron-capture-like signal. There are two sources of such backgrounds, both the product of cosmic muon inelastic interactions: fast neutrons from nuclear spallation and capture, and β -delayed-neutron emission from cosmogenic radioactivities.

5.4.1 Fast Neutron Correlated Background

Fast neutrons created by cosmic muons traversing the laboratory walls and detector structural materials are a source of correlated background in the neutrino detector: a fast neutron may induce a triple coincidence either through multiple elastic scattering in several cells or through secondary gamma production by inelastic interactions. Then having lost large fraction of its energy, the neutron may slow and be captured on gadolinium in the scintillator, completing the fast-slow correlated neutrino-like signature.

Fast neutrons are produced by two processes: muon capture and muon spallation. Muon capture produces neutrons with energies up to 100 MeV, and muon spallation produces neutrons of even higher energy. While the yield and spectral shape of neutrons from muon capture are well understood [64, 65], there is considerable uncertainty regarding the spallation neutrons, which will be discussed in more detail below.

5.4.2 The Simulation

Rather than generate neutrons according to any assumed spectrum, monoenergetic neutrons were simulated, allowing any input spectrum to be put together later from the simulation data.

Neutrons of energy 10, 20, 50, 100, 200, 500, and 1000 MeV were simulated, uniformly distributed inside the 60-cm thick concrete laboratory walls. They were

given momentum isotropically in 4π . Neutrons produced in the structure of the detector itself are not a source of correlated background because the parent muon is necessarily tagged and the event vetoed. After each neutron vertex was generated, a calculation was made to check whether the parent muon of that neutron would be (or had been) tagged by the detector muon veto. For this calculation a spatial direction vector was generated at the neutron vertex with a $\cos^2 \theta$ azimuthal dependence as per the muon angular distribution, and the intersection point with each of the six planes defining the muon veto was calculated. The event was then tagged in the event-by-event data file to indicate whether or not a muon hit the veto. All energy losses, both in the target cell scintillator and in the muon veto scintillator, were recorded event by event. Finally, at the end of tracking, the stopping point of the neutron (and any secondary neutrons) was noted: if any neutron fell below the tracking threshold of 10 keV inside the Gd-loaded scintillator volume, it was assumed to capture and be detected as a delayed neutron signal with the efficiency calculated in section 5.3.2 (with the exclusion of the containment efficiency factor as the neutron is already presumed contained). In this case, a second flag was set in the event-by-event data indicating a neutron capture. Only events with the capture flag set are able to contribute to the correlated background. Details of the neutron tracking from the laboratory walls are given in Appendix B.1.

The following table summarizes the energy and total statistics of the neutrons generated in the 60-cm concrete walls:

Neutron Simulation Statistics	
Neutron Energy	Number of Neutrons Generated
10 MeV	14,454,000
20 MeV	11,335,000
50 MeV	860,000
100 MeV	454,000
200 MeV	473,000
500 MeV	180,000
1000 MeV	49,000

Event-by-event neutron data was analyzed using the same cuts as for the positron sample above. For each neutron energy started in the walls, the probability of producing a triple coincidence was calculated. Figure 5.13 displays the triple coincidence probability as a function of input neutron energy for the 9-block topology. In the figure the efficiency of the muon and capture tags are explored: the top curve is the probability for a triple coincidence with no requirement that a neutron be captured in the scintillator to complete the fast-slow correlation. The next curve illustrates the reduction achieved by requiring that the parent muon of the neutron did not strike the veto. Any veto hit will shut down the detector for at least 10 μsec , effectively removing any fast neutron triple coincidence. The last curve illustrates the true correlated triple coincidence: events here contain a final captured neutron and are produced by neutrons whose parent muon has not hit the veto. The capture flag is most effective at low energies, presumably because most of these neutrons never reach the scintillator at all, the triple coincidence being produced by secondary gammas from the buffer. The dashed curve illustrates the removal of the condition that the muon veto contain less than 20 MeV. In other words, some high energy neutrons veto themselves by recoiling in the muon veto, leaving at least 20 MeV, and then proceeding to the fiducial volume where they produce a fast triple coincidence and finally capture on gadolinium. As expected, this veto is effective only for very high energy neutrons ($>$ few hundred MeV).

Analysis of the triple efficiency for the restricted-9-block and back-to-back topolo-

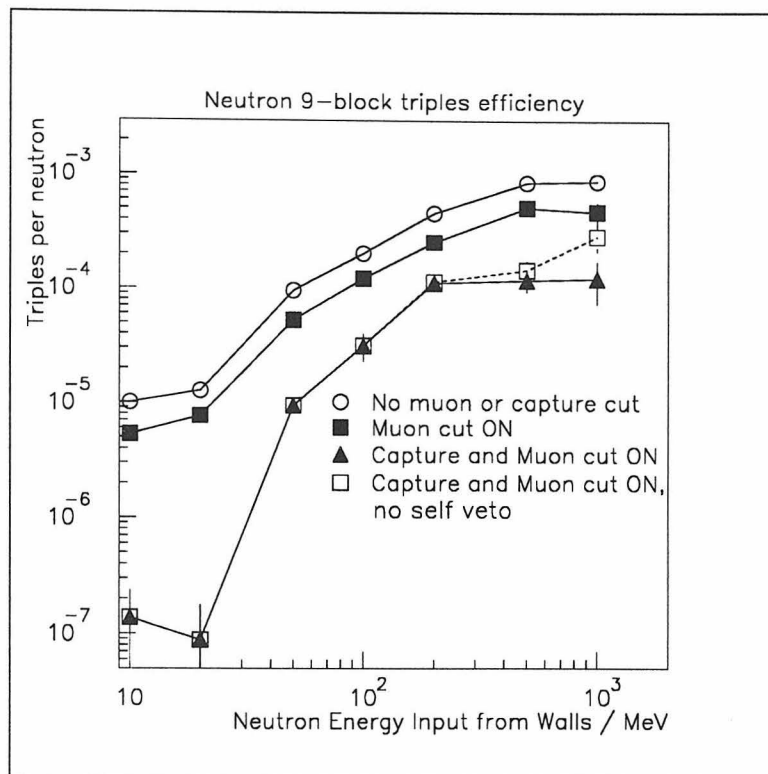


Figure 5.13: Efficiency for the production of triple coincidences in the 9-block topology by neutrons generated in the concrete walls. The lowest curve pertains to events in which a neutron is left in the fiducial volume to capture, the neutron's parent muon did not strike the veto, and the neutron did not self veto by depositing more than 20 MeV in the muon veto.

gies was performed as well, and it was determined that the background reduction factor in going from the 9-block to the back-to-back topology was roughly equal to the signal reduction factor (about 1.6). See Figure 5.14. Thus by keeping the cut loose, one gains in statistics without sacrificing signal to noise. The following results are therefore reported only for the 9-block topology.

5.4.3 Neutron Background Analysis

To estimate the background rate in the neutrino detector, the neutron triple-coincidence efficiency must be folded with the energy spectrum of neutrons produced in the wall and normalized to the production rate per day. In addition, one must take into account correlated events due to neutrons produced inside the detector itself when the

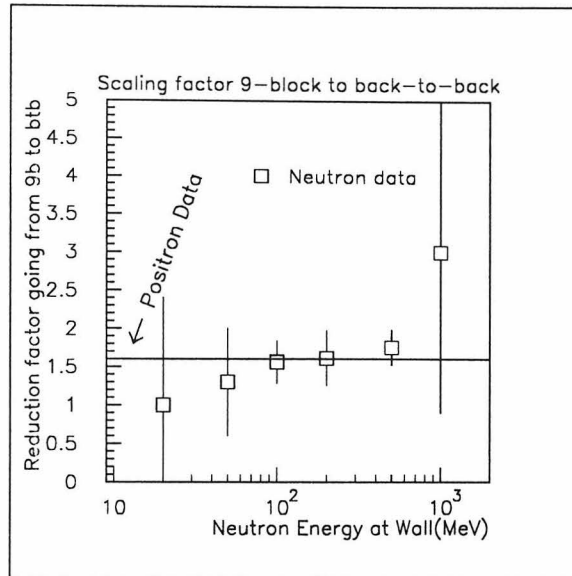


Figure 5.14: The reduction factor in going from the 9-block to the back-to-back topology is displayed for the positron and neutron data. The open squares are the neutron efficiency data, and the signal reduction factor (1.6) is plotted as a horizontal strip. Essentially, the neutron and positron data scale identically and the tighter topological cut only reduces statistics.

parent muon manages to slip through the veto undetected. Appendix B.2 presents a detailed discussion of these calculations for neutrons produced by muon capture and muon spallation. Table 5.3 summarizes the uncorrelated background rate due to these processes.

5.4.4 Correlated Background From μ -Induced Radioactivities

Muons traversing the detector periodically undergo violent nuclear collisions in which they lose a large fraction of their energy. In such collisions high energy particles such as π^- 's are produced. These particles may induce nuclear reactions in the surrounding material producing various nuclei of smaller mass and charge than the nuclei with which they interact. In the fiducial volume of the neutrino detector, such reactions may take place on carbon nuclei, producing, among others, the β -delayed-neutron emitters ^{11}Li and ^9Li . These nuclei may produce correlated background events in the

detector if the emitted electron is able to electromagnetically shower and produce a fast triple coincidence, followed by detection of the emitted neutron. The probability of showering, though a second-order process, is not negligible as each of these nuclei has a relatively large Q -value. In each case, the neutron-unstable state is about 2–3 MeV above the ground state, giving β endpoint energies of about 15 MeV and 10 MeV in the case of neutron emission for ^{11}Li and ^9Li , respectively. The branching to the neutron-unstable state is 35% for ^9Li and 60% for ^{11}Li .

To simulate this detection efficiency, electrons were generated uniformly in the target-cell scintillator with energy picked randomly from β spectra with these endpoints. On average it was found that such β decays have about a 1.9% chance of creating a 9-block triple coincidence. If we then accept a 59% neutron detection efficiency, we arrive at an efficiency of about 1.1 background events per 100 β -delayed-neutron decays.

A quantitative description of the creation of light nuclei by muon inelastic scattering does not exist, but some estimate of the production rate can be gleaned from an examination of data from KAMIOKANDE. In his thesis, Inoue [73] describes the detection of ^{12}N , ^{12}B , and ^{16}N produced in the KAMIOKANDE water Cherenkov detector by inelastic muon interactions with ^{16}O . Correcting for the 7 MeV electron threshold in the detector, one arrives at a production rate of about 6 $A=12$ and 20 ^{16}N nuclei per day. Dividing these rates by the muon flux of 0.13/s and by the 680-ton fiducial volume, one arrives at the normalized production rates of about $8 \cdot 10^{-7}$ per ton and muon of $A=12$ nuclei, and $3 \cdot 10^{-6}$ per ton and muon of ^{16}N . If one assumes that the rate of producing $A=12$ nuclei from ^{16}O is the same as the rate of producing light nuclei from ^{12}C , one can scale the KAMIOKANDE production rates to the neutrino detector at shallow depth. If we make the very conservative assumption that the production rate does not scale with the average muon energy, one estimates that for the 12-ton fiducial volume and a muon rate of about 200/sec, the production rate of light nuclei will be about 170 per day. Assuming an average branching of about 50% to the dangerous β -delayed-neutron decay, we arrive at about 1 correlated background event per day in the detector due to muon-induced radioactivities.

A more realistic estimate might assume that the production rate scales linearly with the average muon energy, as the energy loss formula suggests. In this case the production rates would be down a factor of about 50 and thus completely negligible.

5.4.5 Summary of Correlated Backgrounds

Correlated backgrounds in the neutrino detector arise from neutrons produced by cosmic muons, either through capture, spallation, or the generation of neutron-unstable radioactivities. Large spreads in the calculated and measured spectra of neutrons from muon spallation make an accurate estimate of this background rate difficult. Thus a range of correlated rates is presented based on the various spectral assumptions (see Appendix B.2). Table 5.3 summarizes the contribution to the background rate of the processes described above. The actual rate will be measured during the reactor-off refueling cycle.

Table 5.3: Summary of the correlated backgrounds in the neutrino detector. The various assumptions about the spectral shape of the neutron spallation spectrum are shown. This rate will be measured during the reactor-off refueling cycle.

Background Source	Events per Day
μ Capture in Walls	2.4
μ Spallation in Walls	5 ~ 75
-0.5,10,-1.6	29
-0.5,50,-1.6	75
-1,200,-2	5
$e^{-E/39 \text{ MeV}}$ (KARMEN)	30
μ Capture in Detector (Veto Leakage)	0.4
μ Spallation in Detector (Veto Leakage)	0.09
μ -Induced Radioactivities	1
TOTAL	9 ~ 79
TOTAL Using KARMEN Spectrum	34

5.5 The Uncorrelated Background

Signals in the detector that mimic only the neutron capture or only the positron annihilation cannot produce background events on their own. However, if a positron-like and a capture-like signal happen to overlap in time, they may produce an accidental, or uncorrelated, background event. The sources of such uncorrelated events are natural radioactivities in the laboratory and detector structural materials, muon-induced radioactivities, and “neutron soup,” described below.

5.5.1 Natural Radioactivities

All construction materials contain small amounts of naturally-occurring radioactive contaminants, in particular, the long-lived isotopes ^{40}K , ^{232}Th , ^{238}U , and their daughter activities. Gamma radiation from these isotopes may produce false positron-like signals in the detector through multiple Compton scattering or by pair production. Conceivably, this radiation could also mimic the neutron capture signal, but the use of gadolinium in the scintillator allows the capture signal threshold to be set well above naturally occurring radioactivities, making their contribution to the false capture rate negligible.

The γ -decay cascades of the isotopes ^{40}K , ^{232}Th , ^{238}U , ^{222}Rn , and ^{60}Co were simulated in the structural materials of the detector to investigate their contribution to the uncorrelated background. Appendix B.3 provides details on how the decay schemes of these isotopes were implemented.

Radioactivities in the Laboratory Walls

Gamma radiation from ^{238}U , ^{232}Th , and ^{40}K decays was generated uniformly in the laboratory walls to a depth of 30 cm. The gamma flux entering the lab was investigated as a function of the production depth to determine the infinitive thickness. Figure 5.15 displays the results of this study. At 30 cm, the flux is nearly in saturation, and a comparison of runs using 30-cm and 60-cm production depths show no difference in the induced background rate.

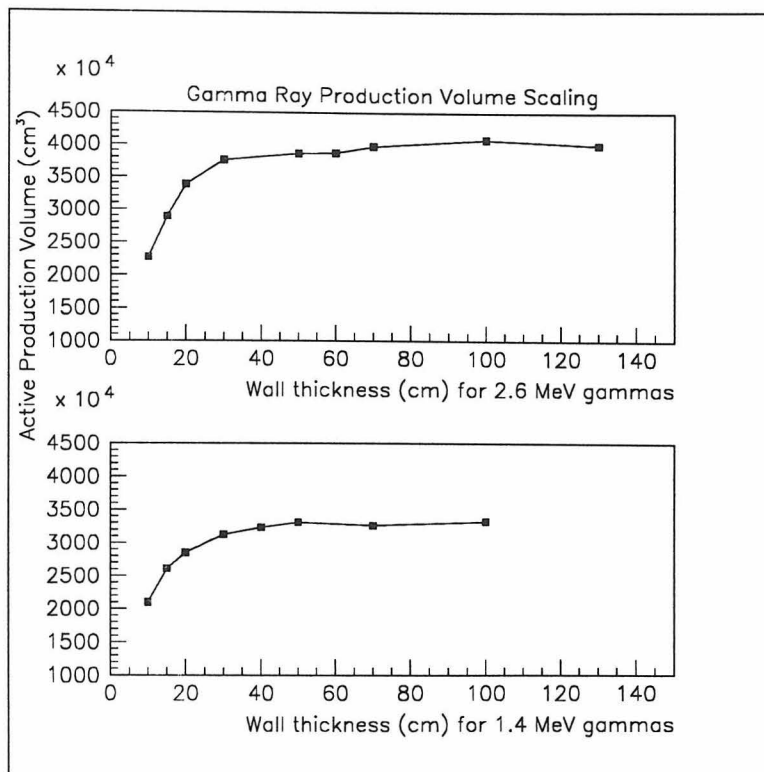


Figure 5.15: Gamma production volume saturation. The entering gamma flux, or active production volume, is plotted as a function of the production depth in the wall. The upper plot shows the production depth curve for 2.6 MeV gammas, relevant for ^{238}U and ^{232}Th . The lower curve displays the production depth curve for 1.4 MeV gammas, relevant for ^{40}K decay.

A total of $18 \cdot 10^6$ ^{238}U gammas, $18 \cdot 10^6$ ^{232}Th gammas, and $17.5 \cdot 10^6$ ^{40}K gammas were simulated. As an example, Figure 5.16 illustrates the propagation of ^{232}Th gammas from the wall to the fiducial volume.

The probability of producing a triple coincidence positron-like signal is then determined per decay in the walls for each of the discussed topologies. In addition, the probability of firing at least one cell between 1 and 10 MeV is investigated as an estimate of the single firing rate of the detector:

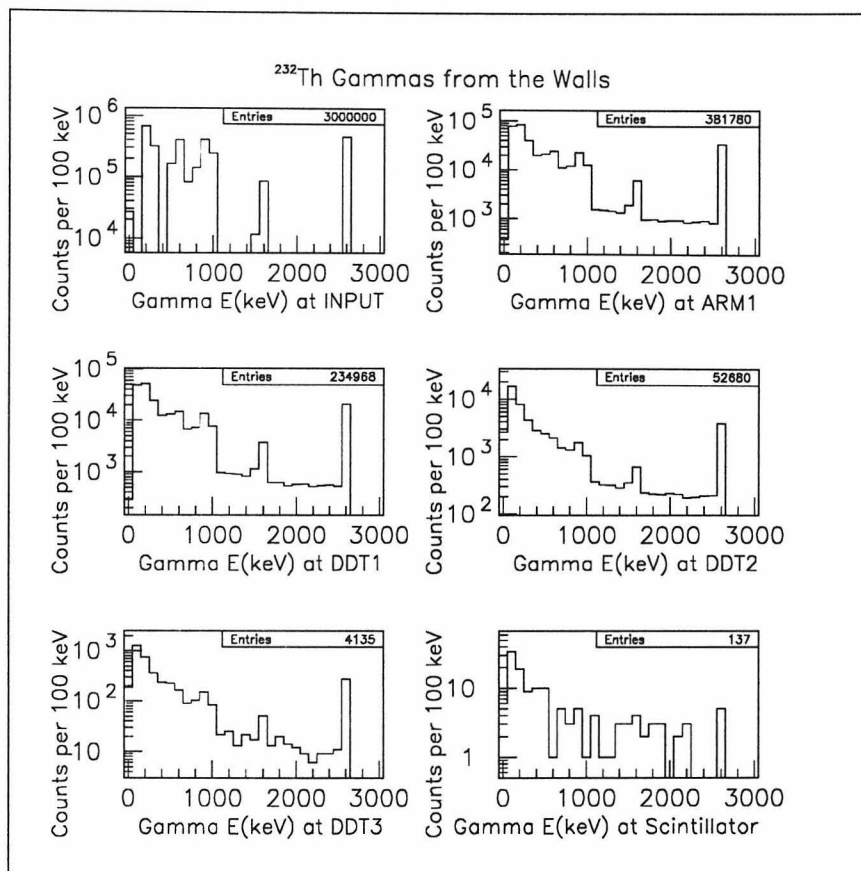


Figure 5.16: Propagation of ^{232}Th gammas from the wall to the fiducial volume. The energy spectrum of ^{232}Th gammas is displayed at the entrance to various detector volumes. See the table in Appendix B.1 for a description of the volume names.

Triple Coincidence Probability: Gammas from Walls				
Probability per Parent Decay				
Isotope	Singles	9 Block	Restricted 9 Block	Back to Back
^{238}U	$8.9 \cdot 10^{-6}$	$1.7 \cdot 10^{-6}$	$4.1 \cdot 10^{-7}$	$4.1 \cdot 10^{-7}$
^{232}Th	$2.5 \cdot 10^{-5}$	$3.3 \cdot 10^{-6}$	$2.6 \cdot 10^{-7}$	$7.7 \cdot 10^{-7}$
^{40}K	$8.2 \cdot 10^{-7}$	$1.2 \cdot 10^{-7}$	$8.4 \cdot 10^{-8}$	$4.2 \cdot 10^{-8}$

The total mass of a 30-cm thick concrete production volume is $3.92 \cdot 10^5$ kg. The concrete used to construct the lab will be made from a mixture of about 20% cement and 80% aggregate and sand. Several cements were measured at Caltech and were all found to contain about 1 to 1.5 ppm of uranium and thorium, and about 0.3 ppm of ^{40}K . Several gravels from the Northern U.S. have been found containing about

0.2 ppm of uranium and thorium, and 0.1 ppm of ^{40}K . The local soil at the Palo Verde site, on the other hand, contains about 3 ppm of thorium, 1 ppm of uranium, and 1 ppm of ^{40}K , and local sources of gravel may be similar. So depending on the gravel selected, the construction concrete will contain about 0.4 ppm of U and Th and 0.15 ppm of ^{40}K , or about 1 ppm of U, 2.6 ppm of Th, and 0.85 ppm of ^{40}K . The background rates due to these concentrations are summarized in Table 5.4.

Radiopurity of the Water Buffer

The water buffer contains nearly 100 tons of purified water in order to shield the detector from neutrons and gamma radiation from external sources. The water itself, however, is also a source of background from contaminants present at low concentrations. Again, gamma radiation from ^{238}U , ^{232}Th , and ^{40}K was simulated, distributed uniformly in the water of the buffer tanks. One million gammas from ^{238}U and ^{40}K decay, and one half million gammas from ^{232}Th decay were simulated to determine the background probabilities per parent decay:

Triple Coincidence Probability: Gammas from the Water Buffer				
Probability per Parent Decay				
Isotope	Singles	9 Block	Restricted 9 Block	Back to Back
^{238}U	$8.4 \cdot 10^{-3}$	$1.3 \cdot 10^{-3}$	$7.8 \cdot 10^{-4}$	$4.1 \cdot 10^{-4}$
^{232}Th	$1.2 \cdot 10^{-2}$	$2.1 \cdot 10^{-3}$	$1.4 \cdot 10^{-3}$	$7.4 \cdot 10^{-4}$
^{40}K	$1.3 \cdot 10^{-3}$	$1.7 \cdot 10^{-4}$	$1.0 \cdot 10^{-4}$	$5.0 \cdot 10^{-5}$

The water used to fill the buffer will most likely be obtained from a large purification plant operated by the Palo Verde reactor. Very clean, mineral-free water is required to cool the reactor and is produced through double distillation and reverse osmosis. The purity typically achievable with such a technique is at the level of a part per trillion, resulting in a decay rate of a few Bq in the entire water buffer. The background rate due to this activity, summarized in Table 5.4, is entirely negligible.

The Buffer Tank Steel

The steel of the water buffer tanks is also a source of uncorrelated background. Gammas produced in the outside walls of the buffer tanks are attenuated in the water before reaching the detector and produce a negligible background. However, the inner surfaces of the steel tanks are in contact with the fiducial volume, producing gamma radiation which easily enters the target cells. Steel generally does not contain ^{40}K , but it does contain uranium and thorium and also ^{60}Co , which is relatively short lived, but introduced in the manufacturing process. Gammas from these isotopes were generated uniformly in the 2.3-mm thick inner steel walls, which account for 1140 kg of material. The background probabilities are tabulated per parent decay:

Triple Coincidence Probability: Gammas from the Steel Walls				
Probability per Parent Decay				
Isotope	Singles	9 Block	Restricted 9 Block	Back to Back
^{238}U	$7.4 \cdot 10^{-2}$	$1.1 \cdot 10^{-2}$	$6.6 \cdot 10^{-3}$	$3.7 \cdot 10^{-3}$
^{232}Th	$8.8 \cdot 10^{-2}$	$1.5 \cdot 10^{-2}$	$9.2 \cdot 10^{-3}$	$6.0 \cdot 10^{-3}$
^{60}Co	$1.7 \cdot 10^{-1}$	$2.2 \cdot 10^{-2}$	$1.4 \cdot 10^{-2}$	$8.1 \cdot 10^{-3}$

Steel samples measured at Caltech were found to contain less than a few ppb of uranium and thorium, and about 2 mBq/kg of ^{60}Co . The background due to these contaminants is summarized in Table 5.4.

The Internal Structural Steel

A number of steel strips and rollers form a frame from which the target cells are suspended. Generated between the target cells, gammas produced in this structural steel have a very efficient solid angle for entering the fiducial volume. Again gammas from ^{238}U , ^{232}Th , and ^{60}Co were simulated, distributed uniformly through the steel support strips, which account for about one half ton of material. The background probabilities per parent decay are tabulated below.

Triple Coincidence Probability: Gammas from the Structural Steel				
Probability per Parent Decay				
Isotope	Singles	9 Block	Restricted 9 Block	Back to Back
^{238}U	$2.1 \cdot 10^{-1}$	$5.0 \cdot 10^{-2}$	$3.5 \cdot 10^{-2}$	$2.0 \cdot 10^{-2}$
^{232}Th	$2.4 \cdot 10^{-1}$	$7.5 \cdot 10^{-2}$	$5.3 \cdot 10^{-2}$	$3.5 \cdot 10^{-2}$
^{60}Co	$4.8 \cdot 10^{-1}$	$1.2 \cdot 10^{-1}$	$8.3 \cdot 10^{-2}$	$5.3 \cdot 10^{-2}$

The Photomultiplier Tubes

Contaminants in the glass and electronic components of the photomultiplier tubes are a source of uncorrelated background. A buffer of 80 cm of inactive mineral oil separates the phototubes from the active target scintillator, but gamma radiation penetrating this buffer can produce false triple coincidences in the detector. Gamma radiation from uranium, thorium, and potassium was simulated, originating in the phototubes coupled to the ends of the target cells. The following background efficiencies were calculated per parent decay.

Triple Coincidence Probability: Gammas from the Photomultiplier Tubes				
Probability per Parent Decay				
Isotope	Singles	9 Block	Restricted 9 Block	Back to Back
^{238}U	$2.3 \cdot 10^{-3}$	$3.2 \cdot 10^{-4}$	$2.2 \cdot 10^{-4}$	$8.2 \cdot 10^{-5}$
^{232}Th	$3.8 \cdot 10^{-3}$	$5.8 \cdot 10^{-4}$	$3.6 \cdot 10^{-4}$	$1.6 \cdot 10^{-4}$
^{40}K	$2.8 \cdot 10^{-4}$	$4.6 \cdot 10^{-5}$	$2.9 \cdot 10^{-5}$	$1.2 \cdot 10^{-5}$

The detector contains 264 phototubes, two per end per cell. We plan to use Philips XP4532 phototubes manufactured using low-background Schott glass containing about 20 Bq of ^{40}K and 1 Bq of uranium and thorium per tube. At this level of radiopurity, the phototubes are a factor of 20 to 30 cleaner than those made from standard glass. The tubes will be made with convex windows to minimize material and will be coupled to the detector using acrylic adaptors. The background rate due to the phototubes is summarized in Table 5.4.

Radon Gas

Radon gas, emanated from the laboratory walls and other construction materials, may enter the air spaces between cells. This volume is estimated to be about 6000 liters. Gammas from the decay of ^{222}Rn were generated uniformly throughout the air spaces in the fiducial volume of the detector, and the following background efficiency was calculated:

Triple Coincidence Probability: Gammas from the Photomultiplier Tubes				
Probability per Parent Decay				
Isotope	Singles	9 Block	Restricted 9 Block	Back to Back
^{222}Rn	$1.8 \cdot 10^{-1}$	$4.7 \cdot 10^{-2}$	$3.3 \cdot 10^{-2}$	$1.9 \cdot 10^{-2}$

To reduce the contribution of radon gas to the background rate, the fiducial volume of the detector will be sealed and ventilated with a flow of compressed radon-free air. By this method we should achieve concentrations significantly below 25 mBq per liter, which is the concentration measured in a ventilated (by outside air) basement room at Caltech. The contribution of radon to the background rate is summarized in Table 5.4.

Acrylic and Light-Tight PVC

The acrylic structure of the target cells and the black PVC wrapping used to make them light tight are a source of gamma background. Gamma radiation from uranium, thorium, and potassium was generated in these plastics to determine the background efficiency below:

Triple Coincidence Probability: Gammas from Acrylic and PVC				
Probability per Parent Decay				
Isotope	Singles	9 Block	Restricted 9 Block	Back to Back
^{238}U	$2.6 \cdot 10^{-1}$	$7.4 \cdot 10^{-2}$	$5.0 \cdot 10^{-2}$	$2.9 \cdot 10^{-2}$
^{232}Th	$2.9 \cdot 10^{-1}$	$9.6 \cdot 10^{-2}$	$7.2 \cdot 10^{-2}$	$4.5 \cdot 10^{-2}$
^{40}K	$3.9 \cdot 10^{-2}$	$7.0 \cdot 10^{-3}$	$4.6 \cdot 10^{-3}$	$2.2 \cdot 10^{-3}$

Clear acrylic is generally very radio pure, typical contaminant levels averaging about $2 \cdot 10^{-11}$ g/g of ^{238}U and ^{232}Th [75]. Each cell is made from 53.5 kg of acrylic, or 3531 kg in the entire detector.

The black PVC is much more radioactive as the addition of color to otherwise pure hydrocarbons often introduces many contaminants. The black pellets used to extrude the PVC casings were measured in Switzerland [76] to contain 1.9 ppb of ^{238}U , 2.7 ppb of ^{232}Th and 3.7 ppb of ^{40}K . Of this material, 250 kg is required to wrap all 66 cells. The background rate introduced by these plastics is summarized in Table 5.4.

The Active Scintillator

The active scintillator itself is a source of background due to intrinsic radioimpurities and those added when the liquid is loaded with 0.1% by weight of gadolinium. Before loading, the scintillator contains uranium and thorium below limits of $3 \cdot 10^{-13}$, and ^{40}K below $4 \cdot 10^{-13}$ [77]. A sample of gadolinium nitrate used to load the scintillator was measured in Switzerland [76] and purity limits were set at $< 7 \cdot 10^{-10}$ g/g of ^{238}U , $< 8 \cdot 10^{-10}$ g/g of ^{232}Th , and $< 6 \cdot 10^{-11}$ g/g of ^{40}K . This sets limits for the 0.1% loaded scintillator of $< 1 \cdot 10^{-12}$ g/g of uranium and thorium, and $< 4 \cdot 10^{-13}$ of ^{40}K .

Inside the scintillator itself, gamma radiation can add with β and α activities which otherwise would not penetrate into the active volume. This greatly complicates the source simulation, but is unnecessary here: these contamination levels will result in less than 0.2 decays per second in the 12 tons of active scintillator. Even with a 100% triple efficiency this would have a negligible effect on the total triples background rate. (See Table 5.4).

This rate is relevant, however, for the capture-like uncorrelated background if β - γ cascades are able to exceed the 3.5 MeV threshold. (α - γ cascades are not dangerous because the light from α particles is so strongly quenched in the scintillator). The only cascade capable of exceeding this threshold is the gamma de-excitation of ^{208}Pb following the β decay of ^{208}Tl in the ^{232}Th decay chain. In this case all β decays are followed by a cascade of 2614 keV and other gamma rays. The endpoint of the β

spectra allow a combination of β and γ radiation reaching nearly 5 MeV if everything is contained in the scintillator. On the other hand, very large β energies are unlikely and using the average energy of the β spectra allows us to reach only 3.8 MeV. If we assume that in half of the cases the β energy exceeds the average and that the gamma energy is always fully contained, we can make a simple estimate of this rate: the above contamination limits correspond to less than 0.05 decays per second of ^{232}Th , or 0.02 Bq of ^{208}Tl . If half of these decays exceed the threshold, the contribution to the capture-like background will be 0.01 Hz.

Conclusion

Referring to Table 5.4, the single firing rate of the detector due to natural radioactivity will be in the range of 75 – 298 Hz, and the 9-block triple coincidence rate in the range of 13 – 48 Hz. The optimistic numbers assume that the low-activity gravel, or something similar, will be used to mix the concrete and that by using a compressed air flow, the radon level can be reduced by a factor of ten over the outside-air-ventilated rate measured at Caltech. The optimistic rates are quite achievable; the pessimistic values are shown for reference and motivation. It is assumed that the natural radioactivities will not contribute to the capture-like accidental rate because of the high threshold except in the case of decay inside the scintillator itself, described above.

5.5.2 Muon-Induced Radioactivities

Based on production rates scaled from KAMIOKANDE data, see section 5.4.4, uncorrelated background from light nuclei is negligible. However, if we assume that neutrons produced by muon spallation in the scintillator are simply ejected from ^{12}C nuclei, we can imagine that ^{11}C and ^{10}C , both β^+ emitters, are produced at the measured muon spallation rate. A spallation rate of $5.5 \text{ n kg}^{-1} \text{ d}^{-1}$ then produces ^{11}C in the 12-ton fiducial volume at a rate of about 0.7 Hz. ^{11}C has a β^+ endpoint energy of only about 900 keV and thus is not efficient at producing triples. However,

^{10}C has a β^+ endpoint of about 2.6 MeV. If we assume that ^{10}C and ^{11}C are produced at the same rate and that the efficiency for producing triples is the same as for neutrino-induced positrons, we arrive at an uncorrelated triples rate of about 0.3 Hz.

5.5.3 Neutron Soup

“Neutron soup” refers to the sea of thermal and nearly thermal neutrons present in the detector which have not, in the process of thermalizing, created a fast triple coincidence. Neutrons produced in the walls which lose enough energy before entering the fiducial volume that they are unable to produce triple coincidences become part of the soup. In addition neutrons produced inside the detector whose fast coincidences are vetoed by their parent muon become part of the soup. As these neutrons capture on gadolinium and are detected, they become false delayed-capture signals which can complete full uncorrelated background signals if they come close enough after false triple coincidences.

The neutron soup background was simulated in two parts: first neutrons generated in the wall were tracked to 10 keV to estimate the rate of neutron captures. Second, neutrons were generated in the interior of the detector and the capture rate was determined taking into account the veto conditions initiated by the parent muons.

Neutrons From the Laboratory Walls

The same data set as for the correlated background estimate was used for this analysis. Monoenergetic neutrons of energies 10, 20, 50, 100, 200, 500, and 1000 MeV were produced in the walls and tracked through the detector until they fell below a 10 keV threshold. At this stopping point, the neutron was assumed to capture in the current material. If this material was active target scintillator, the neutron was presumed to be detected as a capture candidate with an efficiency of 68% (see section 5.3.2). The capture efficiency as a function of neutron energy was, as before, linearly interpolated and folded with the normalized muon capture and muon spallation spectra to determine the actual rate of neutron captures. It was assumed that the muon veto

would have no effect on this rate since the neutrons take several μs to thermalize in the detector before the characteristic $28 \mu\text{s}$ capture time becomes relevant. Thus a $10 \mu\text{s}$ veto initiated by a parent muon which happened to hit the veto would kill a fast triple produced by that neutron but nearly never the capture signal. The following table summarizes the uncorrelated capture-like signal rate due to neutrons from the wall, taking into account the 68% detection efficiency. Again, the result is sensitive to the spectrum of neutrons from muon spallation; several spectral assumptions are shown (see Appendix B.2).

Neutron Soup from Laboratory Walls	
Background Source	Uncorrelated Capture Rate [Hz]
μ Capture in Walls	0.0009
μ Spallation in Walls	0.0034–0.058
-0.5,10,-1.6	0.022
-0.5,50,-1.6	0.058
-1,200,-2	0.0034
$e^{-E/39 \text{ MeV}}$ (KARMEN)	0.0082

Neutrons From Inside the Detector

Neutrons produced inside the detector structure, i.e., in the veto, the buffer, the structural steel, and the fiducial volume, are the main source of uncorrelated capture events. To simulate this capture rate, Monoenergetic neutrons were produced uniformly in all interior detector volumes. (This same data set was used to calculate the correlated background due to the non-zero veto inefficiency). The total mass of the production volume is 175 tons, of which 90% is water or oil. After the generation of each neutron vertex, a muon trajectory was generated from this same vertex to identify events in which the muon would hit the fiducial volume. This would initiate a $100 \mu\text{s}$ veto which would reduce the capture contribution of these events by a factor of $e^{-(100-10)/28\mu\text{sec}}$, where $10 \mu\text{s}$ is subtracted from the veto time to conservatively account for the neutron thermalization time.

The efficiency curve as a function of neutron energy was again linearly interpolated

and folded with the muon spallation spectra to determine the capture rate. In this case the neutrons from muon capture are negligible in comparison to those from spallation because any stopped muon initiates a 300 μ s veto. The table below summarizes the rate of neutron captures due to neutrons produced inside the detector (68% of these are actually detected).

Neutron Capture Rate with and without a μ in the Fiducial Volume	
Background Source	Neutrons Captured per Second
μ Spallation Inside Detector (Disregard fiducial μ hit tag)	
-0.5,10,-1.6	0.70
-0.5,50,-1.6	0.79
-1,200,-2	0.055
$e^{-E/39 \text{ MeV}}$ (KARMEN)	0.84
μ Spallation Inside Detector (Reject fiducial μ hits)	
-0.5,10,-1.6	0.072
-0.5,50,-1.6	0.15
-1,200,-2	0.0086
$e^{-E/39 \text{ MeV}}$ (KARMEN)	0.10

The background capture rate is then given by the following procedure: the events which are tagged by the fiducial hit flag are multiplied by a factor of $e^{-90/28}$ to account for veto rejection and these are added to the events remaining when fiducial hits are rejected. This still underestimates the rate, however, because many near-thermal neutrons are produced in the active target scintillator and presumably all capture (the candidate spallation spectra are all heavily weighted to low energy). These were neglected because the lowest neutron delta function simulated was 1 MeV. To correct for this, the conservative assumption was made that every neutron produced in the 12 tons of active scintillator will capture. Of course these events are all subject to

the 100 μ s veto. A production rate of 5.5 n kg⁻¹ d⁻¹ gives 0.76 Hz of neutrons in the 12-ton active volume. 0.03 Hz then survive the 100 μ s veto to be added to the total rate.

Finally, the total uncorrelated capture-like rate is tabulated below, with the 68% detection efficiency taken into account.

Total Background Capture Rate	
Background Source	Uncorrelated Capture Rate [Hz]
μ Capture in Walls	0.0009
μ Spallation in Walls	0.0034 ~ 0.058
-0.5,10,-1.6	0.022
-0.5,50,-1.6	0.058
-1,200,-2	0.0034
$e^{-E/39 \text{ MeV}}$ (KARMEN)	0.0082
μ Spallation Inside Detector	0.028 ~ 0.14
-0.5,10,-1.6	0.088
-0.5,50,-1.6	0.14
-1,200,-2	0.028
$e^{-E/39 \text{ MeV}}$ (KARMEN)	0.11
Total Capture-Like Rate	0.031 ~ 0.20
Total for KARMEN spectrum	0.12

Neutron Soup Triple Coincidences

The neutron soup is also a source of uncorrelated triple coincidences: gamma rays from capture on gadolinium in the fiducial volume can produce positron-like triple coincidence signals as can 2.2 MeV gammas from neutron capture on protons in the surrounding water buffer. However, both are negligible compared to the contributions from natural radioactivities: for capture on gadolinium, we see above that in the most pessimistic case we have about 0.3 Hz of neutron captures. At a 100% triple efficiency, this would increase the total triples rate by about 1%. For the case of capture on protons in the buffer, we can estimate the total neutron production rate in the 100-

ton buffer to be about 7 Hz. Neutrons produced in the walls and entering the buffer bring another 2–3 Hz. Pessimistically assuming that all these neutrons capture in the buffer, we have the equivalent of a 10 Bq source of 2.2 MeV gammas. Comparing this to the approximately 1 Bq due to uranium and thorium (see Table 5.4), we see that this will add to the triples rate at the level of 10^{-2} Hz, which is completely negligible.

5.5.4 Summary of Uncorrelated Backgrounds

Finally a complete summary of the uncorrelated backgrounds is displayed in Table 5.5. Uncorrelated triple coincidences and capture-like signals combine to form background events if a capture-like signal happens to arrive in the 100 μ sec following an accidental triple coincidence. This rate is thus the product of the triples rate, the capture rate, and the coincidence window:

$$14s^{-1} \cdot (0.04 \sim 0.2)s^{-1} \cdot 100^{-6}s \cdot 86400s/d = 5 \sim 24d^{-1},$$

or 15 per day if the KARMEN spallation spectrum is taken. For reference, if the concrete is made from aggregate as radioactive as the local soil, this rate climbs to 14 \sim 67 per day. A number of local gravels are yet to be measured before a decision about the aggregate is made.

It should also be noted that the 100 μ s window is rather long compared to the 28 μ s capture time of neutrons on Gd. Shortening this window to 50 μ s would reduce the signal (and correlated background) by 14% and the uncorrelated background by 50%. The final determination of this interval will depend of the measured background rates. Similarly, one might note from the preceding tables that the reduction factor for accidental triples in going from the 9-block to the back-to-back topology is a factor of 3–4 rather than the 1.6 seen for the signal and correlated background. Still it will not be clear until the real background rates are known which topology will maximize the statistical significance of the data. The need for a flexible data acquisition system is obvious. The singles rates tabulated in Table 5.4 give an indication of the DAQ requirements if one wanted, for example, to read out the entire detector every time

at least one cell fired between one and ten MeV. This rate will be about 100 Hz.

5.6 Conclusion

A full self-consistent simulation of the Palo Verde neutrino detector was undertaken using GEANT-GCALOR. The efficiency of neutrino detection was modeled by simulating the positron and neutron produced in the inverse- β decay detection reaction. Backgrounds due to natural radioactivities, muon-induced radioactivities, and muon-induced neutrons were studied. The total signal and background rates expected are summarized in Table 5.6. It is expected that the correlated background will be measured during the reactor-off refueling cycles and that the uncorrelated background will be measured continuously. The table shows a signal rate of 51 per day and a background of between 14 and 103 events per day. As a “middle value” we might take the spallation spectrum measured by KARMEN [71]. This would give a correlated rate of about 34 events per day and an uncorrelated rate of 15 per day, or a total background of 49 per day.

Table 5.4: Uncorrelated triple-coincidence background from natural radioactivities.

Material	Size	Isotope	Purity Level		Background Rate [Hz]	
			ppb	Bq/kq	Singles	9-block Triples
Laboratory Walls	392 tons	^{238}U	400	4.9	19	3.5
		^{232}Th	400	1.6	21	2.8
		^{40}K	150	47	12	1.7
		^{238}U	1000	12.4	46	8.8
		^{232}Th	2600	10.5	138	18
		^{40}K	850	264	67	9.5
Water in Buffer	100 tons	^{238}U	0.001	$1 \cdot 10^{-5}$	0.01	$2 \cdot 10^{-3}$
		^{232}Th	0.001	$4 \cdot 10^{-6}$	0.006	$1 \cdot 10^{-3}$
		^{40}K	$3 \cdot 10^{-5}$	$1 \cdot 10^{-5}$	0.002	$2 \cdot 10^{-4}$
Steel Buffer Tanks	1140 kg	^{238}U	1	0.012	0.19	0.025
		^{232}Th	1	0.004	1.1	0.16
		^{60}Co		0.001	0.41	0.068
Steel Support Strips	475 kg	^{238}U	1	0.012	0.23	0.055
		^{232}Th	1	0.004	1.2	0.30
		^{60}Co		0.001	0.47	0.15
Photo-tubes	264 tubes	^{238}U	1.2 Bq/PMT		0.72	0.10
		^{232}Th	1.0 Bq/PMT		0.98	0.15
		^{40}K	20.4 Bq/PMT		1.5	0.25
Radon	6165 l	^{222}Rn	25 mBq/l		27	7.3
		^{222}Rn	2.5 mBq/l		2.7	0.73
Acrylic Tanks	3535 kg	^{238}U	0.017	$2 \cdot 10^{-4}$	0.19	0.055
		^{232}Th	0.021	$9 \cdot 10^{-5}$	0.087	0.029
		^{40}K	$3 \cdot 10^{-4}$	$1 \cdot 10^{-4}$	0.014	0.003
Black PVC	250 kg	^{238}U	1.9	0.024	1.5	0.43
		^{232}Th	2.7	0.011	0.79	0.26
		^{40}K	3.6	1.1	11	2.0
TOTAL Background Rate:					75 ~ 298	12.8 ~ 47.6

Table 5.5: Uncorrelated background rate. The contributions to the triples rate and capture rate are shown for the various sources of uncorrelated background. The background rate per day is calculated assuming a $100 \mu\text{s}$ overlap window. The uncertainty in the rate comes from the imperfect knowledge of the spectrum of neutrons from muon spallation.

Source	Triples Rate [Hz]	Capture Rate [Hz]
Natural Radioactivities	13	0.01
μ -induced Radioactivities	0.3	–
Neutron Soup	< 0.3	$0.03 \sim 0.2$
TOTAL	14	$0.04 \sim 0.2$
EVENTS per DAY 100 μs window	$5 \sim 24$	
For KARMEN spectrum:	15	

Table 5.6: Signal and background rates expected in the neutrino detector for the 9-block topology based on this simulation. The uncertainty in the rates is due to an imprecise knowledge of the spectrum of neutrons from muon spallation. The rates taking the spallation spectrum measured by KARMEN is shown as an example of “middle” values.

Signal Rate	
Neutrino Events	51 per day
Background Rate	
Correlated Events	$9 \sim 79$ per day (KARMEN: 34)
Uncorrelated Events	$5 \sim 24$ per day (KARMEN: 15)
TOTAL	$14 \sim 103$ per day (KARMEN: 49)

Chapter 6

Systems Under Development

As the Palo Verde neutrino detector is prepared for installation, there remain a few systems to be fully worked out. This chapter presents a brief overview of projects currently under development and discusses strategies for their implementation.

6.1 The Neutron Detection Efficiency

In Chapter 4, a method of calibrating the positron detection efficiency of the Palo Verde detector has been described in detail. The other half of the neutrino efficiency, the neutron detection efficiency, must also be measured with an accuracy of a few percent. As indicated in Section 5.3.2, one of the largest uncertainties in the estimation of this efficiency is the lack of a complete understanding of the de-excitation of ^{158}Gd after neutron capture. Thus, a scheme must be developed to generate a known flux of neutrons inside the detector *in situ* to measure the detection efficiency under the true operating conditions. Two neutron sources that look promising are SbBe and AmBe.

6.1.1 The SbBe Source

The compound SbBe source emits neutrons through (γ, n) with a Q-value for the reaction $\gamma + {}^9\text{Be} \rightarrow {}^8\text{Be} + n$ of -1.665 MeV. A 1.69-MeV gamma ray is emitted with a 49% branching ratio in the decay of ^{124}Sb , initiating the above reaction and leaving about 25 keV of kinetic energy for the neutron. This is nicely matched with the kinetic energy range (about 10 ~ 100 keV) of neutrons emitted in inverse β decay initiated by reactor antineutrinos. Thus an SbBe source inserted into a target cell would simultaneously measure the proper neutron leakage efficiency and the Gd

gamma detection probability.

However, there are two main difficulties associated with this source. The first is that SbBe is a source of penetrating 1.69 MeV gamma radiation. Typical SbBe sources emit about 10^7 neutrons per Ci of ^{124}Sb activity. Thus a minimum required strength of about 100 Bq in neutrons would require nearly a MBq of gamma strength. The gamma energy, 1.69 MeV, is below the 3.5 MeV threshold for the Gd gamma burst detection, but at that rate, the chance that an Sb gamma would accidentally add with a Gd gamma burst (within about 100 ns), and thus bias the detection efficiency, is about 10%. This bias could be reduced to an acceptable level of less than 1% by encapsulating the source in 5 cm of lead. This may not be unreasonable as the neutrons will lose very little energy elastically scattering on the heavy lead nuclei as they emerge from the source.

The second difficulty associated with this source is that an absolute calibration of the neutron strength is required. It is not enough to calibrate the gamma strength of the ^{124}Sb as the neutron yield depends in detail on the geometry of the mixed antimony and beryllium. This is not a fundamental problem, but is more difficult than using a “self-normalizing” source such as AmBe, described below.

An SbBe source was used to calibrate the neutron efficiency of the neutrino detector used in the ILL reactor oscillation experiment in Grenoble. [78]

6.1.2 The AmBe Source

The compound AmBe source emits neutrons through (α ,n) with a Q-value of 5.7 MeV. The α particles, from ^{241}Am decay, bring in approximately 5 MeV of kinetic energy, thus producing neutrons of up to about 10 MeV, the exact energy dependent upon slowing of the α 's before interaction, the angle of neutron emission, secondary scattering, etc. In addition, the resulting carbon nucleus is often left in an excited state at 4.4 MeV. About 80% of the time, then, the neutron is accompanied by a 4.4 MeV de-excitation gamma. The fact that the neutrons are quite a bit more energetic than those from neutrino interactions, and those from SbBe, leads to a complication as the

neutron range and leakage must be corrected using Monte Carlo calculations. However, the Gd capture gamma spectrum is still identical to the neutrino interaction case.

A distinct advantage of using AmBe for the calibration is that it is “self-normalizing.” The recoil of fast neutrons or the scattering of the 4.4 MeV radiation (or both) can be used to tag neutron events. After such a high-energy event, the data acquisition can wait for a neutron capture signal with the characteristic 28 μ s time constant. Then the detection efficiency is simply the ratio of capture signals to neutron triggers; no knowledge of the source strength is required. The other advantage of the AmBe source is that the only gamma radiation associated with the ^{241}Am decay is at 60 keV and can be easily removed with a 1 or 2-mm-thick lead encapsulation.

The recent Bugey [21] experiment used AmBe to measure their neutron detection efficiency and claim a precision of 3%.

6.2 The Energy Calibration System

The energy scale of the detector response spectrum will be calibrated using the Compton edges of a number of γ emitters. A detailed description of this calibration method, including the procedure of assigning energy values to features of the Compton spectrum, is described in Section 4.5.1. The full detector should be calibrated once or twice a month, using some or all of the following γ emitters.

Source	γ Energy [keV]	Compton Edge [keV]
AmBe	4439	4197
^{232}Th	2614	2386
^{65}Zn	1119	911
^{54}Mn	842	646
^{137}Cs	662	478
^{22}Na	1274	1062
	511	341
^{203}Hg	279	146
^{57}Co	123	40

Since the radiation from some of these sources is quite low energy and not very penetrating, it is probably necessary to calibrate a group of no more than four cells at a time. One way to do this is to install a small acrylic or Teflon tube, perhaps 1 cm in diameter, in the center of each group of four cells in the detector (see Figure 6.1). Small, encapsulated sources could then be fed through the tube on a string and spectra acquired from the four surrounding cells. To fully instrument the 6 by 11 target cell array, 18 such tubes will be required. Running up to 8 sources through 18 calibration tubes can be quite time consuming and will probably necessitate automation of the system. It would not be difficult, for example, to construct a system of pulleys that could feed a source on one long string back and forth through all 18 calibration tubes. Between calibrations, the tube gains and scintillator transparency would be monitored using an LED system, such as the one described below.

6.3 The LED Gain Monitor

Each of the 66 target cells will be fitted with one or more LED's to allow monitoring of the phototube gains and to make interpolations of the energy scale between source calibration runs. The LED will be driven by a pulser which will also gate the ADC reading out the phototubes. A Gaussian fit to the LED spectrum allows determination

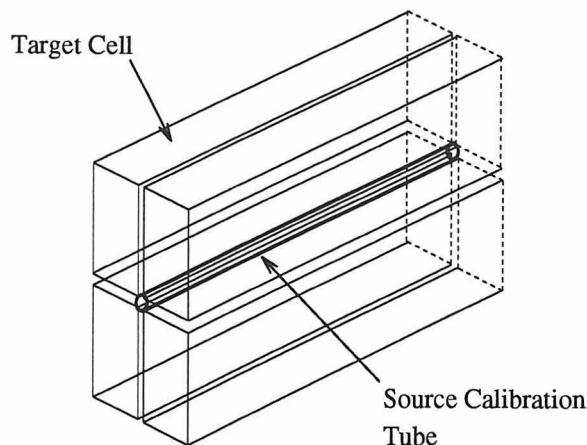


Figure 6.1: A group of four cells illustrating the placement of an energy calibration tube. To fully instrument the 66-cell detector, 18 such tubes would be required.

of the gain of the system as well as the number of photoelectrons per ADC channel:

$$G = \frac{\sigma^2}{P - ped},$$

and

$$N = \left[\frac{P - ped}{\sigma} \right]^2,$$

where P is the position of the LED peak, in ADC channels, ped is the measured ADC charge pedestal, σ is the Gaussian width of the LED peak, and G and N are the system gain and number of photoelectrons, respectively. The determination of these quantities is independent of the absolute LED intensity, i.e., it is not necessary that the LED pulse contain the same number of photons from run to run. However, it is necessary that the LED pulses be stable within a run. Any drifting of the LED output would cause artificial broadening of the peak and therefore an incorrect calculation of the gain and photoelectron calibration. For this reason it may be necessary to install a photodiode monitor next to each LED. Photodiodes are available that are stable to better than 1% and could be used, by reading out their voltage with another ADC, to monitor the intensity of the LED pulses. With such a stabilized light source, a shift in the position of the LED peak would be an immediate indication of a change in either the gain or in the number of photoelectrons generated at the phototube.

The quantities G and N , above, could then be calculated. For a change in G , the high voltage of the phototube would be adjusted to compensate for the gain drift. A change in N , however, cannot be compensated for as it would be caused either by a change in the transparency of the scintillator or by a degradation of the quantum efficiency of the phototube. In this case the LED data would be used to interpolate the calibration until the next radioactive source run which would reestablish the mapping of photoelectrons to energy.

Appendix A

Details on the Positron Detection Efficiency Calibration

A.1 Chemical Preparation of the Source

^{68}Ge is commercially available in the form of germanic acid carried in dilute hydrochloric acid. It can be converted to germanium tetrachloride (GeCl_4) by the addition of concentrated HCl sufficient to bring the solution to eight molar strength. In this form, it is soluble in pseudocumene, a benzene derivative which makes about 30% of the Palo Verde liquid scintillator. A local radiochemical company twice attempted to prepare a source in this manner, but in both cases the source was chemically unstable; a large fraction of the germanium activity would quickly adhere to the walls of the vessel containing it. See section 4.4 for a description of how this determination was made. A likely cause of this instability is the weakness of the Ge-Cl bond which probably caused the germanium to bond immediately with any oxygen present either in the walls of the vessel or in the water contaminating the liquid scintillator. To avoid this problem, the compound tetra-*n*-butylgermane, which saturates the germanium bond sites with relatively strong bonds, was synthesized [54]. Starting from radioactive ^{68}Ge in the form of carrier-free germanic acid in 0.5 M HCl, the tetra-*n*-butylgermane was synthesized as follows.

A.1.1 Isotope Exchange Procedure

Germanium tetrachloride is quite volatile and reacts violently with water. Therefore, all glassware that was to come in contact with the material was dried in an oven and sealed under nitrogen, and the germanium tetrachloride was handled only after being

cooled in an ice bath.

100 μl , corresponding to 100 μCi , of the radioactive germanium solution were added to a dry flask, sealed under nitrogen and cooled in an ice bath. To this solution was added 200 μl of concentrated hydrochloric acid to bring the solution to 8 M in HCl and convert the germanic acid to germanium tetrachloride. Approximately 0.5 g (270 μl) of stable germanium tetrachloride was added and the mixture stirred for 30 minutes in an ice bath to extract the radioactive ^{68}Ge into the GeCl_4 carrier. After stirring, the mixture was allowed to stand for several minutes after which 200 μl of GeCl_4 , now doped with ^{68}Ge , were extracted by syringe from the bottom of the flask with the intention of leaving most of the lighter HCl behind. Over 20% of the ^{68}Ge activity was extracted using this method.

A.1.2 Tetra-n-butylgermane Synthesis

The 200 μl (1.72 mmol) of GeCl_4 doped with ^{68}Ge were placed into a dried 100 ml flask, sealed under nitrogen and cooled in an ice bath. Figure A.1 depicts the apparatus. Through a rubber septum, 5 ml of hexane was injected by syringe to act as a medium for the reaction. While stirring, 7 ml (11.2 mmol) of a 1.6 M n-butyl lithium in hexane solution was slowly added by syringe to provide excess reagent for the synthesis of tetra-n-butylgermane (see Figure A.2). The reaction was stirred for 30 m in an ice bath and then allowed to warm to room temperature and was stirred for another hour. The flask was again cooled in an ice bath and 10 ml of distilled water were added and the mixture stirred vigorously for 10 m. Next the solution was transferred to a 100 ml separatory funnel and allowed to stand for several minutes while the immiscible liquids separated. The lower layer, consisting of water containing lithium chloride, was then drained from the funnel leaving behind the hexane containing the tetra-n-butylgermane. This washing was repeated with another 10 ml of distilled water and then once more, using a saturated sodium chloride solution (brine). Finally, the washed hexane solution was poured into a flask containing approximately two g of anhydrous magnesium sulfate (MgSO_4) and was stirred vigorously for about 20 m in

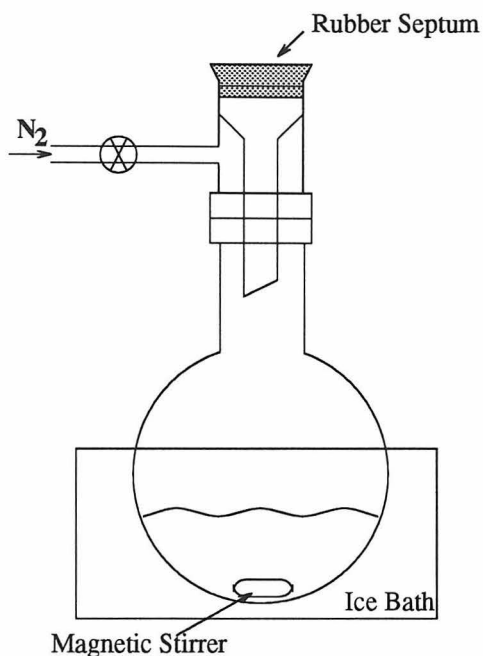


Figure A.1: Tetra-n-butylgermane synthesis apparatus.

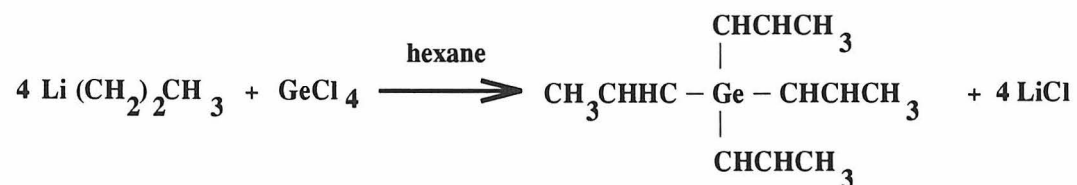


Figure A.2: Tetra-n-butylgermane synthesis reaction.

order to absorb the remaining water. The solution was poured through a fine fritted filter to remove the magnesium sulfate, and the hexane solution was collected in a flask. After collection, the filter still contained a significant amount of ^{68}Ge , so 10 ml of hexane was added to the filter for a second collection. The hexane solution was finally dissolved in about 50 ml of liquid scintillator to make the calibration solution. This solution contained a total of about $20 \mu\text{Ci}$ of ^{68}Ge , or 20% of the amount started with.

A.2 Effect of Ge Loading on Scintillator Properties

A sample of scintillator was prepared and loaded with germanium in the form of tetra-n-butylgermane at the level of 2 ppm. This concentration is approximately a factor of 1000 higher than that to be used in the actual calibration run. Measurements of the scintillator attenuation length and light yield were made to verify that the germanium compound does not affect the optical properties of the scintillator.

A.2.1 Attenuation Length

The attenuation length was measured using the apparatus pictured in Figure A.3. Light from a blue LED, driven by a pulser, passes through a 440 nm filter and then emerges through a small pinhole. The rays are focused to parallel by a 7-cm-focal-length lens placed one focal length away from the pinhole. The parallel beam shines down a 1.5 m hollow aluminum pipe with an inside diameter of about 3 cm. At the bottom of the pipe is a glass window behind which a photomultiplier tube detects the emerging light. Liquid scintillator is filled into the aluminum pipe, and the response of the phototube as a function of the height of the liquid gives a measure of the attenuation length at 440 nm. Data is acquired using a peak-sensing ADC gated by the trigger output of the pulser driving the LED. This method of gating is used to minimize the background from actual scintillation light produced by natural radioactivities. This background was measured with the tube full of scintillator by triggering on the pulser, but unplugging the LED, and was found to contribute less than a part in 10,000. Measurements of the LED peak position were made as the scintillator entered the tube at liquid heights of 20, 40, 60, 80, and 100 cm. The liquid was then drained out and measurements were made at 90, 70, 50, 30, and 20 cm. This staggering of points improved the immunity of the measurement to tube gain drifts or changes in LED light output. The data for the unloaded and loaded scintillator are displayed in Figure A.4. The attenuation lengths of both samples match to within

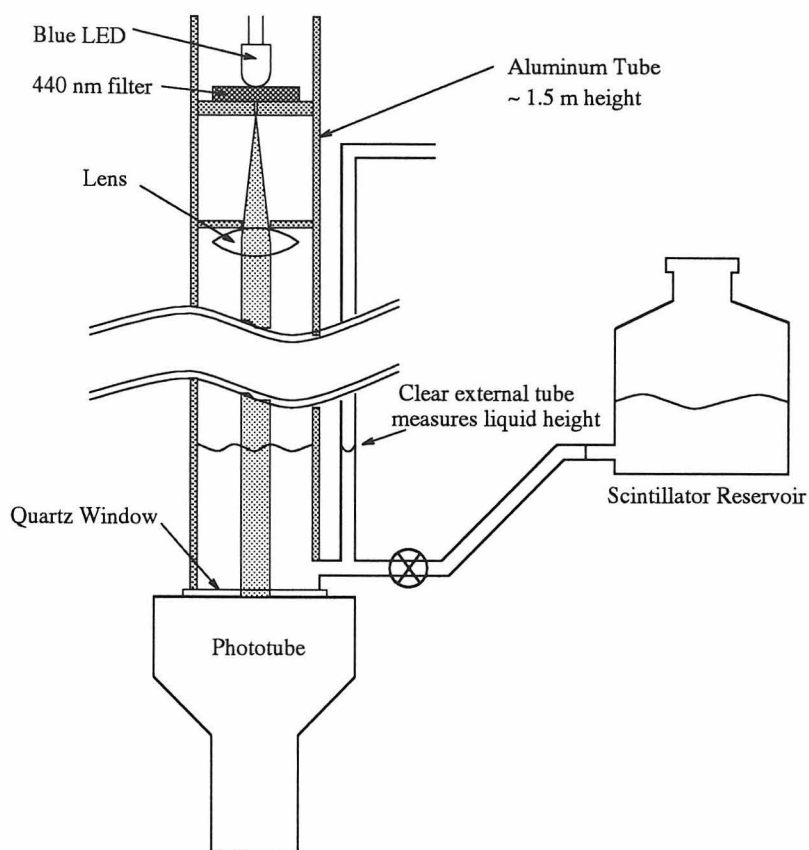


Figure A.3: Apparatus used to measure the attenuation length of liquid scintillator. The scintillator reservoir is raised or lowered and the stopcock opened to change the height of the scintillator in the aluminum measuring tube.

one standard deviation.

A.2.2 Light Yield

The light yield of the Ge-loaded and unloaded scintillators were compared using a simple apparatus. A small Pyrex petri dish, about 5 cm in diameter and 1 cm deep, was optically coupled to a three-inch phototube, oriented vertically. 20 ml of scintillator was then pipetted into the dish and a ^{207}Bi source, which emits 1.06 MeV conversion electrons, was placed above the scintillator. The phototube was then read out into a charge ADC. By comparing the position of the electron peak, which is proportional to the number of photoelectrons produced, using the Ge-loaded and unloaded scintillators, one can compare their relative light output. However, any

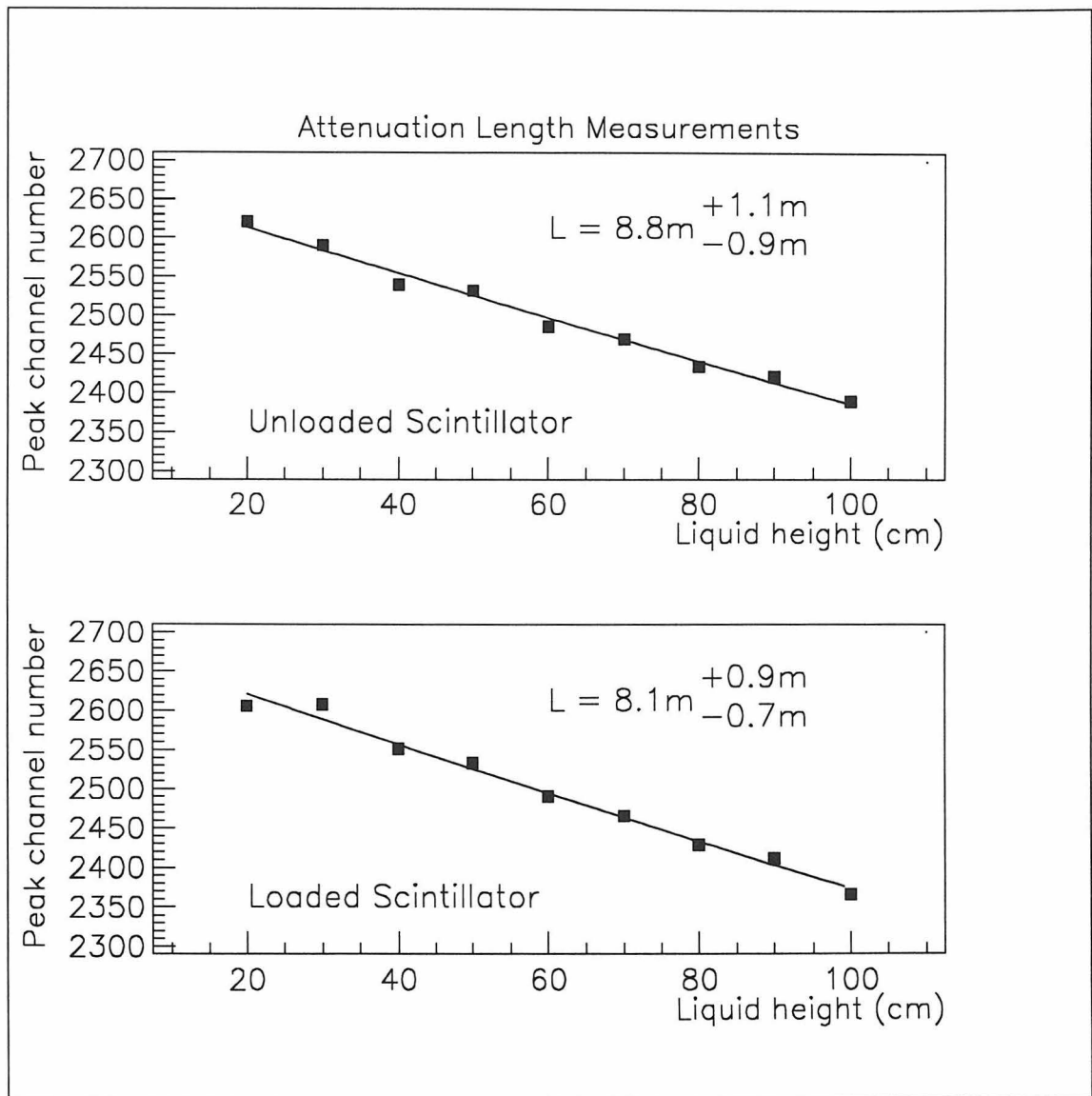


Figure A.4: Attenuation Length of Ge-loaded and unloaded scintillator. The top curve was measured with 1.4 liters of fresh scintillator. The sample was then loaded with tetra-n-butylgermane at the level of 2 ppm of germanium and remeasured. The bottom curve represents this measurement.

change in the phototube gain between the two measurements would cause a shift of the peak position unrelated to the light yield. So to monitor the tube gain, an LED, driven by a pulser, was positioned to shine onto the phototube. Then since the photoelectron distribution obeys Poisson statistics, which becomes essentially Gaussian for a mean value greater than 10 or so, the position of the LED peak will be directly proportional to the number of photoelectrons, N , and the width of the peak will be proportional to the square root of N . The constant of proportionality is just the overall system gain, G , which is a product of the phototube gain and the ADC conversion gain. Thus with a measurement of the LED peak position, P , in channels, and its full-width-half-maximum, $FWHM$, the system gain and number of photoelectrons produced by the LED can be characterized as follows:

$$P = G \cdot N + ped,$$

and

$$\sigma = \frac{FWHM}{2.35} = G \cdot \sqrt{N}.$$

So

$$G = \frac{\left(\frac{FWHM}{2.35}\right)^2}{(P - ped)},$$

and

$$N = \left[\frac{(P - ped)}{\left(\frac{FWHM}{2.35}\right)} \right]^2,$$

where ped is the measured ADC pedestal value. The ^{207}Bi spectra for the Ge-loaded and unloaded scintillator are shown in Figure A.5. Table A.1 summarizes the results. The light yield of the scintillator is unaffected by the addition of 2 ppm of germanium.

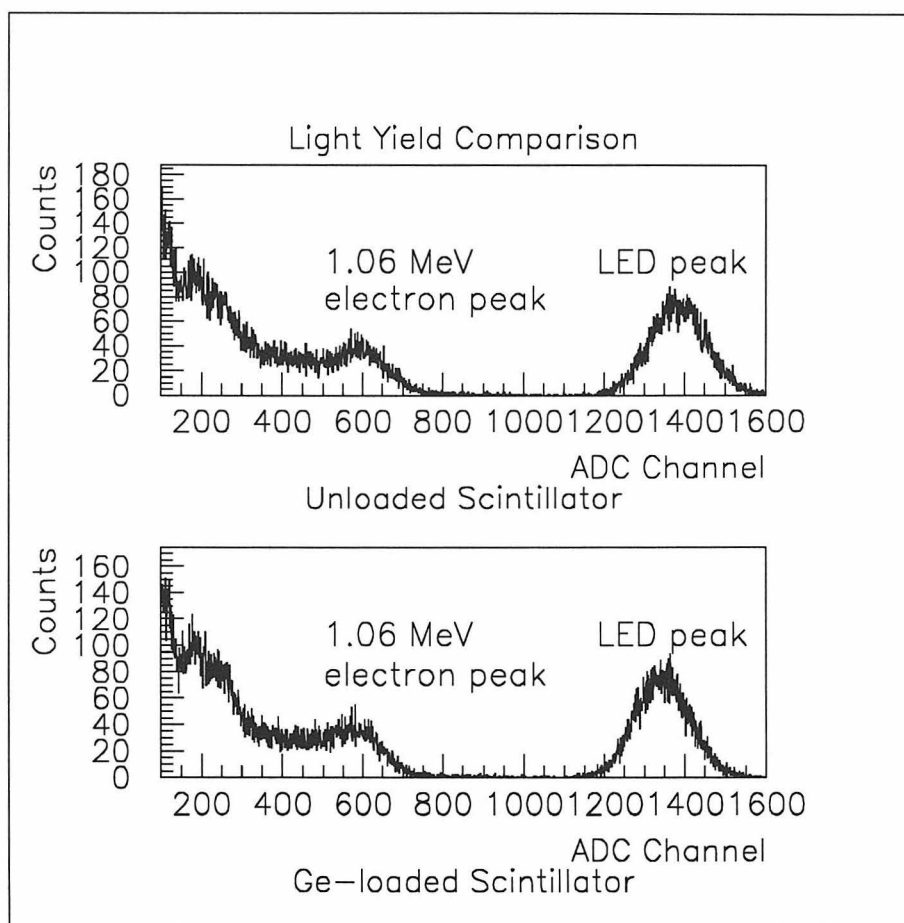


Figure A.5: Spectrum of ^{207}Bi measured using unloaded (top) and Ge-loaded (bottom) scintillator. The 1.06 MeV electron line is visible along with source-related Compton background. An LED was used to monitor the phototube gain and tuned to enter the spectrum well above the bismuth peak.

Table A.1: Results of a measurement of the light yield of unloaded and Ge-loaded scintillator. The (apparatus-dependent) number of photoelectrons per MeV deposited energy are compared and found to agree at the level of one standard deviation. The table summarizes the positions, in ADC channels, of the 1.06 MeV electron line and the LED peaks. The ADC charge pedestal was measured to be 31 channels.

Scintillator:	Unloaded	Ge-loaded
1.06 MeV Electron Line:	585 ± 10	580 ± 10
LED Peak:	1384 ± 1	1344 ± 1
LED Width (σ):	67.6 ± 1	67.1 ± 1
Number of LED Photoelectrons:	401	383
Gain (p.e. / channel):	0.296	0.292
Light Yield (p.e. / MeV)	155 ± 3	151 ± 3

Appendix B

Details of the Detector Simulation

B.1 The Tracking of Neutrons From the Walls

In calculating the neutron backgrounds, neutrons of discrete energies were generated uniformly in a 60-cm-thick concrete wall. It is important to verify that this production volume is sufficient, i.e., that neutrons from deeper in the walls cannot contribute to the background rate. To investigate this, the flux of neutrons exiting the laboratory walls was studied as a function of the production volume. Figure B.1 depicts the active wall volume as a function depth and neutron energy. It is clear from the plots that at large neutron energies (> 100 MeV) the flux of neutrons entering the lab levels off only at production depths of about 120 or 130 cm. However, the neutrons produced at depths of more than 60 cm in the wall are strongly degraded in energy by the time they enter the lab and are not as efficient at producing background as are the neutrons from the first few cm. In fact, 1000 MeV neutrons were generated uniformly in a wall 130 cm thick, and it was found that the induced background was the same as from a 60-cm wall. Thus the 60-cm production depth is determined to be sufficient.

As the neutrons are tracked toward the fiducial volume, histograms of the neutron kinetic energy and secondary gamma energy are produced at the entry point of several interesting volumes. The following table describes the volume names referred to in later figures:

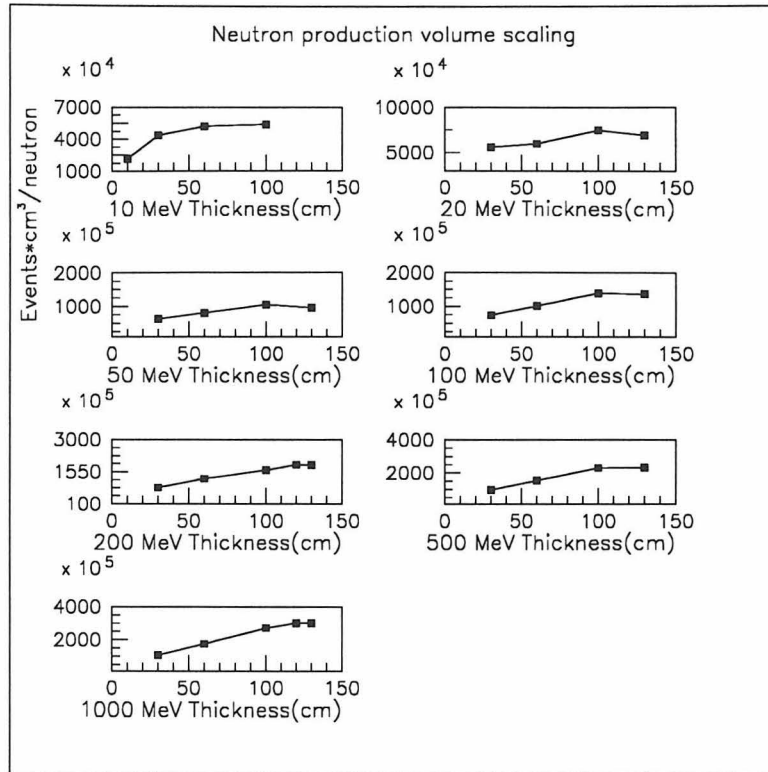


Figure B.1: The flux of neutrons entering the lab is plotted as a function of wall depth. It is found that the flux saturates at depths of about 120–130 cm for the highest energy neutrons. However, it is also determined that the extra flux generated by taking a thicker production volume does not affect the induced background rate because it is so strongly degraded.

Simulation Volumes

- ARM1* : The air inside the laboratory surrounding the entire detector.
- DDT1* : An imaginary surface just outside the muon veto cells.
- DDT2* : An imaginary surface between the muon veto cells and the buffer tanks.
- DDT3* : An imaginary surface enclosing the 9-m tanks (and their oil buffer end caps).
- Scintillator* : The active volume of the target cells (excludes oil, acrylic, air, etc.).

As an example of the neutron propagation from the walls, Figures B.2 and B.3 display neutron and gamma ray spectra due to 20 MeV neutrons produced in the walls.

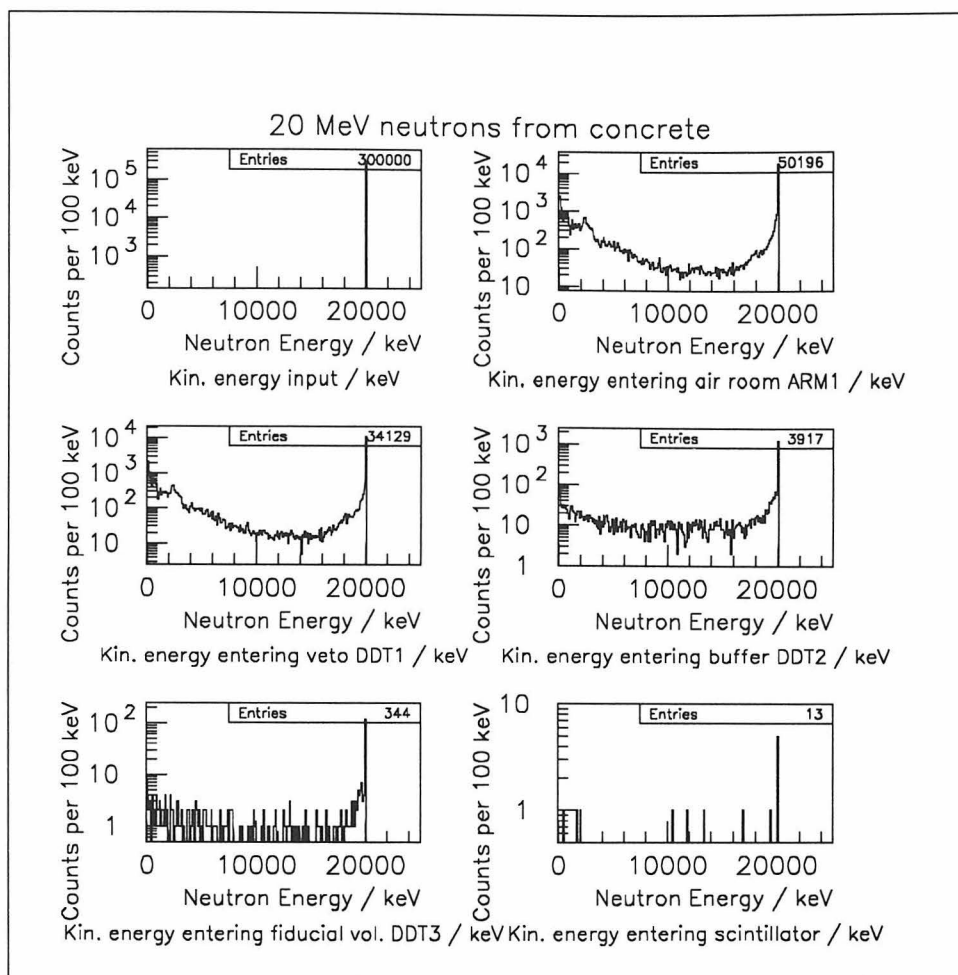


Figure B.2: An example of neutron propagation from the walls. 300,000 20-MeV neutrons are produced in the concrete walls. The neutron kinetic energy is histogrammed as it enters various volumes in the detector.

It is interesting to extract from this data the shielding power of the veto and passive buffer. Some of the reduction in flux between the various volumes is of course due to solid angle (surface area ratios). In order to isolate the real shielding factors of the veto and buffer, a simulation was run in which the veto scintillator, oil buffer, and water buffer were all replaced by air. The flux reductions in this case were assumed to be purely geometrical. The total reduction in flux with the buffers and veto full was then divided by this geometrical reduction factor to arrive at the true bulk shielding

factor for these materials as a function of energy. Figure B.4 displays these shielding factors for the 25-cm-thick veto and 100-cm-thick water buffer.

From the shielding factors and from the concrete production volume scaling, one can also extract approximate neutron removal cross sections. (Removal is defined here as degradation below 2 MeV). The results are approximate because an average thickness was used, and, except in the case of the concrete, the input spectrum is continuous rather than a delta function. (See Figure B.2, for example). But the results serve to show that the neutron removal lengths extracted are at least reasonable. Figure B.5 displays these results.

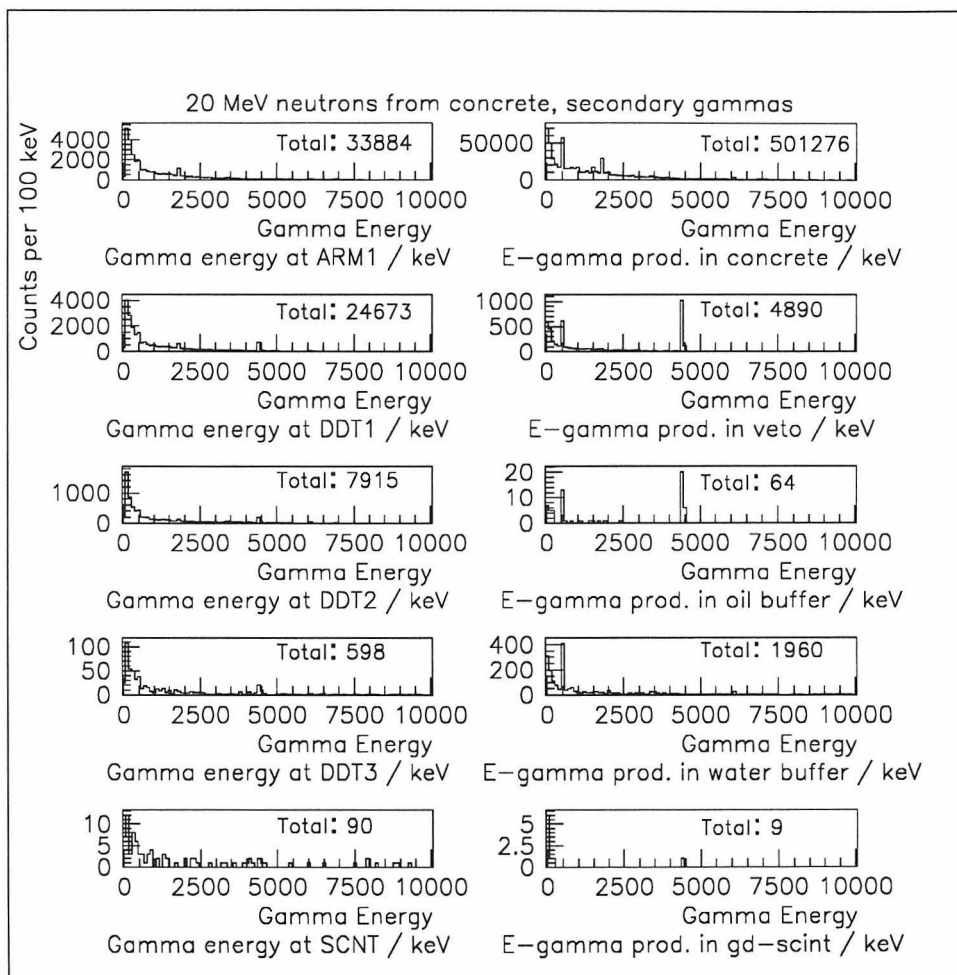


Figure B.3: An example of secondary gammas produced by neutrons from the walls. 300,000 20-MeV neutrons are generated in the concrete. The left column displays the energy of secondary gammas entering various detector volumes. The right column depicts the energy distribution of secondary gammas produced in each volume. The 4.4 MeV and 6 MeV gammas due to inelastic interactions with carbon and oxygen in the oil and water, respectively, are visible.

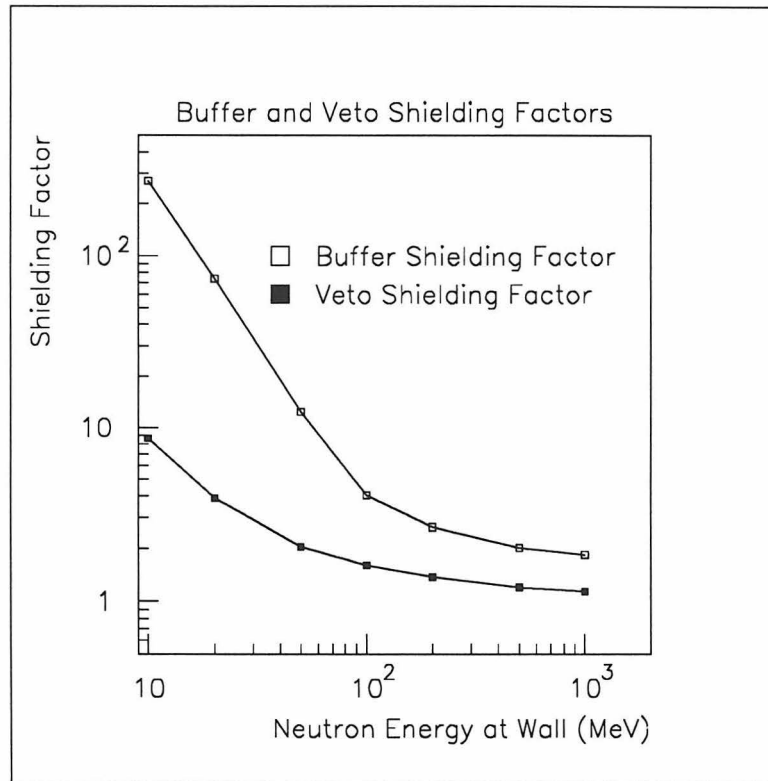


Figure B.4: The shielding factor due to the veto and buffer are displayed. The geometrical flux reduction has been factored out so the curves display true bulk flux removal. The average thickness of the veto is about 25 cm and the buffer, 100 cm.

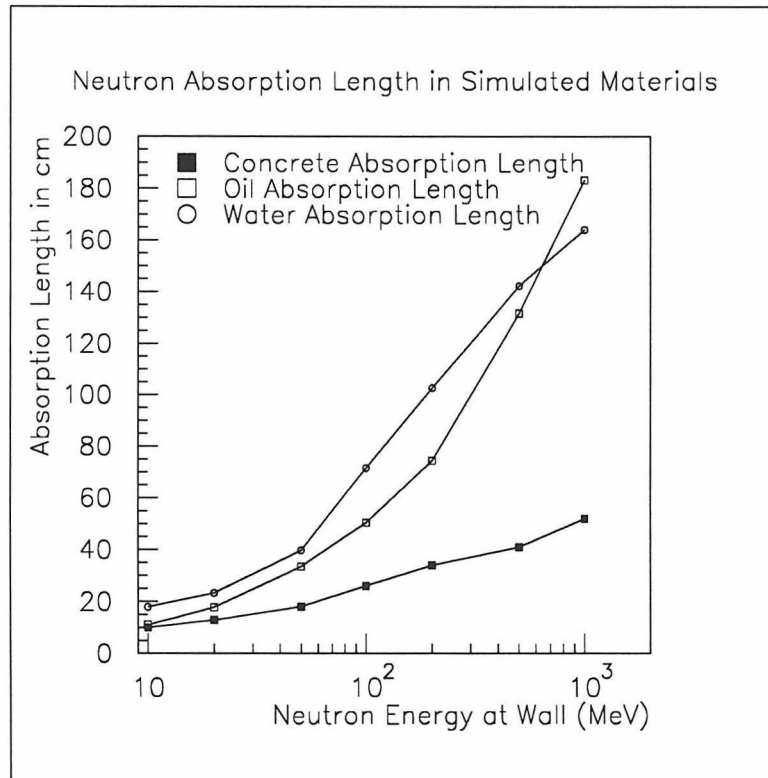


Figure B.5: Approximate neutron removal lengths for oil, water, and concrete extracted from the simulation. Oil and water show roughly the same absorption length, and that in concrete is shorter by a factor of 2 – 3, which is also the density ratio.

B.2 Analysis of the Neutron Spectra From Muon Capture and Spallation

B.2.1 Neutrons From Muon Capture

Neutrons of energy up to 100 MeV are produced by muon capture on nuclei in the laboratory walls. Following the discussion in [65], the neutron production rate can be calculated per kg of rock at the laboratory depth of 46 *mwe*:

$$P(\text{neutrons} \cdot \text{kg}^{-1} \cdot \text{d}^{-1}) = I_{\mu^-} \cdot f_c \cdot f_d \cdot f_n,$$

where

I_{μ^-} = Number of stopping μ^- per kg and day.

f_c = Elemental fractions in target material.

f_d = Fraction of μ^- 's captured (rather than decayed).

f_n = Neutron multiplicity per capture.

The μ^- stopping rate at 46 *mwe* is about 12 per kg and day [65]. Assuming that the concrete is composed mainly of SiO_2 , one can calculate the elemental fraction of oxygen and silicon:

$$(f_c)_j = \frac{a_j \cdot Z_j}{\sum_{i=1}^n a_i \cdot Z_i},$$

where a_j and Z_j are the atomic fraction and charge of the j^{th} element of the compound.

So

$$(f_c)_{Si} = \frac{14}{30} = 0.467, (f_c)_O = \frac{16}{30} = 0.533.$$

And from [65], the capture probabilities on O and Si are

$$(f_d)_{Si} = 0.6, (f_d)_O = 0.2,$$

and the average neutron multiplicity, f_n , is about 1.1. So the neutron production rate

is given by

$$P = I_{\mu^-} \cdot [(f_c)_{Si} \cdot (f_d)_{Si} + (f_c)_O \cdot (f_d)_O] \cdot f_n,$$

or

$$P = 5.1 \frac{\text{neutrons}}{\text{kg} \cdot \text{d}}.$$

The spectrum of these neutrons is measured [64] to go as

$$S(E) \equiv \frac{dN(E)}{dE} = e^{-E/10},$$

where E is the neutron energy measured in MeV. The mass of the production volume, 60 cm of concrete, is calculated to be $8.36 \cdot 10^5$ kg, resulting in $4.26 \cdot 10^6$ capture neutrons produced per day.

The background rate is then calculated by integrating the product of the normalized energy spectrum and the neutron triple coincidence efficiency curve (Figure 5.13). The triple efficiency curve is linearly interpolated such that the triple efficiency between two energies E_1 and E_2 is given by

$$\epsilon(E) = m \cdot E + b.$$

Then the number of background events, N_i , in this energy interval is given by

$$N_i = \int_{E_1}^{E_2} S(E) \cdot \epsilon(E) dE = -[(m \cdot E + 10 \cdot m + b) \cdot e^{-E/10}]_{E_1}^{E_2}.$$

For the same cuts used for the positron data analysis, this results in a background triple rate from muon capture of 3.5 triples per day. The delayed neutron capture is then detected with an efficiency of 68%. (The neutron is presumed to be contained). This gives a correlated background, due to neutrons from muon capture, of 2.4 per day. Figure B.6 shows the contribution of each energy bin to this total.

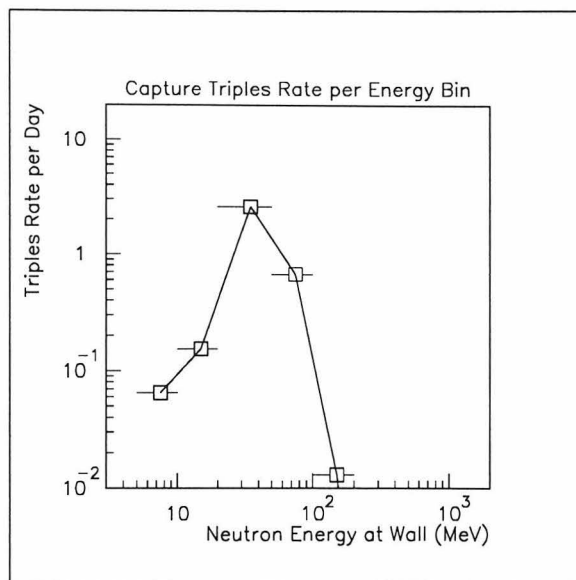


Figure B.6: Triples rate due to neutrons from muon capture as a function of energy in the laboratory walls.

B.2.2 Neutrons From Muon Spallation

Neutrons of several hundred MeV and beyond are produced by muon spallation of nuclei in the laboratory walls. The integral yield of such neutrons has been measured [66] at 20 *mwe* depth to be

$$Y \equiv (3.4 \pm 0.7) \cdot 10^{-5} \frac{n \text{ cm}^2}{\mu \text{ g}}.$$

This yield can then be integrated over all muon path lengths and normalized to the muon flux at 46 *mwe*, which is $14 \frac{\mu}{\text{m}^2 \cdot \text{sec}}$ through a horizontal surface, to arrive at a production rate in terms of neutrons per kg and day: first one relates the flux through a horizontal unit area, I_μ , to the flux per unit horizontal area and solid angle about the vertical, I_o :

$$I_\mu = \int_{\phi=0}^{2\pi} \int_{\theta=0}^{\pi/2} I_o \cdot \cos^2 \theta \cdot \cos \theta \cdot \sin \theta d\theta d\phi = \frac{2\pi}{4} I_o.$$

So at 46 *mwe*, $I_o = 8.9 \frac{\mu}{\text{m}^2 \cdot \text{s} \cdot \text{sterad}}$. Now consider a slab of horizontal area A , thickness d , and density ρ , such that the mass $M = \rho \cdot A \cdot d$ (see Figure B.7). Then the $\rho \cdot x$

path length of a muon traversing the slab at an angle θ with respect to the vertical is given by $\rho \cdot x = d / \cos \theta$. Thus the neutron yield per unit mass is given by

$$I_n = \frac{1}{M} \int_{\Omega} A \cdot I_o \cdot Y \cdot \frac{\rho \cdot d}{\cos \theta} \cos^3 \theta d\Omega = \frac{2\pi}{30} \cdot 86400 \cdot I_o \cdot Y,$$

or

$$I_n = 5.5 \frac{\text{neutrons}}{\text{kg} \cdot \text{d}}.$$

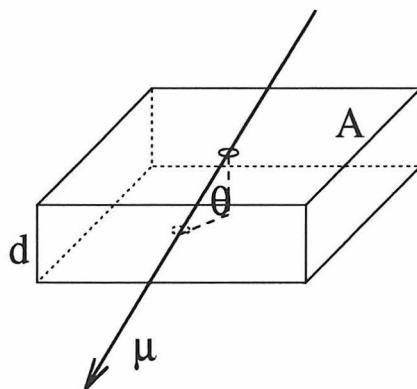


Figure B.7: Muon path lengths integrated over slab of mass M to calculate yield of spallation neutrons per kg and day.

The spectral shape of the neutrons emitted by muon spallation is a matter of some uncertainty. S. Hayakawa [67] finds the differential spectrum of neutrons produced by muons underground to fall off as E^{-2} up to several hundred MeV. J.C. Barton [68] presents a measurement of muon-induced neutrons and states that “neutrons ... fall off as $E^{-0.5}$ between 10 and 50 MeV but more rapidly at higher energies ...” D.H. Perkins [69] presents a calculation of backgrounds in the Soudan 2 detector in which he finds the spectrum of neutrons produced by inelastic muon interactions to fall off as $E^{-1.6}$. A calculation by O.G. Ryazhskaya [70] presents a neutron spectrum falling as E^{-1} up to 200 MeV and steepening to E^{-2} at higher energies. And a measurement by the KARMEN collaboration [71] finds that the spectrum of neutrons from muon interactions fits an exponential spectrum, $e^{-E/39 \text{ MeV}}$.

From a purely mathematical point of view, convergence of the spectrum of neutrons requires that it be flatter than E^{-1} as E approaches 0, and steeper than E^{-1} at large energies. In addition, any spectrum falling more slowly than E^{-2} will have infinite average energy, suggesting that the spectrum must be cut off or fall very steeply at some high energy. As a constraint on the average neutron energy, one can consider the total muon energy loss due to hadronic processes, governed by the formula

$$\frac{dE}{dx} = -bE \text{ [72]}$$

where b is approximately equal to $5 \cdot 10^{-7}$ per g/cm^2 . An average muon energy of about 12 GeV at 46 *mwe* then results in about $6 \cdot 10^{-3}$ MeV loss per g/cm^2 . Comparing this to the neutron production rate of $3.4 \cdot 10^{-5}$ neutrons per g/cm^2 gives an average energy per neutron of about 170 MeV, assuming all of the energy goes to producing neutrons. In fact, a good fraction of the energy probably goes to producing hadronic jets, mesons, etc., so one can probably state that the average energy of neutrons from spallation should be some tens of MeV.

For the purpose of background estimation, several candidate spallation spectra were chosen based on the above constraints. In the case of power-law spectra, it was assumed that the spectrum first falls slowly then changes discontinuously to a steeper power at some “kink” energy. The spectra were assumed to fall abruptly to zero above 1000 MeV, the largest neutron energy simulated. The following table and Figure B.8 summarize the spectra simulated.

E^{-p1} $0 < E < kink$	Kink Energy (MeV)	E^{-p2} $kink < E < 1000$	Average Energy (MeV)
-0.5	10	-1.6	40 MeV
-0.5	50	-1.6	133 MeV
-1	200	-2	5 MeV
$e^{-E/39\text{MeV}}$ (KARMEN)			40 MeV

The average energies of the above power-law spectra are a function of the upper energy cutoff of 1000 MeV. From the above table one can conclude that extending

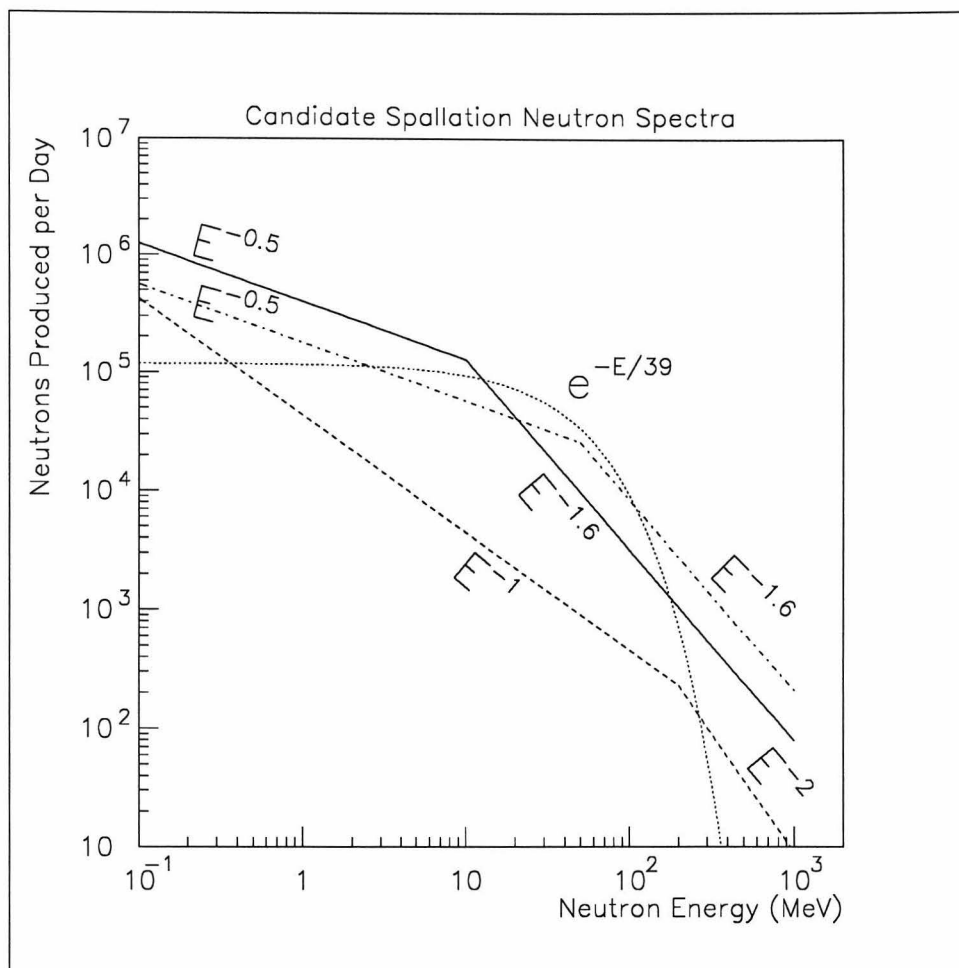


Figure B.8: Candidate neutron production spectra from muon spallation. Three differential power-law spectra are shown with low-energy power, kink, high-energy power parameters of $-0.5, 10, -1.6$; $-0.5, 50, -1.6$; and $-1, 200, -2$. The exponential spectrum measured by KARMEN [71] is also shown with neutron energy going as $e^{-E/39\text{MeV}}$. All spectra are normalized to neutrons produced per day.

the neutron spectra to 1000 MeV is sufficient and perhaps conservative. One might also conclude that the Ryazhskaya spectrum places too many neutrons at low energy, though this is a very approximate constraint.

The background rates were estimated as for the neutrons from muon capture: the triple efficiency curve was linearly interpolated and integrated with the spallation neutron spectrum. The production volume is calculated to be $8.36 \cdot 10^5$ kg, resulting in $4.60 \cdot 10^6$ spallation neutrons produced per day. The number of triple coincidences per day, N_i , produced by neutrons having energy between E_1 and E_2 in the walls is

given by

$$N_i = \left[a_1 \cdot m \cdot \frac{E^{-b_1+2}}{2-b_1} + a_1 \cdot b \cdot \frac{E^{-b_1+1}}{1-b_1} \right]_{E_1}^{E_2}$$

where a_1 is the normalization factor, b_1 is the relevant energy power, and m and b are the slope and intercept of the efficiency interpolation. For the case of the KARMEN [71] exponential fit, the integral is similar to that of the capture neutrons.

Following a triple coincidence, the neutron must capture on gadolinium and be detected. As for the case of the neutrons from muon capture, this efficiency is taken to be 68%. Table B.1 summarizes the background due to spallation neutrons, and Figure B.9 breaks down the spectral contributions. A contour plot is shown in Figure B.10 to illustrate the rate dependence on the spectral parameters.

Table B.1: Background due to neutrons created by muon spallation in the laboratory walls. Four candidate spallation spectra are shown to indicate the sensitivity of this rate to the spectral shape.

E^{-p_1} $0 < E < kink$	Kink Energy (MeV)	E^{-p_2} $kink < E < 1000$	Correlated Events Per Day
-0.5	10	-1.6	29
-0.5	50	-1.6	75
-1	200	-2	5
$e^{-E/39MeV}$ (KARMEN)			30

B.2.3 Leakage Through the Veto

Neutrons produced by muon spallation and muon capture in the interior volumes of the detector are also a source of correlated background if the parent muon manages to leak through the veto undetected. To estimate this contribution, monoenergetic neutrons of the same energies as above were generated in the veto, buffer, fiducial volume, and structural steel of the detector. The total mass of this production volume is $1.74 \cdot 10^5$ kg, the majority water and oil. The spallation neutron production yield is again $5.5 \text{ n kg}^{-1} \text{ d}^{-1}$, resulting in $9.6 \cdot 10^5$ neutrons per day. The capture neutron

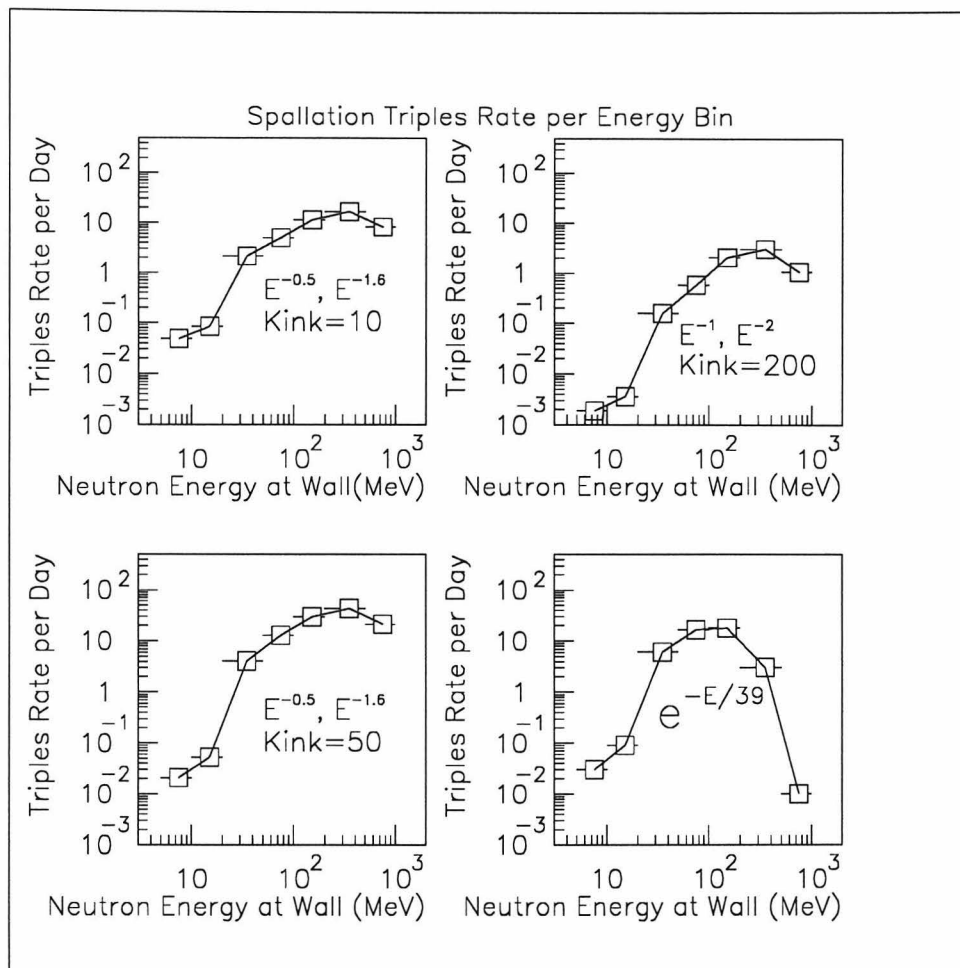


Figure B.9: Triples rate due to neutrons from muon spallation. The spectral contribution to the triples rate is shown for spallation neutrons for each of the four candidate spectra. The contribution of neutrons above 1000 MeV would appear to be non negligible, but consideration of the average neutron energy indicates that cutting off the neutron spectrum at 1000 MeV is probably a good approximation.

production rate is calculated, again following [65], to be $2 \text{ n kg}^{-1} \text{ d}^{-1}$ for H_2O and $1 \text{ n kg}^{-1} \text{ d}^{-1}$ for CH_2 . The ratio of water to oil in the interior production volume is about 1.7 to 1, so we take an average production rate of $1.6 \text{ n kg}^{-1} \text{ d}^{-1}$, giving $2.8 \cdot 10^5$ neutrons per day from muon capture. The background rates are calculated using the same procedure as for neutrons from the walls.

Triple coincidences produced by these neutrons contribute to the correlated background only if the parent muon is undetected. The inefficiency of the muon veto is dominated by leakage through regions of inactive material and cracks in the coverage.

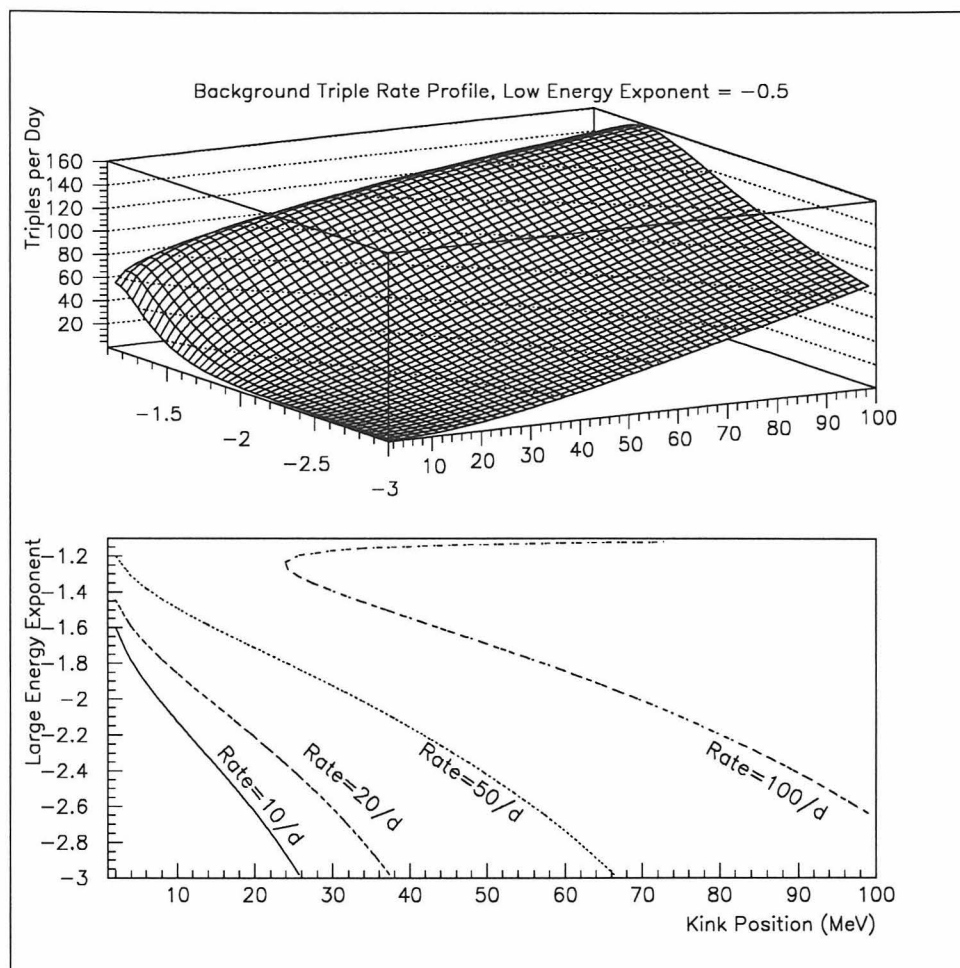


Figure B.10: Contour plot of the background triple rate due to neutrons from muon spallation. The triple rate is plotted as a function of the high-energy exponent and kink position. The low-energy exponent is assumed here to be -0.5 . The lower figure displays contours of constant triple rate. To calculate the correlated background rate, the triples rate should be multiplied by 68%.

A pessimistic estimate of the leakage can be made by taking the ratio of inactive to active surface area and assuming all incident muons arrive parallel to the crack. This results in a leakage rate of about 2%. In the case of neutrons from muon spallation, the muon survives and thus must both enter and exit the detector undetected to be missed. The probability of this occurring is then $4 \cdot 10^{-4}$. In the case of muon capture, the muon disappears and thus must be missed only on entry to be undetected. This probability is then 2%.

In some cases the parent muon may hit the fiducial volume. In this case it is

assumed that the muon is detected because of the large energy deposit in the target cells: as each neutron is simulated, a muon track is generated and a calculation is made to determine whether the muon has hit the fiducial volume. Table B.2 summarizes the results of this calculation: a 98% hermetic veto will allow less than 1 event per day due to neutron production inside the detector by unvetoes muons. If the flag tagging fiducial volume hits is ignored, the rate climbs up by a factor of about 10, but this rate is still small compared to other correlated backgrounds.

Table B.2: Background rate from neutrons produced inside the detector by muons leaking through the veto. The veto is pessimistically assumed to be only 98% hermetic, i.e., a muon has a 2% chance of leaking into or out of the detector without being detected. The worst-case spallation spectrum is assumed: $E^{-0.5}$ from 0–50 MeV, and $E^{-1.6}$ from 50–1000 MeV. A 68% neutron capture detection efficiency is assumed.

Neutron Source	Correlated Events Per Day No Veto	Correlated Events Per Day 98% Hermetic Veto
Spallation	239 / day	0.09 / day
Capture	20 / day	0.4 / day

B.3 Modeling Radioactive γ Cascades

The simulation of natural radioactivity in the laboratory walls and detector structure requires an accurate description of the γ energy spectrum as well as the multiplicity distribution. The radioisotopes investigated, ^{40}K , ^{232}Th , ^{238}U , ^{222}Rn , and ^{60}Co , have complex decay schemes, in some cases including several radioactive daughters. In many cases the nuclei de-excite through intermediate levels, producing several gammas in coincidence and enhancing the probability of mimicking a positron signal in the detector. Thus any accurate estimate of the background rate must include a treatment of multiple-gamma cascades. The full decay schemes of the various isotopes were compiled from the data in [74]. The intensity of each gamma line with a total branching greater than 1% and energy greater than 100 keV was divided between all cascades in which it appeared, and a cascade probability table was calculated. Tables B.3, B.4, B.5, B.6, and B.7 report the cascade probabilities calculated and used in the simulation. At each vertex generated, a cascade was picked randomly according to the probability distribution. The simulation parameters were then saved until all gammas in the chosen cascade had been tracked such that all energy deposits were summed as if the cascade had been a single event. Each isotope and each material was simulated independently to allow subsequent calculation of the background from any combination of contaminants in the material.

Table B.3: Cascade probability table for the ^{238}U decay chain. The absolute intensity of each gamma line is divided among all cascades in which it participates.

^{238}U Cascade Probability Table		
Cascade Probabilities Listed per 100 ^{238}U Decays		
Cascade Gamma Energies	Cascade Probability	Gamma Multiplicity
186 keV	3.3	3.3
352 keV	36.7	36.7
295 keV	18.9	18.9
242 keV	7.6	7.6
2448 keV	1.55	1.55
2204 keV	5.0	5.0
2119 keV	1.21	1.21
1509, 609 keV	2.23	4.46
1408, 609 keV	2.5	5.0
1402, 609 keV	1.4	2.8
1281, 609 keV	1.5	3.0
1847 keV	2.1	2.1
1238, 609 keV	5.9	11.8
1764 keV	15.8	15.8
1120, 609 keV	15.0	30.0
1729 keV	3.03	3.03
1661 keV	1.15	1.15
934, 609 keV	3.2	6.4
1378 keV	4.12	4.12
806, 609 keV	1.23	2.46
769, 609 keV	4.9	9.8
665, 609 keV	1.6	3.2
609 keV	6.6	6.6
TOTAL Multiplicity: 185.98 γ 's per 100 ^{238}U decays		

Table B.4: Cascade probability table for the ^{232}Th decay chain. The absolute intensity of each gamma line is divided among all cascades in which it participates.

^{232}Th Cascade Probability Table		
Cascade Probabilities Listed per 100 ^{232}Th Decays		
Cascade Gamma Energies	Cascade Probability	Gamma Multiplicity
1630 keV	1.5	1.5
1588 keV	3.5	3.5
1459 keV	0.9	0.9
969 keV	11.6	11.6
463, 969 keV	4.6	9.2
911 keV	27	27
836 keV	1.7	1.7
328, 795, 338 keV	2.24	6.72
328, 975, 209 keV	0.8	2.4
795, 338 keV	0.99	1.98
795, 209 keV	0.36	0.72
338 keV	8.67	8.67
773 keV	1.6	1.6
409, 964 keV	2.05	4.1
964 keV	2.65	2.65
270 keV	3.61	3.61
209 keV	3.13	3.13
241 keV	3.9	3.9
238 keV	43.5	43.5
300 keV	3.3	3.3
785, 727 keV	1.1	2.2
727 keV	5.2	5.2
1621 keV	1.5	1.5
511, 583, 2614 keV	7.75	23.25
860, 2614 keV	4.3	8.6
277, 583, 2614 keV	2.44	7.32
583, 2614 keV	20.7	41.4
TOTAL Multiplicity: 231.15 γ 's per 100 ^{232}Th decays		

Table B.5: Cascade probability table for the ^{222}Rn decay chain. The absolute intensity of each gamma line is divided among all cascades in which it participates.

^{222}Rn Cascade Probability Table		
Cascade Probabilities Listed per 100 ^{222}Rn Decays		
Cascade Gamma Energies	Cascade Probability	Gamma Multiplicity
352 keV	36.7	36.7
295 keV	18.9	18.9
242 keV	7.6	7.6
2448 keV	1.55	1.55
2204 keV	5.0	5.0
2119 keV	1.21	1.21
1509, 609 keV	2.23	4.46
1408, 609 keV	2.5	5.0
1402, 609 keV	1.4	2.8
1281, 609 keV	1.5	3.0
1847 keV	2.1	2.1
1238, 609 keV	5.9	11.8
1764 keV	15.8	15.8
1120, 609 keV	15.0	30.0
1729 keV	3.03	3.03
1661 keV	1.15	1.15
934, 609 keV	3.2	6.4
1378 keV	4.12	4.12
806, 609 keV	1.23	2.46
769, 609 keV	4.9	9.8
665, 609 keV	1.6	3.2
609 keV	6.6	6.6
TOTAL Multiplicity: 182.68 γ 's per 100 ^{222}Rn decays		

Table B.6: Cascade probability table for ^{40}K decay. The absolute intensity of each gamma line is divided among all cascades in which it participates.

^{40}K Cascade Probability Table		
Cascade Probabilities Listed per 100 ^{40}K Decays		
Cascade Gamma Energies	Cascade Probability	Gamma Multiplicity
1461 keV	10.5	10.5
TOTAL Multiplicity: 10.5 γ 's per 100 ^{40}K decays		

Table B.7: Cascade probability table for ^{60}Co decay. The absolute intensity of each gamma line is divided among all cascades in which it participates.

^{60}Co Cascade Probability Table		
Cascade Probabilities Listed per 100 ^{60}Co Decays		
Cascade Gamma Energies	Cascade Probability	Gamma Multiplicity
1773, 1332 keV	100	200
TOTAL Multiplicity: 200 γ 's per 100 ^{60}Co decays		

Appendix C

Tests of Neutron Tracking with GEANT–GCALOR

C.1 Summary

The GEANT–GCALOR [57] package was selected to model the interaction of neutrons in the Palo Verde neutrino oscillation detector. A comparison of calculations made with this code and experimental results from a number of published papers is presented. The code is found to be unsuitable for the tracking of neutron beams through thick targets because of approximations made in the cross sections above 20 MeV. However, these approximations do not appear to affect the modeling of neutron energy loss in liquid scintillator. Neutron light production in liquid scintillator was modeled for a number of detector geometries and for neutron energies ranging from 10 MeV to 400 MeV. The calculations were found to agree with the experimental data to about 30%.

C.2 Introduction

Tests of the GEANT–GCALOR neutron code were performed in two parts: the first investigated neutron tracking by modeling the scattering of a neutron beam traversing thick (10 – 100 cm) slabs of iron and concrete. The second investigated detector response by modeling scintillation light production by neutrons. The former is relevant to the propagation of neutrons from production sites in the earth into the detector fiducial volume while the latter is relevant to the detection of background events in the scintillator.

C.3 Neutron Transport Through Concrete and Iron

The transport of neutrons through thick concrete and iron was studied by modeling the experiment of Ref. [79]. In this experiment, the attenuation of quasi-monoenergetic neutron beams traversing concrete and iron slabs is investigated. A narrow, collimated beam of neutrons is incident on a thick slab, and a small detector is placed downstream at zero degrees to the incident beam angle. The detector subtends about 2% of the solid angle from the end of the scatterer. At the neutron energies used, 22 and 32.5 MeV, I found that the simulation showed consistently more neutrons detected downstream than did the experiment. Figure C.1 illustrates a comparison of GEANT-GCALOR and experiment for 32.5 MeV neutrons traversing concrete and iron. A large discrepancy exists between the simulation and the experiment and appears to be due to an underestimation of the total interaction cross section modeled by GCALOR. By tracking neutrons through iron and noting the distance at which the first interaction of any type took place, I extracted the total input cross sections which are compared with experimental data [80] obtained from the BNL NNDC data base (see Figure C.2).

From Figure C.2 it is evident that above 20 MeV a significant fraction of the total cross section is missing. This is also the point at which tracking is passed from the low-energy MICAP package to the NMTC package. This problem was discussed with GCALOR authors Christian Zeitnitz and Tony Gabriel [81, 82]. The authors indicated that the missing cross section is the elastic portion which is implemented above 20 MeV only for hydrogen and helium. The reason this approximation was made is that above 10 MeV or so, the neutron elastic cross section is very forward peaked. Thus neutron elastic scattering at high energy produces only small angular deviations and small energy losses (especially for the heavier elements). So effectively, this approximation replaces small angle scatters with propagation without interaction.

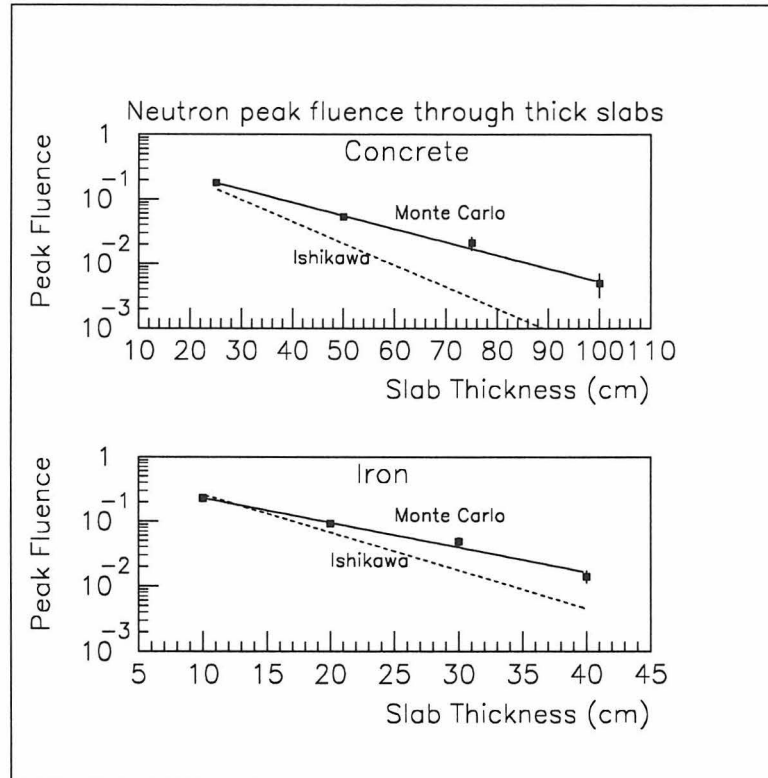


Figure C.1: The peak fluence of neutrons traversing slabs of concrete (top) and iron (bottom) is plotted. The fraction of neutrons emerging from the slab and detected in a downstream detector subtending 2% of 4π is plotted along the y axis. The GEANT-GCALOR simulated data for concrete is fit to an attenuation length of 21.7 cm as compared to the experimental value of 12.9 cm. For iron, GEANT-GCALOR gives 11.5 cm compared to the experimental 7.4 cm.

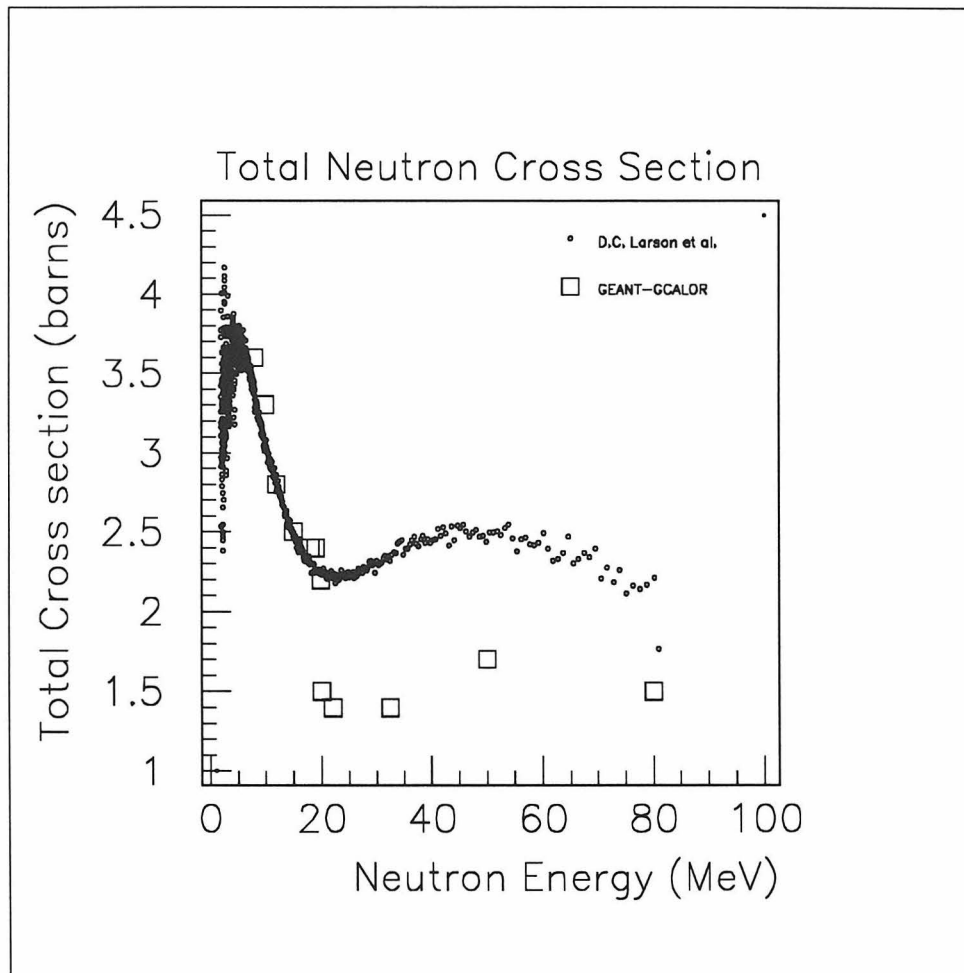


Figure C.2: Total Neutron Cross Section on Iron. Points extracted from a GEANT-GCALOR simulation are compared with experimental data.

C.3.1 Effect on the Palo Verde Detector Simulation

It is clear from Figure C.1 that these approximations made in GCALOR do not allow for reliable tracking of neutron beams where scattering at small angles is certainly important in removing collimated flux. However, in the case of the bulk attenuation of a relatively isotropic neutron source, this approximation seems quite reasonable. Since little energy is lost in forward scattering, the net effect of this cross section, had it been included, would be to further randomize a momentum distribution that was random to begin with. So this will not likely cause problems in tracking neutrons produced in the underground laboratory walls as they make their way towards the detector. The angular distribution of neutrons following muon spallation is unknown but is probably either isotropic or somewhat peaked in the direction of the parent muon. In any case the overall effect is a fairly uniform or somewhat downward-going distribution of neutron momenta that would remain essentially unchanged on average by the inclusion of small angle elastic scattering. As neutrons are tracked toward the fiducial volume, neutrons that should have been kicked away by small angle elastic collisions will be compensated for by those that would have been kicked toward the detector by the same process.

C.4 Neutron Detection Efficiency of Liquid Scintillator

The GEANT-GCALOR code was used to model the response of several different liquid scintillation detectors to incident neutrons. The calculations were compared with experimental data for neutron energies ranging from 10 to 400 MeV.

C.4.1 Neutron Light Production in Scintillator

Liquid scintillators are generally calibrated using gamma emitters: the intensity of light produced is measured as a function of energy deposited by ionizing Compton electrons. Neutrons, however, lose energy through interactions with nuclei, and in

many cases light is generated by ionizing heavy particles such as protons or alphas. These heavy particles, particularly if stopped in the scintillator, ionize more strongly than do electrons, and the resulting high ionization density in the scintillator leads to quenching of scintillation light. This causes less light on average to be produced for the same energy loss by heavy particles. Thus to model light production by neutrons, it is necessary to correct deposited energy for this scintillation light quenching. A subroutine was written to convert energy loss into light output at each tracking step using the semi-empirical model of Ref. [83]. The differential light yield as a function of the particle type and the differential energy loss was parameterized as follows:

$$\frac{dL}{dx} = \frac{dE}{dx} [1 + K(\frac{dE}{dx}) + C(\frac{dE}{dx})^2]^{-1}$$

where constants K and C were fit to experimental data for various particle types. The following table summarizes the energy loss mechanisms of neutrons in scintillator along with the ionizing secondary particle type.

<i>Neutron energy loss and light production</i>	
Interaction	Ionizing Particle
$^{12}\text{C}(n, n'\gamma)^{12}\text{C}$	e (Compton)
elastic np scattering	p
$^{12}\text{C}(n, p)^{12}\text{B}$	p
$^{12}\text{C}(n, d)^{11}\text{B}$	d
$^{12}\text{C}(n, t)^{10}\text{B}$	t
$^{12}\text{C}(n, \alpha)^9\text{Be} \rightarrow n2\alpha$	α

Other processes producing heavier particles are possible, such as the elastic scattering of neutrons on carbon nuclei. However, the recoil energy of these heavier nuclei is quite small, and in addition, the quenching is so strong that any light from these processes can be neglected [83]. The following table lists the fitted constants used to convert deposited energy to light production in electron-equivalent MeV.

Particle	Energy [MeV]	K [g cm ⁻² MeV ⁻¹]	C [g ² cm ⁻⁴ MeV ⁻²]
Proton	10 – 56	87 · 10 ⁻⁴	5 · 10 ⁻⁶
Proton	0.2 – 15	74 · 10 ⁻⁴	15 · 10 ⁻⁶
Deuteron	26 – 42	69 · 10 ⁻⁴	2 · 10 ⁻⁷
Triton	20 – 36	40 · 10 ⁻⁴	28 · 10 ⁻⁶
Alpha	30 – 46	46 · 10 ⁻⁴	14 · 10 ⁻⁷

Neutrons in the Palo Verde detector are simulated up to energies of several hundred MeV, beyond the fitted range here, but it is reasonable to extend the conversion parameterization to higher energies as it is asymptotically flat and in fact shows very little curvature above a few tens of MeV. Figure C.3 illustrates a comparison of simulated and experimental data using the above light yield parameterization.

C.4.2 Neutron Detection Efficiency

The detector response modeling and energy loss simulation were tested by comparing GEANT–GCALOR calculations with a number of published experimental measurements of neutron detection efficiencies [84, 85, 86, 87]. In all cases, Nuclear Enterprises NE213 liquid scintillator was used (density = 0.874 g/cc, H/C = 1.213). The experimental detector geometry and incoming flux of neutrons was modeled using GEANT–GCALOR. The detection efficiency, defined as the number of events with energy deposit exceeding some energy threshold normalized to the number of incident neutrons, was calculated and compared with experiment. A brief description of each experiment follows, and a graphical comparison with the simulation is displayed in figures C.4, C.5, C.6, and C.7.

The experiment of Ref. [84] was performed at the Los Alamos National Laboratory. Neutrons up to 32 MeV were produced by bombarding tritium and deuterium targets with protons accelerated in a Van de Graff tandem. Neutrons up to several hundred MeV were produced at LAMPF by the bombardment of thin metal foils with 800 MeV protons. The neutron energy was determined by time of flight (TOF). In all cases,

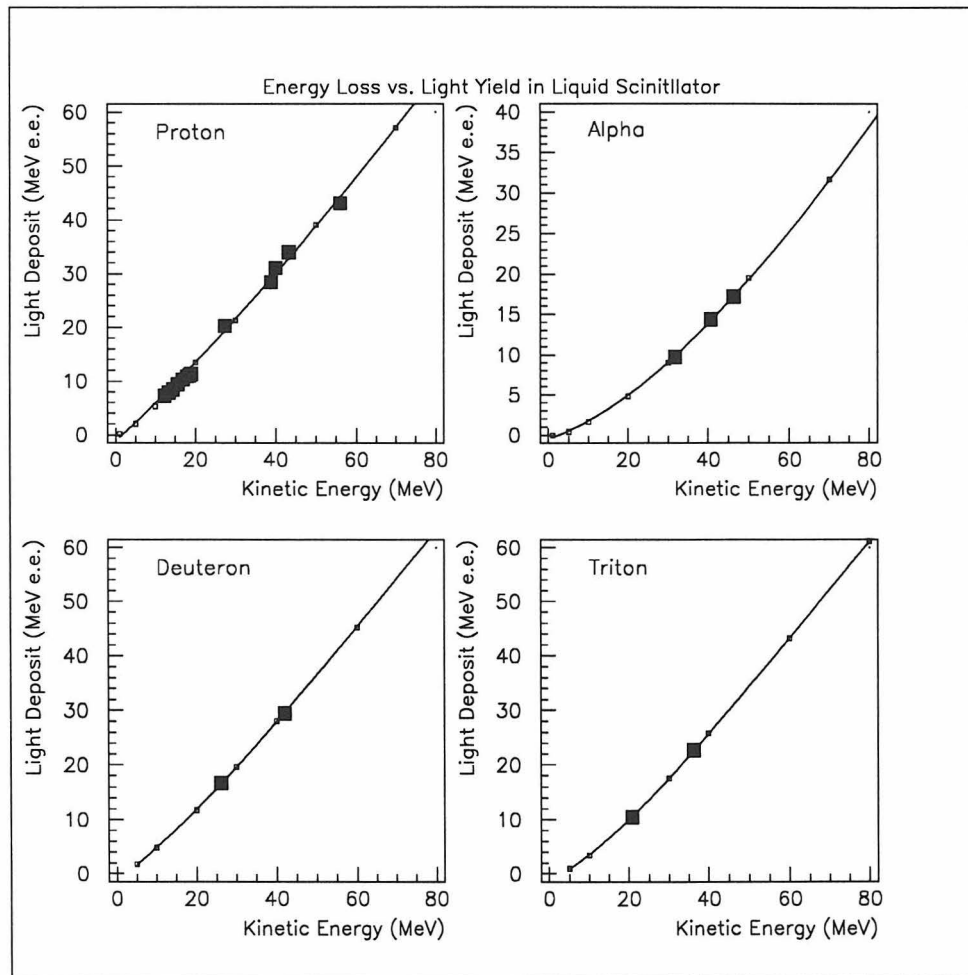


Figure C.3: Light production in electron-equivalent MeV of secondary particles from neutron interactions in liquid scintillator. Large filled squares are experimental data; small open symbols and the fitted curve are simulated data.

the collimated neutrons were detected in a 5.1 cm diameter by 2.5 cm thick NE213 liquid scintillation detector, and the absolute detection efficiency was measured for several energy thresholds.

The experiment of Ref. [85] was carried out at the TRIUMF neutron beam facility. Neutrons were elastically scattered in a plastic (CH_2) target, and the recoil proton was detected to determine the neutron energy and direction. In this manner, neutrons from 50 to 360 MeV illuminated the large face of an NE213 liquid scintillation detector measuring $100 \times 10 \times 10$ cm. The absolute detection efficiency was measured as a function of the energy threshold and incident neutron energy.

The experiment of Ref. [86] was performed at the neutron TOF facility at Tohoku University. Neutrons were produced with energies up to 33 MeV using ${}^9\text{Be}(p,n)$, and their energies were measured using TOF. The neutrons were detected in a cylindrical vessel measuring 100 cm in length and 13 cm in diameter filled with NE213 liquid scintillator.

Finally, the experiment of Ref. [87] was performed at SIN cyclotron. Neutrons were produced by 600 MeV protons on a thick beryllium target. The neutrons were then elastically scattered off protons in a liquid hydrogen target. The scattered protons were detected to allow reconstruction of the neutron energy and momentum. The scattered neutrons were then detected in a 4.5 cm diameter by 3.0 cm thick NE213 liquid scintillation detector. The absolute detection efficiency was measured for several detector thresholds.

In general the simulated efficiency agrees with the measured values at the level of about 30%.

C.5 Conclusion

The GEANT-GCALOR Monte Carlo code was tested by simulating several published neutron experiments. It was found that GCALOR is not suitable for describing the propagation of a neutron beam through a thick target because of approximations made in the elastic cross sections above 20 MeV. However, it is not expected that this will

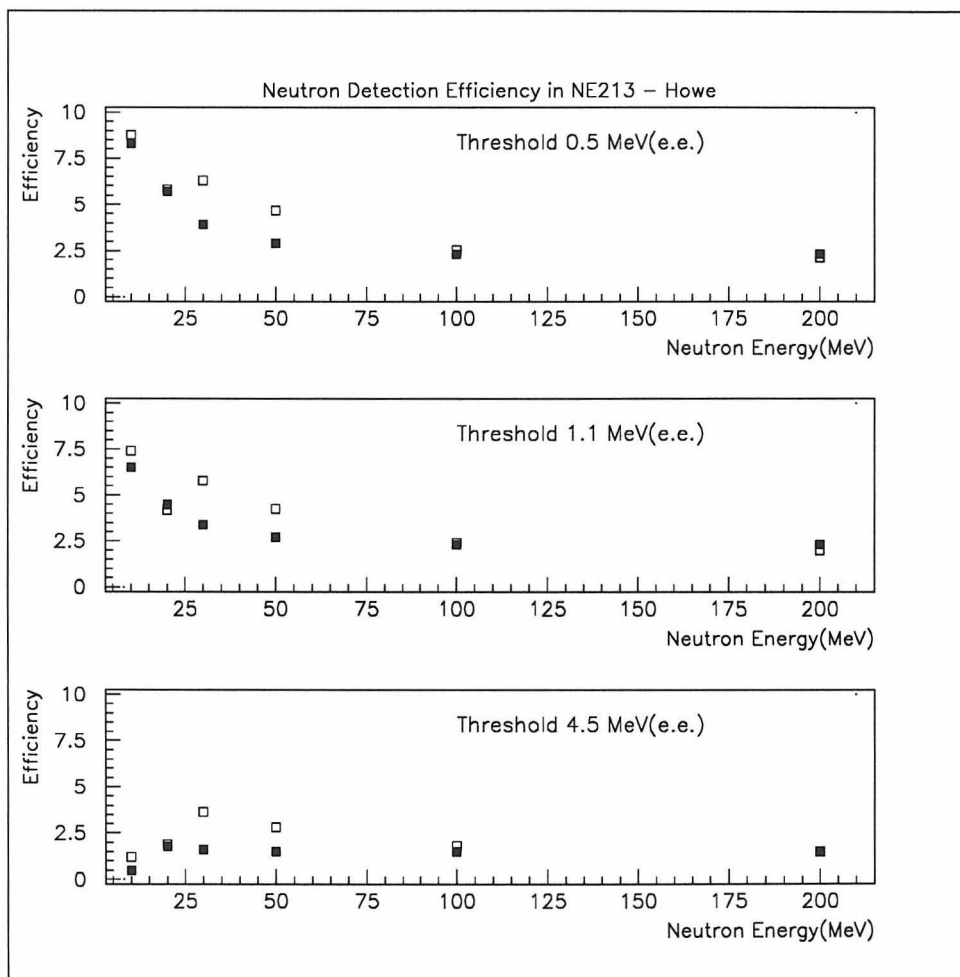


Figure C.4: Neutron detection efficiency: experiment of Howe et al. vs. GEANT-GCALOR. Filled symbols represent experimental data, and open symbols are GEANT-GCALOR results.

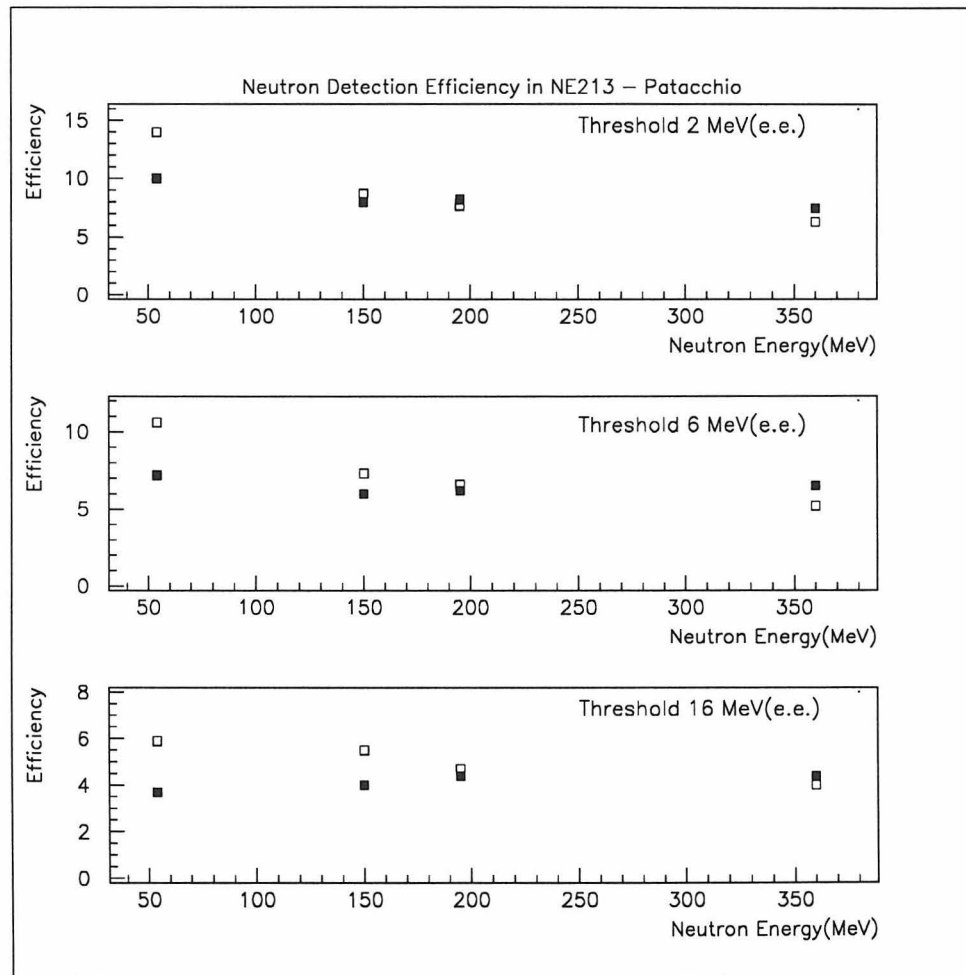


Figure C.5: Neutron detection efficiency: experiment of Patacchio et al. vs. GEANT-GCALOR. Filled symbols represent experimental data; open symbols are GEANT-GCALOR results.

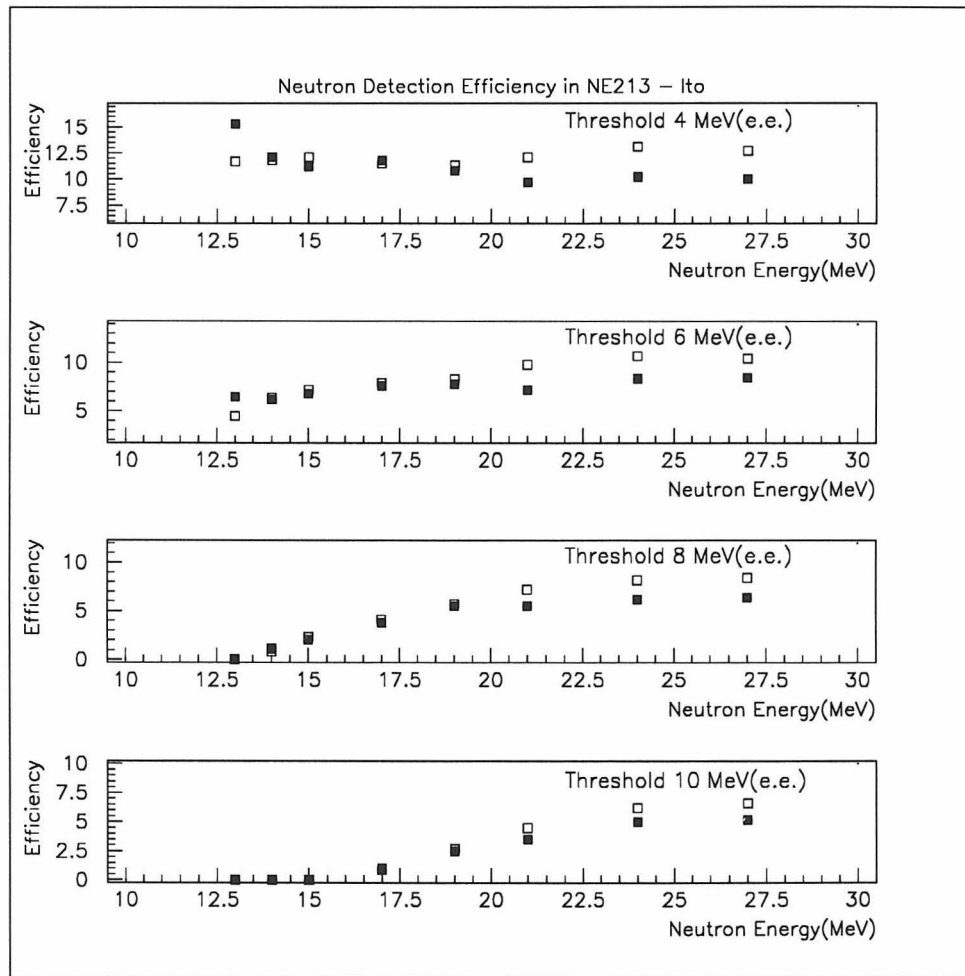


Figure C.6: Neutron detection efficiency: experiment of Ito et al. vs. GEANT-GCALOR. Filled symbols represent experimental data, and open symbols are GEANT-GCALOR results.

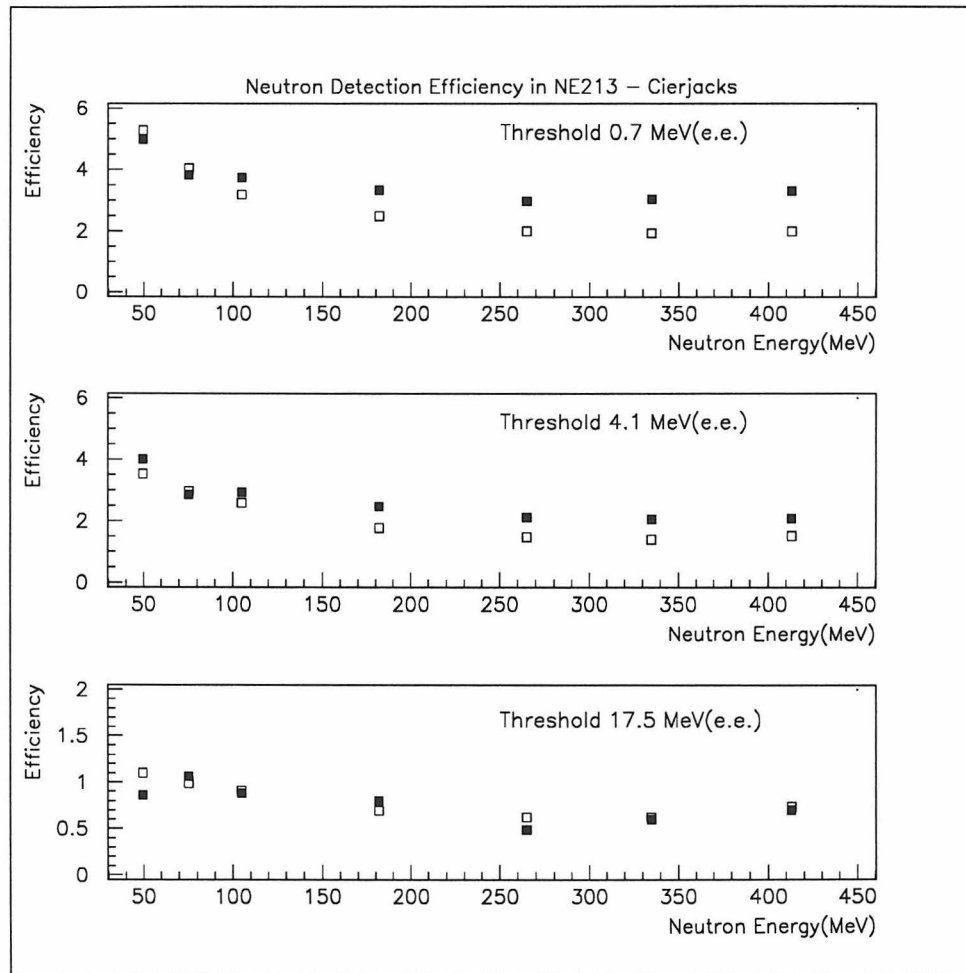


Figure C.7: Neutron detection efficiency: experiment of Cierjacks et al. vs. GEANT-GCALOR. Filled symbols represent experimental data; open symbols are GEANT-GCALOR results.

significantly affect the transport of neutrons relevant to the Palo Verde background calculations because of the randomized angular distribution of those neutrons.

The conversion of neutron energy to electron-equivalent energy was incorporated into the Monte Carlo code following a semi-empirical model and performing the conversion differentially on a step-by-step basis as secondary particles are tracked. This method was found to reproduce the light generation of heavy particles quite well.

GEANT-GCALOR was found to reproduce the energy loss of neutrons and the threshold behavior of scintillation detectors at the level of about 30%. The deposition of energy by neutrons and the threshold response of the detector are relevant for the background calculations made for the Palo Verde neutrino detector.

Appendix D

AmBe Neutron Background Measurement

Early estimates of the neutron background in the neutrino detector were put together from various simulations and calculations. For example, one code was used to estimate neutron attenuation through a slab of material, another was used to track secondary gamma rays, and hand calculations and geometrical assumptions were used to scale the simulations to arrive at the background estimate. This approach has been completely superseded by a full GEANT-GCALOR detector simulation described in Chapter 5. This chapter, however, consists of a previously published internal report (CALT-63-679), reproduced here in its original form, which describes an experimental test of one of these early Monte Carlo codes.

It should be noted that at the time of this report, the neutrino detector was to be installed near the San Onofre Nuclear Generating Station in Southern California. The experimental site has since been relocated to the Palo Verde nuclear power plant in Arizona. In addition, references to the expected signal and background rates and to the sensitivity of the oscillation experiment are not current.

Measurement of Neutron-Induced Triple Coincidences in a Segmented Liquid Scintillation Detector

M. Chen, B. Cook, K. Lou and A. Piepke

*California Institute of Technology, Norman Bridge Lab. of Physics 161-33, Pasadena, CA
91125, USA*

August 19, 1994

Abstract

The Monte Carlo code used to estimate the neutron-induced triple coincidence rate of the San Onofre neutrino detector was experimentally tested.

An array of 15 acrylic detector cells filled with liquid scintillator was exposed to an *AmBe* neutron source emitting fast neutrons. The neutrons were tagged using a *NaI* detector to measure the 4.4 *MeV* γ -radiation emitted by the source. Neutron triple coincidence probabilities were measured for different trigger topologies and energy requirements.

The array was modeled using the same Monte Carlo code that was used to predict the neutron background suppression in the San Onofre detector. Only the geometry of the detector cells and the energy spectrum of the neutrons were modified.

D.1 Introduction

The proposed San Onofre neutrino detector [88] will be located 650 m from the Southern California Edison Nuclear Generating Station at a depth of 25 *mwe*. Reactor anti-neutrinos will be identified by detecting the positron and neutron produced in an inverse β -decay reaction occurring inside the segmented detector. Backgrounds are suppressed by requiring a prompt triple coincidence of the slowing positron with its back-to-back annihilation radiation in adjacent cells, followed by a delayed neutron capture.

Due to the detector's relatively shallow depth, muon-induced fast neutrons are the major component of this correlated background [88]. The energy spectrum of these neutrons, produced either by capture of stopped muons or by spallation reactions caused by through going muons (through the exchange of virtual photons), extends to 100 *MeV* and more. In the detector, these neutrons can induce a triple coincidence either by multiple fast proton recoils in adjacent cells or by multiple-Compton scattering or pair production of the 4.4 *MeV* γ radiation from the excitation of ^{12}C by inelastic neutron scattering. Both mechanisms were MC [89] modeled for the San Onofre detector leading to a suppression factor of 167 due to the requirement of the triple coincidence. (The delayed capture signal gives an additional factor of ~ 2 suppression). This stringent suppression factor is critical to the success of the San Onofre project, allowing just four correlated background counts per day from the estimated fast neutron flux of 1300 per day [88]. Comparing this to our expected signal rate of 34 per day and a required signal to background ratio of 1:1 [88] for full sensitivity to the KAMIOKANDE-allowed atmospheric neutrino oscillation region of parameter space [90], it is clear that we could not tolerate an order of magnitude error in this background efficiency estimate.

Because of the importance of this factor and because the simulation of neutron transport is quite difficult, an experimental verification of the MC code is desirable. We present that verification here, finding fair agreement (factor of two) between a small test detector and the MC code used to model it. Only the neutron spectrum

and the cell geometry differ from the calculation performed for the full San Onofre detector. It should be noted that a factor of two underestimate of the neutron triples efficiency, as this measurement may suggest, would increase the total background by about 30%, from 13 to 18 counts per day. This would still allow complete sensitivity to the interesting atmospheric neutrino region [88].

D.2 The Experiment

D.2.1 The Neutron Source

The *AmBe* source emits neutrons through the reaction ${}^9\text{Be}(\alpha, n){}^{12}\text{C}$, leaving 11.4 *MeV* shared between the neutron and carbon nucleus. Approximately 80% of the time, ${}^{12}\text{C}$ is left in its first excited state with $E_x = 4.4 \text{ MeV}$ [91]. The neutron thus has a maximum energy of 7 *MeV* and is accompanied by a 4.4 *MeV* γ quantum which is used to experimentally tag those neutrons.

The neutron energy spectrum is smeared by two mechanisms: 1) slowing of the α -particle in the source before interaction, and 2) emission of the neutron at various angles with respect to the center-of-mass momentum.

A measured neutron spectrum of the *AmBe* source can be found in [92]. The source was manufactured and calibrated by Amersham and emits $\sim 6.6 \cdot 10^4$ neutrons per second.

D.2.2 The Detector

The experimental setup is depicted in Figure D.1. The detector consists of 15 acrylic cells measuring $20 \text{ cm} \times 9 \text{ cm} \times 88 \text{ cm}$, each filled with 12.54 *l* of liquid scintillator (85% mineral oil, 15% pseudocumene, 4 g/l PPO). Two 3-inch photomultipliers (Philips XP 2312) are optically coupled to each end. The signals of both sides are summed using a LeCroy 428F Linear Fan-in. The HV settings of both sides of each cell were carefully matched using the Compton edge of the γ -radiation of a ${}^{60}\text{Co}$ source.

The detector is shielded by 5 *cm* of *Pb* against the radioactivity of the lab. In addition to this, 2.5 *cm* of *Cu* were placed above and below the cells. Data has been taken with and without this passive shield placed between the source and the detector.

In order to prepare a clean data sample, neutrons interacting in the trigger cell were tagged by requiring a prompt coincidence with a *NaI* detector. The hardware threshold of the *NaI* was set at 2.4 *MeV*. This energy threshold allows acceptance of the full absorption, single and double escape peaks of the 4.4 *MeV* γ -radiation emitted by the source. The time resolution of $FWHM = 3$ *ns* between the trigger cell and the *NaI* was determined using the *AmBe* and a ^{60}Co source. For the data taking we used a rather wide coincidence time of 35 *ns*. The contribution of random coincidences was measured to be $\sim 0.5\%$ and hence is negligible. With the source present, the coincidence requirement reduced the integral counting rate of cell #8 (determined for the interval 200 – 3600 *keV*) by a factor 500 (from 2.02 *kHz* to 4.0 *Hz*). The background rate without source went down by a factor 5300 (from 315 to 0.06 *Hz*).

The energy calibrations of the cells were obtained using various γ emitters. The Compton edges of ^{133}Ba , ^{137}Cs , ^{60}Co and ^{232}Th gave 5 reference points from 207 to 2382 *keV*. The position at the 2/3 maximum point of the Compton edge was associated with the energy of the backscattered photons (see figures D.2 and D.3). These points showed good linearity. Since the lowest calibration point was at 207 *keV*, the error at 50 *keV* was on average $\sim \pm 20$ *keV*. This uncertainty was estimated by comparing the intercept of the linear energy calibration with the measured pedestal of the ADC. The energy calibration was found to vary by 15% between the edges and the center of the detector. The data were not corrected for this effect.

The electronic energy calibration can be converted into energies deposited through nuclear recoil of the neutrons by using the scaling relation of Ref. [93]. According to this reference the recoiling protons give approximately half of the light output of electrons per unit energy, measured for the liquid scintillator NE 213. The dynamic range of the cells was adjusted to cover energies from 40 up to 3600 *keV* to cover the full spectrum of neutrons. Data were also taken with an energy range extended to

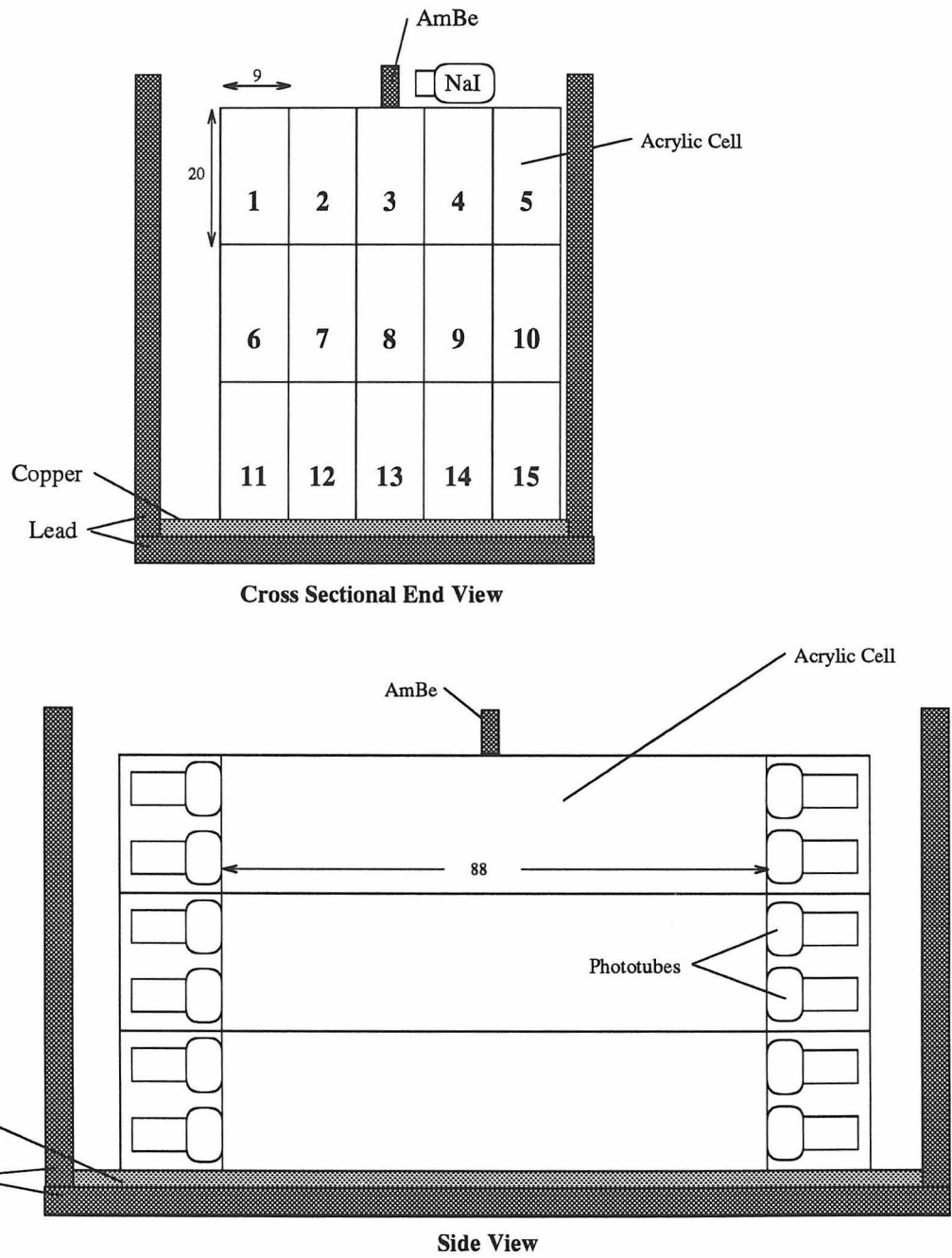


Figure D.1: Cross sectional end and side views of the 15-cell experimental apparatus. Data were taken alternately using cell 3, 8, or 13 as the trigger cell.

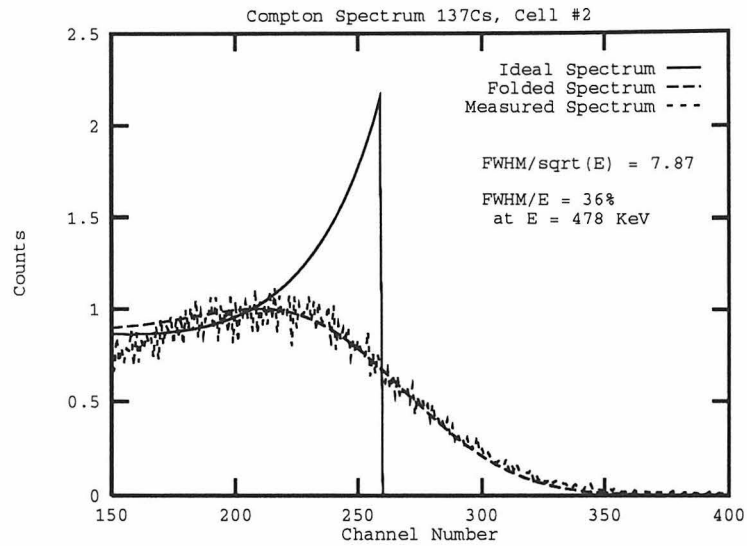


Figure D.2: Compton spectrum of ^{137}Cs ($E_\gamma = 662 \text{ keV}$) measured with cell #2. The solid curve depicts the expected shape calculated using the Klein–Nishina formula. The dashed curve was obtained by folding a Gaussian resolution function with the Compton continuum. The dotted spectrum is the experimental data. This shows that using the canonical half maximum (rather than $2/3$ maximum) point of the Compton edge to define the energy would introduce a $\sim 4\%$ systematic error.

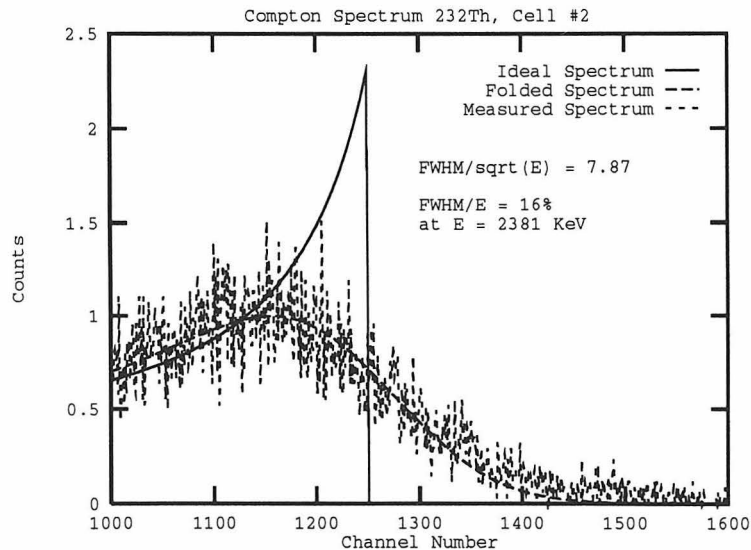


Figure D.3: Compton spectrum of ^{232}Th ($E_\gamma = 2614 \text{ keV}$) measured with cell #2. Note that the data is well described by the same resolution function.

5700 keV to include the Compton edge of the 4.4 MeV γ -radiation, resulting from the excitation of ^{12}C in the scintillator. For these runs the 4.4 MeV γ -line of the *AmBe* source was also used in the energy calibration.

The energy resolution of the detector cells was determined from the shape of the Compton edges of the $E_\gamma = 662$ and 2615 keV lines of ^{137}Cs and ^{232}Th . The Compton continuum, parametrized by the Klein–Nishina formula, was folded with a Gaussian resolution function. Spectra measured with cells #2, 3 and 15 were well described by $\frac{FWHM}{\sqrt{E}} = 7.87$ (energies in keV). From this we concluded that *all* (identical) cells had a resolution of 25% at 1000 keV. Experimental data taken with cell #2 are displayed in figures D.2 and D.3. They show good agreement with the theoretically expected shape.

Neutron data was taken alternately with cell #3, 8 or 13 acting as the trigger cell. Cells #8 and 13 see neutrons which are moderated by the cells above. The three different trigger conditions thus allow a small variation of the neutron energy spectrum. Triggering on cell #8 has the advantage of allowing a larger variety of different triple-coincidence topologies.

D.2.3 Data Taking

Data were taken event by event to allow a detailed off-line analysis. The data acquisition is controlled by an IBM PC with a 486, 66 MHz processor. In order to minimize the dead time of the system, 1000 events are buffered in the memory of the computer before being written to disk. This reduces the number of time-consuming disk operations. The dead time, estimated with a scaler, was typically around 0.08%.

The coincidence between the trigger cell and the *NaI* detector was hardware implemented to enhance the signal to background ratio. A trigger was defined as an energy deposit in the trigger cell above a hardware threshold of 200 keV in coincidence (within 35 ns) with an energy deposit in the *NaI* above a hardware threshold of 2.4 MeV. When such a coincidence occurred, the energies of all 15 cells, digitized by a LeCroy 4300B FERA ADC, and the *NaI* signal, digitized by a LeCroy 2249 W ADC,

were recorded by the computer. Since the ADC gate width used to digitize the cell signal (80 ns) is much larger than the time jitter between different cells ($FWHM=3$ ns measured with a ^{60}Co source), no hardware coincidence between the cells had to be implemented.

A total of $2.3 \cdot 10^6$ tagged neutron recoils were measured in the different experimental configurations to determine the triple coincidence probabilities.

After finishing this part of the experiment we modified the data acquisition to measure the moderation and capture time of the neutrons in order to estimate the full quadruple coincidence probability. In this way we were able to test the neutron sector of the Monte Carlo independently: there is no folding with the electromagnetic sector (simulated through EGS4) as in the case for the triple coincidences where 4.4 MeV γ 's had to be tracked.

A neutron-capture event is identified by the detection of a 2.2 MeV γ produced when a thermalized neutron is captured on a proton. Experimentally, this is measured by first requiring a prompt coincidence between the *NaI* and the trigger cell as described above. The data acquisition then waits for a delayed energy deposit above 800 keV in the sum of all 15 cells. The sum energy signal of all cells is prepared using LeCroy 428F Linear Fan-in's. The number of these sum energy triggers above the hardware threshold is measured with a KSI 3615 CAMAC Scaler for variable delay and integration times. The excess of events in comparison to a background measurement using a very long delay of 1000 μsec gives the time dependence of the capture signal. Due to the very large event rate in presence of the radioactive source, a measurement of the fourfold coincidences as described in the San Onofre proposal [88] is not possible.

A total of $1.7 \cdot 10^6$ delayed coincidences were measured to determine the moderation and capture time of free neutrons in the scintillator.

D.3 Experimental Results

In the following a *single* event is defined as a coincidence between the trigger cell and the *NaI* detector, irrespective of the energy deposited in any other cell. A *triple*

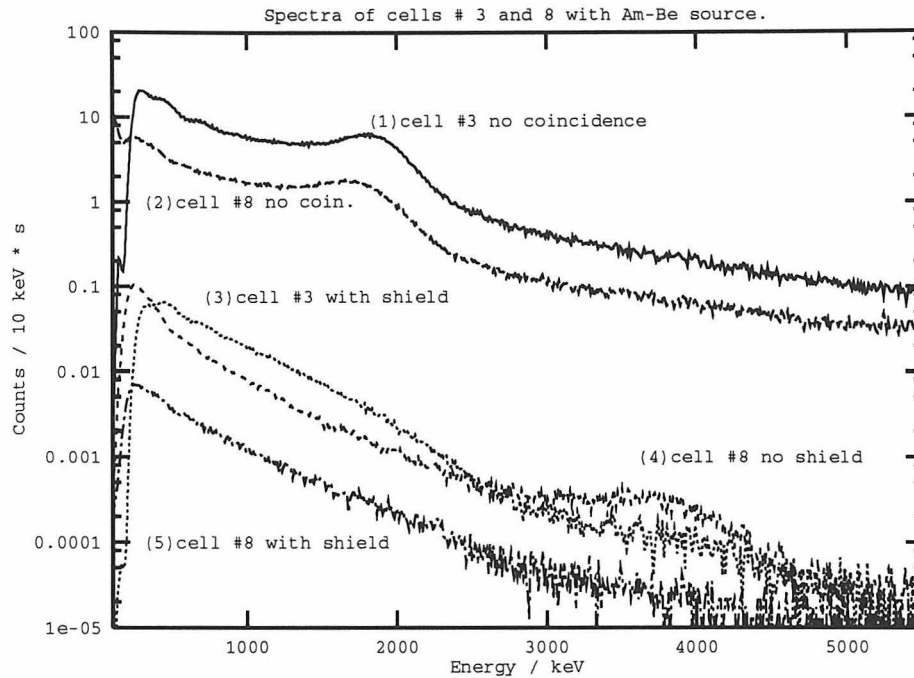


Figure D.4: Energy spectra of the *AmBe* neutron source measured with different detector cells. Spectra 1 and 2, containing 10^6 events each, were measured with cells #3 and 8 without coincidence requirement with the passive shield placed between source and cells. All other spectra correspond to tagged neutron events. Spectra 3 and 5 ($5 \cdot 10^5$ and $9 \cdot 10^4$ events, respectively) were taken with the passive shield in place using the same cells. Spectrum 4 ($5 \cdot 10^5$ events) was measured with cell #8 after removing the shield between source and cells.

is defined as a single accompanied by a specified energy deposit in two other cells with the required back-to-back topology. The triple coincidence probabilities are parametrized as the ratio of *triples/singles* as a function of various energy cuts in the trigger and adjacent cells. This ratio is independent of the source strength, the solid angle of the detector-source arrangement, the acceptance of the *NaI* detector and any variation of the absolute counting rate due to shifts in the data-taking electronics.

Figure D.4 depicts recoil energy spectra of the *AmBe* source measured with cells #3 and 8. The upper two spectra (1 and 2) were measured without requiring a coincidence with the *NaI* detector. The presence of the 2.2 *MeV* Compton edge shows that the fast recoils are superimposed on a background of delayed events. The excitation of the 4.4 *MeV* level of ^{12}C is not visible due to the large background of high-energy neutrons, reaching up to 11.4 *MeV* (equivalent to ~ 5.9 *MeV* of electronic energy).

Other than different counting rates due to solid angle, both spectra are identical. Because of the large source-related background, this data sample cannot be used to measure neutron-induced triple coincidence probabilities for fast neutrons.

Spectra 3 and 5 were measured requiring a prompt coincidence between cell #3 or 8 with the *NaI* detector, respectively. 10 *cm* of *Pb* and 2.5 *cm* of *Cu* were placed between the cells and the source in order to shield the primary γ -radiation emitted by the source. Because of the large mass numbers of the shielding materials, we expect the shape of the neutron spectrum to be unchanged if the measured signal is due to neutrons. Due to the small counting rate of only 0.36 *Hz*, the data have limited statistical accuracy.

Spectrum 4 was also measured using cell #8 but without the passive shield between source and detector. This configuration has the advantage of a tenfold higher counting rate and hence much better statistical accuracy, being comparable to that of spectrum 3. The coincidence requirement of a large energy deposit in the *NaI* prevents primary 4.4 *MeV* γ -rays from contributing to the spectrum. Primary γ -radiation can only contribute through random coincidences. The relative contribution of 4.4 *MeV* γ -ray events (produced via inelastic neutron scattering in the scintillator; taken from 2800–4700 *keV*) in comparison to the neutron continuum (taken from 500–2800 *keV*) is 3.0 and 3.9% for the data sample measured with and without the passive shield between source and cells, respectively. The data taken without passive shield shows an enhanced counting rate at energies below 500 *keV*. This is due to 511 *keV* γ escape radiation from the *NaI* detector since our coincidence requirement accepts the double and single escape peaks of the 4.4 *MeV* γ 's. This is also reflected in the fact that the coincidence energy spectrum measured with the *NaI* detector shows an enhanced double escape peak compared to the spectrum taken without coincidences.

The spectrum taken with cell #3 shows a harder neutron spectrum and smaller contribution of the 4.4 *MeV* γ -radiation (0.9%) than that of cell #8. The single spectrum of cell #13, not shown in Figure D.4, has the highest relative contribution of the γ component of 6.3%. The experimental data shows that the contribution of the 4.4 *MeV* γ -component increases with increasing distance to the source and hence

decreasing neutron flux. Since the γ radiation is emitted by the detector cell itself, its flux is less dependent on the solid angle of the trigger cell with respect to the source.

The delayed component due to neutron capture is effectively suppressed in all coincidence spectra. From these data it is clear that the coincidence requirement is essential for testing the prompt neutron recoil.

D.3.1 Evidence That the Measured Signal is Due to Neutrons

Table D.1: Mean free path lengths in liquid scintillator and the lead-copper shield. Experimental results derived from cell #8 are compared to the expectations for 3 and 7 *MeV* neutrons and 4.4 *MeV* γ -radiation. The experimental errors include both statistical and systematic uncertainties. The relative difference of the absorption in the scintillator and the shield is also given.

Material	Mean free path [cm]			
	Experiment	3 <i>MeV</i> Neutrons	7 <i>MeV</i> Neutrons	4.4 <i>MeV</i> gammas
Scintillator	$12.9^{+1.4}_{-1.0}$	4.9	6.5	39.1
Shield	$7.9^{+1.5}_{-0.4}$	4.3	4.5	2.3
Scint./Shield	$1.6^{+0.4}_{-0.2}$	1.1	1.4	17.0

It is useful to verify that our observed signal is indeed due to neutrons and not, for example, due (in part) to primary 4.4 *MeV* γ -radiation emitted by the source. Any other type of radiation (e.g., alpha radiation of the source) would not be able to penetrate the steel encapsulation of the source.

The mean free path lengths of neutrons and high energetic γ -radiation in the passive shield and the liquid scintillator are quite different. A comparison of measured and expected mean free path lengths can be used to identify the type of radiation creating the measured signal. The counting rate ratios (taken from 250–3600 *keV*) of the runs with and without the passive shield placed between the cells and the detector can be used to determine this mean free path in the shielding material. The counting rate ratio with and without cell #3 placed between the neutron source and cell #8

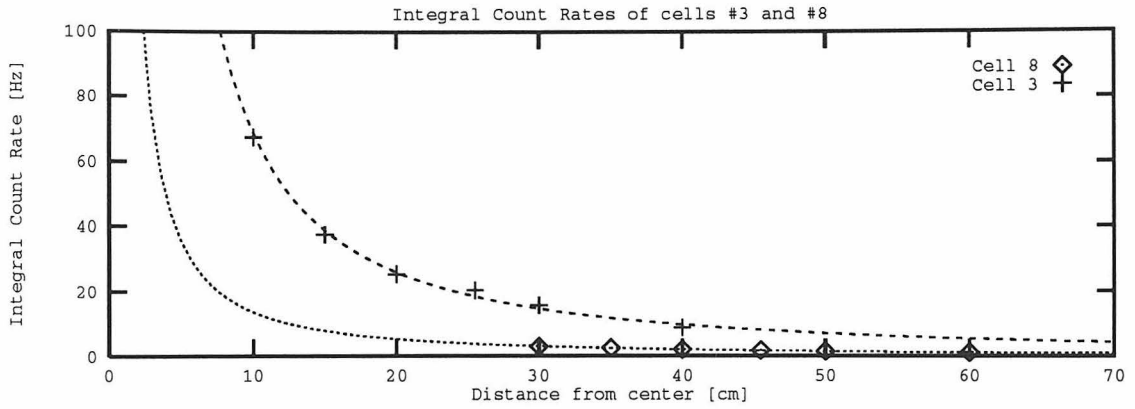


Figure D.5: Measured and fitted dependence of the integral counting rates of cells #3 and 8 (in *counts/s* taken in the energy interval 250–3600 *keV*) on the distance of the source to the center of the detector cell.

is used to estimate the mean free path length in the liquid scintillator.

The solid angle of both detector cells has been measured for six different source distances (relative to the center of the cell) without the passive shield. As can be seen in Figure D.5, the solid angle of both cells is well described by a power law. The fitted exponent is -1.42 ± 0.08 and -1.37 ± 0.08 for cell #3 and 8, respectively.

In this way we find a solid-angle-corrected reduction in counting rate of a factor of 5.3 ± 1.0 for cell #3 and 4.9 ± 0.8 for cell #8 due to the 12.5 *cm* thick passive shield. The presence of cell #3 (20 *cm* of liquid scintillator) reduces the solid angle corrected counting rate of cell #8 by a factor of 4.8 ± 0.7 .

In order to compare these values to the expectations for the different types of radiation, we determine the mean free path lengths, λ . We assume that the absorption for neutrons and γ -radiation can be parametrized through:

$$r(d) = r_0 \cdot e^{-d/\lambda}.$$

Where d is the shielding thickness in *cm*, $r(d)$ is the integral counting rate in *counts/s* taken for the energy interval 250–3600 *keV* with an absorber of the thickness d placed between source and cell and r_0 the integral counting rate without absorber. This is certainly an approximation, because the exponential attenuation law is valid for a beam geometry, which is not exactly realized in our case. Table D.1 contains the

λ -values determined from the experimental data and estimated for neutrons and γ -radiation. The best way to compare the experimental estimate with the expected values is to take the ratio of the radiation lengths of scintillator and passive shield, because the deviation from the beam geometry should, to a certain extent, cancel out.

Since the neutrons have a continuous spectrum, Table D.1 lists the results for neutron energies of 3 and 7 MeV , which covers the main portion of the incident spectrum. Total cross sections for neutron scattering on H , C , Cu and Pb were taken from [94]. The values for the liquid scintillator were calculated assuming a density of 0.8 g/cm^3 and a proton-to-carbon ratio of 1.9. The mass-absorption coefficients for 4.4 MeV γ -radiation were taken from [95]. The absorption coefficient of H_2O and the above density were used to estimate the γ -absorption of the liquid scintillator.

The estimated and measured absorption lengths do not agree within the given error widths for both hypotheses. The good agreement of the relative difference of the radiation length of measured signal and neutron estimate, however, strongly favors the hypothesis that the signal is caused by neutrons.

This hypothesis is further supported by the fact that the spectral shape of the measured signal is not changed by adding the passive shield between the source and cells (see Figure D.4). For γ -radiation we would expect a pronounced energy dependence of the absorption, whereas for neutrons the heavy shielding materials would produce primarily elastic scattering. This reduces the flux by scattering neutrons out of the detector solid angle, but leaves the spectral shape unchanged.

From this we conclude that the measured single events are due to neutrons.

D.3.2 Experimental Triple Coincidence Probabilities

In the San Onofre experiment, the prompt signature for a neutrino event is an energy deposit of $> 1\text{ MeV}$ in the center cell due to positron slowing in coincidence with $50 - 600\text{ keV}$ in two side cells due to Compton scattering of the annihilation 511 keV γ 's. The lower threshold was set at 50 keV based on Monte Carlo simulations [88]

showing a large enhancement of the detection efficiency for low thresholds. In the analysis of the neutron-induced triple coincidence probabilities, we employ the above energy conditions in the side cells and require $> 800 \text{ keV}$ in the center cell for the various trigger topologies and different trigger and shielding conditions. This energy cut is referred to as the *primary cut*. We also investigate the triples probability as a function of the lower energy threshold of the side cells.

As mentioned earlier the energy calibration is subject to a sizeable systematic error near the threshold. Figure D.6 shows the energy spectrum measured with cells #7 and 9 using cell #8 as a trigger. A relative shift of 36 keV is visible. Before applying the energy cuts, the data must be corrected for this systematic shift to produce energy calibrations that are consistent if not absolute. In Figure D.7 the pedestal of cell #7 was shifted to match that of cell #9. The measured binwidth was kept constant, and the spectra are in good agreement after this manipulation. The energy calibration of cell #9 was used as a reference because it showed good agreement between the measured ADC pedestal and intercept of the calibration. Adjustments could also have been made to shift each spectrum to match its measured ADC pedestal, but this would have moved part of the spectra to negative energies. For all energy cuts the first method was used to make the calibrations consistent. The influence of this manipulation on the triples probability was measured and included in the determination of the systematic error.

D.3.3 Influence of the Trigger Topology

Table D.2 shows the triple coincidence probabilities for the different trigger topologies after applying the primary energy cut. Due to the small number of high energetic events, an extension of the energy range of the trigger cell, to include the Compton edge of the 4.4 MeV γ -radiation, does *not* influence the triple probabilities.

The coincidence probabilities for a given topology, listed in Table D.2, are not strongly influenced by the different experimental configurations.

The accidental background can be estimated using the measured singles rates

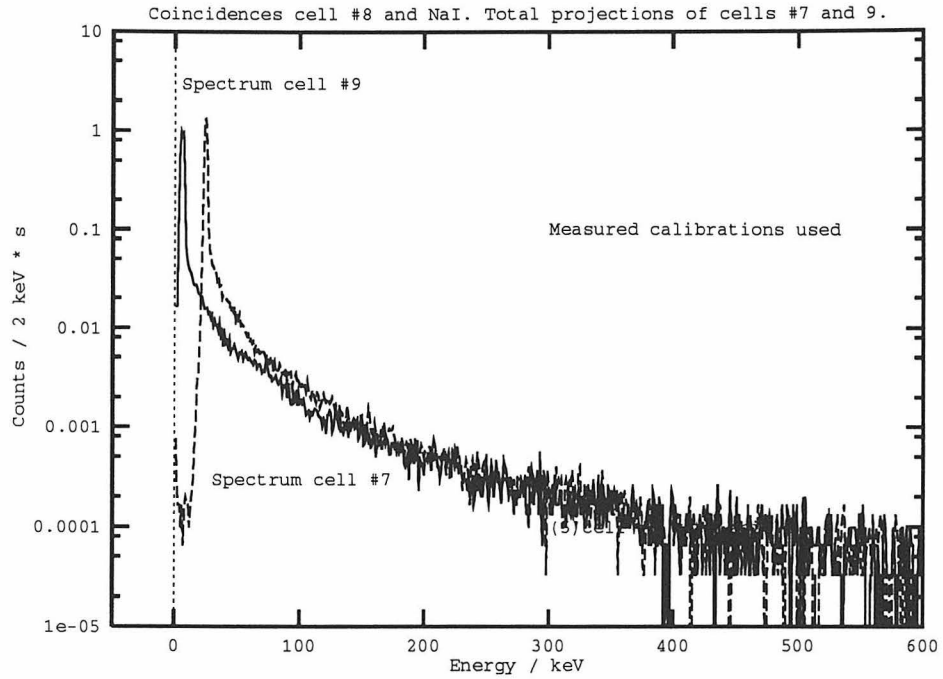


Figure D.6: Energy spectra of cells #7 and 9 using cell #8 as trigger cell. The spectra have been rebinned using the measured energy calibration (compare with following figure).

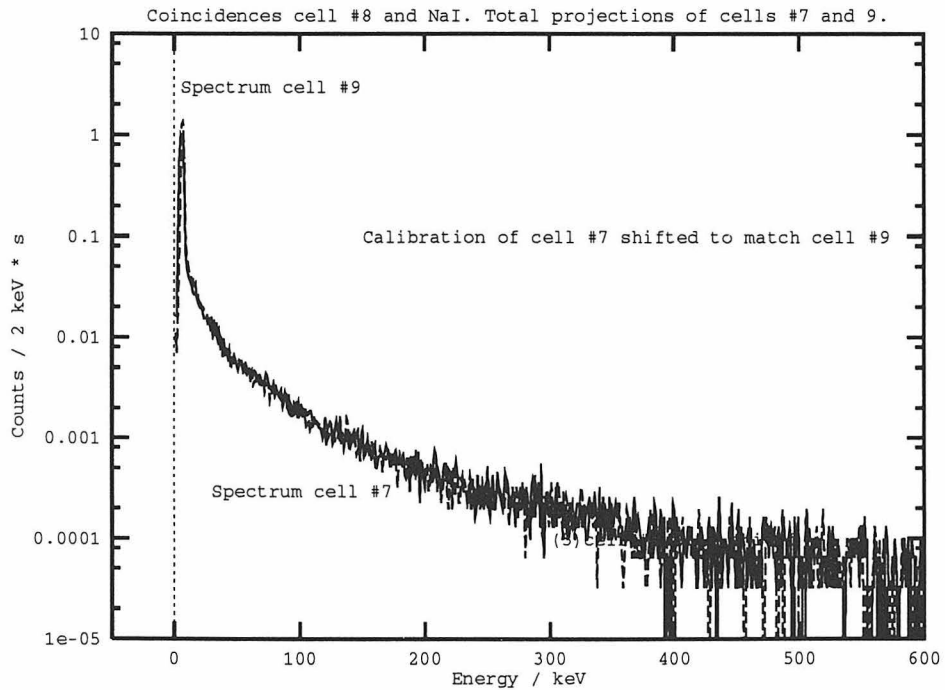


Figure D.7: Energy spectra of cells #7 and 9 using cell #8 as trigger cell. The spectra have been rebinned using the adjusted energy calibration (compare with previous figure).

Table D.2: Experimental triple coincidence probabilities for different trigger cells and trigger topologies. The triple probability is defined as the number of triples divided by the number of singles with the following energy conditions: 800–3600 keV in the trigger cell and 50–600 keV in each side cell. No energy cuts are made on any cells other than the three mentioned. The quoted error corresponds to the statistical uncertainty of the data. The accuracy of these results is dominated by the systematic error of $\pm 43\%$ (see the discussion in section D.3.5). The last column identifying the experimental configuration also contains the number of measured tagged neutron events. In the background runs 3000 events were measured, requiring 1–2 days of measuring time.

Trigger cell #	Side cell #	Triple Probability	Triple Probability Backgr. Subtracted	Experimental Configuration	
3	2 + 4	$(5.6 \pm 0.4) \cdot 10^{-3}$	$(5.4 \pm 0.4) \cdot 10^{-3}$	No passive shield between source and cells. Cut on full absorption peak NaI. ($5 \cdot 10^5$)	A
3	2 + 4	$(9.6 \pm 0.3) \cdot 10^{-3}$	$(9.7 \pm 0.3) \cdot 10^{-3}$	10 cm of Pb and 2.5 cm of Cu between source and cells. No cut on NaI. ($5 \cdot 10^5$)	B
8	7 + 9	$(8.5 \pm 0.3) \cdot 10^{-3}$	$(8.4 \pm 0.4) \cdot 10^{-3}$	No passive shield between source and cells. No cut on NaI. ($5 \cdot 10^5$)	C
8	3 + 13	$(14.5 \pm 0.4) \cdot 10^{-3}$	$(14.5 \pm 0.4) \cdot 10^{-3}$		
8	4 + 12	$(5.4 \pm 0.3) \cdot 10^{-3}$	$(5.2 \pm 0.3) \cdot 10^{-3}$		
8	7 + 9	$(7.7 \pm 1.2) \cdot 10^{-3}$		No passive shield between source and cells. Cut on full absorption peak NaI. ($3.65 \cdot 10^5$)	D
8	3 + 13	$(12.0 \pm 2) \cdot 10^{-3}$			
8	4 + 12	$(3.3 \pm 0.8) \cdot 10^{-3}$			
8	7 + 9	$(6.5 \pm 0.5) \cdot 10^{-3}$	$(5.6 \pm 0.6) \cdot 10^{-3}$	10 cm of Pb and 2.5 cm of Cu between source and cells. No cut on NaI. (10^5)	E
8	3 + 13	$(5.6 \pm 0.4) \cdot 10^{-3}$	$(5.2 \pm 0.5) \cdot 10^{-3}$		
8	4 + 12	$(2.7 \pm 0.3) \cdot 10^{-3}$	$(2.2 \pm 0.4) \cdot 10^{-3}$		
13	12 + 14	$(4.8 \pm 0.5) \cdot 10^{-3}$	$(3.8 \pm 0.6) \cdot 10^{-3}$	No passive shield between source and cells. No cut on NaI. (10^5)	F

due to the source with no *NaI* coincidence requirement. This contribution is very small, e.g., 0.38% for data sample **C**. However, the correlated backgrounds, e.g., true coincidences due to through-going muons or primary cosmic-ray hadrons, are more important for some experimental configurations. To measure this, each data run was followed by a background measurement using the same experimental configuration but without the source. We were thus able to unfold this effect by subtracting the expected number of background events from the singles and triples in the data sample. Table D.2 contains these background-subtracted probabilities as well.

D.3.4 Threshold Dependence

Two energy thresholds were varied in the data analysis: the lower threshold of the center “positron-like” cell, and the lower thresholds of the side “annihilation-like” cells. The latter is the more important since we expect a strong dependence of the positron detection efficiency on this parameter. It is hence important to understand whether the background can be effectively suppressed for low thresholds in the side cells.

Figure D.8 depicts the triple probability curves (horizontal topology) as a function of the lower energy threshold of the side cells. From curve to curve, it is the threshold of the center trigger cell that is varied. Parts a, b and c show the results for triggering on cell #8 for the different experimental configurations. All curves have the same shape and there is little variation introduced due to the cut on the *NaI* spectrum (to exclude the escape peaks) or due to the passive shield. The dependence on the trigger cell threshold is almost negligible (always smaller than 20%). We see, however, a strong dependence (up to factor 8) on the lower threshold of the side cells. Figure D.8d depicts the horizontal triple probability for cell #3 as the trigger cell. We see again the same shape of the threshold dependence. Since the experimental geometries used to measure samples **C** and **D** are identical, the difference must be attributed to the differences in neutron energy spectrum.

Figure D.9 displays the results for the vertical topology of trigger cell #8. Errors shown are statistical only. We see again the same qualitative behavior but an overall higher triple probability than for the horizontal cuts. These enhanced rates are probably due the fact that one of the side cells sees a higher neutron flux and this configuration favors forward scattering, whereas in the horizontal topology we need one or more large angle scatters.

The dependence of the triple probabilities on the upper energy threshold of the side cells is small. For configuration **C** the horizontal and vertical triple rates, shown in Table D.2, go up by a factor of ~ 2 if the energy range of the side cells is extended from 600 to 3600 *keV*.

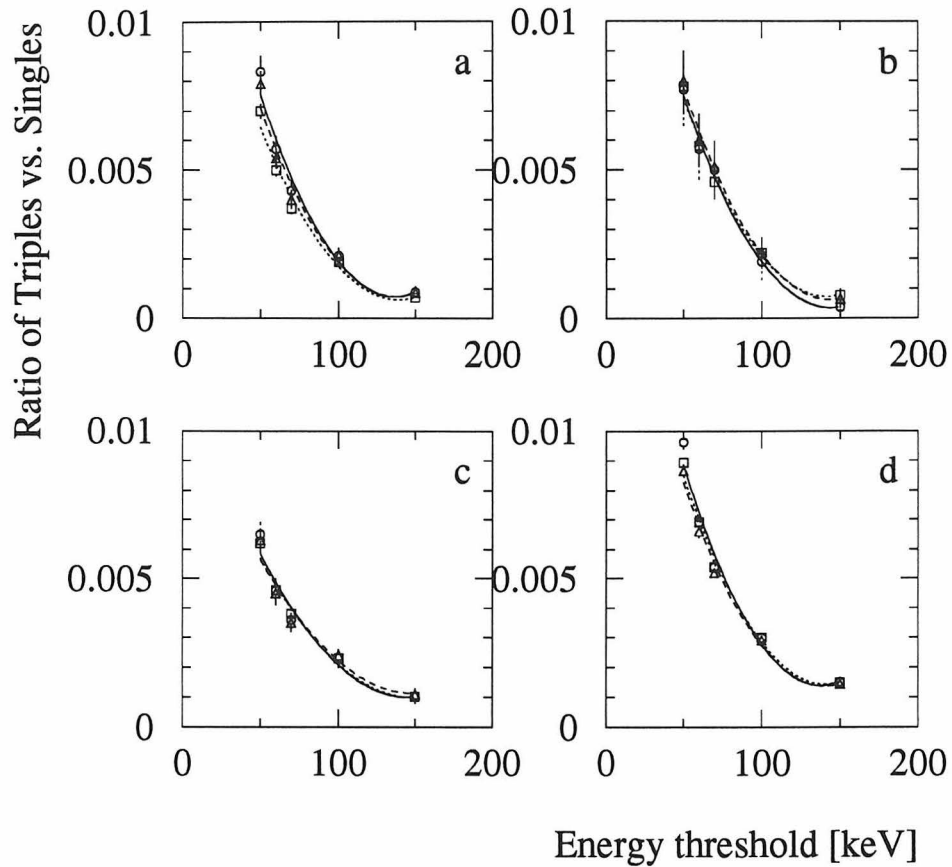


Figure D.8: Triple coincidence probabilities for horizontal topologies as a function of the lower energy threshold of the side cells. Errors shown are statistical only. Upper threshold of the side cells: 600 keV . Trigger cell lower threshold (in keV): 250–square, 600–triangle, 800–circle. a) Trigger: #8; Sides: #7, #9; No shield; No cut on NaI. b) Trigger: #8; Sides: #7, #9; No shield; Cut on NaI full absorption peak. c) Trigger: #8; Sides: #7, #9; Shield between source and cells; No cut on NaI. d) Trigger: #3; Sides: #2, #4; Shield between source and cells; No cut on NaI.

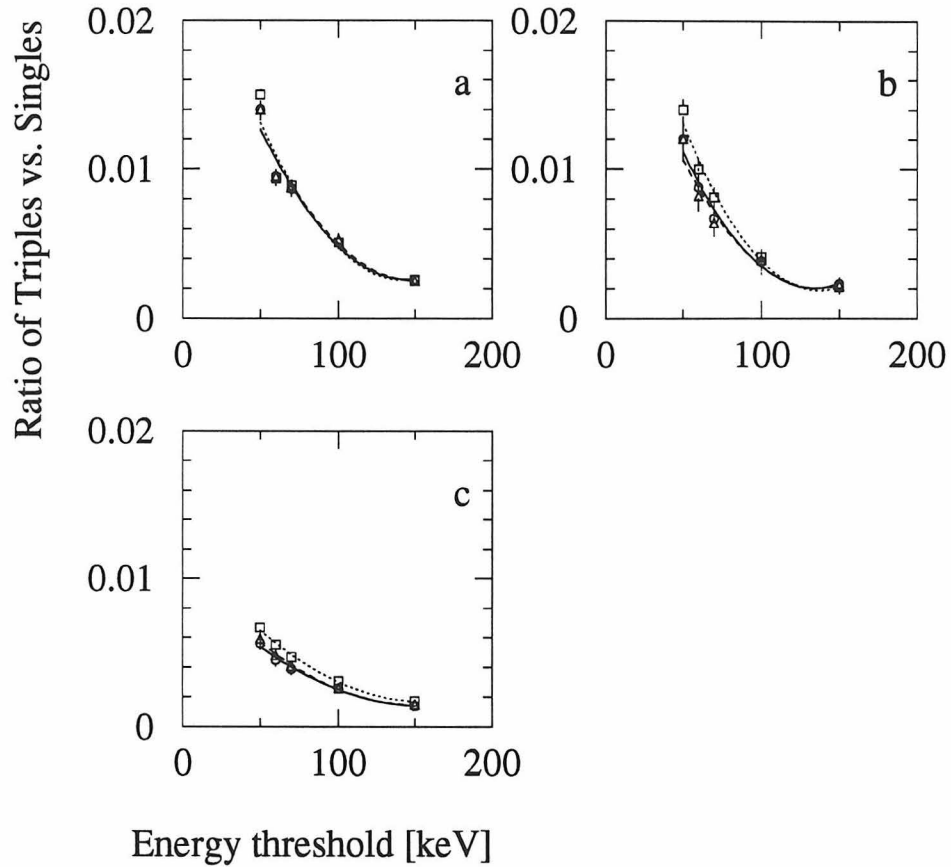


Figure D.9: Triple coincidence probabilities for vertical topologies as a function of the lower energy threshold of the side cells. Errors show are statistical only. Upper threshold of side cells: 600 keV . Lower threshold of trigger cell (in keV): 250–square, 600–triangle, 800–circle. Trigger cell: #8; Side cells: #3, #13. a) No shield; No cut on NaI. b) No shield; Cut on NaI full absorption peak. c) Shield between source and cells; No cut on NaI

D.3.5 Systematic Errors

The main source of systematic error is, as mentioned earlier, the energy calibration. The influence of these sizable uncertainties at low energies on the triple coincidence probability was estimated by repeating the data analysis of run **E** using the adjusted and the measured calibration. In order to understand the influence of this adjustment, the analysis was also performed using a different adjustment in which the ADC pedestal defined the intercept of the energy calibration. The energy calibration was repeated at the end of the data taking to estimate its shift in time. This time drift varied from cell to cell and was in the worst case $\sim 5\%$. The data analysis of run **E** was then repeated using the new calibration. In this way we estimated the systematic error in the triples rate of run **E** to be $\pm 40\%$. Because the threshold dependence of all data sets is so similar, we concluded that the systematic error is the same for all experimental configurations.

Another source of uncertainty arises from shifts in the energy calibration of the *NaI* detector. Since the *NaI* signal was also measured, this shift can be deduced for each experimental run from the position of the γ -peaks of the source. In this way we identified an 8% shift in the position of the 4.4 *MeV* full absorption line during the experimental time. From the data of configuration **E**, we deduced that this changes the triples rate by 15%. The energy calibration of the *NaI* detector was stable within the individual experimental runs. This was verified by dividing the data for each run into 15–20 subgroups and then measuring the position of the 4.4 *MeV* full absorption peak as a function of measuring time.

The total systematic error is thus estimated at $\pm 43\%$, if we assume that both discussed error components are uncorrelated. The accuracy of the experimental triple coincidence probabilities is therefore mainly determined by systematic uncertainties.

In the course of this experiment, the triple coincidence probabilities were measured three times for configuration **E** (see Table D.2). For the horizontal cut (cells #7, 8 and 9), we determined $7.3 \cdot 10^{-3}$, $5.6 \cdot 10^{-3}$ and $6.2 \cdot 10^{-3}$, respectively; for the vertical cut, $11 \cdot 10^{-3}$, $8.4 \cdot 10^{-3}$, and $5.6 \cdot 10^{-3}$. This indicates that the experimental results

are reproducible within the given error limits.

D.4 Neutron Capture and Thermalization

As discussed in section D.2.3, the neutron capture and thermalization times were measured by looking for an excess of counts at a given delay time over those measured for a very large delay (1 *ms*) at which time all neutrons have been captured on protons in the scintillator. This excess measured for various delay times allows a determination of the moderation and capture time of the neutrons. The data taking was split in two parts because the time scale for moderation (few μs) is very different from that of neutron capture (few hundred μs). For the first 20 μs , an integration time of 2 μs was used, and the delay was varied in steps of 2 μs . For the time range of 20–300 μs , an integration time of 20 μs was chosen. The lower energy threshold on the sum energy signal of all cells was set to 770 *keV*, well below the Compton edge of the 2.2 *MeV* γ -radiation emitted in neutron capture on protons.

Figure D.10 summarizes the result of these measurements. The upper figure depicts the time range up to 20 μs . This curve is associated with the moderation time of the neutrons and indicates that most of the neutrons are thermal after about 10 μs . The lower portion of the figure displays delay times up to 300 μs and is associated with the neutron capture time. The data is well described by an exponential decay law with a time constant of $\tau_{capture} = 171 \pm 19 \mu s$. This agrees well with Ref. [96] in which the neutron capture time in a similar mineral–oil–based scintillator is measured to be 160 μs .

D.5 The Monte Carlo Simulation

D.5.1 Inputs

The Monte Carlo simulation is divided into two distinct parts; a neutron code tracks the neutrons, registering proton recoils and γ production. The γ 's are subsequently

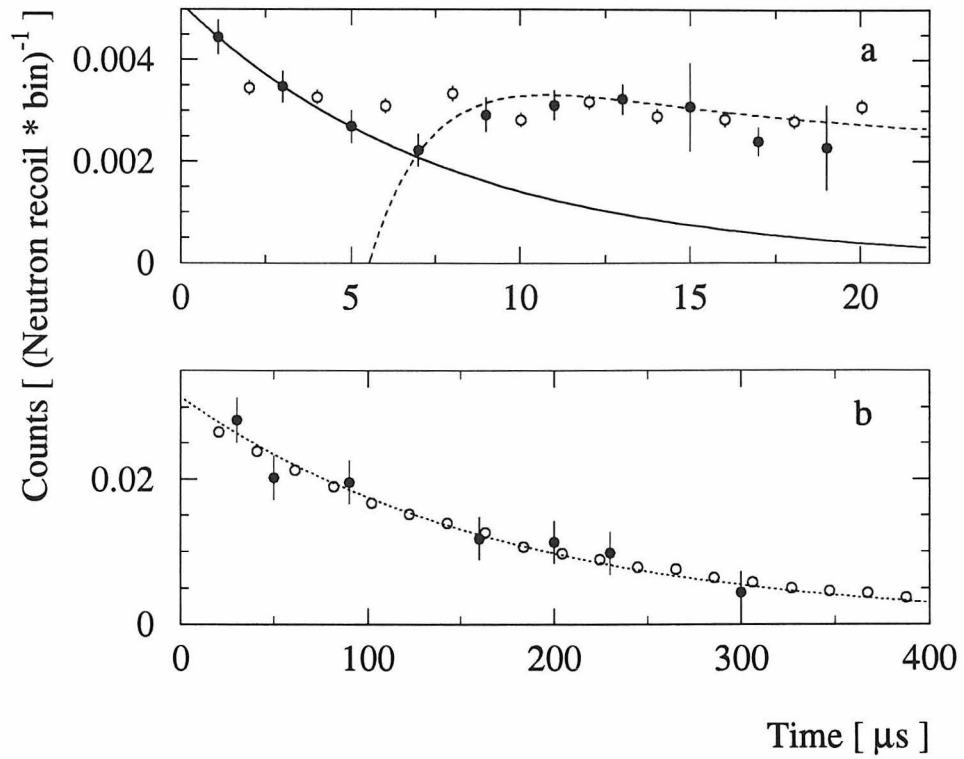


Figure D.10: Background-subtracted number of delayed coincidences as a function of the delay time. In the upper graph a integration time of $2 \mu s$ was used. For the lower curve the bin size is $20 \mu s$. Closed circles represent the experimental data; open circles are Monte Carlo results. The solid and the dashed lines are fits to the experimental data.

followed using the well-established EGS4 code. We concentrate here on a test of the neutron part.

There are three main ingredients in the neutron code: (1) the cross sections, (2) the conversion of the energy of the recoil protons to that of the equivalent electron, and (3) the energy distribution of the neutron source, as mentioned in a previous section. The target is composed of hydrogen and carbon. The interactions of neutrons and ^{12}C include elastic and inelastic scattering as well as the (n, γ) reaction. The corresponding cross sections agree well with published data [97]. For neutrons of kinetic energy below 25 MeV, as in our case, sophisticated processes such as $(n, 2n)$, (n, α) and (n, p) can be neglected, which simplifies the neutron simulation.

The interactions of neutrons with hydrogen include elastic scattering and the (n, γ) reaction, while other processes are negligible. The precision of the $(n, ^1\text{H})$ cross sections proved to be satisfactory since the capture time of the neutron on hydrogen from the simulation is in good agreement with the measurement described earlier.

The kinetic energy of the protons imparted by recoiling neutrons is converted to the equivalent electron energy using an empirical formula given by [93]. The Monte Carlo data was determined to be insensitive to the precision of the conversion rule for low-energy recoil protons.

D.5.2 The Energy Distribution of the Neutron Source

The *AmBe* source emits neutrons through the following reaction: α (5.49 MeV) + $^9\text{Be} \rightarrow ^{12}\text{C} + \text{n} + 11.21$ MeV, where the α particle is produced through ^{241}Am decay. About 80% of the time, the carbon nucleus is left in its 4.43 MeV excited state [91], the remainder of the Q-value energy appearing as kinetic energy of the neutron and carbon nucleus. These neutrons, emitted in coincidence with a 4.43 MeV de-excitation gamma, were selectively used in the experiment. To properly generate the energy distribution of these neutrons, we take the results of Ref. [91], reproduced here as Figure D.11. Depicted are the angular distribution of neutrons with respect to the α momentum, and the neutron energy as a function of emission angle. By

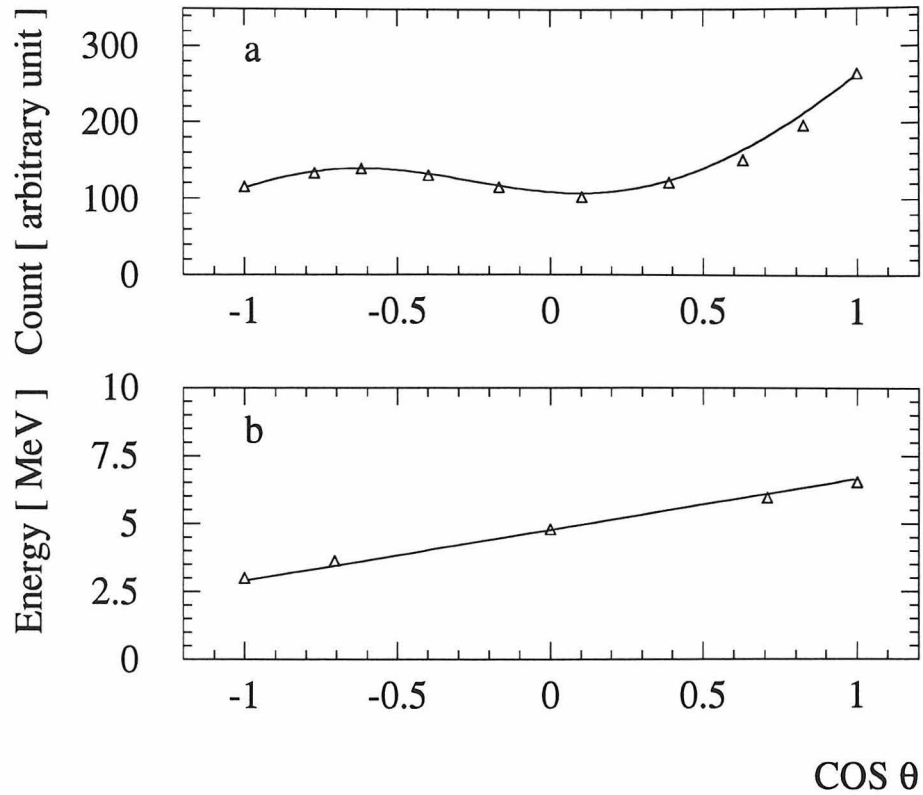


Figure D.11: Neutrons emitted in coincidence with a 4.43 MeV gamma ray from the *AmBe* source: a) Neutron emission probability versus angle in $\cos(\theta)$. b) Neutron energy versus angle in $\cos(\theta)$. θ is measured with respect to the α -particle momentum. The solid lines are parameterizations of the data used to generate the input neutron spectrum.

folding the two spectra, the energy spectrum of the emitted neutrons is generated (see Figure D.12). This spectrum was an input to the Monte Carlo simulation.

D.5.3 The Simulation

The actual trigger was simulated in the Monte Carlo code, as were the details of the neutron source such as its geometry and distance from the scintillator cells. A trigger was defined as the deposit of at least 250 keV, either from proton recoil or inelastic carbon excitation, in the trigger cell. These events are defined as singles, and are

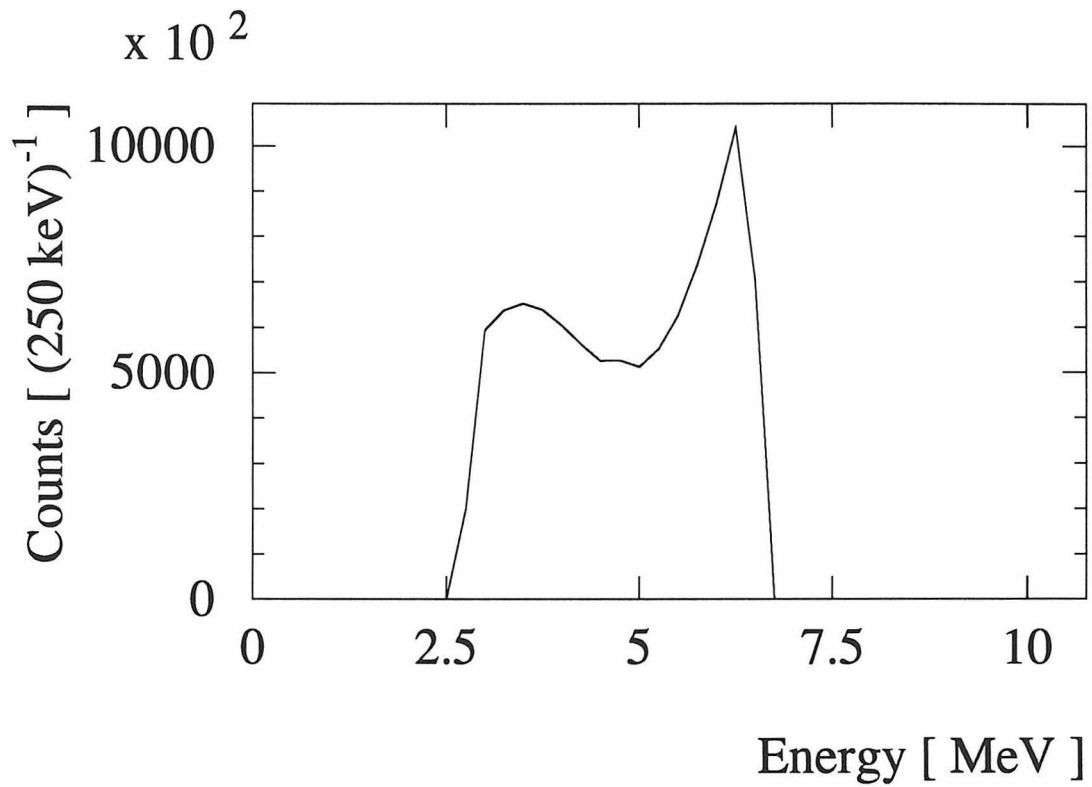


Figure D.12: The energy distribution of the neutron source obtained by folding the spectra of the preceding figure. It represents the neutrons emitted in coincidence with an excitation of the 4.43 MeV state of carbon. This is the input spectrum of the Monte Carlo code.

compared with the experimental data.

D.5.4 Results and Comparison with the Experiment

Neutron Thermalization and Capture on Hydrogen

The distribution of the neutron capture and thermalization times are shown in Figure D.10, where they are compared to measured results. The simulation yields a time constant for neutron capture on protons of $178 \pm 1 \mu s$, which is in good agreement with the measured value of $171 \pm 19 \mu s$ discussed previously.

Measured and Simulated Energy Distribution of *Single* Events

Figures D.13 and D.14 show a comparison of the Monte Carlo and experimental data on the energy distribution of singles for different trigger schemes. The spectra are not normalized to each other and thus depict absolute event rates. Shown also in the figures are the individual contributions from recoiling neutrons and 4.4 MeV gammas. Figure D.15 depicts the simulated energy spectrum of the 4.4 MeV gammas Compton scattering in the trigger cell. The absolute integrated singles rates obtained experimentally and through Monte Carlo simulation are listed in Table D.3.

Table D.3: Integrated absolute singles event rates presented for three different trigger cells. Experimental rates are compared with Monte Carlo simulated rates.

cell #	experiment (Hz)	Monte Carlo (Hz)
3	40.8	53.9(2)
8	3.5	3.00(6)
13	0.6	0.30(3)

Measured and Simulated Triples to Singles Ratio

Table D.4 gives the triple coincidence probabilities measured, and those calculated by Monte Carlo. On average, the measured and simulated triple coincidence probabilities

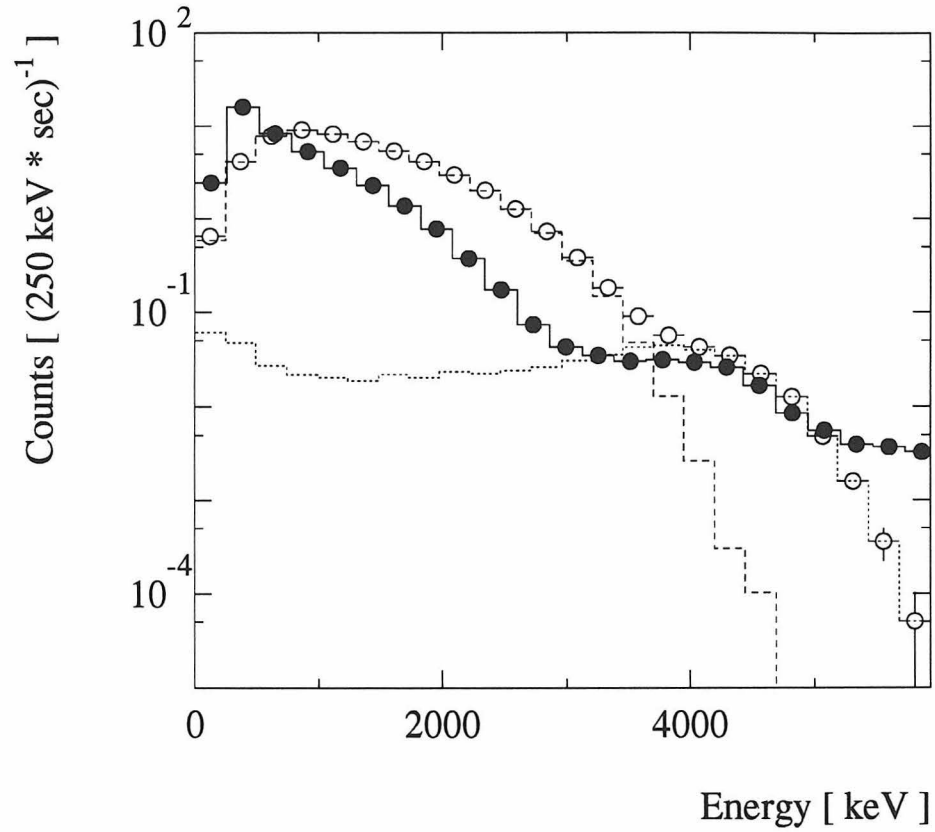


Figure D.13: Comparison of the measured and simulated energy distribution of cell #3. The closed circles indicate the experimental data; open circles represent the Monte Carlo result. The neutron and gamma components computed by the Monte Carlo codes are indicated by dashed or dotted line, respectively.

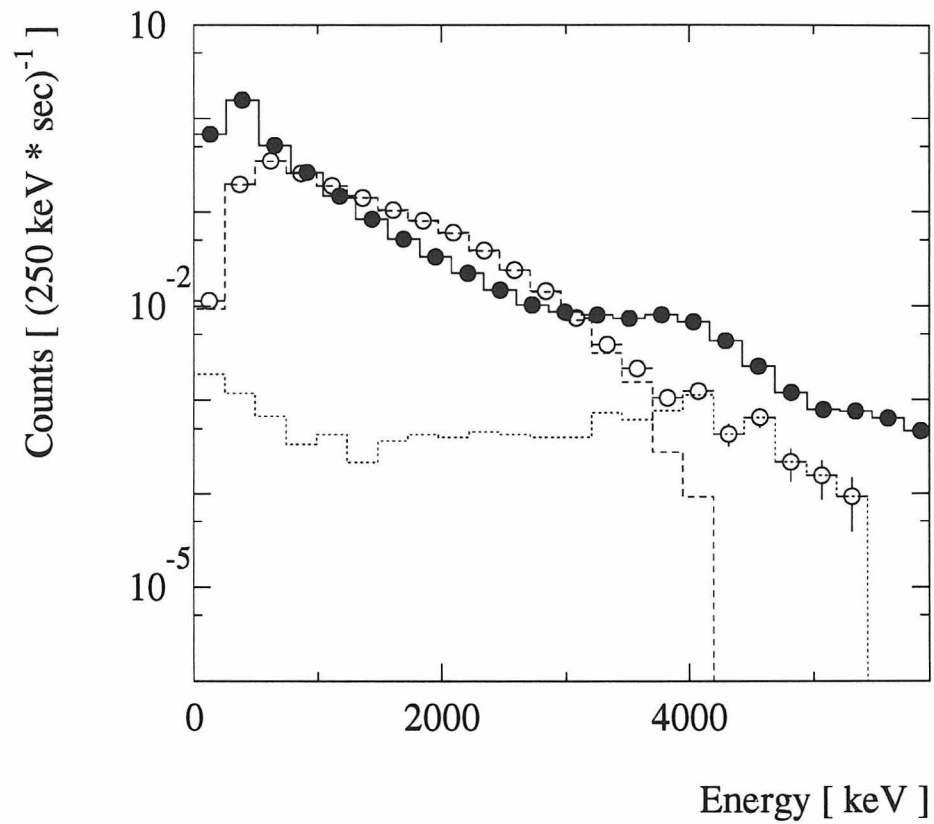


Figure D.14: Comparison of the measured and simulated energy distribution of cell #8. The closed circles indicate the experimental data; open circles represent the Monte Carlo result. The neutron and gamma components computed by the Monte Carlo codes are indicated by dashed or dotted line, respectively.

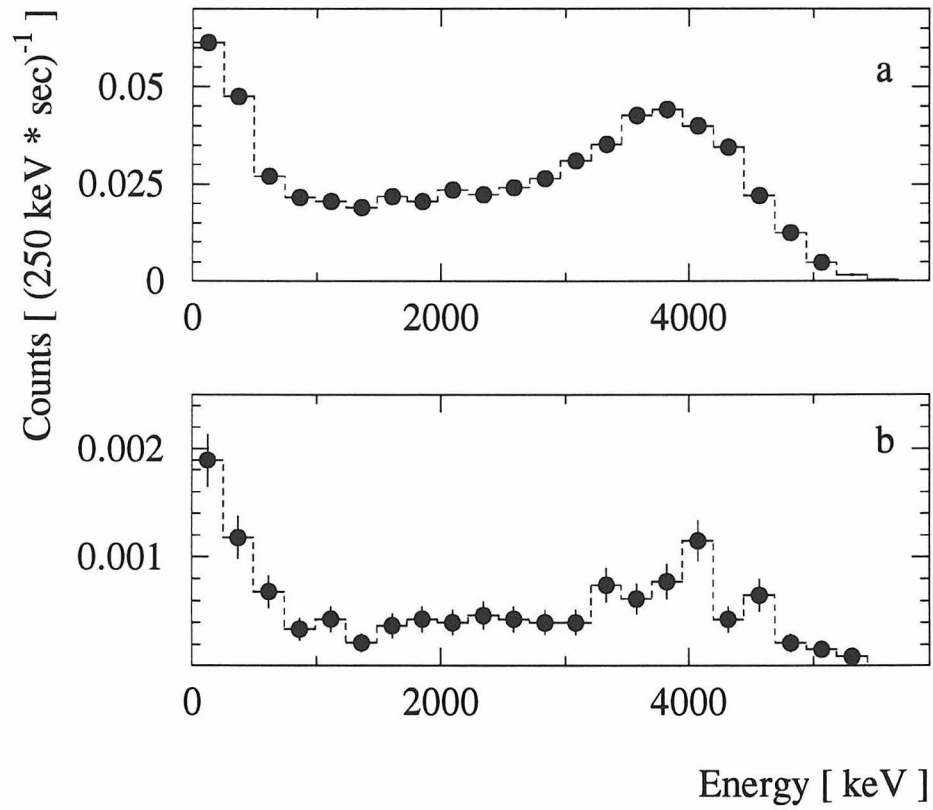


Figure D.15: Energy deposit due to 4.43 MeV gamma rays, computed by the Monte Carlo code, for a) cell #3, and b) cell #8.

agree within a factor 2.4. Due to the large experimental errors, the deviations are on the 2σ level. That fact that the MC numbers seem to be generally too low indicate that the deviation is most likely due to systematic errors. Figure D.16 provides a graphical comparison of these data. Figure D.17 further illustrates the suppression brought about by the triple coincidence requirement.

Table D.4: Comparison of experimental and Monte Carlo triple-coincidence probabilities. All numbers were derived applying the primary energy cut described previously. From the experimental data sample (Exp) the unshielded background-subtracted values were taken. The quoted error combines statistical and systematic uncertainties for the experimental data. For the Monte Carlo (MC) data, only the statistical errors are given. In order to estimate the deviation of both data samples, the difference of the MC and experimental results was divided by the folded error of both numbers. The distribution of the differences should be centered around zero for identical data samples. The division then transforms the distribution into a standard normal distribution.

Trigger cell #	Side cell #	Exp [10^{-3}]	MC [10^{-3}]	Deviation [σ]
3	2 + 4	5.4 ± 2	2.40 ± 0.08	1.5
8	7 + 9	8.4 ± 4	2.5 ± 0.3	1.6
	3 + 13	14.5 ± 6	1.7 ± 0.3	2.2
	4 + 12	5.2 ± 2	1.0 ± 0.3	2.1
13	12 + 14	3.8 ± 2	4 ± 1	–

Individual Components of the Triple Events

Using the Monte Carlo code, the individual components of the triple events were investigated and broken down according to those produced solely by neutron recoils, those produced solely by 4.4 MeV excitation gammas, and those produced through a combination of both. The contribution to the triples rate from neutrons alone is clearly dominant as shown in Table D.5. Of the triple events produced by gammas, only about 10% come from e^+e^- pair production.

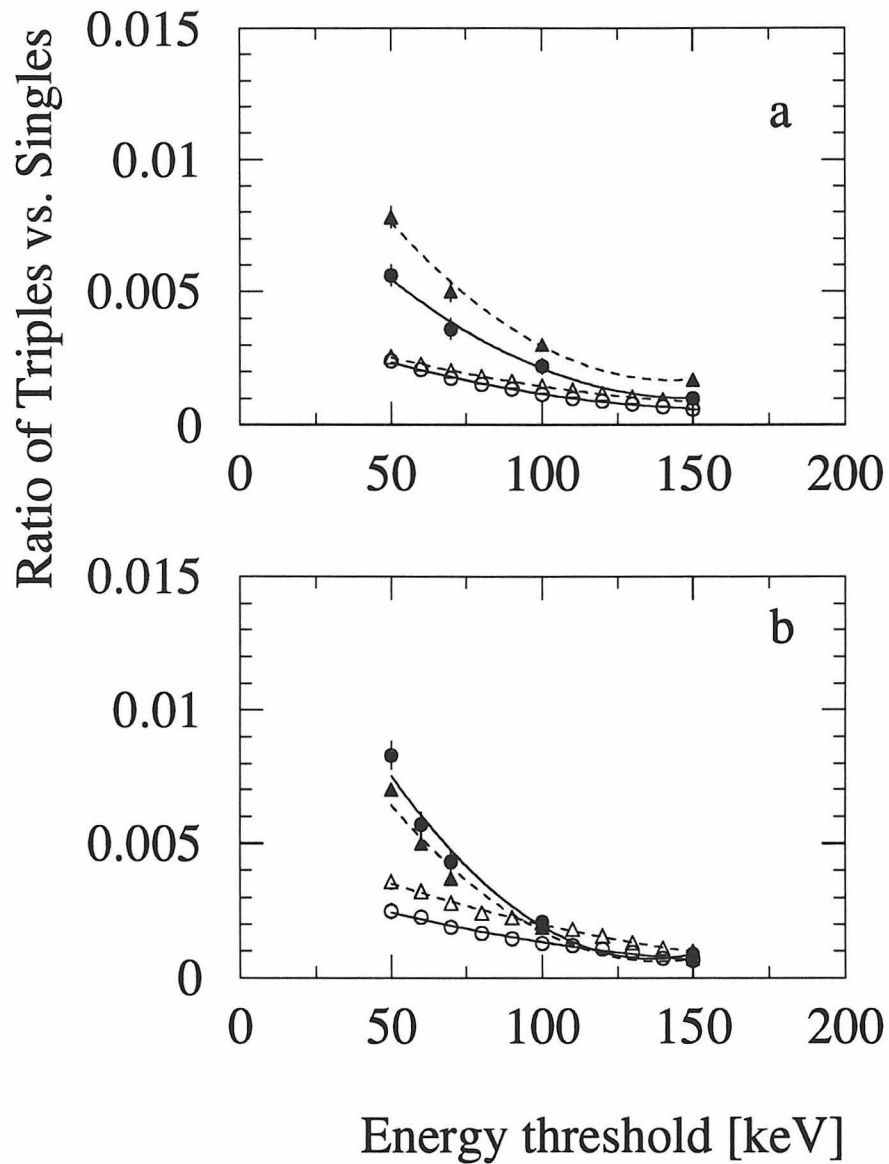


Figure D.16: The ratio of the triple over single events, a) requesting cell #3 as the trigger cell. b) cell #8 as the trigger cell. Closed symbols represent experimental data and open symbols represent Monte Carlo results. In both experimental and Monte Carlo data, the energy cut in the center cell, #3 or #8, ranges from 250 keV to 3600 keV for the triangles, and 800 keV to 3600 keV for the circles. The low energy cut of the side cells, cell #2 and 4 in a) and cell #7 and 9 in b), varies from 50 keV to 150 keV as indicated along the abscissa. The upper energy cut for the side cells remains at 600 keV. The solid and dashed lines guide the eye.

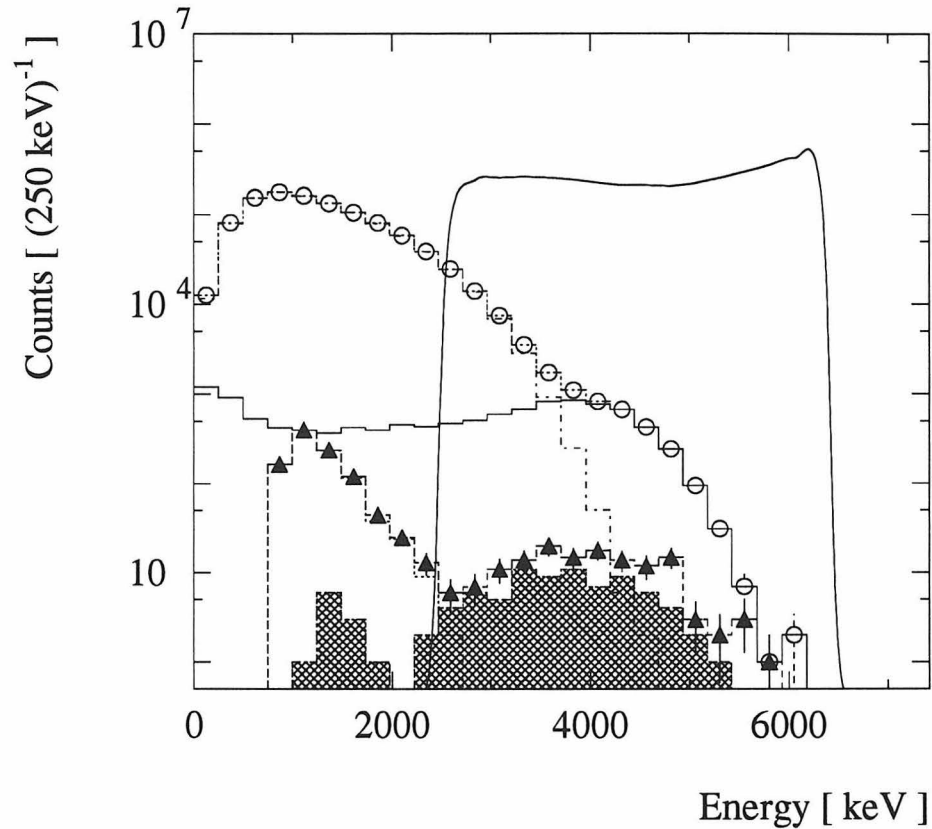


Figure D.17: Graphical overview of the background rejection of neutrons using Monte Carlo data from trigger cell #3. The solid line represents the input neutron spectrum, containing $4 \cdot 10^6$ events. The open circles represent $1 \cdot 10^6$ *single* events triggering cell 3. (The neutron and gamma components are indicated by the dot-dashed and solid histograms, respectively). The closed triangles represent 1600 *triple* events (the neutron and gamma components are indicated by the dashed histogram or hatched area, respectively). The strong background reduction due to the triple coincidence requirement is readily visible.

Table D.5: Fractions of triples produced by neutrons alone, gammas alone, and by combined neutron and gamma processes. Neutrons clearly dominate the triple rate.

cell #	neutron [%]	gamma [%]	neutron and gamma [%]
3	0.86(3)	0.08(1)	0.06(1)
8	0.94(10)	-	0.01(1)

D.6 Conclusion

The Monte Carlo code used to estimate neutron-induced triple coincidence probabilities was experimentally tested. We find fair agreement (factor ~ 2.4) between measured and simulated triple-coincidence rates. The measured and simulated singles spectra also show fair agreement and we find that fine tuning, e.g., changing the spectral shape of the neutrons emitted by the source, can lead to better agreement. In addition, we find that the simulation correctly reproduces the factor ~ 100 singles rate drop in going from cell 3 to cell 13, and verifies the independence of the triples/singles ratio on the trigger cell used. We also find good agreement between the measured and simulated neutron capture and thermalization times.

Because the detector size and the energy spectrum of the neutrons is quite different from that of the planned San Onofre detector, this experimental result cannot be used to draw direct conclusions about the large setup. What we have shown is that the Monte Carlo code correctly models neutron transport and interactions in our test setup. The relevant questions for the San Onofre detector are how reliably a different geometry can be parametrized, and how precisely the code will work at larger neutron energies. While the first point seems to be trivial, the second will be studied in more detail. The code studied here will be compared to a new version of GEANT 3.16 (CERN) and the hadronic code CALOR (Oak Ridge) which includes non-standard processes such as $(n, 2n)$, (n, α) , and (n, p) . CALOR has recently been updated to allow tracking of low energetic neutrons. The imperfect treatment of those low-energy neutrons in GEANT prevented its use in the past. Apart from the contribution of

these non-standard reaction channels at higher neutron energies ($> 20 \text{ MeV}$), the extrapolation seems to be rather safe, since all cross-section curves show a smooth energy dependence [97].

The planned San Onofre experiment would still have its full sensitivity should a factor ~ 2.4 increase in neutron-induced triple coincidences be valid there. The correlated neutron-induced background would then go up from 4 to 10 *cpd* in comparison to an expected ν -signal rate of 34 *cpd*.

Bibliography

- [1] M. Gell-Mann and A. Pais, Phys. Rev. **97** (1955) 1387.
- [2] B. Pontecorvo, Sov. Phys. JETP **6** (1958) 429.
- [3] Z. Maki et al., Prog. Theor. Phys. **28** (1962) 870.
- [4] S. Weinberg, Phys. Rev. Lett. **19** (1967) 1264.
- [5] S. Bilenky and B. Pontecorvo, Phys. Reports **41** (1978) 225.
- [6] For example see C. Quigg, *Gauge Theories of the Strong, Weak, and Electromagnetic Interactions* (Addison-Wesley Publishing Co., New York 1983).
- [7] P. Raczka, A. Szymacha, Phys. Rev. **D49** (1994) 1655.
- [8] G. Fogli, E. Lisi, G. Scioscia, Phys. Rev. **D52** (1995) 5334.
- [9] F. Boehm and P. Vogel, *The Physics of Massive Neutrinos, 2nd Edition* (Cambridge University Press, Cambridge, England, 1992).
- [10] J.N. Bahcall and R. Davis, Science **191** (1976) 264.
- [11] R. Davis, Prog. Part. Nucl. Phys. **32** (1994) 13.
- [12] K.S. Hirata, et al., Phys. Rev. **D44** (1991) 2241.
- [13] J.N. Abdurashitov et al., Phys. Lett. **B328** (1994) 234.
- [14] P. Anselmann et al., Phys. Lett. **B357** (1995) 237.
- [15] S.P. Mikheyev and A.Y. Smirnov, Sov. J. Nucl. Phys. **42** (1985) 1441.
- [16] L. Wolfenstein, Phys. Rev. **D17** (1978) 2369.
- [17] P.F. Harrison, D.H. Perkins and W.G. Scott, Phys. Lett. **B349** (1995) 137.

- [18] H. Kwon et al., Phys. Rev. **D24** (1981) 1097.
- [19] G. Zacek et al., Phys. Rev. **D34** (1985) 2621.
- [20] Y. Declais et al., Phys. Lett. **B338** (1994) 383.
- [21] B. Achkar et al., Nucl. Phys. **B434** (1995) 503.
- [22] K.C. Wang et al., *Neutrino-84, 11th Int. Conf. Neutrino Physics and Astrophysics* eds. E.K. Kleinknecht and E.A. Paschos, Singapore: World Scientific (1984) 177.
- [23] L.A. Ahrens et al., Phys. Rev. **D31** (1985) 2732.
- [24] L. Borodovsky et al., Phys. Rev. Lett. **68** (1992) 274.
- [25] F. Bergsma et al., Phys. Lett. **142** (1984) 103.
- [26] C. Angelini et al., Phys. Lett. **B179** (1986) 307.
- [27] C. Athanassopoulos et al., Phys. Rev. Lett. **75** (1995) 2650.
- [28] B. Armbruster et al., Nucl. Phys. **B38** (1995) 235.
- [29] G.N. Taylor et al., Phys. Rev. **D28** (1983) 2705.
- [30] E.B. Brucker et al., Phys Rev. **D34** (1986) 2183.
- [31] N. Ushida et al., Phys. Rev. Lett. **57** (1986) 2897.
- [32] F. Dydak et al., Phys. Lett. **b134** (1984) 281.
- [33] K. Winter, Nucl. Phys. **B38** (1995) 211.
- [34] N.W. Reay et al., Fermilab Proposal P803, *Muon Neutrino to Tau Neutrino Oscillations* (1993).
- [35] J.N. Bachall and R. Ulrich, Rev. Mod. Phys. **60** (1988) 297.
- [36] Y. Fukuda et al., Phys. Lett. **B335** (1994) 237.

- [37] R. Becker–Szendy et al., Nucl. Phys. **B38** (1995) 331.
- [38] M. Goodman, Nucl. Phys. **B38** (1995) 337.
- [39] K. Daum et al., Z. Phys. **C66** (1995) 417.
- [40] M. Aglietta et al., Europhys. Lett. **15** (1991) 559.
- [41] E. Ables et al., *The Minos Collaboration at FNL*, Proposal (1995).
- [42] J.P. Revol, in *Frontiers in Neutrino Astrophysics*, ed. Y. Suzuki, Universal Academy Press, Tokyo (1993).
- [43] J. Seguinot et al., LPC 92-31, College de France (1992).
- [44] F. Boehm et al., *The Caltech Neutrino Experiments at San Onofre*, Caltech (1993); F. Boehm et al., *Proposal for the San Onofre Neutrino Oscillation Experiment*, Caltech (1994).
- [45] H. de Kerret et al., *The Chooz Experiment*, Proposal, LAPP report (1993).
- [46] S. Ahlen et al., Nucl. Instr. and Meth. **A324** (1993) 337.
- [47] K. Schreckenbach et al., Phys. Lett. **B99** (1981) 251.
- [48] F. von Feilitzsch et al., Phys. Lett. **B118** (1982) 162.
- [49] A. A. Hahn et al., Phys. Lett. **B218** (1989) 365.
- [50] P. Vogel and J. Engel, Phys. Rev. **D39** (1989) 3378.
- [51] P. Vogel, Phys. Rev. **D29** (1984) 1918.
- [52] The Particle Data Group, *Particle Properties Data Booklet*, Phys. Lett. **B239** (1990).
- [53] A. Piepke, "Note on the calibration of a 9 m cell using compton edges of γ point sources," California Institute of Technology internal report (1995) unpublished.

- [54] Thanks to Dr. J. Bercaw, Dr. M. Boehm, and Dr. D. Jamriska for helpful discussions of this chemistry.
- [55] G. Zacek, F. von Feilitzsch, R. Mössbauer, L. Oberauer, V. Zacek, F. Boehm, P. Fisher, J. Gimlett, A. Hahn, *Phys. Rev. D* **34(9)** (1986) 2621–2636.
- [56] B. Crasemann, et al., *Phys. Rev.* **102(5)** (1956) 1344.
- [57] GEANT Detector Description and Simulation Tool, CERN program library, CERN-CN Division, Geneva, Switzerland. GEANT ver. 3.16 and GCALOR interface ver. 1.04 were used.
- [58] C.K. Hargrove, et al., *Nucl. Instr. and Meth.* **A357** (1995) 157-169.
- [59] K.H. Beckurts and K. Wirtz, *Neutron Physics* (Springer-Verlag, New York, N.Y. 1964).
- [60] National Nuclear Data Center, Brookhaven National Laboratory, Online Nuclear Data Service, telnet:130.199.112.132.
- [61] M.A. Ali, et al., *J. Phys. G: Nucl. Part. Phys.* **20** (1994) 1943–1953.
- [62] R.C. Greenwood, et al., *Nucl. Phys.* **A304** (1978) 327–428.
- [63] This model was taken from A. Gavron, “Statistical-Model Calculations with Angular-Momentum Coupling” in *Computational Nuclear Physics 2: Nuclear Reactions*, ed. K. Langanke, J.A. Maruhn, S.E. Koonin, Springer-Verlag, New York, N.Y. (1993); thanks to Dr. Karlheinz Langanke for running this code.
- [64] T. Kozłowski, et al., *Nucl. Phys.* **A166** (1971) 145.
- [65] S. Charalambus, et al., *Nucl. Phys.* **A436** (1985) 717.
- [66] M.C. Chen, *Experiments in Neutrino Mass and Mixing*, Thesis, California Institute of Technology, Pasadena, CA (1994).
- [67] S. Hayakawa, *Phys. Rev.* **84** (1951) 37.

- [68] J.C. Barton, "The Spectrum of Neutrons at 60 hg m⁻²," in *Proc. of the 19th Int. Conf. on Cosmic Rays*, La Jolla 1985, Physical Society, London Institute of Physics, London (1985) 98.
- [69] D.H. Perkins, "Calculation of the Neutron Background in Soudan 2," Internal Report, Soudan 2 collaboration, (1990).
- [70] O.G. Ryazhskaya, "Is there an Excess of Electron Neutrinos in the Atmospheric Flux?," Internal Report, Laboratori Nazionali del Gran Sasso, L'Aquila, Italy (1994).
- [71] J. Kleinfeller, Karmen collaboration, private communication (1996).
- [72] T.K. Gaisser, *Cosmic Rays and Particle Physics*, Cambridge University Press, Cambridge, England (1990).
- [73] K. Inoue, Thesis, Kamiokande, Japan (1993).
- [74] *Table of Isotopes*, ed. C.M. Lederer and V.S. Shirley, John Wiley and Sons, New York, N.Y. (1978).
- [75] Annex 14, *SNO Collection of Annexes*, SNO collaboration (1987).
- [76] Thanks to Dr. Jean-Luc Vuilleumier of the Institut Physique Neuchatel, Neuchatel, Switzerland.
- [77] Appendix 3, ICP-MS Analysis, (15 September, 1992).
- [78] H. Kwon, *Experimental Investigations of Neutrino Oscillations at a Fission Reactor*, Thesis, California Institute of Technology, Pasadena, CA (1981); H.Kwon et al., *Phys. Rev.* **D24**, (1981) 1097.
- [79] T. Ishikawa, Y. Miyama, T. Nakamura, *Nuclear Science and Engineering*, **116** (1994) 278-290.

- [80] D.C. Larson, J.A. Harvey, N.W. Hill, “Measurement of Neutron Total Cross Sections at Orela to 80 MeV”, Private Communication to *NNDC/BNL* on 8 Aug. 1986.
- [81] Christian Zeitnitz, Institute für Physik, Universität Mainz, D-55099 Mainz, private communication.
- [82] Tony Gabriel, Oak Ridge National Laboratory, Oak Ridge, TN, private communication.
- [83] S. Mouatassim, G.L. Costa, G. Guillaume, B. Heusch, A. Huck, and M. Moszynski, *Nucl. Instr. and Meth.* **A359** (1995) 530–536.
- [84] S.D. Howe, P.W. Lisowski, G.J. Russel, N.S.P. King and H.J. Donnert, *Nucl. Instr. and Meth.* **227** (1984) 565–570.
- [85] V. Patocchio, G.D’Erasmus, E.M. Fiore, L. Fiore, N. Grion, G. Guarino, A. Pantaleo and R. Rui, *Nucl. Instr. and Meth.* **A305** (1991) 150–157.
- [86] S. Ito, K. Maeda, T. Fukuda, O. Konno, T. Suda, M. Takeya, T. Terasawa, *Nucl. Instr. and Meth.* **A354** (1995) 475–478.
- [87] S. Cierjacks, M.T. Swinhoe, L. Buth, S.D. Howe, F. Raupp, H. Schmitt, L. Lehmann, *Nucl. Instr. and Meth.* **192** (1982) 407–413.
- [88] F. Boehm et al., Proposal for the *San Onofre Neutrino-Oscillation Experiment*, January 1994.
- [89] A version of the neutron code BALL modified by T.J. Radcliffe (1991) has been used. This program is based on the code MODER written by R. Heaton for the SNO detector (1986).
- [90] K.S. Hirata et al., *Phys. Lett.* **B280** (1992) 146.
- [91] F. Ajzenberg-Selove and P. H. Stelson, *Phys. Rev.* **120** (1960) 500.
- [92] E. A. Lorch, *Int. J. Appl. Radiat. Isotopes* **24** (1973) 588.

- [93] K. H. Maier and J. Nitschke, *Nucl. Instr. and Meth.* **59** (1968) 227.
- [94] D. J. Hughes and J. A. Harvey, 'Neutron Cross Sections', Brookhaven National Laboratory–Upton–New York, 1955.
- [95] J. H. Hubbell, 'Photon Cross Sections, Attenuation Coefficients and Energy Absorption Coefficients from 10 *keV* to 100 *GeV*', National Bureau of Standards, NSRDS–NBS **29** (1969).
- [96] F. Boehm, E. Bonvin, S. Hatamian, H. Henrikson, S. Ludtke, K. van Bladel and P. Willems, *Nucl. Instr. and Meth.* **A300** (1991) 395.
- [97] S. F. Mughabghab, M. Divadeenam and N. E. Holden, 'Neutron Cross Sections', 4th ed., Academic Press Inc., 1981-1984. V. McLanne, C. L. Dunford and P. F. Rose, 'Neutron Cross Section Curves', Academic Press Inc., 1988.